2009

Behaviour of Corroded X46 Steel Pipe under Internal Pressure and Axial Load

Halima Dewanbabee
University of Windsor

Behaviour of Corroded X46 Steel Pipe under Internal Pressure and Axial Load

By

Halima Dewanbabee

A Thesis
Submitted to the Faculty of Graduate Studies
through Civil and Environmental Engineering
in Partial Fulfillment of the Requirements for
the Degree of Master of Applied Science at the
University of Windsor

Windsor, Ontario, Canada

2009

Behaviour of Corroded X46 Steel Pipe under Internal Pressure and Axial Load

by

Halima Dewanbabee

APPROVED BY:

_____
Dr. D. Green, Outside Department Reader
Mechanical, Automotive and Materials Engineering

_____
Dr. M. K. S. Madugula, Department Reader
Department of Civil and Environmental Engineering

_____
Dr. S. Das, Principal Advisor
Department of Civil and Environmental Engineering

_____
Dr. J. B. Kennedy, Co-Advisor
Department of Civil and Environmental Engineering

_____
Dr. T. Bolisetti, Chair of Defense
Department of Civil and Environmental Engineering

19 June 2009

Author's Declaration of Originality

I hereby certify that I am the sole author of this thesis and that no part of this thesis has been published or submitted for publication.

I certify that, to the best of my knowledge, my thesis does not infringe upon anyone's copyright nor violate any proprietary rights and that any ideas, techniques, quotations, or any other material from the work of other people included in my thesis, published or otherwise, are fully acknowledged in accordance with the standard referencing practices. Furthermore, to the extent that I have included copyrighted material that surpasses the bounds of fair dealing within the meaning of the Canada Copyright Act, I certify that I have obtained a written permission from the copyright owner(s) to include such material(s) in my thesis and have included copies of such copyright clearances to my appendix.

I declare that this is a true copy of my thesis, including any final revisions, as approved by my thesis committee and the Graduate Studies office, and that this thesis has not been submitted for a higher degree to any other University or Institution.

Abstract

Corrosion is a major cause for buried gas pipeline failure. Current design guidelines are limited to pressure loading for assessing corroded pipeline's integrity. A few studies were conducted by other researchers to determine the remaining bending or pressure strength of the corroded pipelines under combined loading. No study was conducted to determine the axial compressive strength of the corroded pipelines although it could be the major cause of pipeline failure.

Therefore, the current study was completed using full-scale tests and a parametric study using FEA to assess the integrity of X46 corroded pipe subjected to severe axial compression and internal pressure.

Test specimens showed high ductility and never ruptured. The finite element analysis, however, showed that this pipe may rupture if internal pressure and/or corrosion dimensions are changed. The parametric study helped to develop a guidelines that the pipeline operators can use for assessing the safety of their corroded pipelines.

Dedication

To My Children
Maliha and Mehran

Acknowledgements

Table of Contents

List of Figures

xvii

List of Tables

List of Symbols

A	A geometric parameter used for geometrical calculation of corrosion defect
A_0	Original area of metal prior to metal loss
A_{eff}	Effective area of the metal loss based on an iterative calculation
A_{pipe}	Cross sectional area of the pipe
$C_{Applied}$	Applied axial compressive force on pipe wall
C_{Net}	Net axial compressive force on pipe wall
C_a	Longitudinal force exerted by the downward moving soil
C_e	Axial load in the pipe due to the end cap
C_l	Longitudinal compressive force exerted by the downward moving soil
C_t	Thermally induced axial compressive force in the pipe wall
C_v	Axial load in the pipe due to the Poisson ratio effect
D	Nominal outer diameter of the pipe
E	Elasticity modulus of the pipe material
F	Design factor
F_x	External applied longitudinal force (N)
J	Joint factor
L	Maximum projected length of the corroded region
L_A	Axial dimension of corrosion
L_C	Circumferential dimension of corrosion
L_{eff}	Total effective length of the corrosion area
M	Folias factor
M_{bc}	Critical bending moment capacity

M_y	External applied bending moment (Nmm)
P	Maximum Allowable Operating Pressure (MAOP)
$P_M / P_C / P_S$	Compressive net load when the test discontinued
P_U	Ultimate compressive net load capacity
P_Y	Compressive net load at yielding
P_{cap}	Burst capacity (pressure) of a corroded pipe
P_{corr}	Allowable corroded pipe operating pressure under internal used in DNV-RP-F101
$P_{corr,comp}$	Allowable corroded pipe pressure of a single longitudinal corrosion defect under internal pressure and superimposed longitudinal compressive stresses (N/mm2)
P_f	Failure pressure
Q	Length correction factor (bulging factor)
R_i	Internal radius of the pipe
$StD[d/t]$	Standard deviation of the measured (d/t) ratio (based on the specification of the tool)
T	Temperature factor
Z	Inertia moment coefficient
c	Circumferential length of corroded region used in DNV-RP-F101
d	Depth of corrosion
f_u	Tensile strength to be used in design
f_y	Yield strength to be used in design
h	Over closure of the surfaces
p	Internal pressure of the fluid in the pipe
pc	Contact pressure between two surfaces at a point
p_y	Internal pressure that cause yielding of the pipe material in the circumferential (hoop) direction
t	specified nominal wall thickness of pipe

$(d/t)_{meas}$	Measured (relative) defect depth
α	Coefficient of thermal expansion for the pipe material
ΔT	Difference between tie-in temperature and the operating temperature
Δ_U	Displacement at ultimate (maximum) compressive net load
ε_d	Factor for defining a fractile value for the corrosion depth
ε_{ln}^{pl}	Logarithmic or true plastic strain
ε_{nom}	Nominal strain or engineering strain
$\bar{\varepsilon}_0^{pl}$	Initial equivalent plastic strain
$\bar{\varepsilon}^{pl}$	Equivalent plastic strain
$\Delta\bar{\varepsilon}^{pl}$	An increment of the equivalent plastic strain
$\bar{\varepsilon}_f^{pl}$	Equivalent plastic strain at failure
ξ	Usage factor for longitudinal stress
γ_d	Partial safety factor for corrosion depth
γ_m	Partial safety factor for longitudinal corrosion model prediction
γ_{mc}	Partial safety factor for circumferential corrosion model prediction
μ	Friction coefficient
ν	Poisson's ratio
η	Partial safety factor for longitudinal stress for circumferential corrosion
σ_A	Elastic longitudinal compressive stress due to applied longitudinal force
σ_B	Elastic longitudinal compressive stress due to applied bending moment
σ_{L-nom}	Longitudinal stress in the nominal pipe wall
σ_f	Flow stress
σ_{nom}	Nominal stress or engineering stress
σ_{true}	True stress
σ_u	Ultimate tensile strength
σ_y	Yield stress of pipe material
σ_θ	Hoop stress

τ_1 and τ_2 Two orthogonal components of shear stress

τ_{eq} Equivalent frictional stress

τ_{crit} Critical stress

θ Ratio of circumferential length of corroded region to the nominal outside circumference of the pipe, $(c/\pi D)$

1 Introduction
1.1 General

Buried steel pipelines are widely employed system in North America for transporting natural gas, crude oil, and petroleum product. Due to its great extensions and to economic and environmental reasons, it is important to ensure the safe and efficient operation of the pipelines. Although the performance of pipelines has been excellent, their increasing age has raised concerns among pipeline operators, particularly with respect to corrosion. According to the National Energy Board of Canada, 63% of pipeline ruptures (shown in Figure 1.1) were caused by external and internal corrosion during the year 1991 – 2006 (NEB, 2008). In the USA during the 16-year period from 1985 through 2000, the most significant cause of failure in gas and oil pipelines was external interference or third party damage (27.6%). However, failures due to internal (12.8%) and external corrosion (9.9%) defects had a similar rate (Carolyn and Harvey, 2004).

Moreover, due to increased demand and scarcity of the gas, new oil and gas resources are explored in remote regions. Therefore, gas pipelines are being extended into new and more severe environments such as arctic and sub-arctic regions, ancient and currently active landslide region. This requires a better understanding and powerful analytical tools capable of analyzing all the potential adverse conditions. For example, the longitudinal compressive force developed by the downward movement of a landslide or by the difference between the pipeline in service and its tie-in temperature could cause excessive axial deformation. Because of this axial deformation, a pipeline may deform into the elastic-plastic range and form wrinkles. If this deformation exceeds the pipeline axial load capacity it may even rupture.

Although landslide-induced pipeline accidents are uncommon, specific accidents can be catastrophic. Leaks or ruptures can result in immediate fire and explosion hazards as well as lingering environmental impacts. The costs can be huge for emergency response, loss of revenues for downtime, environmental reclamation, possible regulatory fines and related litigation. There are a few accidents reported by the Transportation Safety Board

of Canada that indicate that axial compression load and deformation due to landslides and temperature variation could be detrimental for the integrity of pipelines. In 1997 such an accident occurred on the Westcoast Energy Inc. pipeline in British Columbia. Approximately 85,000 m^3 of natural gas were released and ignited. The pipeline ruptured as it was compressed longitudinally beyond its capacity due to a land slide (TBS, 2007).

1.2 Statement of Problem

Corrosion is inevitable, and therefore, ensuring the integrity of corroded pipelines is of major concern. Until now only the pressure capacity of the corroded pipeline has been considered for the pipeline integrity. The existing codes and standards such as ASME B31G (ASME, 1991), DNV-RP-F101 (DNV, 2004), CSA Z662-07 (CSA, 2007) provide methodologies which are useful for calculating the allowable operating pressure for varying degrees of corrosion damage on existing pipeline. With such procedures an operator could decide whether a corroded pipeline could remain in service or require repair or replacement of the section affected by the corrosion.

Although these assessment techniques are very helpful and are being used by the pipeline operators to determine the allowable operating pressure for the existing corroded pipeline, they do not address a number of ambiguities associated with application of these criteria to service-induced corrosion metal loss. For example, ASME B31G (ASME, 1991) considers only internal pressure; longitudinal loads due to landslides, settlements and temperature variation are ignored. As there is no guideline available to pipeline operator regarding the axial capacity of the corroded pipeline it is necessary to develop a criterion for assessing the integrity of the corroded pipeline for excessive longitudinal deformation.

1.3 Objectives and Scope

The present research work was initiated to provide the information regarding the behaviour of corroded steel pipe when it is operated under severe axial compressive force and large deformation. Consequently, the following issues are the primary objectives of this research project.

1. To determine the load-deformation behaviour of the externally corroded X46 pipe subjected to combined monotonically increasing axial load and constant internal pressure.

2. To undertake a parametric study to determine the effect of varying internal pressure, depth of the corrosion, and circumferential dimension of corrosion on the load-deformation behaviour of the X46 grade corroded steel pipe.

3. To investigate the modes of failure and the effect of varying internal pressure, depth of the corrosion, circumferential dimension of corrosion on these failure modes of the X46 corroded steel pipe subjected to combined monotonically increasing axial load and constant internal pressure.

The scope of this project was limited to investigation of the load-deformation behaviour of API 5L X46 steel pipe having *D/t* value around 34 under monotonic axial compression and constant internal pressure. A total of ten full-scale tests and sixty five numerical models having above mentioned material and geometric properties were analyzed to investigate the load-deformation behaviour and failure modes of corroded steel pipe subjected to combined monotonically increasing axial load and constant internal pressure. Although, later six of ten test specimens were tested under cyclic load to obtain the remaining strength of these specimens under cyclic loading, the load deformation behaviour of these specimens under cyclic loading is beyond the scope of this project. Thus, the behaviour under cyclic deformation is included in Appendix A.

1.4 Organization of the Thesis

This thesis is divided into six major chapters and two other small chapters: the first chapter is Introduction and very last chapter Chapter 8 is Summary, Conclusions, and Recommendations. Chapter 2 summarizes the findings of previous works obtained from the literature and existing codes/standard on corroded steel pipe subjected to internal pressure and/or bending moment and axial compressive force. Chapters 3 and 4 discuss the full-scale test program and the results obtained from the tests. In the following two chapters, Chapters 5 and 6, numerical modelling of full-scale tests and coupon tests and the comparisons of the behaviour obtained from experiments and numerical simulations

are discussed. Chapter 7 discusses the results obtained from the parametric study done by analyzing sixty five numerical models.

Comparison of Rupture by Cause
NEB (1991-2006)

20%

7%

7%

3%

63%

Corrosion

External Interference

Material (Manufacturing or Construction)

Geotechnical

Other Causes
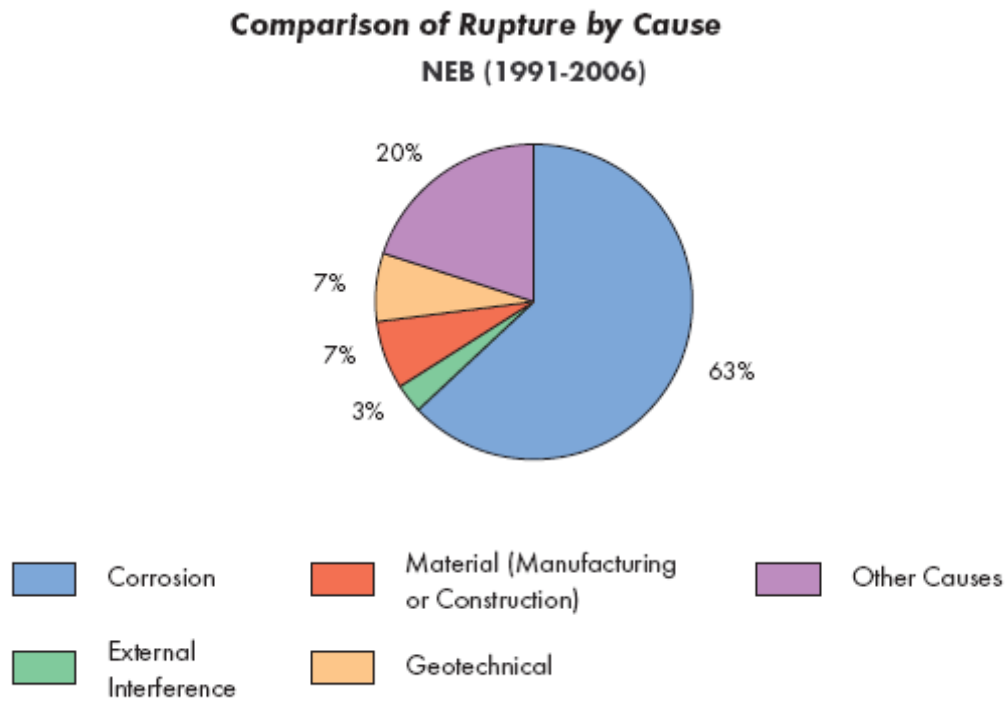
Figure 1.1 Causes of rupture of energy pipeline according to NEB (NEB, 2008)

2 Literature Review
2.1 General

A review of the literature has been conducted to investigate how current guidelines and the previous research works address the corrosion problem in pipeline industry. It has been found that current codes have the guidelines for allowable operating pressure of the corroded pipe and most of the research works have been conducted to determine the pressure capacity or bending moment capacity of the corroded pipe. The focus of the review has been mainly to understand the behavior of the corroded pipe under combined axial compression and internal pressure. Although current codes and the research works focused on the burst pressure with or without some extent of axial stress due to axial compression and/or bending moment, these papers have been very helpful to understand the problem related to pipeline corrosion and axial compression. Most of the literatures presented here are based on the experimental study. Some of the literatures presented here are also based on studies using finite element analysis (FEA). This chapter also includes two technical papers that discussed the analytical solutions to calculate the bending moment capacity and burst pressure capacity of corroded energy pipeline.

2.2 Causes of Pipeline Corrosion

Underground pipelines may be required to sustain several environmental hazards. The corrosion process occurs naturally on unprotected steel exposed to the environment. Usually pipelines suffer various degrees of deterioration due to aggressive environments. Material corrosion is the most common form of pipeline structural deterioration and is a matter of serious concern for both the strength and durability functions of steel pipelines. Corrosion may act on the pipeline either internally or externally or both.

Buried pipelines are typically protected from external corrosion using coatings and cathodic protection. However, improper coating installation, coating failure due to mechanical damage or improper use of cathodic protection can lead to significant external corrosion. Coating degradation is a result of soil stresses, excessive operating temperatures, hydrostatic testing, poor application and time. A poorly coated line or a line

with deteriorated coating becomes difficult and sometimes impossible to be cathodically protected. If the coating deterioration is intermittent along the pipeline, it is usually uneconomical and ineffectual to install rectifiers and ground beds at these exposed areas in order to restore the potentials to protective levels. This may lead to corrosion consisting of individual pits, or groups of pits, or areas of general thinning of the pipe wall. In addition, preferential corrosion often occurs beside girth, spiral, and seam welds, which can be due to metallurgical differences between parents and weld metals, and less effective coating of welds with present field coating techniques. Corrosion faults in pipelines due to the degradation of coating are increasingly becoming a major problem in North America as many pipelines are approaching 40 to 50 years of age. Over the last few years, there has been general recognition of this problem and the importance of assessing the severity of corrosion damage on pipelines.

Polyethylene tape was introduced in the 1960's as a protective coating for pipelines. It was installed by spirally wrapping a continuous sheet of polyethylene around the pipe in the field. Unfortunately, this coating tends to disbond from the pipe during service due to soil stresses and/or improper installation. In many cases, the disbonded coating wrinkles and fills with water and the pipe is preferentially corroded in this area. The resulting defects tend to be relatively long and groove-like with a nearly uniform depth. In other instances, the spiral joint between adjacent wraps of the coating fails resulting in spirally oriented corrosion grooves in the pipe. Disbondment of the coating can also occur at the weld reinforcement over the longitudinal and/or girth welds which results in 'tenting' of the coating. As with wrinkling, tenting creates a gap between the coating and pipe surface which can fill with water and result in localized corrosion at or near the weld.

Asphalt-based coatings are commonly used to protect pipelines from external corrosion. Although this coating has not had the problems of polyethylene tape, placement of the pipe in the trench while the coating is still soft, or in the presence of certain types of gravel can result in piercing of the coating. This generally creates small, deep corrosion pits where the coating is pierced while the rest of the pipe remains uncorroded. This coating may also be susceptible to disbondment leading to corrosion. Today, plant-applied coatings such as fusion bonded epoxy are more common and are of higher quality

than previous coatings which were installed in the field. However, the girth welds must still be coated in the field after the pipe sections are welded together. Various forms of tape wrap and heat-shrink sleeves are used in these areas. Therefore these areas are very susceptible to corrosion attack.

Cathodic protection utilizes an imposed electric current and sacrificial anode to impede corrosion in pipelines. Although this is a proven method of protection, incorrect adjustment of the current to the pipe can allow corrosion to occur and may result coating disbandment.

In addition to external corrosion damage as a result of coating degradation and loss of cathodic protection, internal corrosion has been found to be a major problem in oil and gas pipelines. Crude oil at normal production temperatures without dissolved gases is not, by itself, corrosive. The economics of controlling corrosion (the extent of corrosion) in many oil fields are dependent on efficient separation of crude oil from other species. Water is present in crude oil and its complete removal is difficult. Water may settle on the bottom of the pipe and act as an electrolyte causing internal corrosion. Water also tends to hydrolyse other materials, particularly chlorides, to form an acidic environment which is favourable for corrosion. CO_2 and H_2S gases, in combination with water, define most of the corrosion problems in oil and gas production. Other problems include microbiological activity and the solids accumulation. The mechanisms of CO_2 corrosion are generally well defined; however, the reality inside a pipeline becomes complicated when CO_2 acts in combination with H_2S, deposited solids, and other environments. H_2S can be highly corrosive, but can, in some cases, form a protective sulfide scale that prevents corrosion. Microorganisms can attach to pipe walls and cause corrosion damage. Solids, such as formation sand, can both erode the pipeline internally and cause problems with under-deposit corrosion, if stagnant. Oxygen is not found in oil reservoirs and much is done to ensure that no oxygen enters the production environment; however, in many cases, a few parts per million (ppm) of oxygen will enter the pipelines, greatly exacerbating corrosion problems.

2.3 Types of Corrosion

Energy pipeline are subjected to both external and internal corrosion. The following sub-sections discuss various types of corrosion that occur in buried pipelines.

2.3.1 External Corrosion

As shown in Figure 2.1 according to the National Energy Board of Canada, external corrosion accounts for about 48% of ruptures on Canadian transmission pipelines from year 1994 to 2003 (Jeglic, NEB). Corrosion in the external wall of the pipeline occurs due to environmental conditions such as soil moisture content, type of soil , pH value etc. All environments are corrosive in some manner. Corrosion environments can be placed into four major categories: liquid, underground, atmospheric, and high temperature. External corrosion in the form of pitting and general metal loss results from either coating defects, inadequate cathodic protection, or both. The potential for microbially-induced corrosion (MIC) on buried pipelines is controlled by availability of nutrients, water, and electron acceptors. Usually soil moisture content and bacterial cell counts are greater in backfill material than in undisturbed earth adjacent to a pipeline. Trench backfill is not as consolidated and allows greater penetration of moisture and increased oxygen diffusion. Anaerobic bacteria thrive in waterlogged dense soil. Alternating moisture and oxygen concentrations will influence the growth of bacterial populations. Despite the numerous mechanisms that one would predict for MIC of buried pipelines, most failures have been attributed to the presence and activities of sulfate-reducing bacteria (SRB) and acid-producing bacteria (APB). In general, sandy soil favours APB; high clay soils support populations of both kinds of organisms. Another form of external corrosion, stress-corrosion cracking results from stress that causes clusters of cracks to develop and grow until the pipe fails. External stress corrosion crack results from the accumulation of the moisture on the pipe surface at an imperfection in the pipe coating. Certain corrosives in the moisture in conjunction with normal operating stresses cause cracking. To protect against all forms of external corrosion and cracking, several coating materials are used including asphalts, polyolefin tapes, and fusion-bonded epoxies (FBE). Line pipe is further protected from external corrosion by cathodic protection (CP).

2.3.2 Internal Corrosion

According to the Alberta Energy Utilities Board (AUEB) report, Statistical Series 57, July 2002, between April 2001 and March 2002 the total number of failures in Alberta due to internal corrosion in both gathering and transmission pipelines (gas and liquid) for the past 20 years are more than 5,000, averaging to almost one failure per day (Papavinasam et al., 2006). Corrosion on the internal wall of a natural gas pipeline can occur when the pipe wall is exposed to water and contaminants in the gas, such as O_2, H_2S, CO_2, or chlorides. The nature and extent of the corrosion damage that may occur are functions of the concentration and particular combinations of these various corrosive constituents within the pipe, as well as of the operating conditions of the pipeline. For example, gas velocity and temperature in the pipeline play a significant role in determining if and where corrosion damage may occur. In other words, a particular gas composition may cause corrosion under some operating conditions but not others. Therefore, it would be difficult to develop a precise definition of the term "corrosive gas" that would be universally applicable under all operating conditions. Corrosion can take the form of general or localized metal loss in pipe wall and it may also give rise to cracks in the pipeline material. The rate of corrosion depends on pipe materials, type of products being transported through pipelines, and corrosion inhibitor. Corrosion may also be caused or facilitated by the activity of microorganisms living on the pipe wall. Referred to as microbiologically influenced corrosion, or MIC, this type of corrosion can occur when microbes and nutrients are available and where water, corrosion products, deposits, etc., present on the pipe wall provide sites favorable for the colonization of microbes. Microbial activity, in turn, may create concentration cells or produce organic acids or acid-producing gases, making the environment aggressive for carbon steel. The microbes can also metabolize sulfur or sulfur compounds to produce products that are corrosive to steel or that otherwise accelerate the attack on steel.

2.4 Classification of Corrosion in Pipeline Industry

Corrosion in a pipeline is very difficult to characterise. Typically, it has an irregular depth profile and extends in irregular patterns in both longitudinal and circumferential

directions. It may occur as a single defect or as a cluster of adjacent defects separated by full thickness (uncorroded) material. There are no clear definitions of different types of corrosion defects. The simplest and perhaps most widely recognised is pitting corrosion defined as corrosion with a length and width less than or equal to three times the uncorroded wall thickness, and general corrosion defined as corrosion with a length and width greater than three times the uncorroded wall thickness. The Pipeline Operators Forum (POF) has developed a set of specifications and requirements for the inspection of pipelines by intelligent pigs, including definitions of types of metal loss features (pinhole, pitting, slotting, grooving and general) (POF, 2005). This classification is done according to their geometric parameter. These parameters of the defect are length L, width W, depth d, and reference wall thickness t. A geometrical parameter, A, is introduced and used for the geometrical classification of the corrosion defect detected by a tool. This parameter is needed especially for pipes with t < 10 mm. The geometrical parameter A is linked to the Non Destructive Examination (NDE) methods in the following manner:

> A is taken as 10 mm if thickness (t) is less than 10 mm otherwise A is taken as thickness of the pipe.

The corrosion dimension is determined according to the Figure 2.2 and Figure 2.3. The projected length of the corrosion on the longitudinal axis of the pipe gives the length, L, of an individual defect. The width, W, of an individual defect is given by its projected length on the circumference of the pipe. The projected length of W between S (starting point) and E (ending point) shall be considered in the clockwise direction, looking downstream. Corrosion depth (d) is measured by the distance between the top surface of the pipe and the deepest point of the metal loss as shown in Figure 2.3.

According to Pipeline Operator Forum (POF, 2005) the corrosion defects are classified as general type corrosion, pitting corrosion, axial grooving etc. depending on the width (W), length (L) and the geometric parameter (A) of the corrosion as shown in Table 2.1 and Figure 2.4.

2.5 Current Codes and Standards

The evaluation of the integrity of corroded pipeline continues to be a concern for the pipeline industry. Many empirical and semi empirical method were developed (for example ASME B31G criterion, DNV RP-F101 equation etc.) to predict the failure of the corroded pipes. The failure in these codes refers to burst of the corroded pipelines. Although the current codes are very helpful to assess the residual pressure strength of the pipeline with varying degree of corrosion damage and allow the pipeline operators to avoid many unnecessary expenses of repair, they are only limited to determination of the pressure capacity with or with out super imposed axial compressive stress due to bending moment and/or axial compression. The ASME B31G (ASME, 1991) is considered to be very conservative for modern highly ductile pipe material as this criterion is based on the material yield strength. The DNV-RP-F101 (DNV, 2004) presents an acceptance equation for calculating allowable operating pressure with or with out superimposed axial stress. Nevertheless everyone agrees that the pressure capacity alone does not guarantee the future integrity of the corroded pipeline (Smith and Grigory, 1996, Bjørnøy and Sigurdsson, 2000). Therefore, collapse due to axial compressive stress and bending stresses are still matter of concern for the corroded pipelines.

2.5.1 ASME B31G-1991 Equation

In early 1970, a criterion was developed by the American Gas Association (AGA)'s Pipeline Research Committee (PRC) which is renamed as PRCI (Pipeline Research Council International) to evaluate the serviceability of corroded pipe and this criterion is described in "ANSI/ASME B31G Manual for Determining the Remaining Strength of Corroded Pipeline" (ASME, 1991). The B31G criterion uses a flow stress concept, to account for large scale yielding; a fracture mechanics based "Folias" correction for pipe bulging, due to the internal pressure acting along a longitudinal through-thickness crack in a pressurized pipe, and a semi- empirical fracture-mechanical formula for calculating the remaining pressure strength of corroded pipes. This semi-empirical fracture mechanics based mathematical expression was developed based upon pressuring actual corroded pipe to failure in an extensive series of full-size burst tests. The basic principle of fracture mechanics is that the resistance of the material to unstable fracturing in the

presence of a defect is related to the size of the defect and inherent metal property, that is toughness. The tougher the material, the larger the flaw that can be tolerated before failure will occur. Also the bigger the defect, the lower the pressure at which a leak or rupture will occur. However, based on test results, it was concluded that pipe steel have adequate toughness and toughness is not a significant factor that controls the failure. Rather failure is controlled by the size of the flaws and the flow stress which is equal to 1.1 times the yield stress of the material. This criterion also assumes that the circumferential or hoop stress which is the maximum principal stress in the defect free pipe controls the failure. The failure pressure of a corrosion defect is related to the material flow stress through a bulging factor (M), known as Folias factor, and the amount of material loss due to corrosion. The Folias factor (M) is represented by Equation 2.1

$$M = \sqrt{1 + \frac{0.8L^2}{Dt}} \tag{2.1}$$

Where L is the maximum projected length of the corroded region shown in Figure 2.5; D is the nominal outer diameter of the pipe, and t is the specified nominal wall thickness of pipe shown in Figure 2.5.

The material flow stress σ_f has been taken as 1.1 times the Specified Minimum Yield Strength (SMYS) of the pipe material and the area of the metal loss was approximated as parabolic shaped area and defined by two simple parameters of the metal loss; (i) its overall projected length L and (ii) maximum depth d, which is taken as 2/3 dL. Therefore, including the safety factor F = 0.72 the Maximum Allowable Operating Pressure (MAOP), P, according to B31G criterion is calculated by Equation 2.2

$$P = F \frac{\sigma_f 2t}{D} \left[\frac{1 - \frac{2}{3}\frac{d}{t}}{1 - \frac{2}{3}\frac{d}{t}\frac{1}{M}} \right] \tag{2.2}$$

However, for long corrosion defects, the equation obviously converges towards a too high capacity due to the 2/3 factor. Therefore, for a length exceeding a specified value ($L > 4.48\sqrt{Dt}$), the capacity is assumed to be independent of length (infinite length) and a rectangular shape of corrosion defect is assumed. Hence for long defects the MAOP is obtained by Equation 2.3

$$P = F\frac{\sigma_f 2t}{D}\left[1 - \frac{d}{t}\right]$$ (2.3)

The B31G criterion is very conservative since the material flow stress σ_f is taken as 1.1 times the Specified Minimum Yield Strength (SMYS). This criterion only covers corrosion and other forms of loss of wall thickness with relatively smooth contours and causes less stress concentration such as electrolytic corrosion, galvanic corrosion, and loss of wall thickness due to erosion. This criterion does not consider other loads or stresses due to bending and/or axial loads. The corrosion assessment codes in Canada, the United States, and Europe are based on this criterion (ASME, 1991).

2.5.2 CSA Z662-07 Guideline

The guideline for allowable operating pressure for corroded pipeline in Canadian Standard Association code CSA Z662-07 (2007) is adopted from the available criteria using by the pipeline industry such as ASME B31G (1991), the 0.85dL method (Kiefner, and Vieth 1990), and the effective area method (Kiefner and Vieth, 1990). The code states that the Maximum Operating Pressure (MOP) should be less than or equal to the failure pressure of the pipe (P (fail)) containing the corroded area determined in the 0.85dL method and the effective area method which are the slightly modified from the ASME B31G criteria. According to CSA Z662-07 clause 10.9.2.5 (CSA, 2007)

$$MOP \le P(fail)(FLJT)$$ (2.4)

Where F = design factor (clause 4.3.6)

        L = location factor (clause 4.3.7)

J = joint factor (clause 4.3.8)

T = temperature factor (clause 4.3.9)

The value of F is 0.8 and the values of L, J, T are less than or equal to 1 which makes the criteria more conservative than that it has been adopted from.

The 0.85dL method, a modified method of B31G criterion, is the assessment criterion based on a simple geometric idealization of the shape of the corroded area, suitable for simple hand calculations. In this method the area of metal loss is taken as $0.85dL$ instead of 2/3 dL (area of metal loss used in ASME B31G criterion). The estimated failure pressure, P is given by the following equations:

$$P = \left(\frac{2t}{D}\right)\bar{\sigma}\left[\frac{1-0.85\dfrac{d}{t}}{1-\left(0.85\dfrac{d}{t}\right)M^{-1}}\right]$$ (2.5)

The Folias Factor for 0.85dL method is calculated as follows

$$M = \sqrt{1+0.6275\frac{L^2}{Dt}-0.003375\left(\frac{L^2}{Dt}\right)^2} \quad \text{for} \quad \frac{L^2}{Dt} \le 50$$

or (2.6)

$$M = 0.032\frac{L^2}{Dt}+3.3 \quad \text{for} \quad \frac{L^2}{Dt} > 50$$

Where $\bar{\sigma}$ = Flow Stress = SMYS + 68.9 MPa

L = The total length of the corrosion area

D = Nominal outside diameter of the pipe

t = Nominal wall thickness of the pipe

SMYS = Specified Minimum Yield Strength in MPa

d = Maximum depth of the corrosion area

M = Folias Factor for the 0.85 dL Area criterion

In the Effective Area method the effective area of the corrosion is determined through an iterative calculation procedure that results in a minimum predicted pressure. The iterative calculation procedure uses the corresponding lengths and corrosion pit depths to calculate an effective area of missing metal and an effective length. These effective areas and effective lengths are used to calculate a predicted pressure. The minimum predicted pressure that is the result of this iterative calculation procedure is presented as the safe maximum pressure for the corroded area. This safe maximum pressure in Effective Area method is calculated using the following equation

$$P = \left(\frac{2t}{D}\right)\bar{\sigma}\left[\frac{1-\dfrac{A_{eff}}{A_0}}{1-\left(\dfrac{A_{eff}}{A_0}\right)M^{-1}}\right] \tag{2.7}$$

The Folias Factor for Effective Area method is calculated as follows

$$M = \sqrt{1+0.6275\frac{L_{eff}^2}{Dt}-0.003375\left(\frac{L_{eff}^2}{Dt}\right)^2} \quad \text{for} \quad \frac{L_{eff}^2}{Dt} \le 50$$

$$\text{or} \tag{2.8}$$

$$M = 0.032\frac{L_{eff}^2}{Dt}+3.3 \quad \text{for} \quad \frac{L_{eff}^2}{Dt} > 50$$

Where $\bar{\sigma}$ = Flow Stress = SMYS + 68.9 MPa

L_{eff} = The total length of the corrosion area

A_0 = Original area of metal prior to metal loss, $L_{eff}t$

A_{eff} = The effective area of the metal loss based on an iterative calculation

D = Nominal outside diameter of the pipe

t = Nominal wall thickness of the pipe

SMYS = Specified Minimum Yield Strength in MPa

d = Maximum depth of the corrosion area

M = Folias Factor for the Effective Area criterion

2.5.3 DNV RP-F101 Criterion

The ASME B31G (ASME, 1991) criterion is validated against the extended AGA (American Gas Association) database, which includes low-grade steel materials and old burst tests. But high quality pipeline manufactured in the last 20-30 years are using pipe material that has a ductile behaviour and whose toughness is reasonably high. In addition, the corrosion detection method has been improved and measurement of the shape and size of the corrosion is quite accurate now. Therefore, a new method has been developed in recent year that is less conservative as it makes use of the fact that the pipeline material is more ductile and toughness is higher and measurement of corrosion dimension is quite accurate.

DNV RP-F101 is a result of co-operation between BG (British Gas) Technology and DNV. The results from their respective projects were merged, and formed the technical basis for the recommended practice DNV RP-F101 "Corroded Pipelines".

BG (British Gas) Technology performed more than 70 burst tests on pipes containing machined corrosion defects and developed a comprehensive database of 3D non linear finite element analysis for the burst pressure of the corroded pipe. A failure criterion was developed using these test results. In the same time period, DNV investigated the integrity of the corrode pipelines with the focus on assessment methods for modern materials and the determination of safety factors using reliability methods. The DNV project generated a database of 12 burst tests on pipes containing machined corrosion defects, including the influence of superimposed axial and bending loads on the failure pressure (Bjørnøy and Sigurdsson, 2000). A comprehensive database of 3D non-linear finite element analyses of pipes containing defects was also produced. Probabilistic methods were utilized for code calibration and the determination of partial safety factors.

In DNV RP-F101 (2004) recommendations are given for assessing corrosion defects subjected to:

1) Internal pressure loading only

2) Internal pressure loading combined with longitudinal compressive stresses

The compressive longitudinal stress can be due to axial loads, bending loads, temperature loads and the validation of these effects have been addressed in the DNV and BG Technology projects.

The equation in DNV-RP-F101 for the failure pressure is given as:

$$P_f = \frac{2t\sigma_u}{(D-t)} \frac{(1-(d/t))}{1-\frac{(d/t)}{Q}}$$

(2.9)

Where $Q = \sqrt{1 + 0.31\left(\frac{l}{\sqrt{Dt}}\right)^2}$

(2.10)

Q = Length correction factor (Bulging factor).

A = Projected area of corrosion in the longitudinal plane through the wall thickness (mm^2) (Figure 2.6)

D = Nominal outside diameter (mm)

σ_u = Ultimate tensile strength (N/ mm^2)

t = Uncorroded, measured, pipe wall thickness (mm) (Figure 2.6)

d = Depth of corrosion (mm) (Figure 2.6)

l = Length of corrosion (mm) (Figure 2.6)

The form of the equation is similar to the ASME B31G (1991) equations (Equation 2.2) but the flow stress has been changed to σ_u and the bulging factor has been significantly modified. This equation is intended to give a good estimate of the actual failure pressure for a smooth shaped rectangular corrosion defect, and is on average slightly conservative (Bjørnøy and Sigurdsson. 2000).

DNV-RP-F101 equation assumes rectangular defect shapes and therefore if the equation is used for other shapes, as for instance the parabolic shape shown in Figure 2.6, the equation underestimates (conservative) the burst capacity.

In DNV-RP-F101 (2004) there are two equations of interest, namely the capacity equation and acceptance equation. The capacity equation predicts the capacity of a

corroded pipeline as precisely as possible, for known pipeline dimensions, defect shape and size, and material properties. The expression of the burst capacity for a single longitudinally oriented, rectangular shaped, corrosion defect was developed based on a large number of FE analyses, and a series of full scale burst tests. The effect of each important parameter was investigated using finite element analyses while the accuracy of the analyses was verified by a large number of full-scale burst tests.

The simplified capacity equation for calculating burst capacity (P_{cap}) of a rectangular shaped defect is given as

$$P_{cap} = 1.05 \frac{2t.\sigma_u}{(D-t)} \frac{(1-(d/t))}{1-\frac{(d/t)}{Q}}$$ (2.11)

Where $Q = \sqrt{1+0.31\left(\frac{l}{\sqrt{Dt}}\right)^2}$ (2.12)

The factor 1.05 in the capacity equation is determined from comparison with laboratory test results with rectangular shaped metal loss defects.

The design equation (acceptance equation or equation to give the safe operational pressure), which should give the pressure at which the pipeline with corrosion defects can be operated i.e. an allowable pressure. The basis for the equations is finite element analyses and burst test results where the material properties and the pipe and defect dimensions are measured, and limited to high toughness materials and smooth shaped metal loss defects. When assessing a corrosion defect in a pipeline, although the material grade is usually known the actual material properties at the location of the defect will not be known, and the defect is measured with some degree of uncertainty. This is where the design equation is used, and where the uncertainties are accounted for.
The acceptance equation in DNV-RP-F101 is

$$P_{corr} = \gamma_m \frac{2tSMTS}{(D-t)} \frac{(1-\gamma_d(d/t)^*}{\left(1-\dfrac{\gamma_d(d/t)^*}{Q}\right)} \qquad (2.13)$$

Where $Q = \sqrt{1+0.31\left(\dfrac{l}{\sqrt{Dt}}\right)^2}$ \qquad (2.14)

$$(d/t)^* = (d/t)_{meas} + \varepsilon_d.StD[d/t] \qquad (2.15)$$

$(d/t)_{meas}$ = Measured (relative) defect depth

ε_d = Factor for defining a fractile value for the corrosion depth

γ_d = Partial safety factor for corrosion depth

γ_m = Partial safety factor for longitudinal corrosion model prediction

$StD[d/t]$ = Standard deviation of the measured (d/t) ratio (based on the specification of the tool)

SMTS = Specified minimum tensile strength

The safety factors are pre-determined for three target reliability levels, namely $10^{-3}, 10^{-4}$ and 10^{-5} annual failure probabilities and inspection accuracy. From the inspection accuracy and confidence level the standard deviation in the sizing accuracy can be determined. The standard deviation is further used to determine the γ_d safety factor and the ε_d fractile value.

The method for assessing corrosion defects under internal pressure and compressive longitudinal loading has been validated against seven full scale tests on 324 mm (12 inch) nominal diameter, 10.3 mm nominal wall thickness, Grade X52 linepipe (Bjørnøy and Sigurdsson, 2000). The method for assessing fully circumferential corrosion under internal pressure and compressive longitudinal loading has been validated against three full scale tests on 324 mm nominal diameter, 10.3 mm nominal wall thickness, Grade X52 linepipe (Bjørnøy and Sigurdsson 2000). This method is only valid for single defects. The allowable corroded pipe pressure of a single longitudinal corrosion defect subject to internal pressure and longitudinal compressive stresses can be estimated using the following procedure:

First the nominal longitudinal elastic compressive stresses are calculated at the corrosion defect based on nominal pipe thickness using following equations

$$\sigma_A = \frac{F_x}{\pi(D-t)t} \tag{2.16}$$

$$\sigma_B = \frac{4M_y}{\pi(D-t)^2 t} \tag{2.17}$$

Where

F_x = External applied longitudinal force (N) and

M_y = External applied bending moment (Nmm)

σ_A = Elastic longitudinal compressive stress due to applied longitudinal force

σ_B = Elastic longitudinal compressive stress due to applied bending moment

The combined nominal longitudinal stress is:

$$\sigma_L = \sigma_A + \sigma_B \tag{2.18}$$

The allowable corroded pipe pressure is calculated, including the correction for the influence of compressive longitudinal stress as follows:

$$P_{corr,comp} = \gamma_m \frac{2tf_u(1-\gamma_d(d/t)^*)}{(D-t)\left(1-\frac{\gamma_d(d/t)^*}{Q}\right)} H_1 \tag{2.19}$$

Where

$$H_1 = \frac{1+\frac{\sigma_L}{\xi f_u}\frac{1}{A_r}}{1-\frac{\gamma_m}{2\xi A_r}\frac{\left(1-\gamma_d(d/t)^*\right)}{\left(1-\frac{\gamma_d(d/t)^*}{Q}\right)}} \tag{2.20}$$

$$A_r = \left(1 - \frac{d}{t}\theta\right)$$

f_u = Tensile strength to be used in design

and f_y = Yield strength to be used in design

$P_{corr,comp}$ is not allowed to exceed P_{corr} given in Equation 2.13.

Where ξ = usage factor for longitudinal stress .Depending on safety class it varies from 0.9 (low safety class) to 0.8 (high safety class).

If the circumferential extent of the corrosion covers the entire diameter of the pipe then the allowable pressure is calculated using following equation. Note that this equation is not valid for full circumferential corrosion defects with longitudinal length exceeding $1.5t$

$$P_{corr,circ} = \min\left[\gamma_{mc} \frac{2tf_u}{(D-t)}\left(\frac{1 + \dfrac{\sigma_L}{\xi f_u}\dfrac{1}{A_r}}{1 - \dfrac{\gamma_{mc}}{2\xi}\dfrac{1}{A_r}}\right), \gamma_{mc}\frac{2tf_u}{(D-t)}\right] \qquad (2.21)$$

Where $A_r = \left(1 - \frac{d}{t}\theta\right)$

$P_{corr,circ}$ is not allowed to exceed P_{corr} given in Equation 2.13. Also the longitudinal pipe wall stress in the remaining ligament should not to exceed η fy, in tension or in compression where η is a partial safety factor for longitudinal stress for circumferential corrosion. The longitudinal pipe wall stress shall include the effect of all loads, including the pressure.

$|\sigma_{L-nom}| \le \eta f_y (1 - (d/t))$ where σ_{L-nom} is the longitudinal stress in the nominal pipe wall. For all the equations the defect depth greater than 85% of the pipe thickness is not acceptable.

It is obvious that these codes/standards provide the safe operating pressure for corroded pipelines. However, none of these codes/standards provide the guidelines on how to assess the integrity of corroded pipelines when pipelines are being operated within the

safe maximum operating pressure of corroded pipe, and either axial or bending load or both increases.

2.6 Studies on load deformation behaviour of corroded pipeline

In this section previous researches that have been completed to study the behaviour of the corroded pipe under combined loads are presented. Although the focus of this section is to review the previous works that were undertaken to investigate the deformation behaviour of the corroded pipe under combined monotonically increasing axial compressive load and internal pressure it was found that no work was done in this area. However, a significant number of researches have been completed on pressure capacity and bending capacity of the corroded pipe under internal pressure alone or under combined internal pressure, certain amount of axial load and bending moment. In this section research work only on burst pressure capacity, bending moment capacity, local buckling (wrinkling) behaviour of the corroded pipe subjected to combined internal pressure, axial loading and bending moment are presented. Most of the studies presented here were undertaken by Southwest Research Institute (SwRI) to predict the residual strength of the corroded pipe suitable for use in service conditions that reflect combined loading. They developed an experimental database and numerical database in the process of development and validation of their PC based software SAFE (Shell Analysis Failure Envelope) to assess the bending capacity and pressure capacity and wrinkle behaviours of corroded pipe under combined internal pressure, axial compression, and bending . The research works presented in this section can be divided into two groups, namely, analytical and experimental models and numerical models. The analytical and experimental models are validated against their respective numerical model and vice versa.

2.6.1 Analytical and Experimental Models

An analytical model was developed to analyze internally pressurized corroded pipe by Smith and Grigory (1996) from SwRI as a part of three phase study for progressive development of their readily-usable PC based program SAFE (Shell Analysis Failure Envelope). The model was validated against 13 full-scale tests and numerical model

analysis. Once the validation was completed their model was further improved to accommodate actual non uniform corrosion profile to determine the maximum rupture pressure and bending moment capacity. Two dominant failure modes were identified associated with combined effect of pressure, bending, and a constant axial loading on the corroded pipe section in the supporting experiment and the numerical analysis, namely (i) rupture and (ii) bending collapse. Combining all the works from these three phases, (the analytical model, the experimental model and the numerical model) a failure criterion was developed to determine the collapse moment and rupture pressure capacity with internal pressure and axial stresses due to axial loading and bending moment. Also a global buckling criterion was developed to determine the critical moment capacity approximating collapse of the midsection due to reduction of the bending stiffness.

The development of the rupture criterion was done by incorporating the hoop stress due to internal pressure and axial stress due to axial load and bending moment into von Mises yield criterion. The bending collapse criterion was developed from the failure bending strength and failure modes observed from the parametric study which was carried out using numerical model. The numerical model was developed using finite element method and validated using data from 13 full-scale tests. The parametric study was undertaken to investigate the effect of temperature variation and size of the corrosion on bending collapse load and failure. The effect of the internal pressure in the calculation of critical moment capacity, M_{bc}, was not considered. A linear correlation of the inertia moment coefficient Z with M_{bc} observed at ΔT equal to $0^{\circ} F$ and $130^{\circ} F$ was found. An average linear coefficient of 7.8 was derived from least square fits of data generated at these two temperatures. Similarly an average linear coefficient of 14.66 was derived from the least square fits of data generated at a constant Z. Using these linear dependences a conservative pressure independent lower bound bending collapse criteria was developed as shown by Equation 2.22

$$M_{bc} = 7.8Z - 14.66\Delta T - 1780 \tag{2.22}$$

Combining the rupture criteria and the bending collapse criteria which provided a conservative pressure independent bending moment limit an operational pressure moment domain was deduced which provide maximum pressure and maximum bending moment (or maximum curvature) predictions for an axially restrained pipeline subjected to thermal expansion due to a temperature difference ΔT with corrosion depth, axial length, and circumferential length as shown in Figure 2.7.

The figure indicates that the rupture failure on the compression side of the pipe precedes failure on the tension side. But the criteria are designed to evaluate the rupture pressure and bending collapse capacity for corrosion defect located both the compression and the tension sides of the pipe to determine which condition is most critical.

Grigory and Smith (1996) carried out full-scale experimental tests on thirteen corroded pipe specimens subjected to internal pressure, bending moment and axial loading of constant magnitude as a part of their above mentioned three-phase study program undertaken for the analysis of internally pressurized degraded (corroded) pipes which sustain large settlement and/or axial load due to temperature variations. The specimens were fabricated from 1.22 m outside diameter, 11.7 mm wall thickness (*D/t* of 104), API X65 grade steel pipes. To avoid replacing the entire length pipe for each experiment, a single central pipe section was installed between two reusable and thicker sections. The central section was 3.7 m long with overall length of about 18.3 m. The defects were artificially machined with uniform depth on both sides of the bending plane to assess which side (tension or compression) would be more critical. The shape of the corrosion was square or rectangular with a uniform corrosion depth. The corrosion were located on both tension and compression side of specimens 1 to 9. Specimen 10 had corrosion on the tensile side only while specimens 11 to 13 had the corrosion on compression side. To evaluate the residual pressure strength after wrinkling, specimen 13 was deflected until the wrinkle was formed (or up to peak moment was applied) and from this point it was pressurized until failure. The loading sequence for most of the tests was, basically, divided in three steps. In the first step, a pressure of 6.9 MPa was applied. The second step consisted of applying four-point bending up to a specified transverse deflection, while holding the internal pressure constant. In the third step, the specimen was tested in

monotonically increasing pressure until failure. Failure in this case refers to rupture in the pipe wall. Before applying this three steps loading sequence in specimen 9 to 13 the axial loading was applied first to simulate the thermal stress in the pipeline due to a temperature rise of $135°F$ ($57.22°C$). In addition, axial loading was adjusted due to Poisson's ratio and pressure acting on the pipe end plates.

This experimental program was developed as a means of validation of their analytical and numerical model from which a rupture pressure and bending collapse criteria was developed for the pipe having corrosion defects and subjected to combined internal pressure, axial compression, and bending moment. In addition to that it was found from this experimental program that at least three failure modes exist in the corroded pipe in combined pressure, bending, and axial loading condition as discussed next.

1) A hoop stress dominated axial direction rupture in the axial direction that occurs on nominally compressive side of the pipe

2) An axial stress dominated rupture in the circumferential direction that occurs on the nominally tension side of the pipe

3) A bending, or global collapse due to a loss of bending stiffness which initiates in the reduced cross section of the pipe

Their study was primarily to determine the remaining pressure strength and bending strength under combined internal pressure, bending moment with or without axial compressive load. They did not however, study the reserve strength and complete post-wrinkling behaviour of corroded pipe under monotonically increased axial load and internal pressure.

Bjornoy and Sigurdsson (2000) performed 12 burst tests as a part of the development of the DNV RP-F101 "Corroded Pipelines" (2004). This recommendation practice provides guideline to assess the integrity of corroded pipelines subjected to internal pressure, internal pressure combined with longitudinal compressive stress either from axial compression or bending moment. The focus of the experimental program was mainly to study the influence of superimposed axial and bending load on the failure pressure of the pipe with a single corrosion defect. The test results were also compared with the capacity

equation and acceptance equation (allowable operating pressure) given in DNV RP-F101 which were derived from the numerical studies performed in the BG Technology project and the DNV project. All the test specimens were made from seamless X52 grade steel pipe with 324 mm nominal diameter and 10.3 mm nominal wall thickness and thus, D/t value was 31. Of these twelve tests, nine were with rectangular shape longitudinal corrosion defects with the length of the corrosion in the longitudinal direction and three were with circumferential corrosion defects with the length of the corrosion in the circumferential direction covering entire outer circumference of the pipe. Two tests were performed with internal pressure only; three tests were performed with internal pressure and bending moment and the remaining tests were conducted with combined internal pressure and axial compression. Four point bending load was applied to the specimens which were tested under combined internal pressure and external bending moment. All tests were performed at a low loading rate allowing yielding of the material to take place. The burst capacities obtained from the tests with different load combinations were compared with the burst pressure obtained from the capacity equation for internal pressure only and acceptance equation (design) described in DNV RP-F101 and the von Mises yield surface for the nominal pipe (based on uncorroded wall thickness). It was observed that the burst pressure obtained from these test results were higher than the burst pressures calculated using the capacity equation.

The goal of their study was primarily to obtain the remaining burst pressure capacity (burst strength) of the corroded pipe with or without super imposed axial and/or bending stress. Furthermore, the results obtained from this experimental program were only used to validate the capacity equation described in DNV RP-F101 (2004). Therefore, the magnitude of the initial internal pressure and the superimposed bending moment and axial compressive load were chosen arbitrarily for all twelve tests. Finally, the specimens were pressurized until rupture and the burst pressures were recorded and compared with the capacity equation described in DNV RP-F101 (2004). In this experimental program, they did not make any attempt to determine the remaining bending strength or axial compressive strength of the corroded pipe under combined loading conditions.

The research work performed by Bai and Hauch (2001) proposed an analytical solution for calculating the bending moment capacity of corroded pipe under combined pressure, longitudinal force and bending moment. This solution is actually a modification of the analytical solution for calculation of bending moment capacity for noncorroded pipe under combined loading (pressure, axial loading and bending moment) condition proposed by Mohareb (1994). The corrosion defect was assumed to be symmetrical to the plane of bending which represents the worst case scenario. In this solution the moment capacity was defined as the moment at which the entire pipe cross section yields. The derived bending moment capacity equations were compared with the result from the finite element analysis. Four capacity equations were presented to cover four scenarios namely i) corroded area in compression; ii) corroded area in compression and some area in tension; iii) corroded area in tension and iv) most corroded area in tension and some area in compression. To reduce the complexity of the capacity equations, some assumptions were made for the pipe at maximum loading. The diameter-to-wall thickness (D/t) ratio was limited to 15-45 and it was assumed that the cross-section remains circular during the application of bending moment. It was also assumed that the entire cross section yielded at bending collapse. The material model was assumed to be elastic-perfectly plastic and the defect region was symmetric around the plane of bending. The corrosion defect was considered of infinite length and did not cause local stress concentration. In the analytical solution the von Mises yield criteria was used to obtain the longitudinal stress in terms of hoop stress and material yield strengths. While calculating the hoop stress due to internal pressure it was assumed that defect width had very minor influence on the collapse pressure and this assumption was confirmed by the numerical model as well.

For finite element analysis a shell model was developed and the input data used was D/t = 25; d/t = 0.3; material yield strength 450 MPa and material ultimate tensile strength 530 MPa. Although in the analytical solution the material model was assumed to be elastic perfectly plastic a Ramberg-Osgood material curve was used as input to the analyses and the finite element model represented one-quarter of a pipe section with a model length three times the pipe diameter. A parametric study was conducted to investigate the

influence of defect depth and defect width on moment capacity and was compared with the result obtained from the analytical solution. From the numerical studies it was concluded that both negative and positive bending moment capacity increased with decreasing super imposed longitudinal compressive force and decreasing internal pressure and moment capacity increased with decreasing defect width. The results from numerical model also confirmed that there was a significant reduction in the bending collapse capacity occurred when a corrosion defect was introduced on a non corroded pipe specimen and after that the capacity decreased slowly with increasing defect width.

The developed analytical solution only calculate the remaining bending moment capacity under combined internal pressure, axial loading and bending moment and it was developed using von Mises yield criteria. Therefore, the bending moment capacity was defined as the moment at which the entire pipe cross-section yields. This assumption makes this analytical solution very conservative.

In an effort to assess the integrity of piping systems in nuclear power plants the failure mode, bending moment capacity, and deformation ability were investigated by Kim and Park (2002) on 113.8 mm outside diameter and 7.8 mm thick – Sch80 carbon steel corroded pipe through 22 full-scale pipe experiments under 4-point bending and with or without internal pressure. The applied bending was displacement control and the displacement rate was 2mm/min. Their test results indicated that the failure mode of the pipe with defect depended on the magnitude of internal pressure, axial thinning length, as well as stress type, corrosion depth and circumferential extent of the defect. Five failure modes were observed in the experimental program and these were (i) cracking, (ii) local buckling (wrinkle), (iii) ovalization, (iv) cracking after local buckling, and (v) ovalization after local buckling. It was found that when compressive stress was applied to the corroded region local buckling occurred regardless the corrosion dimension and magnitude of the internal pressure. However, when the tensile stress was applied to the corroded region the pipe failed from cracking, ovalization depending on the corrosion dimension and magnitude of the internal pressure. The inclination of crack occurrence at corroded region decreased with increasing axial length of the corrosion and with decrease in internal pressure. However, an increase in circumferential extent of the corrosion

promoted crack occurrence at a given axial thinning length and internal pressure. The result also indicated that the bending moment capacity and deformation ability were dependent on stress state in the corroded region and dimension of the corrosion. With increase in axial length of the corrosion for applying tensile stress to the corroded region the bending moment capacity was dependent on circumferential extent of corrosion but the deformation ability was proportionally increased regardless the circumferential extent. For applying compressive stress in the corroded region the bending moment capacity was decreased with increase in axial length of the corroded region. For same corrosion geometry the load carrying capacity under compressive stress was higher than that under tensile stress for a short axial length. This was reversed for a long length of corroded area. In this research work they did not make any attempt to find the effect of corrosion depth on the failure mode and load carrying capacity and corrosion depth was taken 74% of pipe thickness for all 22 tests.

2.6.2 Numerical Models

As an alternative to the empirical methods, the finite element analysis has been used to assess the integrity of corroded pipes subjected to combined loading because it is financially feasible and provides a means to reduce the excess convertism in current methods. With the availability of high speed computers, it is possible to use sophisticated numerical analysis to obtain good results for the corroded pipeline problems.

Roy et al. (1997) carried out numerical simulations by finite element method in each of the thirteen corroded full-scale pipe failure tests carried out by Grigory and Smith (1996) for predicting failure in corroded oil transmission pipe under combined loading. Each of the thirteen corroded full-scale pipe was modeled using twenty-node hybrid brick elements. Only one quarter of the pipe was modeled due to geometric and loading symmetries. Their analysis took into account elastic–plastic strain hardening as well as large inelastic deformations. The true-stress versus plastic logarithmic-strain was calculated from the nominal stress strain curve obtain from tensile tests. Due to anisotropy in the steel, tensile tests were performed in the longitudinal and circumferential directions. The stress–strain curve referred to longitudinal direction was

taken as a material characteristics curve. The load sequence was followed as it was in the corresponding experiment. Using the developed model, 30 parametric studies were conducted in order to fully define the failure envelope described in their analytical solution (Smith and Grigory, 1996). The study attempted to quantify the effects of load path, constrained thermal expansion, and corrosion patch location on internal pressure and bending moment at failure. Three primary failure mechanisms were observed in the parametric study, (i) longitudinal rupture, (ii) circumferential rupture and (iii) bending collapse. Rupture failure was defined by zero slope of the applied load vs. deformation curve where load was the pressure or the bending moment and the deformation was defined as the true equivalent plastic strain within the thinned region. Bending collapse was defined as loss of bending stiffness at the pipe mid-section indicated by zero slope of the moment vs. deflection curve. It was found that the loss in bending stiffness was caused by a combination of wrinkling of the pipe wall, ovalization of the pipe cross section, and by the progressive softening of the material through yielding in the thinned region. From the parametric study the following observations were found:

1) Increase in corrosion depth results in a decrease in failure pressure all other parameters being equal.

2) Increase in corrosion depth reduces the maximum moment capacity in the corroded section all other parameter being equal.

3) Critical moment reduces much with depth of circumferentially oriented patch than axial narrow patch. Because reduction in the area moment of inertia of pipe section due to a circumferential corrosion with increased depth is greater than that due to a narrow axial corrosion with identical increased in depth.

4) For constant depth the rupture pressure decreases with increased axial length of the corrosion

5) Increased circumferential extent of corrosion is detrimental for bending moment capacity.

Nicilelle and Smith (1997) developed a finite element model by including the non linear material behaviour of the steel pipe using a multi-linear kinematic hardening plasticity model to investigate the wrinkling behaviour of the corroded pipe under combined axial,

bending, and internal pressure loading. The numerical procedure combined ABAQUS four noded, large deformation shell element S4R and Mroz (Mroz, 1967) constitutive model with true stress-strain material definition to accurately model the wrinkle behaviour. The material model was incorporated in ABAQUS by invoking a user developed material subroutine UMAT and was verified in a single element (5 in x 5 in x 0.5 in thick) uniaxial and cyclic loading test. The results of the finite element analysis for deflection, curvature and moment capacity of the pipe at wrinkle were investigated and compared with the full-scale test data. During the testing program, a full-scale 48 in diameter X65 steel pipe section of the Trans-Alaska pipeline was subjected to multiaxial loading. 15 in x 15 in x 0.15t. Corrosion in the pipe was physically simulated using reduced wall thickness section of the pipe and was located on the compression side of the bending plane. Deflections, curvature, and magnitude of the applied load were measured for comparison to the finite element simulations. The amount of axial load applied to simulate the axial compression for $75°F$ ($23.89°C$) temperature differences and compensation for axial tensile load due to end cap and Poisson's effect. At the beginning of the test and the FEA simulation bending due to static weight of the specimen (steel plus water) was applied followed by axial load representing applied fluid temperature deferential and internal pressurization with compensating axial load. Then bending was applied until a wrinkle was formed and finally internal pressurization with compensating axial load was applied until the pipe rupture (this step is not simulated in the FEA). Wrinkling of the pipe in the FEA model was indicated by a reduction in the applied bending moment with increasing lateral displacement. Bending was deflection control in the test and the simulation until the wrinkle of the pipe occurred. With in each displacement increment the modified RIKs algorithm was used to ensure that the solution converged. From the compared data (test and FEA) they concluded that the combined ABAQUS/Mroz procedure was well suited for the wrinkling analysis of the corroded pipe.

Smith et al. (1998) performed a full-scale testing program and finite element analysis to develop a wrinkle prediction procedure for corroded pipes under combined loading. The research work was initiated when a second type of failure mode was encountered due to

the loss of bending stiffness within the corroded region prior to rupture of the pipe during the initial rupture tests to the development of the procedure for the prediction of rupture in corroded pipe subjected to combined pressure, axial loads and bending (Smith and Grigory, 1996). A database was developed by performing a minimum number of full-scale tests to provide data for validation of the FE procedure, followed by a "surrogate" testing using the validated procedure to investigate the effects of a wide range of corrosion and loading parameter on the wrinkle capacity. The numerical program utilized finite element analyses that include the non linear anisotropic material behaviour of the steel pipe through the use of a multi-linear kinematatic hardening model. During the experiment and FEA the curvature, deflection and moment capacity at wrinkling were measured. Wrinkle in a pipe was defined when a peak moment was achieved. This peak was indicated by a zero slope in moment verses deflection behaviour and it was seen that this peak moment was affected by wall loss in the maximum bending region as well as the magnitude of the internal pressure, axial compression (or tension) and axial bending imposed. Initially twenty full-scale test of X65, 48 inch diameter pipe section with a 0.462 inch wall thickness were tested for rupture and wrinkling. Of these planned rupture test wrinkling or incipient wrinkling was produced in eleven tests.

General corrosion was simulated by mechanically grinding to remove wall thickness with a specific axial length (L_a), circumferential width (L_h) and depth (d). The sequence of load application for each test was designed to simulate which would be experienced by a pipe in service. Four distinct load steps were required to produce this load path and induce wrinkling with in the specimen. In first step the load was due to filled water and the pipe static weight. Then the axial load and the pressure were applied. In the last step the lateral deflection was applied until the wrinkle formed keeping the axial and pressure load constant. The axial load simulating a ΔT (temperature differential) equal to $-80°F$ (end cap tests), $0°F$ and $135°F$ only were investigated. Close examination of the results for these test results (Grigory and Smith, 1996) showed that the wrinkling instability point strongly corresponded to the depth and hoop length corrosion parameters as well as the initial pressure and temperature differential applied. With this knowledge a full scale test matrix was developed for parametric study aimed at defining the change in

wrinkling moment and curvature capacities produced when a single key corrosion or loading parameter was varied from a nominal test case. The nominal test case was designed to represent the set of corrosion and loading conditions most likely to analyze on TAPS (Trans Alaska Pipeline System) pipe section.

In the FEA the capabilities of the commercially available finite element analysis program ABAQUS was coupled with the Mroz (Mroz, 1967) constitutive model for simulating metal plasticity. It was found in their previous study that a combination of large deformation effects, structural non-linearities and accurate finite strain material anisotropy descriptions were required for accurate prediction of pipe wrinkling (Nicilelle and Smith, 1997). The Mroz procedure, encoded in a series of subroutines and interfaced with ABAQUS is an anisotropic, multi-linear, kinematic hardening constitutive model well suited to the simulation of material anisotropy. S4R shell element were used which was capable of managing the large deformation effects associated with wrinkling of pipe wall. To accommodate the effects of material anisotropy, properties of the pipe steel were entered in ABAQUS via UMAT (User Defined MATerial) option of the analysis code. The UMAT was designed to interface with the Mroz (Mroz, 1967) constitutive model, and required the input of the material definitions in true stress-strain space. To obtain the material property ASTM round bar specimens taken from the hoop and longitudinal material direction were tested in tension and compression instead of API 5L flattened strip specimens to avoid the further alteration of hoop direction material properties imposed by the flattening process required to produce the coupon according to API specification. Few important conclusions on wrinkle behaviour were made from this study on corroded pipe. When all other parameter held constant an increase in internal pressure caused significantly decrease the moment at wrinkling while corresponding deflection and curvature increased. An increase in the hoop length of corrosion significantly reduced the moment, displacement and curvature achieved at wrinkling while reducing the hoop length extent increased these quantities. When the defect was a longitudinal axial corrosion the moment capacity, displacement and the curvature capacity increased and this was attributed to the formation of multiple wrinkles with in the defect region.

Although all the research works on corroded pipeline stated above considered the combined loading effect, the objective was to investigate the pressure capacity (burst strength) or the bending moment capacity of the corroded pipe under combined internal pressure, longitudinal axial force, and bending moment. No research work has been found that investigated the collapse capacity and the post wrinkling behaviour of the corroded pipe that is subjected to constant internal pressure and monotonically increasing axial compressive force.

Table 2.1 Classification of Corrosion (POF, 2005)

Anomaly dimension class	Definition
General	$\{[W \geq 3A\ ] \text{ and } [L \geq 3A]\}$
Pitting	$\{([1A \leq W < 6A\ ] \text{ and } [1A \leq\ L < 6A] \text{ and } [0.5 < L/W < 2\ ]) \text{ and not } ([W \geq 3A] \text{ and } [L \geq 3A]\}$
Axial grooving	$\{([1A \leq W < 3A\ ] \text{ and } [L/W \geq 2]\ \}$
Circumferential grooving	$\{([L/W \leq 0.5\ ] \text{ and } [1A \leq\ L < 3A]\ \}$
Pinhole	$\{[0 < W < 1A] \text{ and } [0 < L < 1A]\}$
Axial slotting	$\{[0 < W < 1A] \text{ and } [L \geq 1A]\}$
Circumferential slotting	$\{[W \geq 1A] \text{ and } [0 < L < 1A\ ]\}$
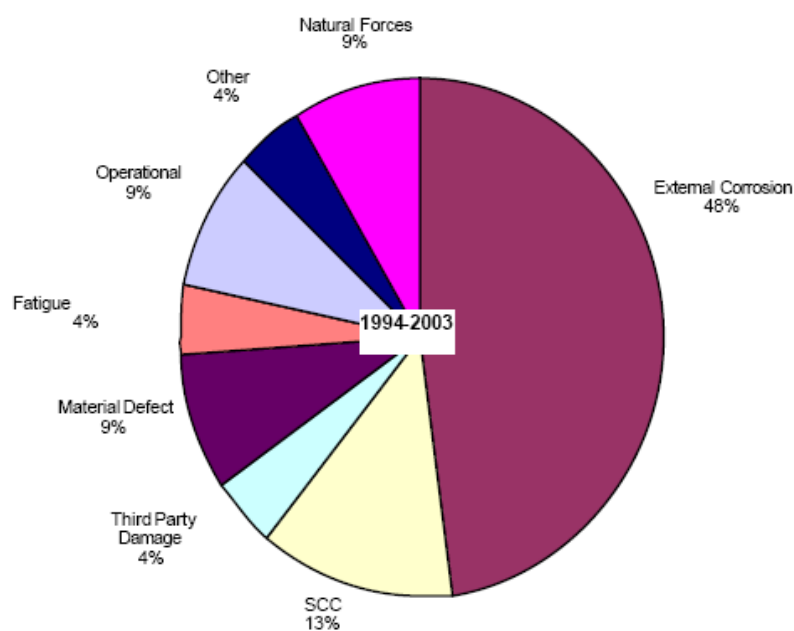
Figure 2.1: Causes of pipeline rupture in Canada, reported by the National Energy Board of Canada (Jeglic, NEB)
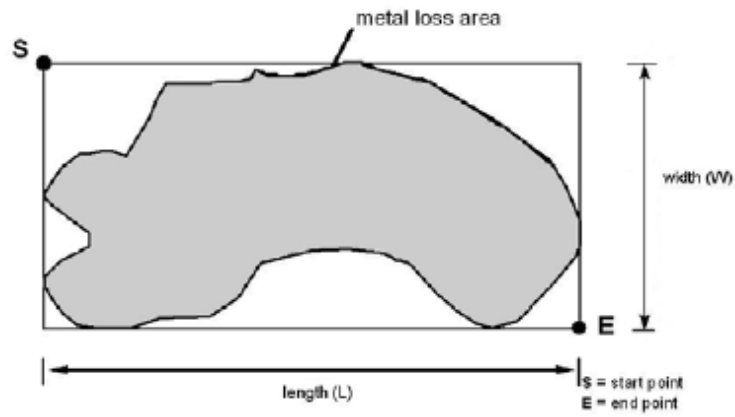
Figure 2.2 Length and width of corrosion (POF, 2005)
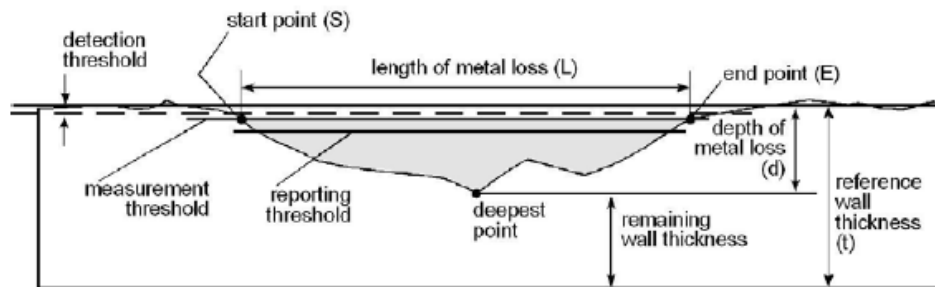
Figure 2.3 Measurement of corrosion dimension
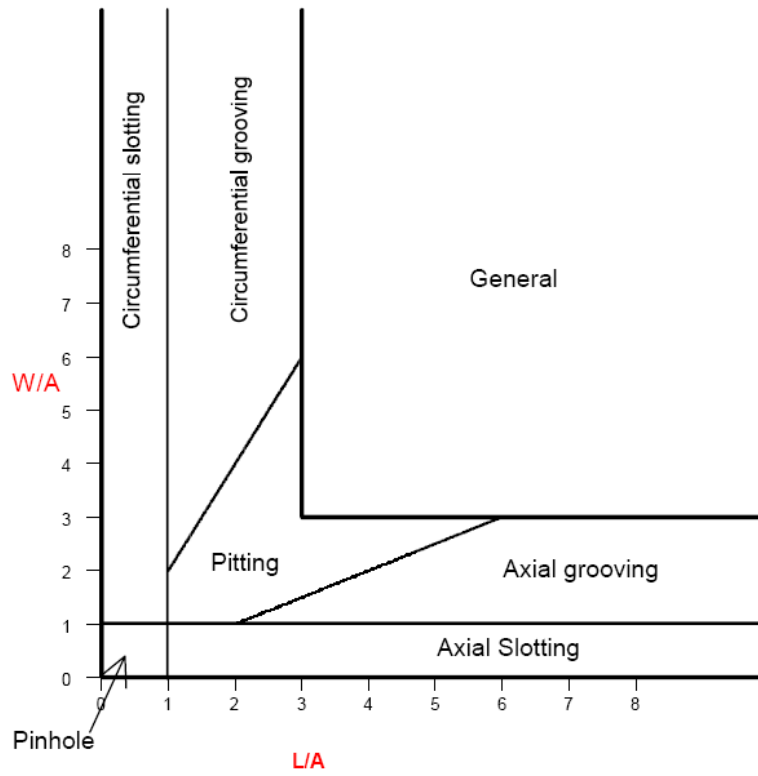
The geometrical parameter A is linked to the NDE methods in the following manner:

If t < 10 mm then A = 10 mm
If t ≥ 10 mm then A = t

Figure 2.4 Measurement of corrosion dimension (POF, 2005)
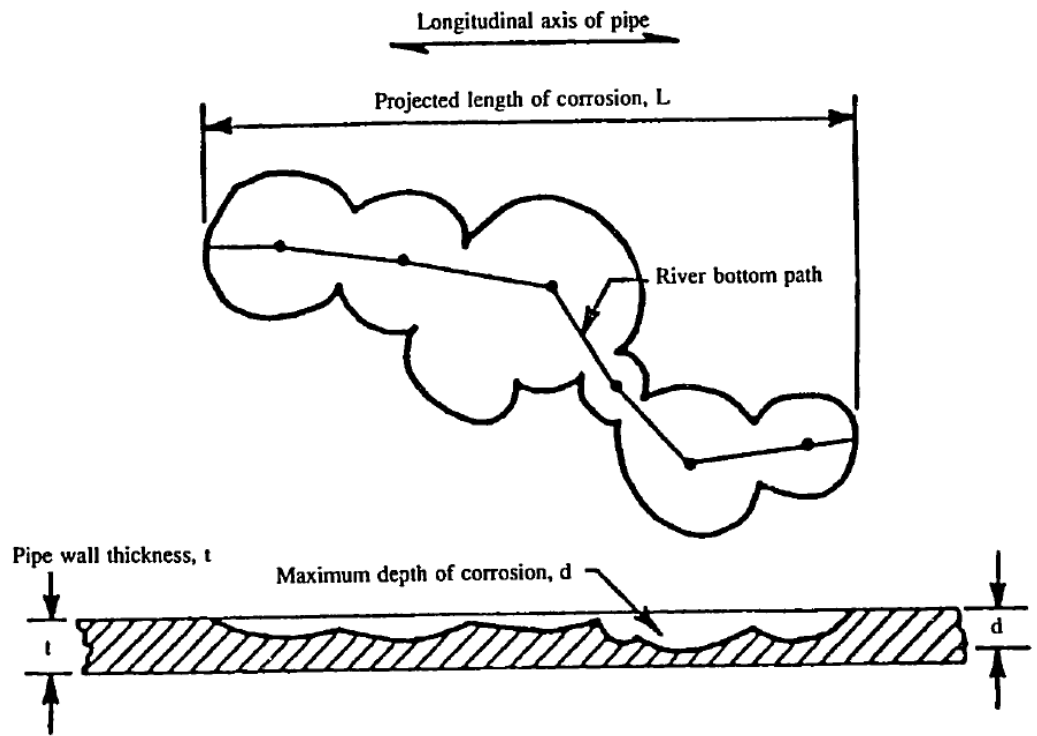
Figure 2.5 Corrosion parameter used in ASME B31G-1991 (ASME, 1991)
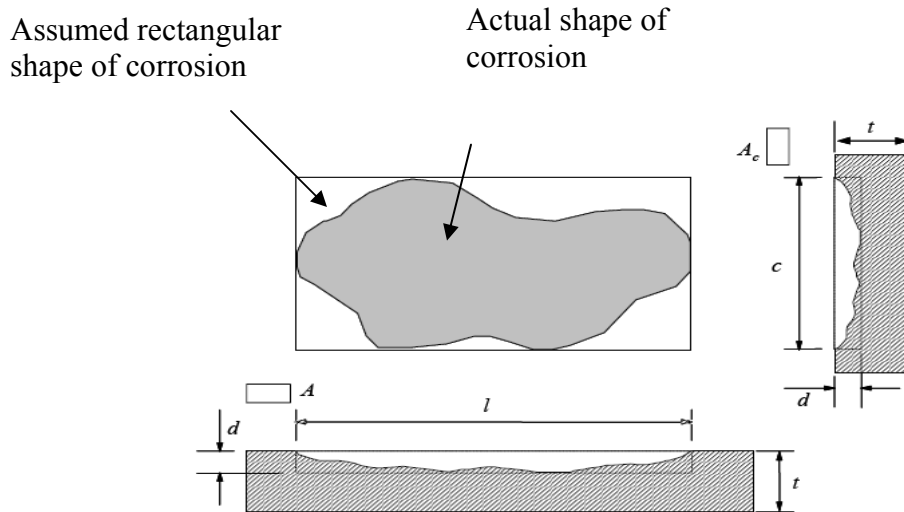
Figure 2.6 Defect shape and dimension (DNV-RP-F101 (2004))
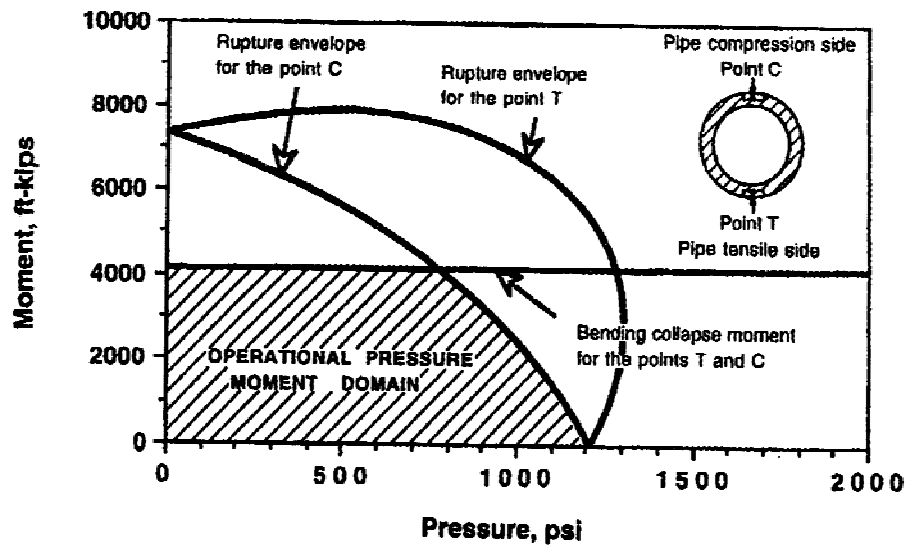
Figure 2.7 Typical engineering model pressure – bending moment plot
(Smith and Grigory (1996))

3 Experimental Program

3.1 General

As reported in the literature review, a number of experimental studies were found and these studies were undertaken to determine the collapse capacity of the corroded steel pipe under combined internal pressure and bending moment (Smith et al. 1996, Grigory and Smith 1996, Roy et al 1997, Bjornoy and Sigurdsson 2000). However, no study was undertaken to investigate the load deformation behaviour under combined internal pressure and axial compressive load of corroded line pipes. This project focuses on establishing the load deformational behaviour of a corroded pipeline when it is subjected to internal pressure and axial compression that may develop due to soil movement and/or differential temperature. It is not economically feasible to try to cover the entire range of pipeline geometries, corrosion defect geometries, material properties, internal pressures that may exist in the field in an experimental program. Therefore, it was the goal of the project to establish an experimental database for the oil and gas steel pipe that was locally available and for different sizes and shapes of the corrosion defects and internal pressure for the investigation of the axial collapse capacity of the corroded gas pipeline.

The results of the experiments were then used to validate a developed numerical model. Once the validity of a predictive model was established, it was utilized to perform a series of analyses in order to predict the effect of different corrosion defect parameter and various amounts of internal pressure on the load deformation behaviour of the corroded steel line pipe under combined axial compression and internal pressure. Finally, a failure criterion was developed from the results of these analyses.

3.2 Selection of Specimen Parameters

It is necessary to perform full scale testing in order to experimentally determine the load deformation behaviour of pipes in the field. Therefore, the size of pipes tested was selected such that it represented the size of pipes typically used in the oil and gas pipeline industry. The selected diameter was in the range of pipe diameters supplied by major suppliers of steel pipes in the Canadian market. The pipe specimens were made of 168 mm (6 in) outer diameter, 5 mm thick API 5L X46 steel pipes. Most of the pipelines in

current practice have a *D/t* ratio ranging from 20 to 80. The diameter to thickness ratio (*D/t*) of the test specimens was around 34 which falls in this range. The length of the specimen was selected to avoid Euler buckling and was long enough to allow local buckling to develop in the corrosion defect regions that are not influenced by the end conditions.

3.3 Selection of Boundary Conditions

Since the research work was planned to investigate the collapse capacity of the corroded pipe under axial compressive force and internal pressure the end restrained conditions were chosen accordingly. The bottom end of the vertically placed specimen was fixed for all six degrees of freedom. The axial compressive load was applied on the top of the specimen where all six degrees of freedoms were free. Due to the presence of corrosion on one side of the specimen, the pipe geometry for corroded specimens was unsymmetrical and hence, the rotation occurred in the pipe specimen in the direction of corrosion when it was subjected to longitudinal compressive force and/or displacement.

3.4 Selection of Corrosion Shape

According to the classification of Pipeline Operators Forum (POF), a general type corrosion was selected for the test specimens where longitudinal extent of the corrosion remains same for all of the tests. Various corrosion types such as pitting, general, longitudinal groove etc are discussed in literature review chapter. Cosham and Hopkins (2004) concluded from various studies that the length of the corrosion is the most important corrosion parameter for burst strength of the pipe subjected to the internal pressure only and the circumferential dimension of the corrosion has greater effect on the strength of the corroded pipe subjected to axial compression and bending moment (Roy et al. 1997). Therefore, longitudinal dimension of the corrosion in this study was kept unchanged (50 mm) for all test specimens whereas, the circumferential dimension was varied to investigate its effect on the axial load capacity of the corroded pipe. Two different circumferential corrosion dimensions, 50 mm and 175 mm (3.5 times of 50 mm), were used for the test specimens in this study.

3.5 Selection of Internal Pressure

The maximum allowable operating pressure (MAOP) for uncorroded pipe is $0.8p_y$ (CSA-Z662-07). Current guidelines and standards recommend a lower MAOP for corroded pipelines and the MAOP reduces as the extent of corrosion defect increases. A detail discussion on reduction of MOAP with corrosion defect according to CAS-Z662-07, ASME B31G-1991, and DNV-RP-F101 has been made in Chapter 2. In this experimental program the internal pressure (p) was varied to examine the effect of the internal pressure on axial load capacity of the corroded pipe. Therefore, two different internal pressures equivalent to $0.2p_y$ and $0.4p_y$ (where p_y is the internal pressure required to cause yielding of the pipe material in the circumferential (hoop) direction) were selected in this study. The selected internal pressures were below the MAOP for the respective corrosion defect according to CSA-Z662-07 or other existing codes/standards for corroded steel pipelines.

3.6 Modelling of Field Conditions

The axial load that was applied to the test specimens in order to simulate the axial force in an operating pipeline is evaluated by superimposing the effects of temperature differential and/or axial force due to land slide, Poisson's ratio effect, and internal pressure, as described below.

3.6.1 Axial Load Caused by the Thermal Effects

When a line pipe is installed at a temperature much lower than the pipe operating temperature, it subsequently attempts to expand longitudinally because of the differential thermal effect between the operating temperature and the tie-in temperature. However, its longitudinal movement is restrained by the presence of anchors, adjacent pipe segments and fittings, as well as by the friction provided by the surrounding soil. Under full restraint condition which can be idealized as shown in Figure 3.1, the thermally induced axial compressive load C_t develops.

$$C_t = EA_{pipe}\alpha(\Delta T) \tag{3.1}$$

Where C_t = the thermally induced axial compressive force in the pipe wall

A_{pipe} = the cross sectional area of the pipe

E = the elasticity modulus of the pipe material

α = the coefficient of thermal expansion for the pipe material usually taken as $11.70 \times 10^{-6} / C°$

ΔT = the difference between tie-in temperature and the operating temperature which could be in the range of $40°$ to $50° C$ for artic and sub-artic field line pipe.

If the temperature differential is large enough, the resulting axial force can cause the pipeline to buckle leading to considerable vertical, lateral, or combined movement of the pipe and may involve elastic-plastic deformation and wrinkling of the pipe.

3.6.2 Axial Load Caused by the Landslide

As shown in Figure 3. 2 (a), when a pipeline is aligned on a unstable slope susceptible to landslide, it will be subjected to compressive stress in the lower part of the landslide and tensile stresses in the upper part of the landslide by the force (C_a) exerted by the downward moving soil. The free-body diagram of two pipe segments are shown in Figure 3.2 (c) where pipe segment A is subjected to axial tension (due to reaction force R_A) and pipe segment B is subjected to axial compression C_l (reaction force R_B) due to the axial force, C_a acting on section of pipe shown by broken vertical line in Figure 3.2(b), caused by the landslide. The compressive stresses cause buckling (wrinkling) and may lead to rupture in the pipeline, especially if corrosion exists on the compression area. However, it is almost impossible to quantify the force (C_a) exerted on the pipe section since the movement of the soil is hard to be quantified and the interaction between soil movement and pipe wall is also very complex.

3.6.3 Axial Load Resulting From the Poisson's Ratio Effect for Hoop Stresses

When internal pressure is applied to a pipe segment, the cross section of the pipe segment expands and as a result, the segment perpendicular to the cross section shorten longitudinally because of the Poisson's ratio effect arising from circumferential stresses. As in thermal expansion if this longitudinal shrinkage or shortening is prevented due to a plane strain condition at each end, tensile forces develop in the pipe wall. In the field, this shortening is prevented, for a longitudinally restrained pipe, because of the presence of adjacent pipe and the surrounding soil. For a laboratory specimen, this restraint is not present and axial shortening is, therefore, not prevented. Thus, in order to simulate field conditions, an additional axial tensile force, C_v, is to be applied to the ends of the specimen.

$$C_v = -A_{pipe} v \sigma_\theta \tag{3.2}$$

where C_v = axial load in the pipe due to the Poisson ratio effect

A_{pipe} = cross sectional area of the pipe segment

v = Poisson's ratio; and

σ_θ = the hoop stress.

The negative sign in Equation 3.2 denotes tensile force acting on the specimen.

3.6.4 Axial Load Caused by Internal Pressure Acting on Closed Ends of Specimens

In test specimens, both ends of the pipe must be closed to hold the internal pressure and the internal pressure acting on the closed ends of the pipe results in axial tensile force acting on the specimen. The buried field line pipe has no closed end and therefore, such tensile force does not exist in the field. In order to properly simulate field conditions, it is therefore, necessary to apply a compensating compressive axial force to the ends of the test specimen that has the value as shown in Equation 3.3

$$C_e = \pi R_i^2 p_i \qquad\qquad (3.3)$$

where R_i = internal radius of the pipe and

p_i = internal pressure of the fluid in the pipe.

3.6.5 Total Axial Load

The load on pipe wall for line pipe on the unstable slope in the field is C_{Net} or C_N

$$C_{Net} = C_t + C_l + C_v \qquad\qquad (3.4)$$

This load (C_{Net}) must be same for net load on lab test specimen as well. Since the lab specimens have end caps, the equivalent load that needs to be applied on the lab specimens is $C_{Applied}$ or C_A

$$C_{Applied} = C_{Net} + C_e \qquad\qquad (3.5)$$

The value of C_l depends on severity of landslide and complexity of interaction between soil movement and pipe wall. It is nearly impossible to estimate the value of C_l which can be very large. Hence, in the test specimens, $C_{Applied}$ was increased monotonically until the maximum load value was reached.

3.7 Test Variables

The objective of this study is to create an experimental database that focuses on the investigation of the effect of various parameters on load-deformation behaviour of the axially loaded corroded pipe. The parameters chosen are (Table 3.1 and Table 3.2)

1. internal pressure ($0.2 \, p_y$, $0.4 \, p_y$)
2. circumferential dimension of the corrosion patch (50 mm and 175 mm), and
3. corrosion depth , d ($0.25 \, t$ and $0.50 \, t$)

It is not reasonable to conduct a large number of experiments for wide ranges of various parameters and investigate their effect on the axial load deformation behaviour of the corroded pipe.   Therefore, in the experimental program the test variables are limited to the above mentioned values (see Tables 3.1 and 3.2). However, in the parametric study which was conducted using a FEA model, these parameters were varied in a wider range.

3.8 Preparation of the Specimen

Ten specimens were fabricated (including the control specimens) from 168 mm outer diameter, 5 mm thick (D/t ~ 34) API 5L X46 steel pipes. Each of the specimens was 610 mm (24 in) long. The outside surface of the specimen was sand blasted and grinded slightly to remove the rust to provide a clean surface for the installation of strain gages. A schematic of the pipe specimen is shown in Figure 3.3. The two ends of the specimen were bevelled to 60° as shown in Figure 3.4 to facilitate the welding of two end plates of 50 mm thick. These end plates were welded in order to hold the water pressure. On these two end plates, arrangements were made for the inlet and outlet of water needed to fill up and pressurize the specimen. To avoid eccentricity, the specimen was aligned carefully at the centroid of each end plate. The end plates were welded to pipe specimen using fillet weld (hold parts in place) by 6010 electrodes, 3/32 inch diameter at 85 Amps. Each weld pass was done with 7018 electrodes, 1/8 inch diameter at 130 Amps. The completed weld consists of three passes of fillet weld over the tack welds. All welding was Shielded Metal Arc Welding (Stick) and was done on a Lincoln, Idalarc 250 welding machine. In order to avoid potential end effects on the local buckling behaviour of the tested specimen and to prevent the local buckling in the immediate vicinity of the two ends, the ends of the specimen were confined by means of 76 mm wide steel collars made from the same pipe.

3.9 Detail of the Corrosion

Corrosion patch with uniform depth was machined at mid length of pipe specimen. To reduce the effect of the stress concentration at the interface between corroded area and uncorroded area, small transition region with radius of 3 mm (fillet) was provided at the end of the corrosion patch. Figure 3.5 shows a typical corrosion patch with its transition.

Longitudinal dimension of the corrosion is denoted by L_A and circumferential dimension of the corrosion is denoted by L_C as shown in Figure 3.5a. The thickness of the pipe specimen and depth of the corrosion are denoted by t and d, respectively. Table 3.1 and Table 3.2 list the corrosion patch dimensions for all ten specimens.

3.10 Designation of the Specimen

Each of the specimens has been given a designation as shown in Table 3.1 and Table 3.2 that can be interpreted to recognize most of the attributes of the test. For example, for specimen CP20d00, the first character (*C*) indicates that this is a control specimen, next three characters (*P20*) indicate that the internal pressure is 20% of p_y, and the last three characters (*d00*) indicate that the depth of corrosion d is 0% of actual pipe thickness t. Similarly, the first character of the specimen having square shape corrosion is S (as in SP20d25) and that for rectangular shape corrosion is R (as in RP20d25).

3.11 Material Property

All the pipe specimens were made from same D/t value (~ 34) and same material. Therefore, the tension coupon specimens were obtained from one of the pipes. All the coupon specimens were obtained from the longitudinal directions of the pipe segment away from the seam weld to avoid any residual stress effect on the material behaviours. The tension coupon specimens were prepared and tested in accordance with ASTM E 8/E 8M-08 specification (ASTM, 2008). A total of five coupon tests were performed. An extensometer of 50.8 mm (2 in) gauge length was mounted on the tension coupon to measure the longitudinal strain in the middle portion of the coupon and load verses deformation response was recorded until rupture. In one of the five specimens one longitudinal and one transverse strain gage were mounted to calculate the Poisson's ratio.

The purpose of these coupon tests was to obtain mechanical properties of pipe steel until rupture. This information is a vital input in the finite element analysis. The stress strain behaviour obtained from these tests is shown in Figure 3.6 The material properties obtained from these test are shown in Figure 3.7 and Table 3.3. A detailed discussion on the material property will be discussed in Chapter 5.

3.12 Details of Test Specimen
3.12.1 Control Specimen

Two control specimens (CP20d00 and CP40d00 in Tables 3.1 and 3.2, respectively) that had no corrosion defect were used to determine the effect of different parameter on the axial collapse capacity and load deformation behaviour of the corroded pipe specimen. One of the specimens was pressurized to a constant pressure of $0.2\,p_y$ and the second one was pressurized to $0.4\,p_y$ during the test. Preparation of these specimens is same as described before. These two control specimens are included in both Group 1 and Group 2.

3.12.2 Group 1 Specimens

Group 1 consisted of the test specimens having square shape corrosion with two different depths. The dimension of the corrosion is 50 mm x 50 mm that is, the rectangular corrosion shape was used. There were four corroded specimens tested in Group 1 and two control specimens (CP20d00 and CP40d00). These specimens were further divided in two sub groups depending on the applied internal pressure. First sub group, named as Group 1A, consisted of the specimen SP20d25 and SP20d50 in which internal pressure was $0.2\,p_y$. However, the corrosion depth was varied to 25% and 50% of actual pipe thickness, respectively. Second subgroup, named as Group 1B, consisted of the specimens having internal pressure $0.4\,p_y$. The specimens of this subgroup were SP40d25 and SP40d50 where the corrosion depths are 25 % and 50% of the actual pipe thickness, respectively. Detail test parameters for Group 1 specimens are shown in Table 3.1.

3.12.3 Group 2 Specimens

Group 2 consisted of the test specimens having rectangular corrosion with two different corrosion depths and two control specimens, CP20d00 and CP40d00. The dimensions of the corrosion are 50 mm in longitudinal direction and 175 mm in circumferential direction. There were 4 corroded specimens in Group 2. Like Group 1, these specimens were also further divided in two sub groups depending on the applied internal pressure during the test. First sub group, named as Group 2A, consists of the specimen RP20d25

and RP20d50 in which internal pressure was 0.2 p_y, but, the corrosion depth are 25% and 50% of pipe actual thickness, respectively. Second subgroup, named as Group 2B, consists of the specimen having internal pressure 0.4 p_y. The specimens of this subgroup are RP40d25 and RP40d50 where the corrosion depths are 25% and 50% of the actual pipe thickness, respectively. Detail test parameters for Group 2 specimens are shown in Table 3.2.

3.13 Test Setup

The experimental program was carried out in the Structural Engineering Laboratory at the University of Windsor. A sketch and a photograph of the test setup for the program are shown in Figures 3.8 and 3.9, respectively. Each specimen was placed vertically on strong steel base that rested on strong floor under the 1800 kN (400 kip) capacity axial compression load cell and 3000 kN capacity universal loading jack which were used to apply a concentric axial load to the specimen. The load was applied by a hydraulic pump through the loading jack. A swivel head was also mounted on top of the top end plate to avoid eccentricity. A photograph of the swivel head is shown in Figure 3.10.

For first three tests (CP20d00, SP20d25, SP20d50) only three LVDTs were used, one with the jack (LVDT3) and one on the corrosion side (LVDT2) and third one on the opposite side of the corrosion patch (LVDT1). These LVDTs are named as LVDT3, LVDT2, and LVDT1, respectively as shown in Figure 3.11 and the corresponding net load-deformation behaviour of the respective specimens are shown at the end of this chapter. For the remaining tests, the LDVT attached to the jack was removed since it was showing much softer behaviour for some reasons. Therefore, for the remaining, tests a total of four LVDTs were used, one on each side of the end plate to measure vertical shortening of the specimen due to applied axial compressive load. The relative positions of these four LVDTs are shown in Figure 3.12. The LVDT at opposite face of the corrosion side and the corrosion side are named as LVDT1 and LVDT4, respectively. The LVDT2 and LVDT3 shown in Figure 3.12 are placed at *90°* apart from LVDT4. The values of LVDT2 and LVDT3 were averaged to get the deformation of the pipe specimen which was used to plot the net load-deformation behaviour in Chapter 4. For first three

specimens (CP20d00, SP20d25 and SP20d50), the deformation values from LVDT3 (attached to the jack) were corrected and then used to plot the net load-deformation behaviour in Chapter 4. The correction was done by adding net load-deformation behaviour obtained from LVDT1 up to the ultimate net load and net load-deformation behaviour obtained from LVDT3 from ultimate net load to the net load at the end of the test. Two rotation meters $90°$ apart from each other on horizontal plane were placed on the top end plate to capture the rotation of each vertical plane due to unsymmetrical geometry of the corroded specimen because of the presence of the corrosion patch.

3.14 Instrumentation
3.14.1 Electrical Resistance Strain gauges

On average ten channels of electrical resistance $(350\,\Omega)$ strain gauges of 5 mm gauge length were installed on each pipe specimen to determine the strain distribution in and around the corrosion patch for the corroded specimens. For control specimens, a wider area was gauged to obtain longitudinal strains in and around wrinkle. For control specimens these strain gauges were placed near the two confining collars to capture the strain distribution within the wrinkle, specially at the foot and crest of the wrinkle, as the wrinkle was expected to form in the vicinity of the colors. The strain gauge locations for the gauges that were in and around the wrinkle for the control specimens CP20d00 and CP40d00 are shown in Figures 3.13. The other strain gauges are not shown in this Figure. For all corroded specimens the strain gauges were placed within the corrosion patch as it was known that the wrinkle would form within this region. The strain gauges were installed before the application of any internal water pressure and the axial compression. Therefore, these gauge measured the material strain from the beginning of the test. The strain gauges used in test were capable of measuring strain up to 5% to 15% depending on the type of gauges or adhesive used. A typical layout of the strain gauge position for the specimen in Group1 and Group2 are shown in Figure 3.14 and Figure 3.15, respectively. The strain gauges are arranged in rows 1, 2, and 3 and column a, b, c, and d. Each strain gage position will be identified with its corresponding row and column number such as 1a, 2a etc.

3.14.2 LVDT (Linear Voltage Displacement Transducer)

Four spring loaded LVDTs were installed along the length of the specimen on four sides of the pipe in order to measure its shortening due to applied axial compression. These LVDTs were capable of measuring deflection up to ± 150 mm (6 in).

3.14.3 Rotation Meters

Due to the unsymmetrical geometric condition caused by simulated corrosion patch on one side of the pipe, the test specimen bended on to the corrosion side after formation of the wrinkle. Two electronic rotation meters were installed on top of end plate to capture the rotations of the two vertical planes due to bending.

3.14.4 Fluid Pump

An air pressure driven water pump of maximum capacity of 4500 psi (31 MPa) fluid pressure was used to pressurize the water inside the test specimen. The pressure was controlled and recorded by the data acquisition system through a pressure transducer.

3.14.5 Data Acquisition System

An analog output module, Data Scan 7021, manufactured by Adept Scientific located in England was used to record all the test data. Each of the modules had eight channels. Four analog modules were connected in the data acquisition system. A total 18-20 data channels were required to collect the data for the. The local measurement speed was set to be one reading per second. Data collection was facilitated using Dalite software, recording all readings electronically into a computer file.

3.15 Test Procedure

The same load sequence was maintained for all the test specimens. First the specimen was filled with water, then the desired pressure (either 625 psi (4.3 MPa) for $0.2\,p_y$ specimens or 1250 psi (8.6 MPa) for $0.4\,p_y$ specimens) was applied. The pipe specimen was allowed to expand when the pressure was being applied. This was done by detaching the loading jack from the pipe specimen. Keeping this pressure constant, a monotonic

axial axi-symmetric compressive force ($C_{Applied}$ in Equation 3.5) was applied until the wrinkle initiated (for example, point U in Figure 3.16). As the wrinkle initiated and started to grow, the applied load began to drop as the axial displacement increased as shown in Figure 3.16 through the region *U-S*. The peak value that the applied load ($C_{Applied}$) reached, at the onset of the wrinkle formation and it is indicated by *U*. The point C indicates the total deformation between 30 mm and 40 mm. At this point (wrinkle closure) the load-deformation curve becomes flat. Beyond this point the load started to increase as the inside surfaces of the pipe wall at the ends of the wrinkle came into contact. The point S indicates the total deformation between 40 mm and 45 mm. There is a point *M* in the region *U-C* which represents the total deformation between 10 mm and 25 mm. Most of the tests (Test no 1-8 in Table 3.1 and Table 3.2) were stopped at this point. Only Test 9 (RP40d25) and Test 10 (RP40d50) were continued until the deformation reached point C and S, respectively and the load started to increase beyond this point. The load–deformation responses of the test specimens in terms of net load (C_{Net}) are attached at the end of this chapter (Figure 3.17 to Figure 3.26).

Table 3.1 Test Matrix for Group1: Square Corrosion

Test No.	Specimen	Corrosion Shape	Internal Pressure (% of p_y)	Corrosion Dimensions		
				Axial mm	Circ. mm	Depth d (% of t)
1	CP20d00 (Control Specimen)	None	20	0	0	0
2	SP20d25	Square	20	50	50	25
3	SP20d50	Square	20	50	50	50
4	CP40d00 (Control Specimen)	None	40	0	0	0
5	SP40d25	Square	40	50	50	25
6	SP40d50	Square	40	50	50	50

Table 3.2 Test Matrix for Group 2: Rectangular Corrosion

Test No.	Specimen	Corrosion Shape	Internal Pressure (% of p_y)	Corrosion Dimensions		
				Axial mm	Circ. mm	Depth d (% of t)
1	CP20d00 (Control Specimen)	None	20	0	0	0
7	RP20d25	Rectangle	20	50	175	25
8	RP20d50	Rectangle	20	50	175	50
4	CP40d00 (Control Specimen)	None	40	0	0	0
9	RP40d25	Rectangle	40	50	175	25
10	RP40d50	Rectangle	40	50	175	50

Note: Specimens 1 and 4 of Group 2 are same as Specimens 1 and 4 of Group 1 since these specimens are control (uncorroded) specimens for $0.2\,p_y$ and $0.4\,p_y$ internal pressures, respectively.

Table 3.3 Material Properties for X46 grade steel pipe

Modulus of Elasticity	200 GPa
Yield Stress (0.2% offset strain)	340 MPa
Ultimate Tensile Stress	420 MPa
Strain at Rupture	32 %

$$C_t \quad C_t = EApipe\alpha\,(\Delta T)$$
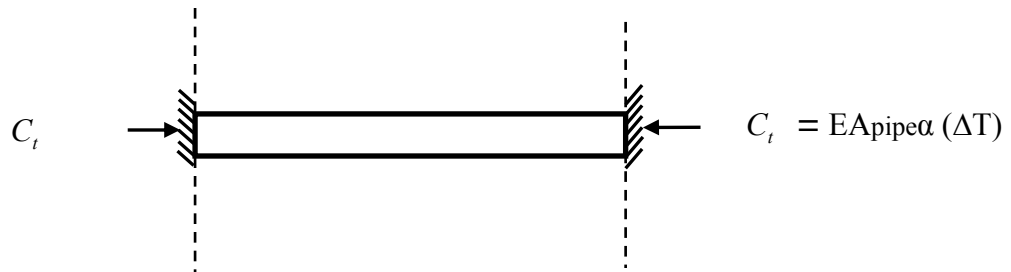
Figure 3.1 Longitudinal compressive force along pipeline due to temperature difference

Direction of landslide movement

Pipeline

Ground slope

Tension
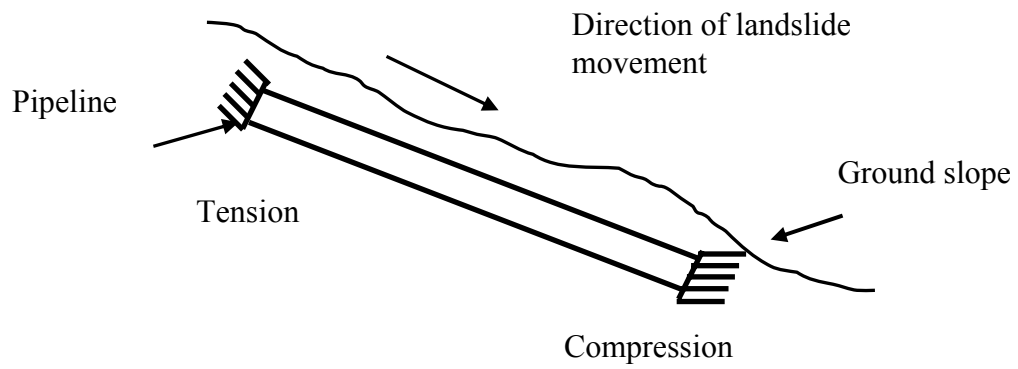
Compression

a) Pipeline subjected to landslide movement

Segment A   Segment B

C_a
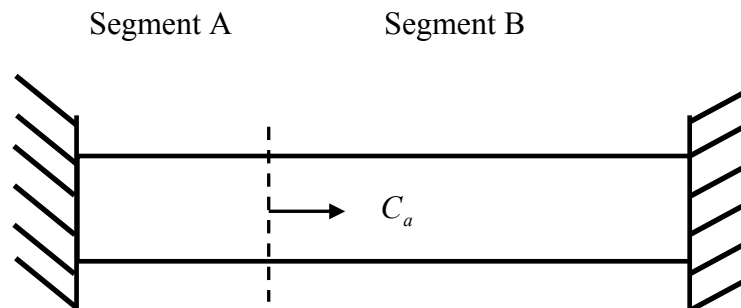
b) Pipeline under axial force C_a due to landslide

Segment A

RA ←□→ RA

Segment B

$R_B = C_l$ →□← $R_B = C_l$
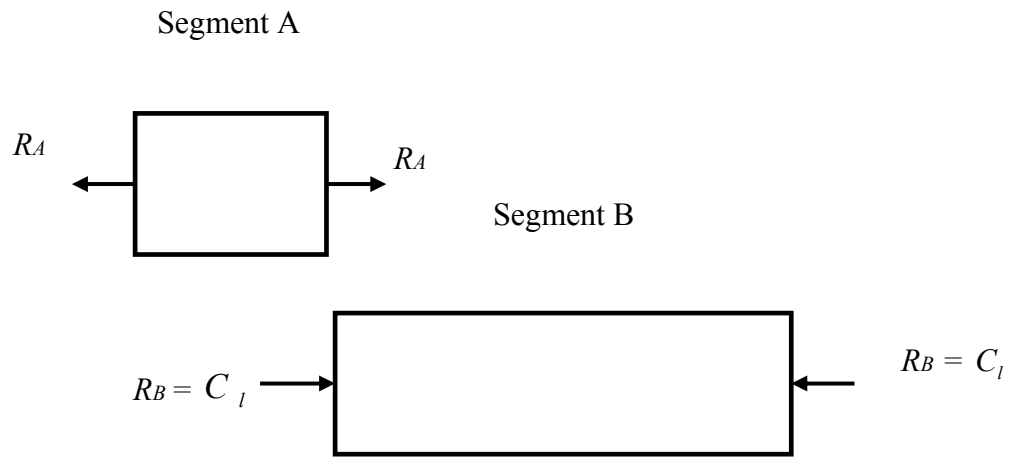
c) Free-body Diagram

Figure 3.2 Longitudinal compressive force due to landslide

50 mm top end plate

Water outlet

L = 610 mm

168 mm dia pipe

L_e = 458 mm
(Net length)

76 mm Collars

50 mm bottom end plate

Water inlet
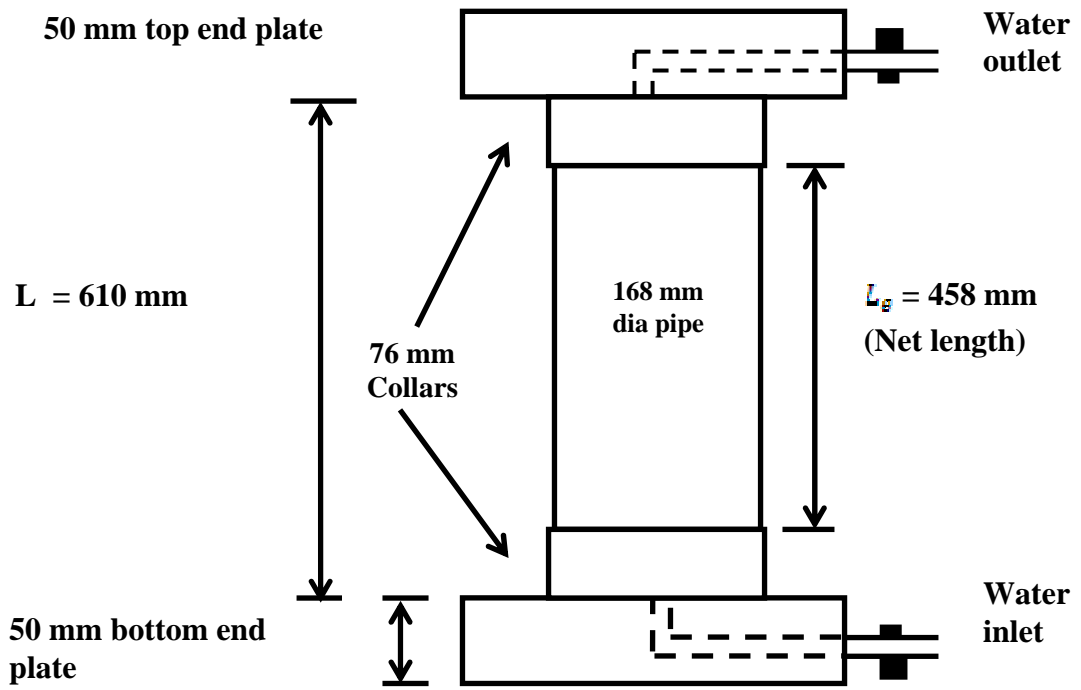
Figure 3.3 Schematic of a typical pipe specimen
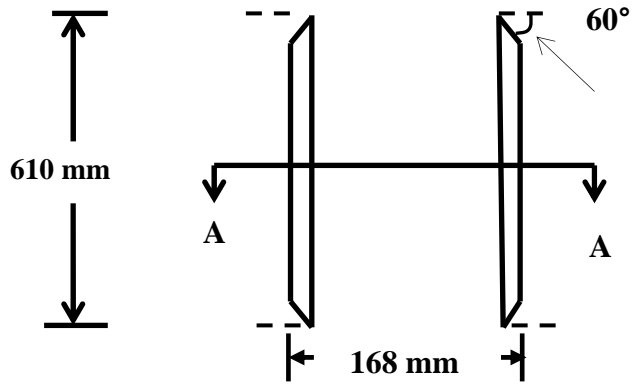
a) Sectional elevation of uncorroded pipe specimen
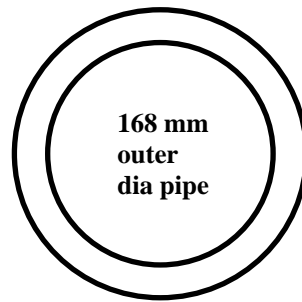
b) Section A-A

Figure 3.4 Cross sectional view of a typical pipe specimen

L_A
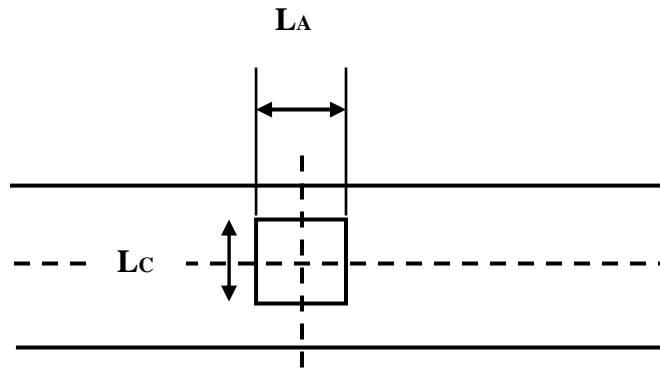
a) Top elevation view of corrosion patch

b) Photograph of corrosion patch

Fillet Radius = 3 mm

$L_A/2$

t

d
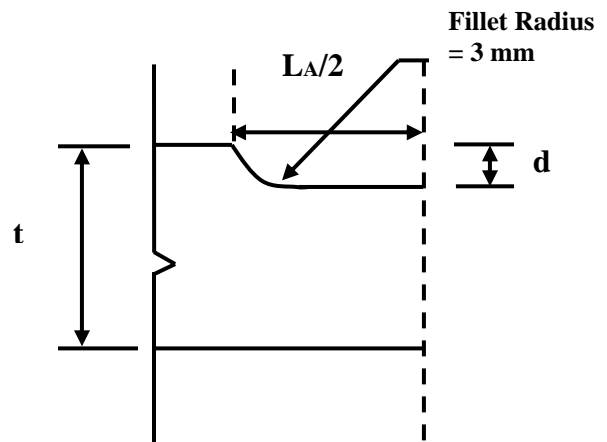
c) Sectional view of corrosion patch

Figure 3.5 Detail of corrosion defect on the pipe specimen
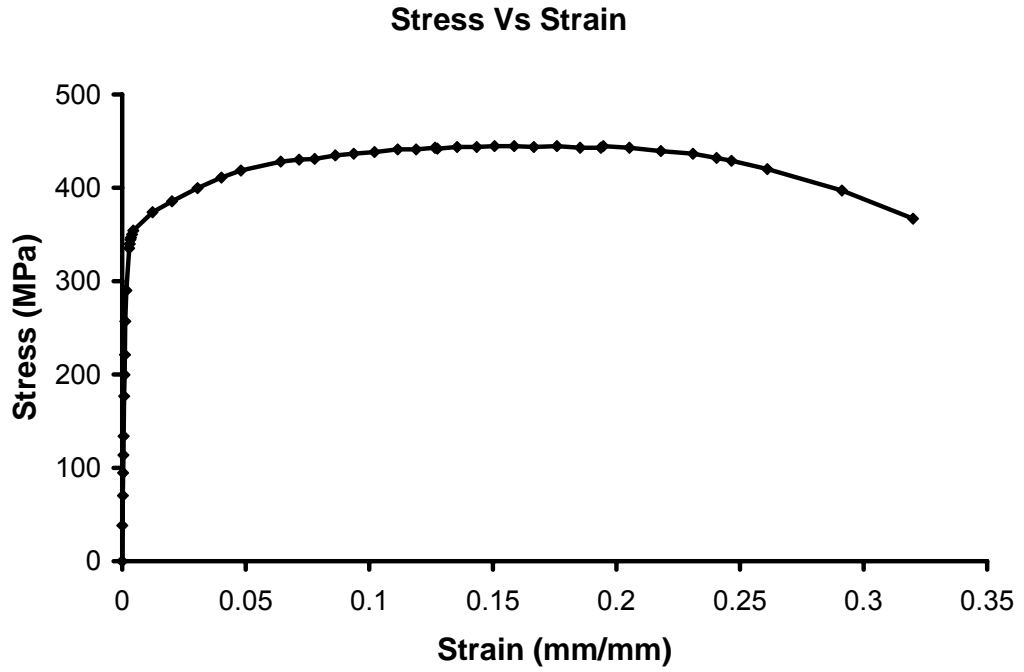
Stress Vs Strain

Figure 3.6 Nominal stress-strain behaviour of a typical coupon specimen

Stress Vs Strain
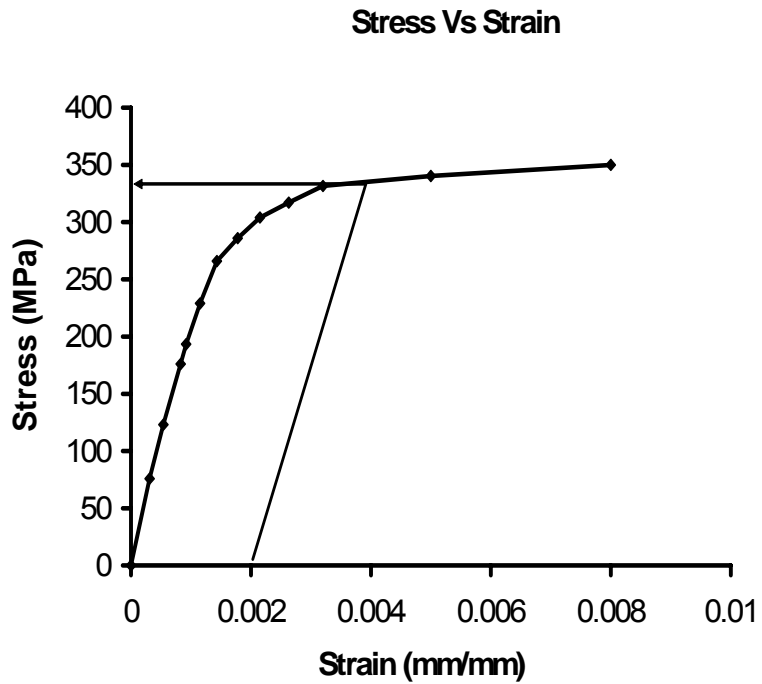
Figure 3.7 Yield stress at 0.2 % offset strain of a typical coupon specimen
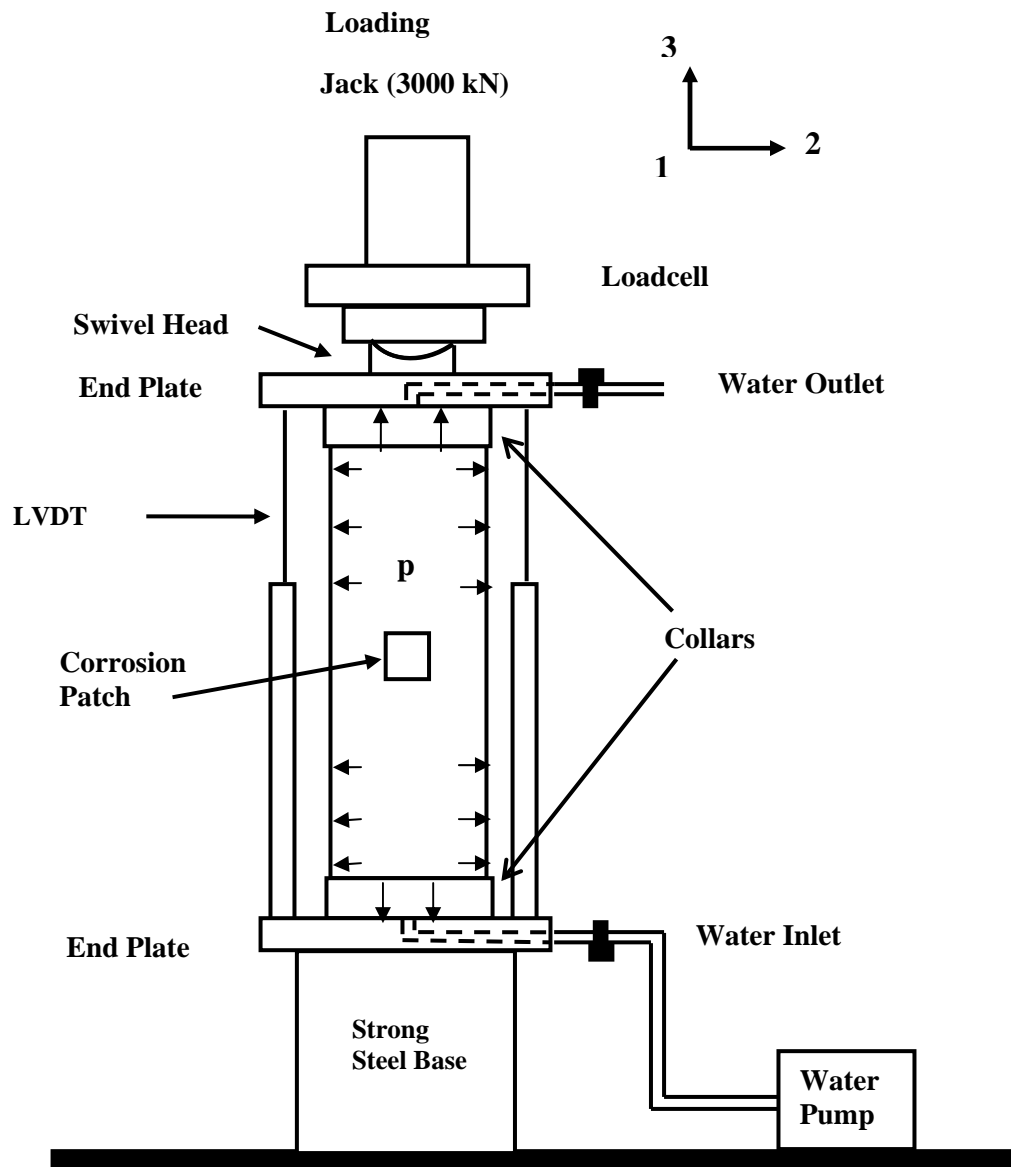
Figure 3.8 A Schematic of typical test setup
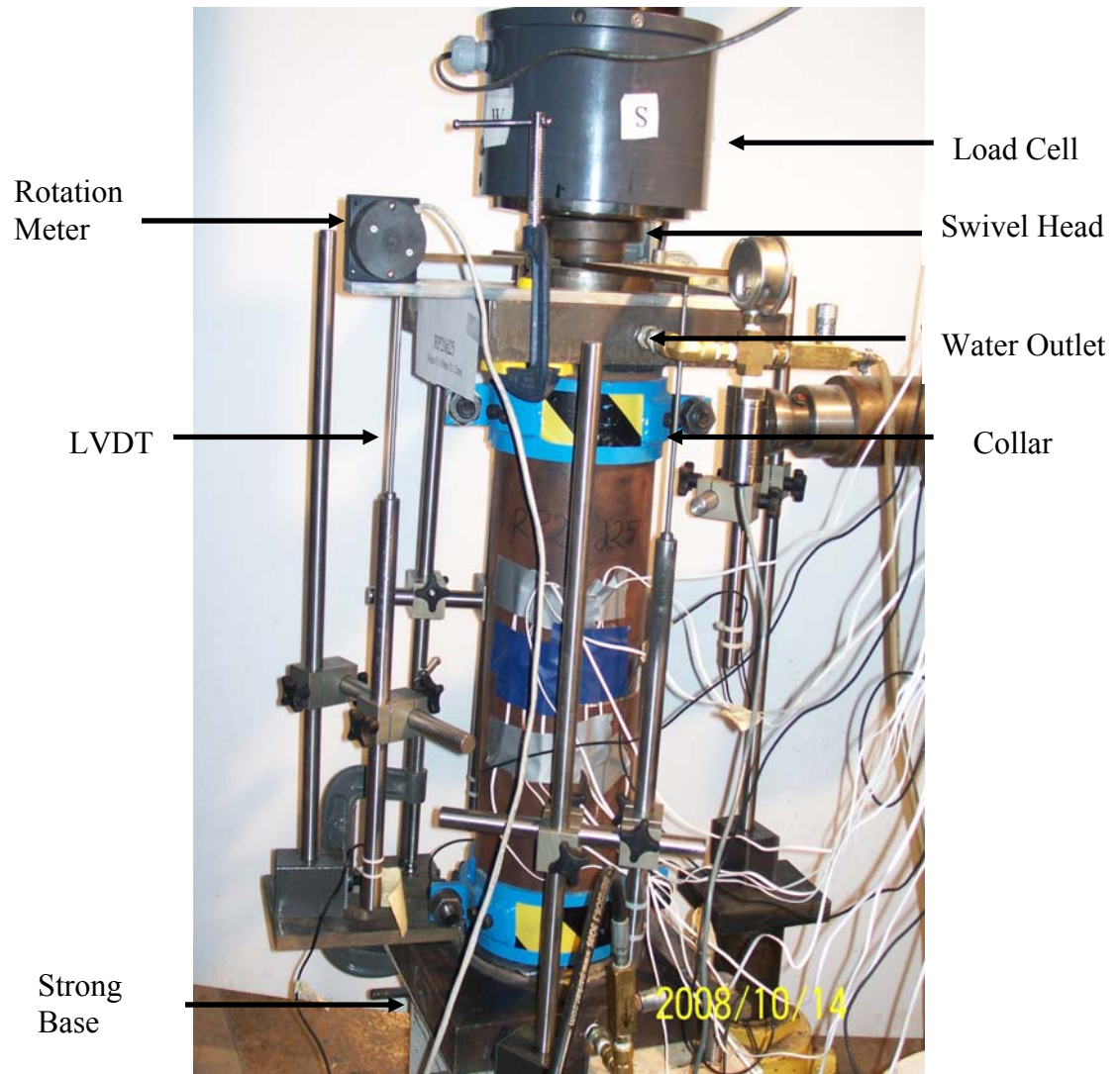
Figure 3.9 A photograph of typical test setup

Load Cell

Swivel Head

Top End
Plate

Top Collar

Pipe
Specimen
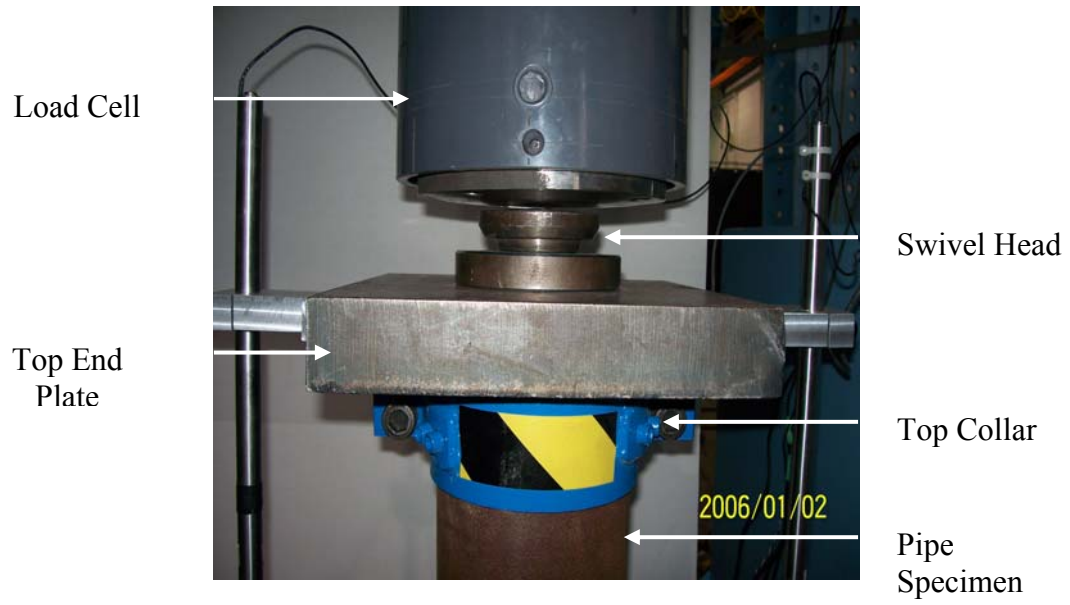
Figure 3.10 Swivel head
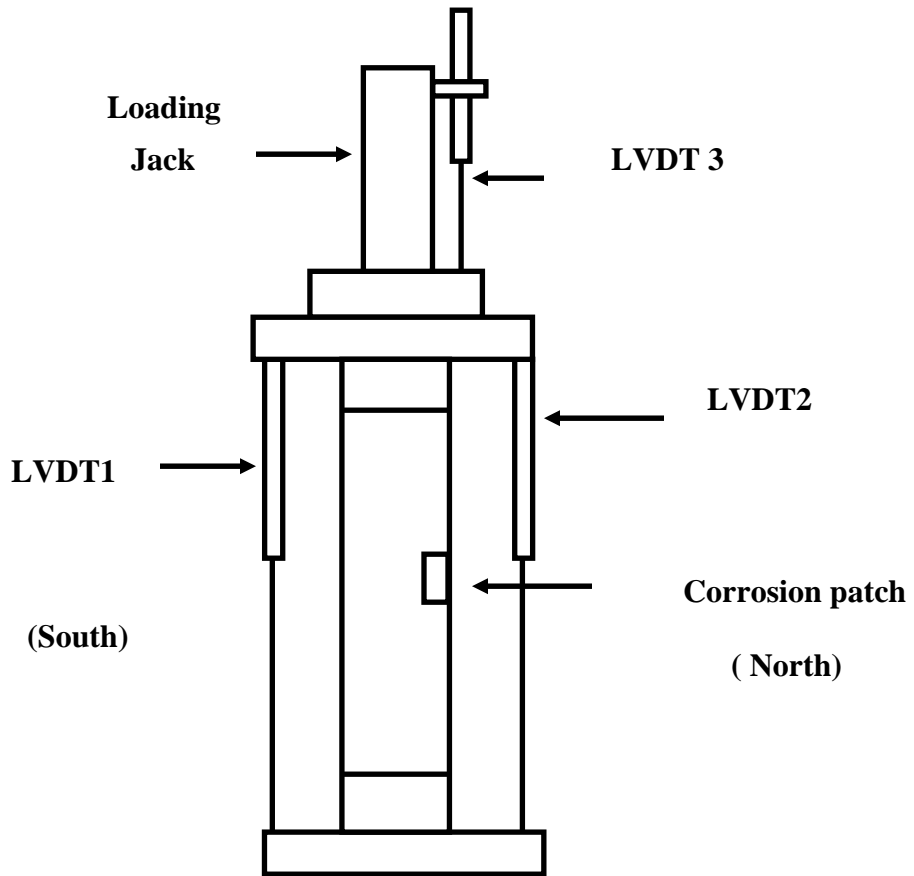
Figure 3.11 LVDT positions for CP20d00, SP20d25, SP20d50

Corrosion Side

LVDT4
(North)

LVDT2
(West)

Top End Plate

LVDT3
(East)

LVDT1
(South)
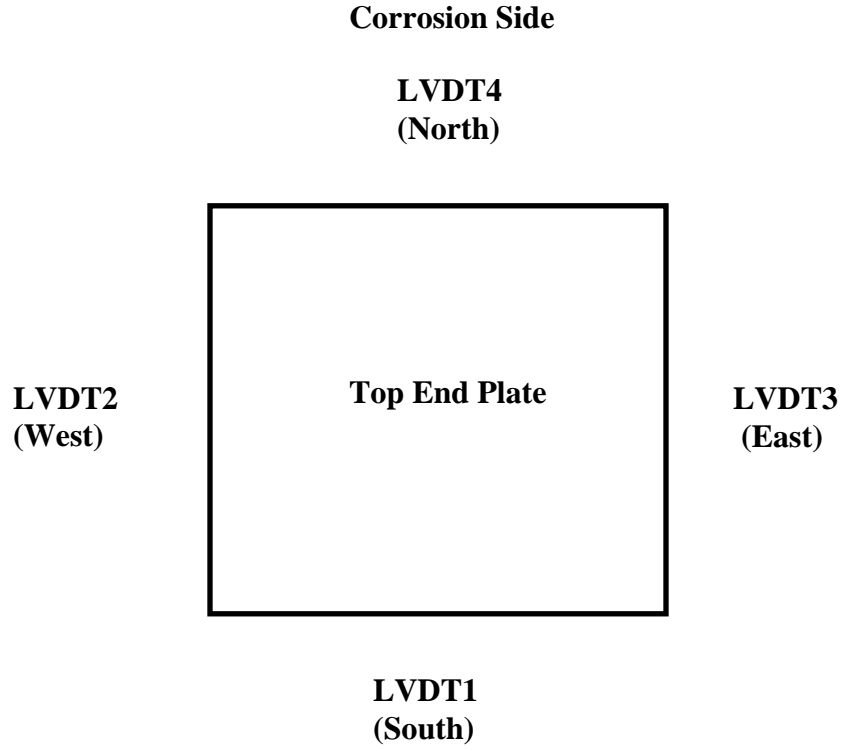
Figure 3.12   Plan view for LVDT positions for the last seven tests

1
2
3
4
5

Top Foot
Crest
Bottom Foot
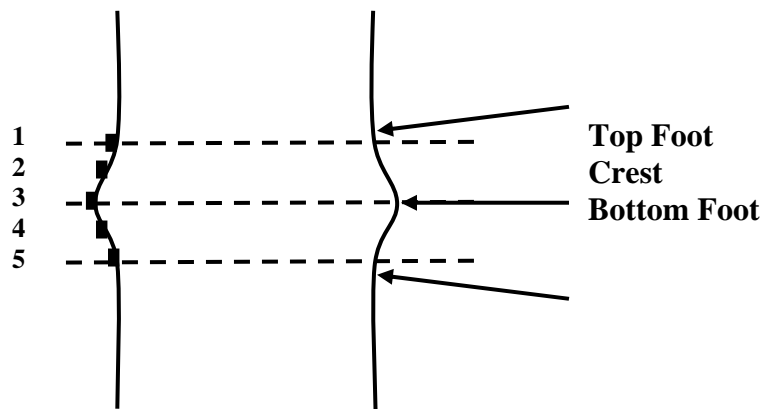
Figure 3.13 Typical layout of strain gauges in and around the wrinkle for the control specimens

6 mm

6 mm

$L_A/2$

a b c

1

2

3

$L_C/2$
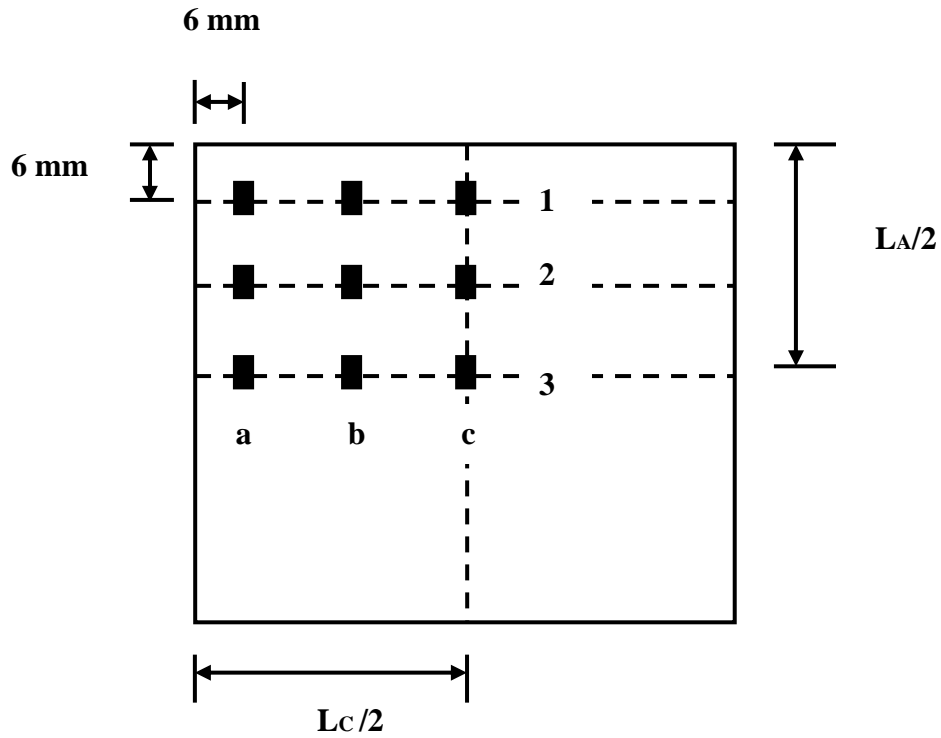
Figure 3.14 Strain gauge positions for the corroded specimens of Group 1

6 mm

10 mm

$L_A/2$

a b c d

1

2

3

$L_C/2$
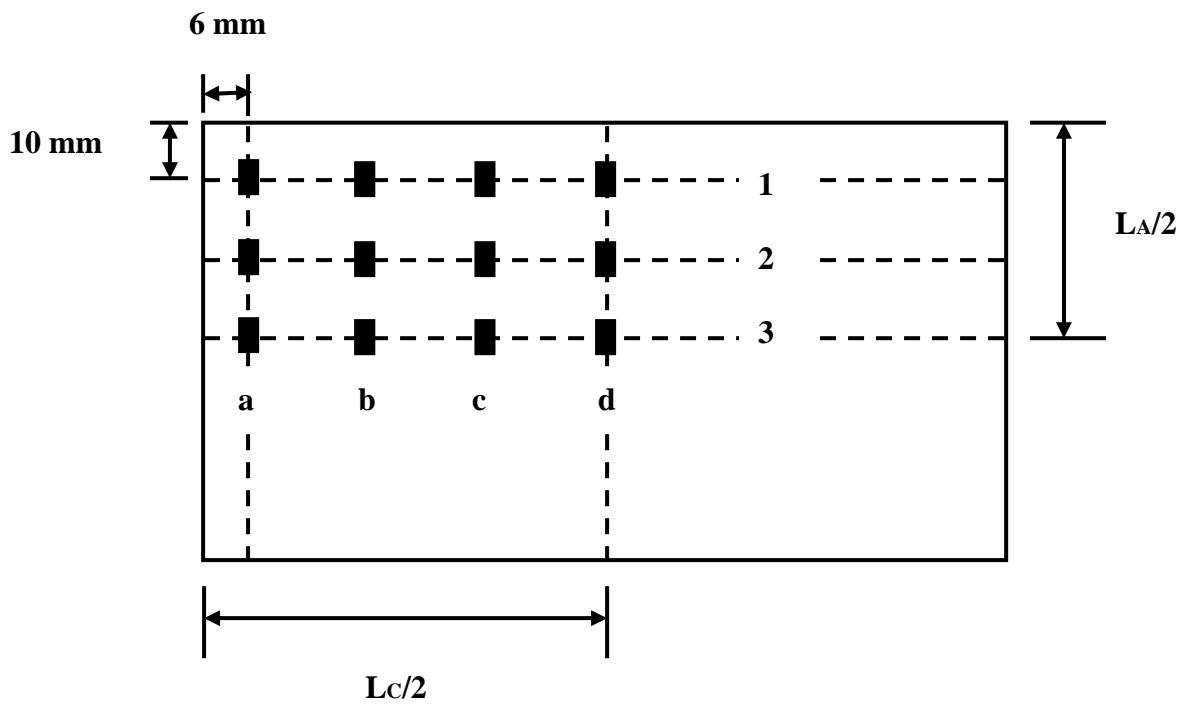
Figure 3.15 Strain gauge positions for the corroded specimen of Group 2
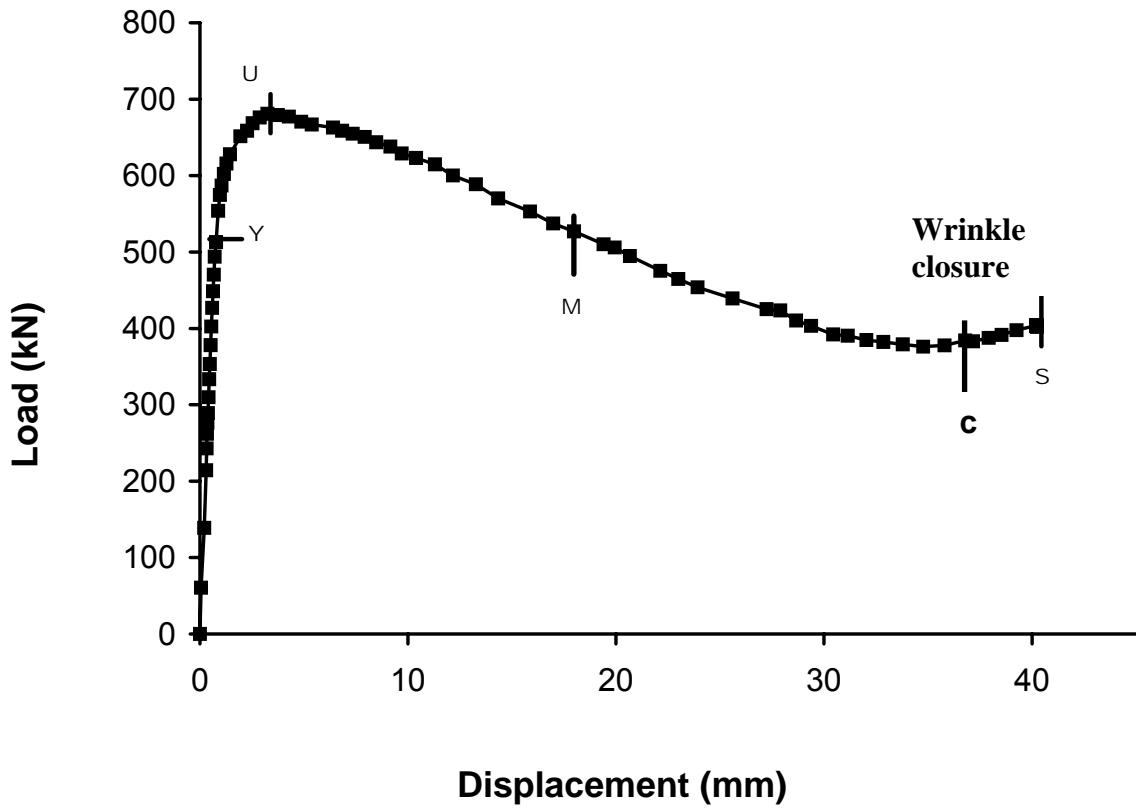
Figure 3.16 Typical load-deformation response
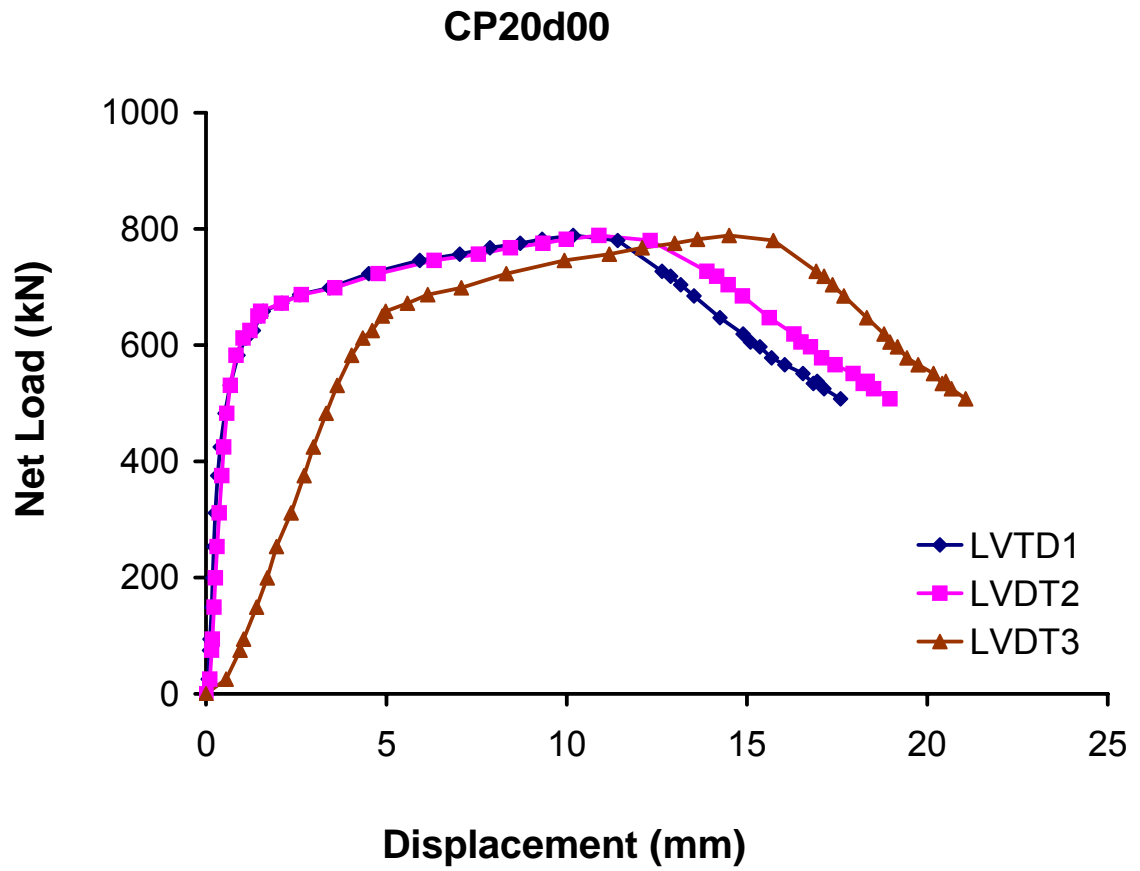
CP20d00

Figure 3.17 Net load deformation behaviour of control specimen CP20d00
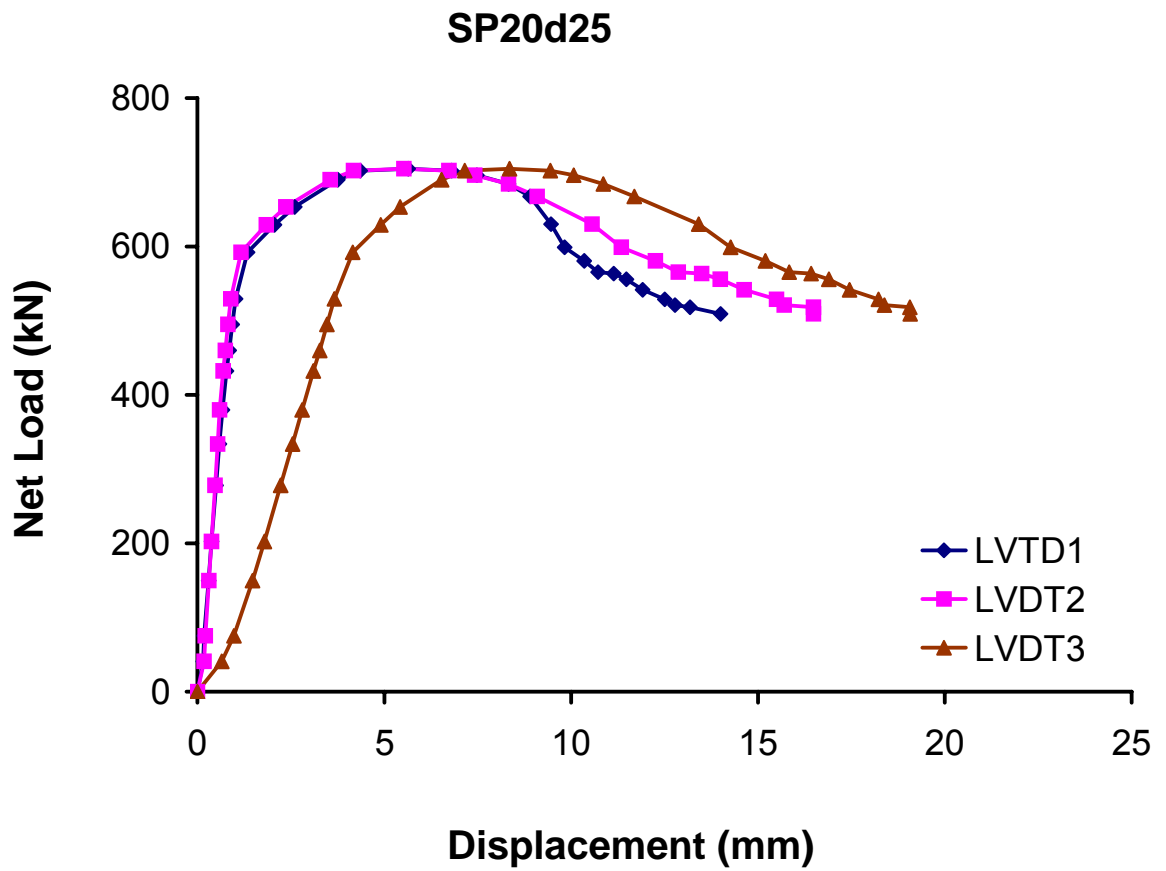
Figure 3.18 Net load deformation behaviour of specimen SP20d25
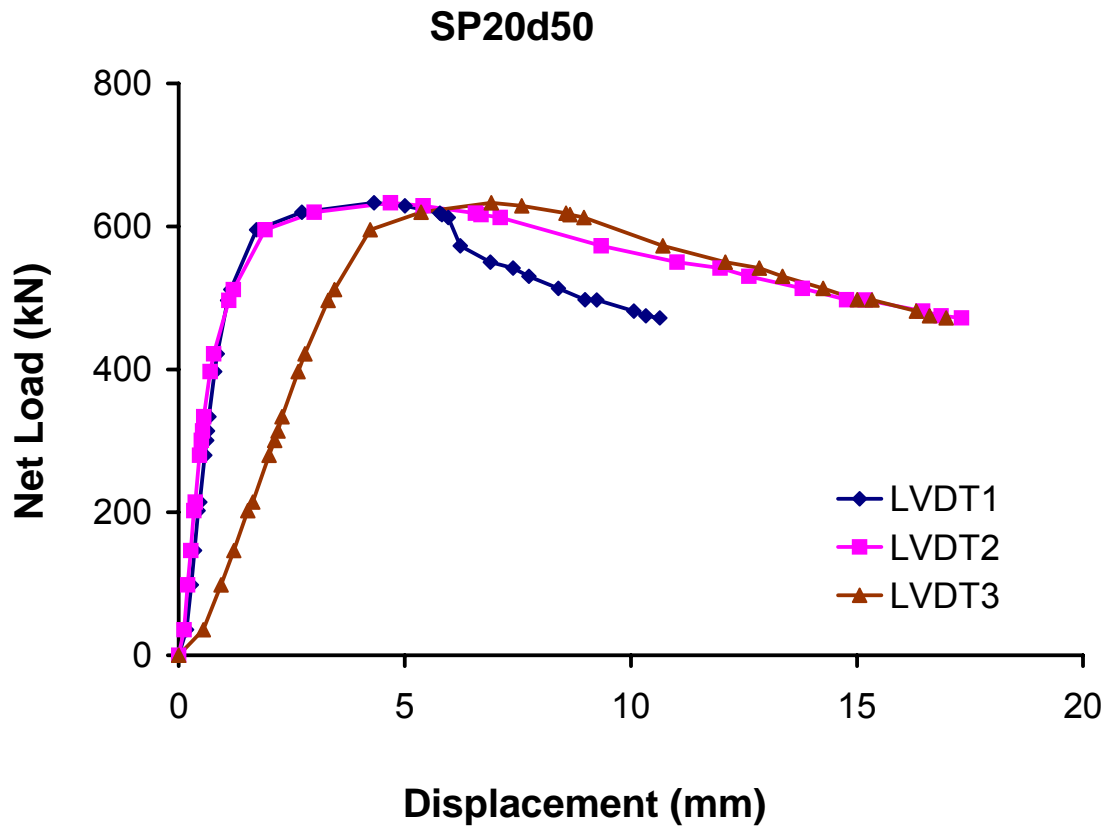
Figure 3.19 Net load deformation behaviour of specimen SP20d50
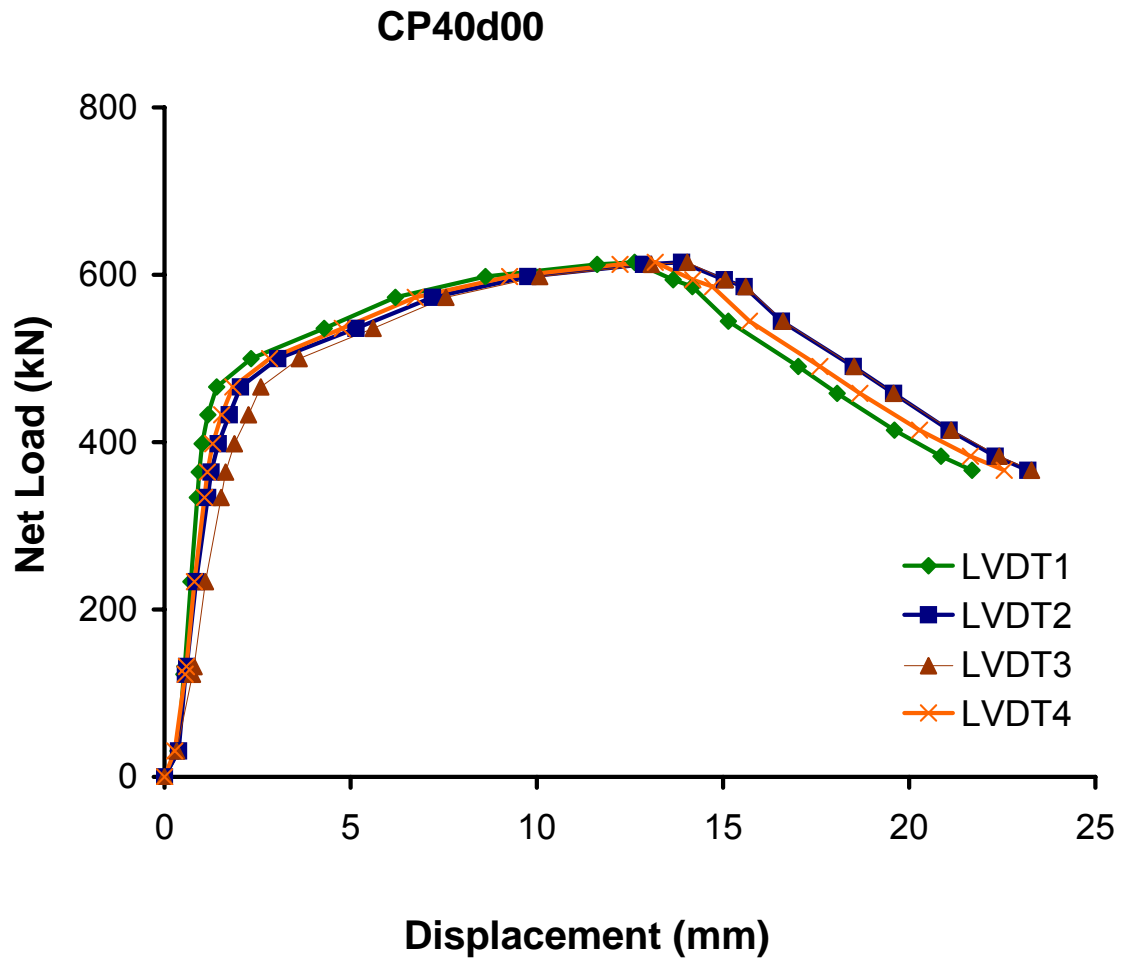
CP40d00

Figure 3.20 Net load deformation behaviour of control specimen CP40d00
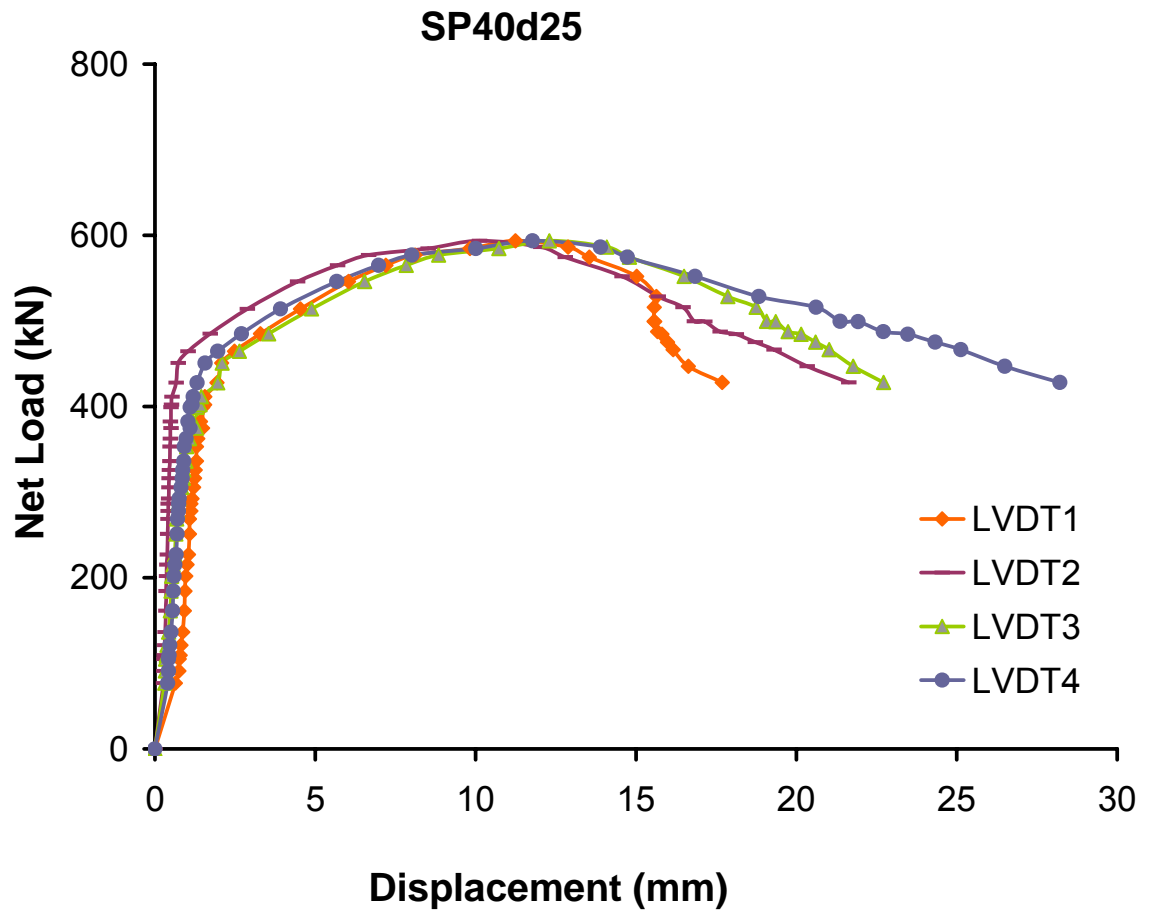
Figure 3.21 Net load deformation behaviour of specimen SP40d25
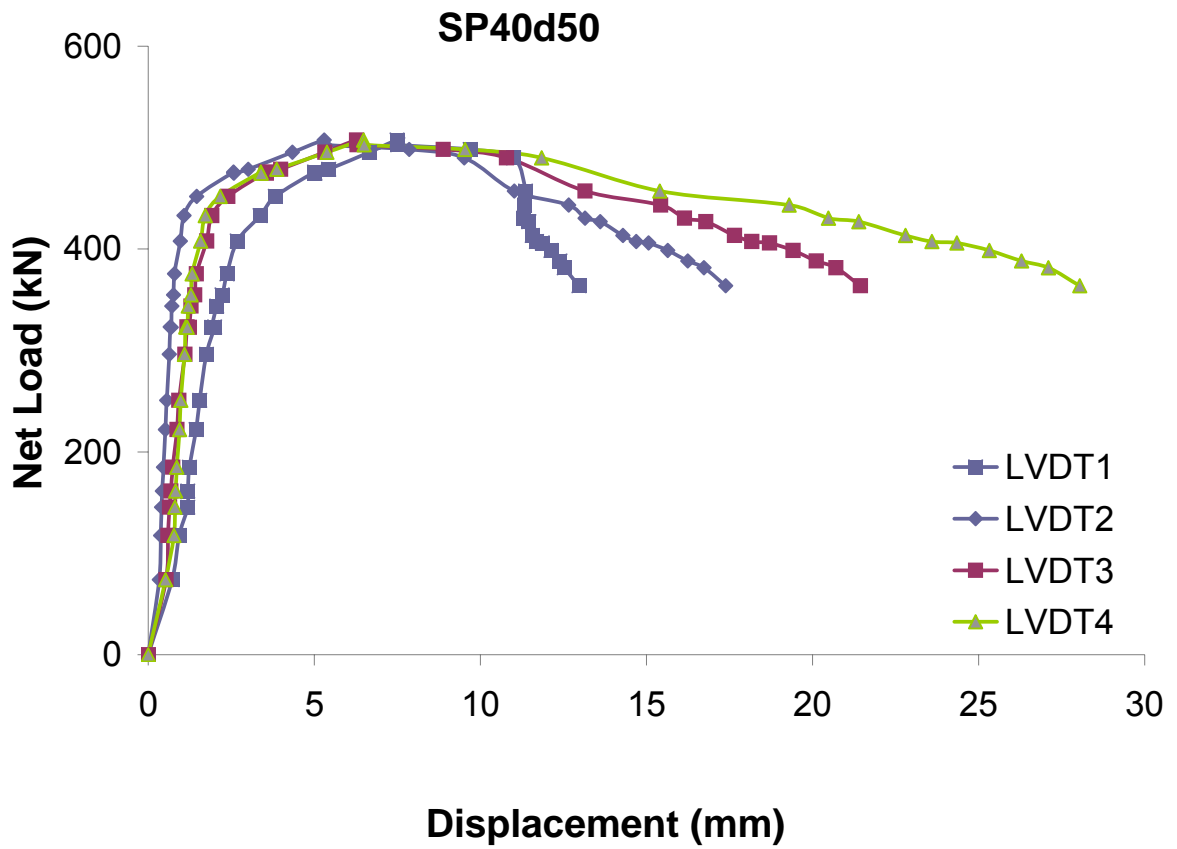
Figure 3.22 Net load deformation behaviour of specimen SP40d50
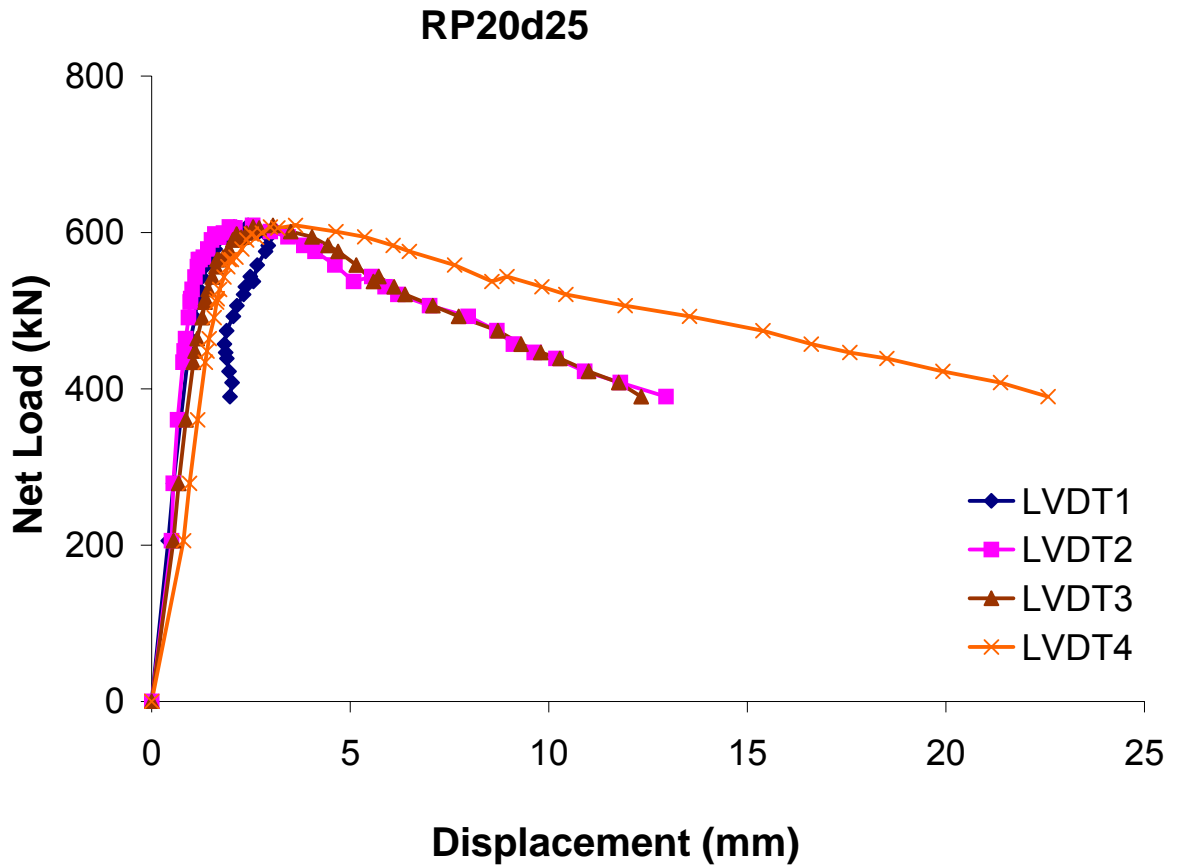
RP20d25

Figure 3.23 Net load deformation behaviour of specimen RP20d25
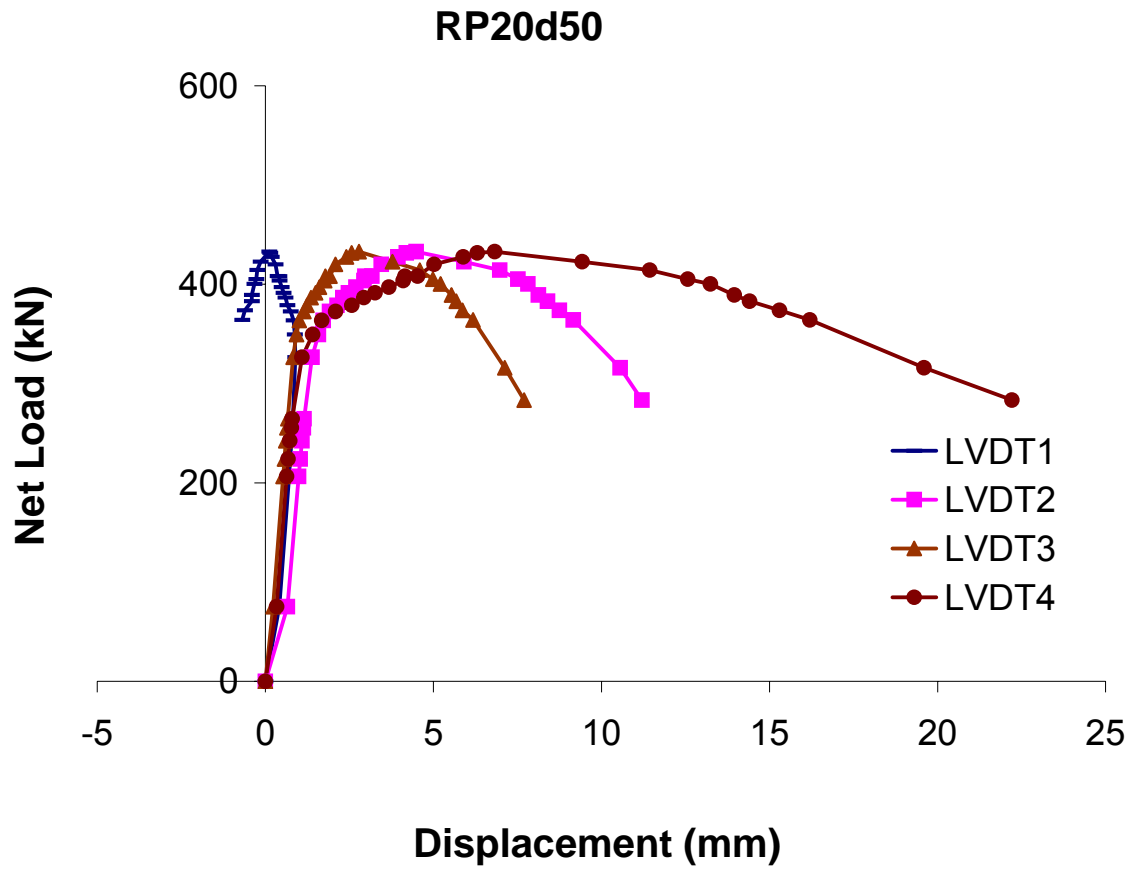
Figure 3.24 Net load deformation behaviour of specimen RP20d50
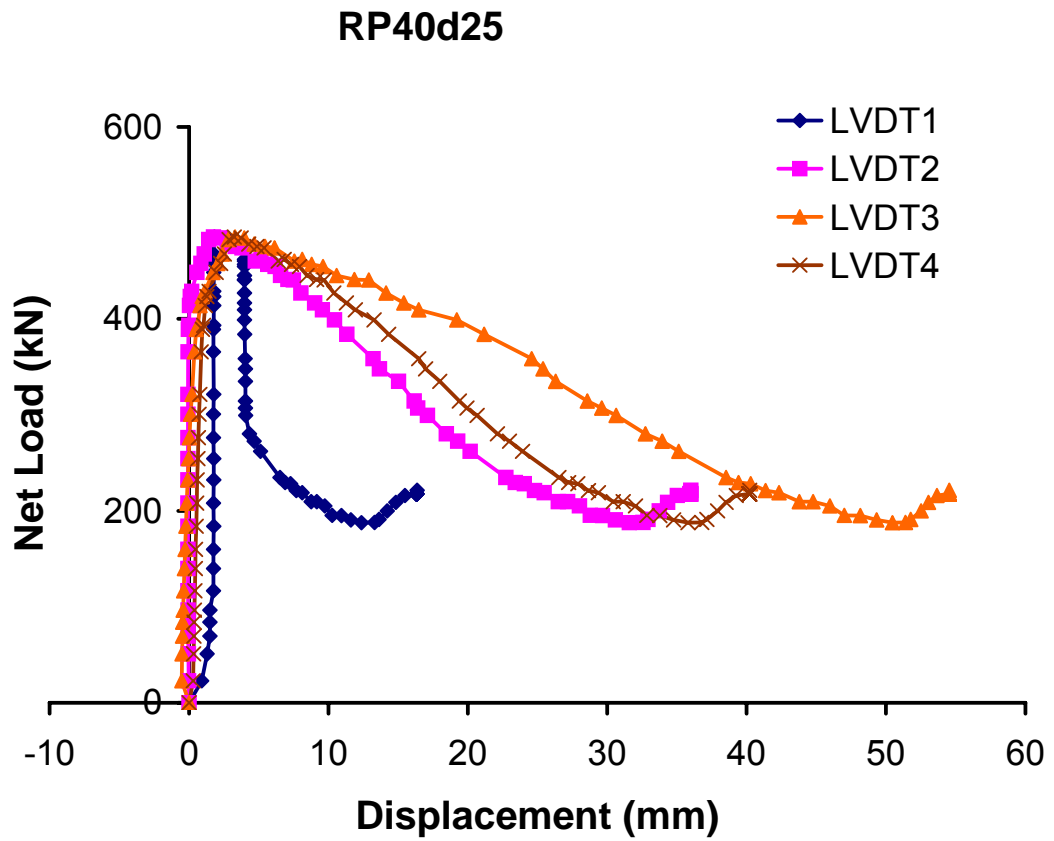
Figure 3.25 Net load deformation behaviour of specimen RP40d25
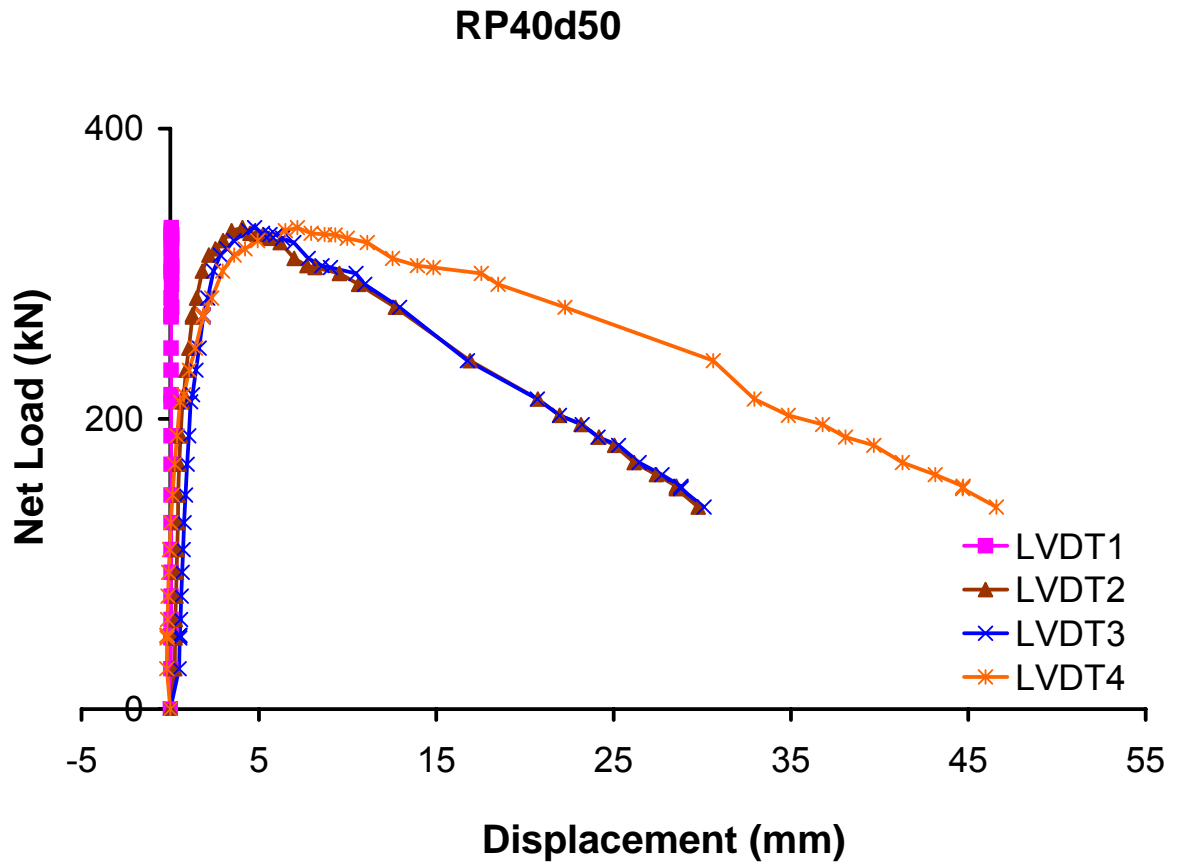
Figure 3.26 Net load deformation behaviour of specimen RP40d50

4 Experimental Results

4.1 General

The purpose of this chapter is to present the results obtained from the experimental program described in chapter 3 for different groups of specimens tested under monotonic loading. The detail of these groups is given in the previous chapter. The results presented in this chapter are in the form of net load vs. deformation response of the corroded pipe under combined internal pressure and compressive axial load and the strain histories at various critical locations (for example foot and crest) of the wrinkle that develops due to combined axial load and internal pressure. The net load is the load in the pipe wall and calculated using Equation 3.4. The effects of different test parameters such as increased internal pressure, depth of corrosion (d), and circumferential dimension of corrosion (L_C) on the net load deformation behaviour of the corroded pipe will also be discussed in this chapter. The net load and the displacement at points Y and U, as described in section 3.15 and Figure 3.16 will be used to investigate the effect of the test parameters in this chapter. The net load and displacement at point U will be called the net load capacity (P_U) and deformation ability (Δ_U), respectively. In this chapter, the displacement values obtained from LVDT3 which was attached to the jack were used to plot the net load deformation behaviour of Group1A (specimens CP20d00, SP20d25, SP20d50 as discussed in section 3.12.2). For all other specimens, an average displacement value from LVDT2 and LVDT3 (Figure 3.12) was used to plot the net load deformation behaviour. It is also important to note that the net load on the pipe was used for these plots instead of total applied load. It should also be mentioned that throughout this chapter (in figures and text) the positive strain and displacement values indicate compression.

Later on, it was decided to apply cyclic deformations on the wrinkled pipe specimens to determine their remaining strengths under cyclic loading history. The scope of this research did not include cyclic loading on wrinkled pipe specimen. Therefore, the results of the cyclic loading specimen are included as Appendix A.

4.2 Discussion on behaviour of Group 1A
4.2.1 Load Deformation Behaviour

Group 1A (square corrosion patch and $0.2p_y$ pressure) consists of two corroded specimens, SP20d25 and SP20d50 and one control specimen CP20d00 which has no corrosion defect (Table 3.1). During loading, the level of internal pressure was kept unchanged to $0.2\,p_y$ for these specimens. The corrosion dimensions (length and width) of specimens SP20d25 and SP20d50 are the same (50 mm x 50 mm). However, for the second specimen the corrosion depth (thickness loss due to corrosion) is double ($0.5t$) of the first specimen which has a corrosion depth (*d*) of $0.25t$. Their behaviours are compared with a control specimen CP20d00. Their specifications are given in Table 3.1 in the previous chapter. The control specimen was loaded axially and the load was increased monotonically while the pressure was kept unchanged (Figure 4.1). The maximum net load reached was 788 kN and then the load capacity started to drop because of the initiation of the wrinkle (Figure 4.2). The test was discontinued when the net load was 508 kN and the displacement was 17.6 mm (point M in Figure 4.2) since the wrinkle was large. Similar trend was found for the corroded specimens. Two corroded specimens, SP20d25 and SP20d50 were loaded in the same way. However, the ultimate net loads (P_U) for these two specimens were 715 kN and 639 kN, respectively, and subsequently the load capacity decreases. These tests were discontinued when the net load capacity at point M (P_M) dropped to 509 kN and 500 kN, respectively. As expected, the net load and the displacement at point *U* (ultimate net load) are the lowest for the specimen SP20d50 as the loss of wall thickness due to corrosion of this specimen is greater than for the other two specimens. A summary of net load and corresponding displacement at point Y, M and U (Figure 3.16) is given in Table 4.1. The percent change (or reduction) of these values (Tables 4.1, 4.3, 4.5, 4.7) as compared to the control specimen is calculated using following equation

$$\% \text{ Change} = \frac{C_{Value} - S_{Value}}{C_{Value}} \times 100 \qquad (4.1)$$

Where C_{value} is the value of net load or displacement at point Y or U or M (or S) for the control specimen ; S_{Value} is the value of net load or displacement at point Y or U or M (or S) for the corroded specimen.

Figure 4.2 shows the global load deformation behaviour obtained from the three specimens of Group 1A. In Figure 4.2 point Y represents global yielding of the pipe specimen, point U is the point when maximum (ultimate) load capacity was obtained, and point M is when the test (monotonic load test) was discontinued. It should be noted that the net load on pipe was used to plot Figure 4.2 instead of the total applied load and the applied load vs. displacement plot is provided in Appendix B (Figure B.1). The displacement value from LVDT3 which was mounted on the jack was first corrected (Section 3.13) prior to being used in this figure. A group photograph of the deformed specimens of this group is provided at the end of this chapter (Figure 4.3).

4.2.2 Local Strain Behaviour

The maximum local strain values at or near the foot and the crest of the wrinkle for specimen CP20d00, SP20d25 and SP20d50 are shown in Table 4.2 and the respective net load vs. strain (%) plot are shown in Figure 4.4 , Figure 4.5, and Figure 4.6. The positive strain value represents compressive strain in these figures. The numbers referred in the parenthesis in the legends of these plots are the actual location of the strain gauges as shown in Figure 3.13 (for CP20d00) and Figure 3.14 (for SP20d25 and SP20d50). The number shown before the parenthesis is strain gauge number as marked on the specimens. The stain values at the foot and the crest for the control specimen CP20d00 could not be captured as it was difficult to anticipate the exact position and size of the wrinkle for this specimen. But SG5 was located at 2.5 mm below the top foot of the wrinkle (Figure 4.7) and therefore, its value went up to 4.8% strain in compression and then went in the reverse direction as the wrinkle continued to grow. The maximum compressive strains at the foot of the wrinkle of the specimen SP20d25 and SP20d50 are 4.6% and 11.3%, respectively. These maximum values were obtained when the test was discontinued, that is at point M (Figure 3.16). The maximum compressive strains at the crest of the wrinkle of these two specimens are 2.6% and 1.2 %, respectively (Figure 4.5 and 4.6

81

respectively). Beyond these points, these values move to the reverse direction and go into the tensile zone as the wrinkle continues to grow. It is noticeable that the strain value at the crest of the wrinkle starts to go in the reverse direction as early as 1.2% of strain for the specimen SP20d50 where the corrosion depth is greater than the other specimen SP20d25.

4.3 Discussion on behaviour of Group 1B
4.3.1 Load Deformation Behaviour

Group 1B (square corrosion patch and $0.4p_y$ pressure) consists of two corroded specimens, SP40d25 and SP40d50 and one control specimen CP40d00. The specimens of these group are same as Group 1A but during the test, these specimens were pressurized to a level of $0.4p_y$. Figure 4.8 shows the global net load deformation behaviour obtained from the three specimens in Group 1B. Again, the net load on pipe was used to plot Figure 4.8 instead of the total applied load and applied load vs. displacement plot is provided in Appendix B (Figure B.2). The average displacement value from LVDT2 and LVDT3 (Figure 3.12) was used in this figure. The behaviour of these two corroded specimens is compared with the control specimen (CP40d00) that had no corrosion defect and which was also pressurized to a level of $0.4p_y$ in the test. Their specifications are given in Table 3.1 in the previous chapter. The axial load was applied and increased monotonically as was done for the specimens in Group1A. The maximum load capacity, P_U (at point U) for these specimens were 611 kN, 595 kN, and 511 kN, respectively. The internal pressure was kept constant. Beyond point U, the load capacity gradually dropped as the displacement continued to increase. The test for the control specimen (CP40d00) was discontinued at load (P_M) 367 kN and the displacement 21.7 mm (Point M). The tests for two corroded specimen SP40d25 and SP40d50, were abandoned when the net load capacities (P_M) dropped to 434 kN and 369 kN, respectively. Similar to specimens in Group 1A, the net load and the displacement at point U of these specimens decreased with increasing corrosion depth of the specimen. A summary of the net load and load point displacement at point Y, M and U (Figure 3.16) is given in Table 4.3 and a group

photograph of the deformed specimens of this group is provided at the end of this chapter (Figure 4.9).

4.3.2 Local Strain Behaviour

The maximum local strain values at or near the feet and the crest of the wrinkle for specimen CP40d00, SP40d25, and SP40d50 are shown in Table 4.4. The net load vs strain (%) plots for specimen CP40d00 and SP40d25 are shown in Figure 4.10, Figure 4.11 respectively. Figure 4.12 and Figure 4.13 represent the net load vs. strain distribution at the crest and foot of the wrinkle of the specimen SP40d50. The numbers referred in the parenthesis in the legends of these plots are actual location of the strain gauges on the specimen as shown in Figure 3.13 (for control specimen) and Figure 3.14 (for SP40d25 and SP40d50). The number shown before the parenthesis is strain gauge number as marked on the specimens. For example, SG7 (5) in Figure 4.10 indicates that the actual location of this strain gauge is at the bottom foot of the wrinkle as shown in Figure 3.13 but in the test this strain gauge was marked as SG7. The maximum stain values at two feet of the control specimen CP40d00 are 9.4% and 10%. The exact position of the crest could not be captured but the position of SG4 (4) was near the crest and the maximum compressive stain (%) at the initiation of the wrinkle at this position is 3%. The maximum compressive strains (%) at the foot of the wrinkle of the specimen SP40d25 and SP40d50 are 15.4 % and 15.2 %, respectively. These maximum values are defined as the stain values at the test stop points M (Figure 3.1). The maximum compressive strains at the crest of the wrinkle of these two specimens are 3.9% and 1.2% respectively (Figure 4.11 and Figure 4.12, respectively). Beyond these points these values start to move in the reverse direction and go toward the tensile zone as the wrinkle continues to grow. It is noticeable that the strain value at the crest of the wrinkle starts to go in the reverse direction as early as 1.2 % of stain for the specimen SP40d50 where the corrosion depth is greater than the other specimen SP40d25.

4.4 Discussion on behaviour of Group 2A
4.4.1 Load Deformation Behaviour

Group 2A consists of two corroded specimens (rectangular corrosion patch and $0.2p_y$ pressure), RP20d25 and RP20d50 and one control specimen CP20d00. The corrosion dimensions of the two specimens were same (50 mm x 175 mm) except that, in second specimen the corrosion depth ($0.5t$) was double that of the first specimen. The test parameter of these specimens are same as Group 1A, however, only the circumferential dimension of the corrosion (L_C) was 3.5 times longer than that for the specimens in Group 1A. The internal pressure was kept constant at $0.2p_y$. Figure 4.14 shows the global load deformation behaviour obtained from the three specimens of Group 2A. Again, the net load on was used to plot Figure 4.14 pipe instead of the total applied load and applied load vs. displacement plot is provided in Appendix B (Figure B.3). The average displacement value obtained from LVDT2 and LVDT4 (Figure 3.12) was used in this figure.

The behaviour of the specimens in this group are compared with a control specimen (CP20d00) and with the respective specimens of Group 1A to investigate the effect of increased circumferential dimension of the corrosion (L_C). Their specifications are given in Table 3.2 in the previous chapter. Like the two corroded specimens in Group 1A, the ultimate net load (P_U) for RP20d25 and RP20d50 reached to 616 kN and 433 kN, respectively and then the load capacity started to drop. These tests were discontinued when the load capacities (P_M) dropped to 390 kN and 264 kN, respectively. As compared to Group1A this group shows less stability. It can be observed that for these two corroded specimens, although the net load capacity (P_U) at point U decreases as the corrosion depth of the specimen increases the displacement (Δ_U) at point U increases with increasing corrosion depth. This observation is different (opposite) from that of Group 1A where both the load capacity (P_U) and the displacement (Δ_U) at point U decreased with increasing corrosion depth of the specimen. A summary of the net load at point Y and the net load and displacement at point U and M (Figure 3.16) is given in Table 4.5

and a group photograph of the deformed specimens in this group is provided at the end of this chapter (Figure 4.15).

4.4.2 Local Strain Behaviour

The maximum local strain values at or near the foot and the crest of the wrinkle for specimen CP20d00, RP20d25 and RP20d50 are shown in Table 4.6. For this group high elongation (±15%) glue (KYOWA CC-36) was used to bond the strain gauges to the pipe surface and as a result, higher tensile strains at the crest of the wrinkle could be obtained. The net load vs. strain (%) plots at the crest of the specimens RP20d25 and RP20d50 are shown in Figure 4.16 and Figure 4.17, respectively. Figure 4.18 and Figure 4.19 represent the net load vs. strain distribution at the foot of the wrinkle for specimens RP20d25 and RP20d50, respectively. The numbers referred in the parenthesis in the legends of these plots are the position of the strain gages as shown in Figure 3.13 and Figure 3.15. The maximum compressive stain (%) values at the foot of the specimen RP20d25 and RP20d50 are 12.3% and 13.9%, respectively. These maximum values are defined as the stain values when the test was discontinued, that is at point M (Figure 3.16). The maximum compressive strains (%) at the crest of the wrinkle of the specimen RP20d25 and RP20d50 were 1.5% and 0.5% respectively. These maximum values are defined as the stain values at the initiation of the wrinkle growth. Beyond this point the strain goes in reverse direction and reaches to the tensile zone as the wrinkle grows. Like Group 1A and Group 1B it is also noticeable that the strain value at the crest of the wrinkle starts to continue in reverse direction as early as 0.5 % of stain for the specimen RP20d50 where the corrosion depth is greater than the other specimen RP20d25 for which this value is 1.5%. The maximum tensile strains at the crest of the wrinkle at point M (Figure 3.17) of these two specimens are 8.7 % and 4.7 %, respectively.

4. 5 Discussion on Behaviour of Group 2B
4.5.1 Load Deformation Behaviour

Group 2B consists of two corroded specimens, RP40d25 and RP40d50 and a control specimen CP40d00. The corrosion size for these specimens is same as for Group 2A. Hence, the parameter of these specimens are same as Group 2A but during the test these

specimens were pressurized to $0.4 p_y$ to study the effect of increased pressure on load-deformation behaviour of the corroded specimens. The net load-deformation plot of this group is given in Figure 4.20 and applied load vs. displacement plot is provided in Appendix B (Figure B.4). The test on control specimen CP40d00, was repeated because the load deformation behaviour obtained from the first test did not seem right. The repeat test was conducted on a shorter (300 mm long) specimen for verification and the load-deformation behaviour became even worse and it may be due to the end effects. Therefore, in Figure 4.20 the load-deformation behaviour obtained from first test for this control specimen (610 mm long) is used. Their specifications are given in Table 3.2 in the previous chapter. The ultimate net load (P_U) of RP40d25 and RP40d50 reached to 509 kN and 352 kN, respectively and then the load capacity started to drop (Table 4.7). These tests were discontinued when the load capacities dropped to 230.7 kN and 169 kN, respectively. As compared to Group2A, this group also shows less stability than Group 1B and the net load capacity (P_U) at point U decreases as the corrosion depth of the specimen increases but the displacement (Δ_U) at point U increases with increasing corrosion depth. A summary of the net load at point Y and the net load and displacement at point U and S or C (Figure 3.16) is given in Table 4.7. The photograph of the deformed specimens of this group is shown in Figure 4.21. The test for specimen RP40d25 was discontinued at point S where the deformation continued up to 41 mm beyond the wrinkle closure point C but the test for specimen RP40d50 was discontinued at wrinkle closure point C.

4.5.2 Local Strain Behaviour

The maximum local strain values at or near the foot and crest of the wrinkle for specimen CP40d00, RP40d25, and RP40d50 are shown in Table 4.8. The net load vs strain (%) plots at the crest of the specimens RP40d25 and RP40d50 are shown in Figure 4.22 and Figure 4.23, respectively. Figures 4.24 and 4.25 represent the net load vs. strain distribution at the feet of wrinkle of the specimen RP40d25 and RP40d50, respectively. The numbers referred in the parenthesis in the legends of these plots are the position of the strain gages as shown in Figure 3.13 and Figure 3.15. The maximum compressive

stain (%) values at the foot of the control specimen RP40d25 and RP40d50 are 13.7% and 10.6%, respectively. These maximum values are defined as the strain values when the tests were discontinued, that is at point S (for RP40d25) or point C (for RP40d50). The maximum compressive strains (%) at the crest of the wrinkle of the specimen RP40d25 and RP40d50 are 1.4 % and 0.2 %, respectively. These maximum values are defined as the stain values at the initiation of the wrinkle (at U). Beyond this point the strain value starts to go in reverse direction and reach to the tensile zone as the wrinkle grows. Like all other groups it is noticeable that the strain value at the crest of the wrinkle starts to continue in reverse direction as early as 0.2 % of stain for the specimen RP20d50 where the corrosion depth is double of the other specimen RP20d25 for which this value is 1.4%. The maximum tensile strains at the crest of the wrinkle at point S of these two specimens are 5.4 % and 9.3 %, respectively.

4.6 Effect of Pressure and Corrosion Dimensions
4.6.1 Effect of Internal Pressure

Group 1B and Group 2B specimens were pressurized to $0.4p_y$ during the tests and their behaviours are compared with Group 1A and Group 2A specimens, respectively to investigate the effect of increased pressure on load-deformation behaviour of corroded steel pipe under combined internal pressure and axial load. Specimen in Group 1A and Group1B were pressurized to $0.2p_y$ level.

4.6.1.1 Net Load Capacity

It can be seen from Figure B.5, Figure B.6, Figure B.7, Figure B.8 and Figure B.9 attached in Appendix B that there is no apparent effect of the increased internal pressure on applied load capacity of the test specimens. But Figure 4.26 shows that the net load capacity at points *Y* and *U* decrease with increased internal pressure for two control specimens. This observation is also confirmed in Figure 4.27, Figure 4.28, Figure 4.29, and Figure 4.30 where the net load deformation behaviours of two similar corroded specimens (corrosion geometry and depth are same) having two different internal pressures were compared. The specimen that was pressurized to $0.2p_y$ (lower pressure)

shows higher net load capacity at points Y and U than the specimen which was pressurized to $0.4p_y$ (higher pressure). Table 4.9 summarizes and compares the net load value of different specimens at points Y and U.

4.6.1.2 Displacement at Ultimate Net load

For all groups the load-deformation curves show increased deformation ability for increased internal pressure. It can be seen from the net load deformation curves shown in Figure 4.26, Figure 4.27, Figure 4.28, Figure 4.29, and Figure 4.30 that the displacement at point U for the specimen pressurized to higher pressure ($0.4p_y$) is higher than the specimen having same corrosion geometry and depth but pressurized to a lower pressure ($0.2p_y$). Table 4.9 summarizes and compares the displacement value of different specimens at point U.

4.6.2 Effect of Corrosion Depth

One specimen from each group (a group being defined by a single level of internal pressure) has a corrosion depth (d) of $0.50t$ and their behaviours are compared with the specimens of the same group that have a corrosion depth of $0.25t$ to investigate the effect of increased corrosion depth on load-deformation behaviour of corroded steel pipe under combined internal pressure and axial load. The wall thickness of the virgin pipe (control specimen) is t.

4.6.2.1 Net Load Capacity

Tables 4.1, 4.3, 4.5, and 4.7 summarize and compare the effect of increased corrosion depth on net load-deformation behaviour of different groups. For the specimens in all four groups (1A, 1B, 2A, and 2B) the load-deformation curves show softer behaviour for increased depth of corrosion. Figure 4.2, Figure 4.8, Figure 4.14 and Figure 4.20 show that due to the increased corrosion depth the change in net load capacity at point Y is not much for Group 1A and Group 1B specimens, however for Group 2A and Group 2B, the net load capacity at point Y decreases with increased corrosion depth of the specimen. Specimen RP20d25 and RP40d25 have 172 kN and 167 kN higher net load capacity at

point Y than the specimen RP20d50 and RP40d50, respectively. From the same figures it can also be observed that the increased corrosion depth reduces the net load capacity at point U for all groups and this reduction is more significant for the specimens in Group 2A and Group 2B, where the size of the corrosion patch was larger.

4.6.2.2 Displacement at Ultimate Net Load

It can be seen from the net load-deformation curve for Group 1A and Group 1B (Figure 4.2 and Figure 4.8) and from Tables 4.1 and 4.3 that the displacement at point U for the specimen having $0.50t$ corrosion depth is less than the specimen having $0.25t$ corrosion depth. But for Group 2A and Group 2B where the specimens have greater circumferential extent of corrosion, the displacement at point U for the specimen having $0.50t$ corrosion depth is greater than the specimen having $0.25t$ corrosion depth. The increase in value of displacement at point U is 12.5% for Group 2A and it is 29.7% for Group 2B. The effect of increased depth on net load-deformation curve for Group 2A and Group 2B are shown in Figure 4.14 and Figure 4.20 and Table 4.5 and Table 4.7 summarize the values of the displacement at point U for these groups.

4.6.3 Effect of Circumferential Length of Corrosion Defect

The specimens of Group 2A and Group 2B had greater circumferential dimension of corrosion defect than the specimens of Group 1A and Group 1B. The purpose was to investigate the effect of increased circumferential dimension of corrosion defect on load-deformation behaviour of corroded steel pipe under combined internal pressure and axial load. It should be noted that circumferential extent of corrosion is believed to have greater influence on axial and bending strength (Cosham and Hophinks 2004; Roy et al. 1997). The former two groups have 3.5 times greater extent of circumferential dimension than the later two groups.

4.6.3.1 Net Load Capacity

Figure 4.31, Figure 4.32, Figure 4.33, and Figure 4.34 compare the effect of increased circumferential dimension of corrosion defect on net load-deformation behaviour

between two specimens having same level of internal pressure, one from Group 1 and another from Group 2. These two specimens from two groups have same test parameter except that the specimen from Group 2 has greater (3.75 times longer) circumferential corrosion dimension than the specimen from Group 1. From the above mentioned figures, it can be seen that the load-deformation curves show softer behaviour and therefore, the net load capacity is much lesser at point Y and U (P_U) for the specimen with increased circumferential length of corrosion than the corresponding specimen of Group 1. Table 4.10 summarizes and compares the value of net load capacity at point Y and U and deformation ability (Δ_U) at point U for each pair of specimen. Table 4.10 also shows that due to the increased circumferential corrosion dimension the decrease in net load capacity at point Y and point U is greater for the specimen having corrosion depth $0.5d$. The percent change values in this table are calculated using the following Equation

$$\%\text{Change} = \frac{V_S - V_R}{V_S} \times 100 \qquad\qquad (4.2)$$

Where V_S is the net load or deformation value at point Y or U for the specimens having square corrosion (L_C = 50 mm) and V_R is the net load or deformation value at point Y or U for the specimens having rectangular corrosion (L_C = 175 mm). It should be noted that all other test parameters such as internal pressure and corrosion depth were the same for these two specimens.

4.6.3.2 Displacement at Ultimate Net Load

It can be seen from Table 4.10 that for the specimen from Group 2 having increased circumferential dimension of corrosion, the displacement at point U is less than the corresponding specimen from Group 1.

4.7 Summary

Finally from this experimental program the following observations can be made:

1) Increased internal pressure reduces the net load capacity (P_U) but increases the deformation ability (Δ_U) for specimens having the same corrosion geometry and the depth.

2) Increased corrosion depth reduces the net load capacity (P_U) for all the specimens having square and rectangular shaped (L_C is 3.5 times of L_A) corrosion defects. It is observed from the experimental program that increased corrosion depth reduces the deformation ability (Δ_U) for the specimen having square shape corrosion but increases the deformation ability (Δ_U) for the specimen having rectangular shape (L_C is 3.5 times of L_A) corrosion.

3) Increased circumferential dimension of corrosion reduces both the net load capacity (P_U) and the deformation ability (Δ_U).

Table 4.1 Test result for Group 1A

| Specimen | At First Yield (Point Y) | | At Maximum Load (Point U) | | | | At End of Test (Point M or S) | | $\dfrac{P_M}{P_U}$ | $\dfrac{\Delta_M}{\Delta_U}$ |
| | Net Load P_Y | | Net Load P_U | | Displacement Δ_U | | Net Load P_M | Displacement Δ_M | | |
	Value (kN)	% Reduction	Value (kN)	% Reduction	Value (mm)	% Reduction	Value (kN)	Value (mm)	%	%
CP20d00	542	-	788	-	10.2	-	508	17.6	64.5	172.5
SP20d25	529	2.4	715	9.3	6.7	34.3	509	16.5	71	246
SP20d50	496	8.5	639	18.9	5.4	47.0	500	14.8	78	274

Table 4.2 Maximum strain values for Group 1A

Specimen	At Maximum Load (Point U)		At End of Test (Point M or S)		Maximum Local Strain (%)		
	Net Load (kN)	Displacement (mm)	Net Load (kN)	Displacement(mm)	Tensile strain at crest (%)	Compressive strain at crest (%)	Compressive strain at foot (%)
CP20d00	788	10.2	508	17.6	?	?	?
SP20d25	715	6.7	509	16.5	*	2.6	4.6
SP20d50	639	5.4	500	14.8	-0.16	1.2	11.3

? indicates that the value could not be captured as none of the strain gauges went to tension
* indicates that the strain value did not go to tension
- sign indicates tensile strain

Table 4.3 Test result for Group 1B

| Specimen | At First Yield (Point Y) | | At Maximum Load (Point U) | | | | At End of Test (Point M or S) | | $\dfrac{P_M}{P_U}$ | $\dfrac{\Delta_M}{\Delta_U}$ |
| | Net Load P_Y | | Net Load P_U | | Displacement Δ_U | | Net Load P_M | Displacement Δ_M | | |
	Value (kN)	% Reduction	Value (kN)	% Reduction	Value (mm)	% Reduction	Value (kN)	Value (mm)	%	%
CP40d00	465	-	611	-	12.6	-	367	21.7	60	172.22
SP40d25	410	11.8	595	2.6	11.1	11.9	434	21.5	72.94	193.7
SP40d50	376	19	511	16.37	5.8	53.96	369	19.4	72.21	331.5

Table 4.4 Maximum strain values for Group 1B

Specimen	At Maximum Load (Point U)		At End of Test (Point M or S)		Maximum Local Strain (%)		
	Net Load (kN)	Displacement (mm)	Net Load (kN)	Displacement (mm)	Tensile strain at crest (%)	Compressive strain at crest (%)	Compressive strain at foot (%)
CP40d00	611	12.6	367	21.7	*	3	9.6
SP40d25	595	11.1	434	21.5	*	3.9	15.4
SP40d50	511	5.8	369	19.4	-0.2	1.2	15.2

* indicates that the value did not go to tension

- sign indicates tensile strain

Table 4.5 Test result for Group 2A

| Specimen | At First Yield (Point Y) | | At Maximum Load (Point U) | | | | At End of Test (Point M or S) | | $\frac{P_M}{P_U}$ | $\frac{\Delta_M}{\Delta_U}$ |
| | Net Load P_Y | | Net Load P_U | | Displacement Δ_U | | Net Load P_M | Displacement Δ_M | | |
	Value (kN)	% Reduction	Value (kN)	% Reduction	Value (mm)	% Reduction	Value (kN)	Value (mm)	%	%
CP20d00	542	-	788	-	10.2	-	508	17.6	64.46	172.5
RP20d25	443	18.3	616	21.8	3.2	68.6	390	12.6	63.31	393.8
RP20d50	288	46.9	433	45.0	3.6	64.7	264	10.3	61.0	286.11

Table 4.6 Maximum strain values for Group 2A

Specimen	At Maximum Load (Point U)		At End of Test (Point M or S)		Maximum Local Strain (%)		
	Net Load (KN)	Displacement (mm)	Net Load (kN)	Displacement (mm)	Tensile strain at crest (%)	Compressive strain at crest (%)	Compressive strain at foot (%)
CP20d00	788	10.2	508	17.6	?	?	?
RP20d25	616	3.2	390	12.6	-8.7	1.5	12.3
RP20d50	433	3.6	264	10.3	-4.7	0.5	13.9

? indicates that the value could not be captured and none of the strain gauges went to tension
- sign indicates tensile strain

Table 4.7 Test result for Group 2B

| | At First Yield (Point Y) | | At Maximum Load (Point U) | | | | At End of Test (Point C or S) | | $\dfrac{P_M}{P_U}$ | $\dfrac{\Delta_M}{\Delta_U}$ |
| | Net Load P_Y | | Net Load P_U | | Displacement Δ_U | | Net Load P_M | Displacement Δ_M | | |
Specimen	Value (kN)	% Reduction	Value (kN)	% Reduction	Value (mm)	% Reduction	Value (kN)	Value (mm)	%	%
CP40d00	465	-	611	-	12.6	-	367	21.7	60.06	172.2
RP40d25	403	13.3	509	16.7	3.7	70.6	230.7	40.2	45.3	1086.5
RP40d50	273	41.3	352	42.4	4.8	61.9	159.1	31.2	45.2	650

Table 4.8 Maximum strain values for Group 2B

Specimen	At Maximum Load (Point U)		At End of Test (Point M or S)		Maximum Local Strain (%)		
	Net Load (kN)	Displacement (mm)	Net Load (kN)	Displacement (mm)	Tensile strain at crest (%)	Compressive strain at crest (%)	Compressive strain at foot (%)
CP40d00	611	12.6	367	21.7	*	3	10
RP40d25	509	3.7	230.7	40.2	-5.4	1.4	13.7
RP40d50	352	4.8	159.1	31.2	-9.3	0.2	10.6

*indicates that the value did not reach to that zone
- sign indicates tensile strain

Table 4.9 Effect of internal pressure

| Specimen | At First Yield (Point Y) | | At Maximum Load (Point U) | | | | At End of Test (Point M or S) | |
	Net Load (kN)	% Change from $0.2p_y$	Net Load (kN)	% Change from $0.2p_y$	Displacement (mm)	% Change from $0.2p_y$	Net Load (kN)	Displacement (mm)
CP20d00	542	-	788	-	10.2	-	507.5	17.6
CP40d00	465	14.2	611	22.5	12.6	23.5	367	21.7
SP20d25	529	-	715	-	6.7	-	509	16.5
SP40d25	410	22.5	595	16.8	11.1	65.7	434	21.5
SP20d50	496	-	639	-	5.4	-	500	14.8
SP40d50	376	24.2	511	20.0	5.8	7.4	369	19.4
RP20d25	443	-	616	-	3.2	-	390	12.6
RP40d25	403	9.0	509	17.4	3.7	15.6	230.7	40.2
RP20d50	288	-	433	-	3.6	-	264	10.3
RP40d50	273	5.2	352	18.7	4.8	33.3	159.1	31.2

The % change is calculated for higher pressure ($0.4p_y$) specimen with respect to the same specimen but with lower pressure ($0.2p_y$) using the following equation

$$\text{\% Change} = \left| \frac{V_{0.2p} - V_{0.4p}}{V_{0.2p}} \right| \times 100$$

Where $V_{0.2p}$ is the value for the specimen pressurized to $0.2p_y$ and $V_{0.4p}$ is the value for the specimen pressurized to $0.4p_y$.

Table 4.10 Effect of circumferential extent of corrosion defect (Lc)

Specimen	At First Yield (Point Y)		At Maximum Load (Point U)				At End of Test (Point M or S)	
	Net Load (kN)	% Change from Group 1 Specimen	Net Load (kN)	% Change from Group 1 Specimen	Displacement (mm)	% Change from Group 1 Specimen	Net Load (kN)	Displacement (mm)
SP20d25 (1)	529	-	715	-	6.7	-	509	16.5
RP20d25 (2)	443	16.3	616	13.8	3.2	52.2	390	12.6
SP20d50 (1)	496	-	639	-	5.4	-	500	14.8
RP20d50 (2)	288	41.9	433	32.2	3.6	33.3	264	10.3
SP40d25 (1)	410	-	595	-	11.1	-	434	21.7
RP40d25 (2)	403	1.7	509	14.4	3.7	66.7	230.7	40.2
SP40d50 (1)	376	-	511	-	5.8	-	369	19.4
RP40d50 (2)	273	27.4	352	31.1	4.8	17.24	159.1	31.4

The number in the parentheses in Column1 indicates group numbers. For Group 1, the circumferential dimension of the corrosion defect was 50 mm and for Group 2, it was 175 mm (3.75 times longer)

$$\% \text{ Change} = \left| \frac{V_1 - V_2}{V_1} \right| \times 100$$

Where V_1 is the value for the specimen in Group 1 in Column 1 and V_2 is the value for the specimen in Group 2 in Column 1.
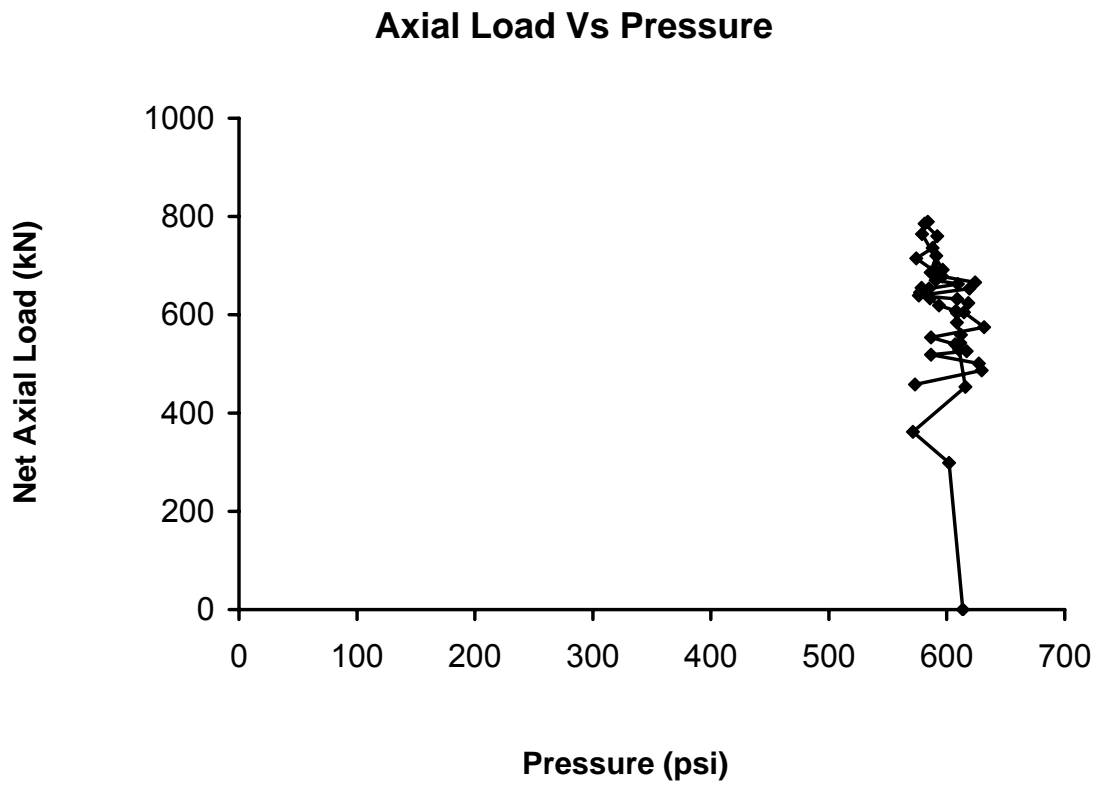
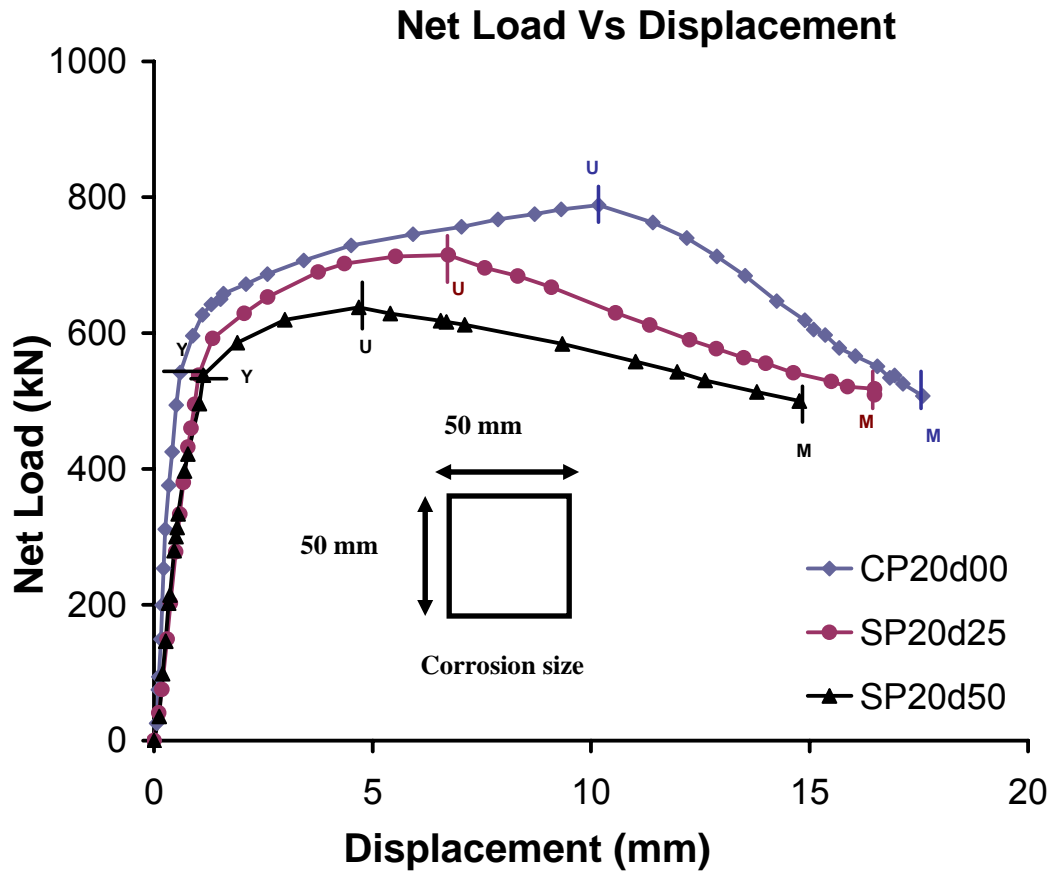Figure 4.1 Typical plot for axial compressive load vs. pressure

Figure 4.2 Net load vs. displacement for Group 1A specimen

Figure 4.3 Deformed shape of Group 1A specimens (Square shape corrosion with 0.2 p_y)
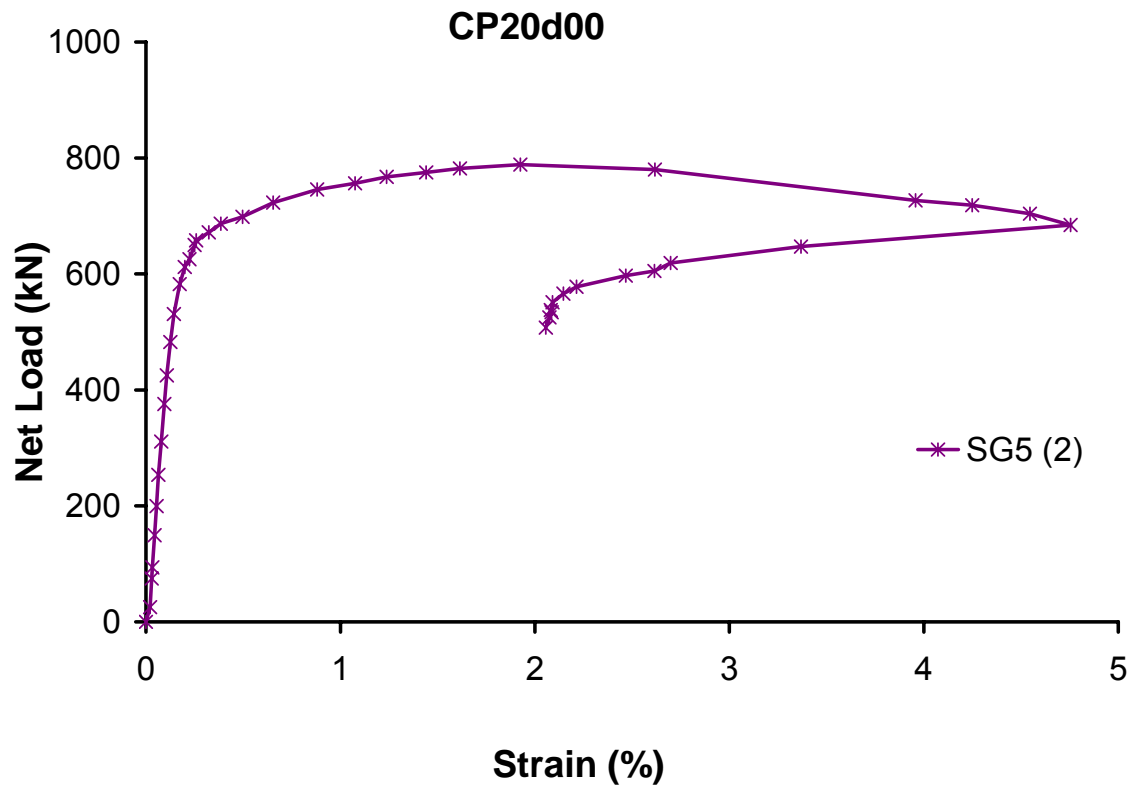
Figure 4.4 Net load vs. local strain value for specimen CP20d00

(The positive value indicates a compressive strain and the number in the parenthesis in the legend indicates actual strain gauge position (as shown in Figure 3.13))

Figure 4.5 Net load vs. local strain value for specimen SP20d25

(The positive value indicates a compressive strain and the number in the parenthesis in the legend indicates actual strain gauge position (as shown in Figure 3.14))

Figure 4.6 Net load vs. local strain value for specimen SP20d50

(The positive value indicates a compressive strain and the number in the
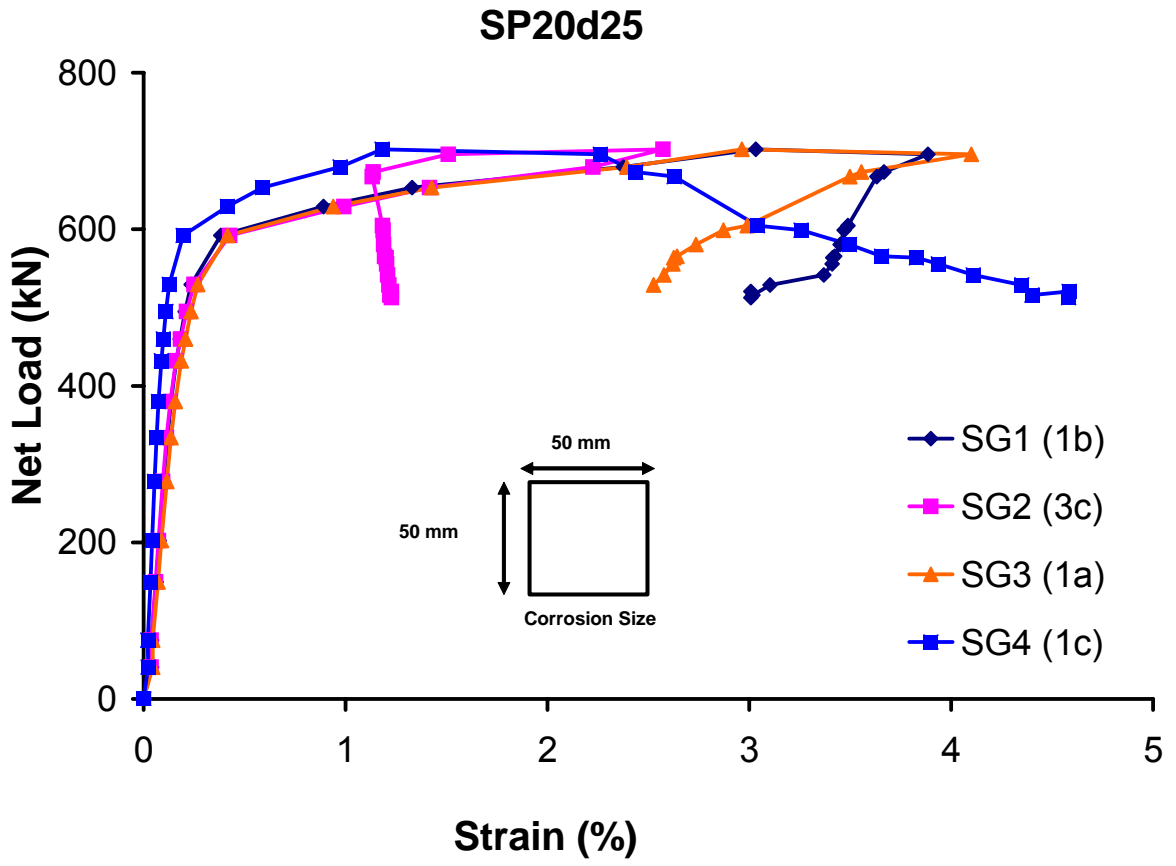parenthesis in the legend indicates actual strain gauge position (as shown in
Figure 3.14))

Figure 4.7 SG5 (2) at CP20d00

Figure 4.8 Net load vs. displacement for Group 1B specimen

Figure 4.9 Deformed shape of Group 1B specimen (Square shape corrosion with $0.4p_y$)

Figure 4.10 Net load vs. local strain value for specimen CP40d00

(The positive value indicates a compressive strain and the number in the parenthesis in the legend indicates actual strain gauge position (as shown in Figure 3.13))
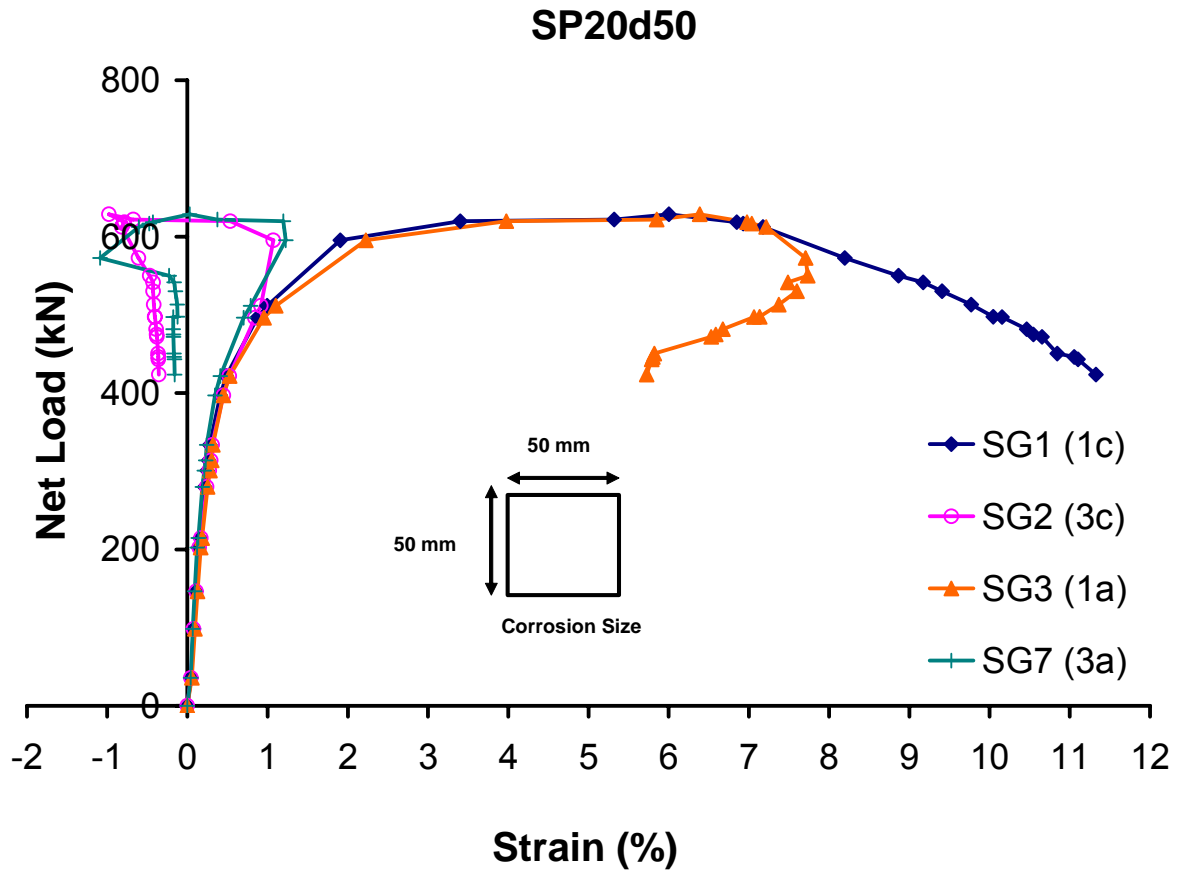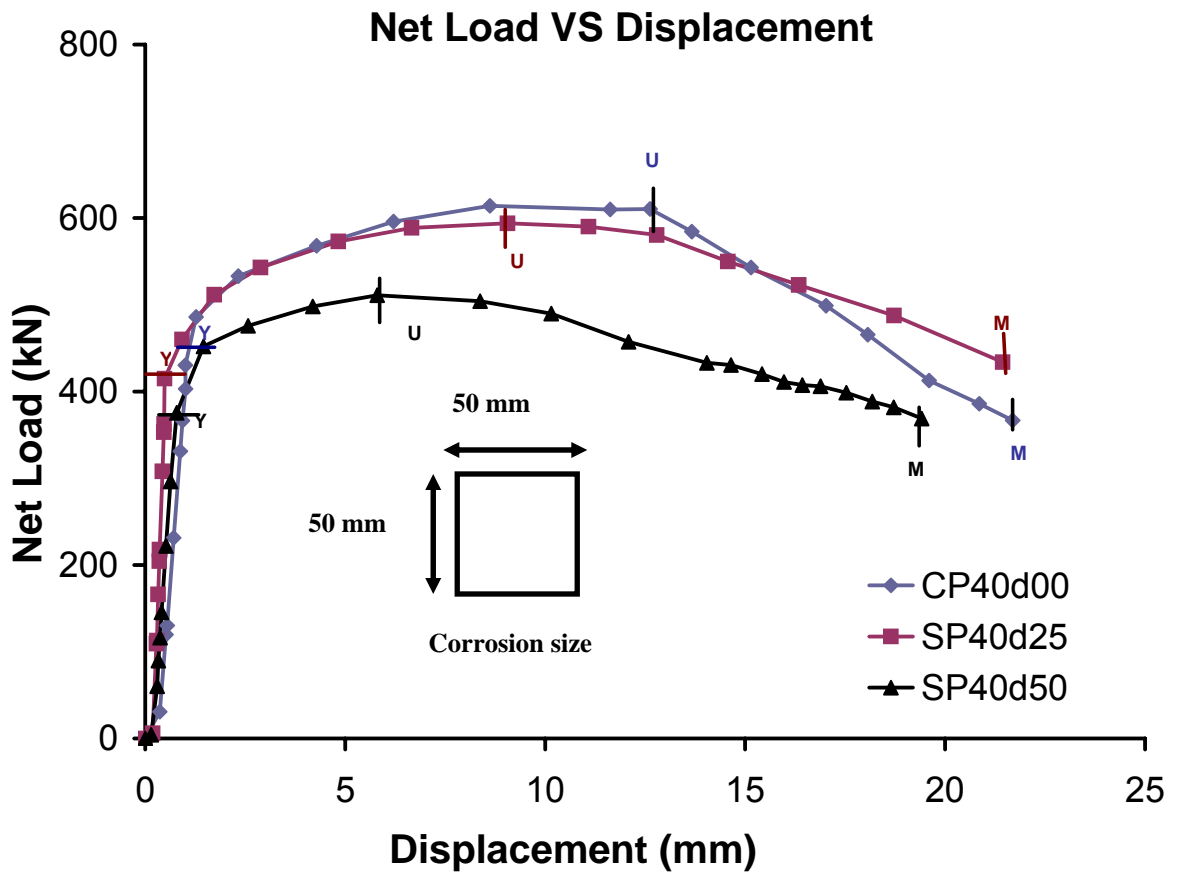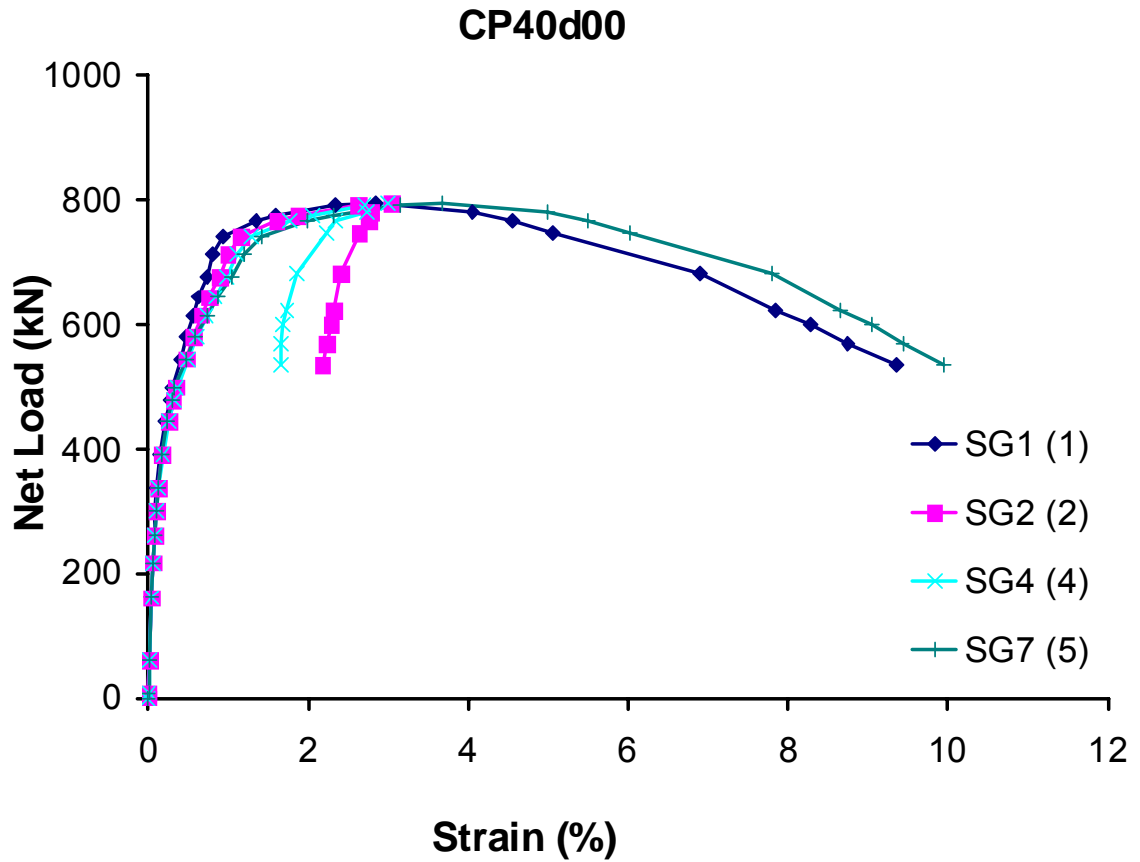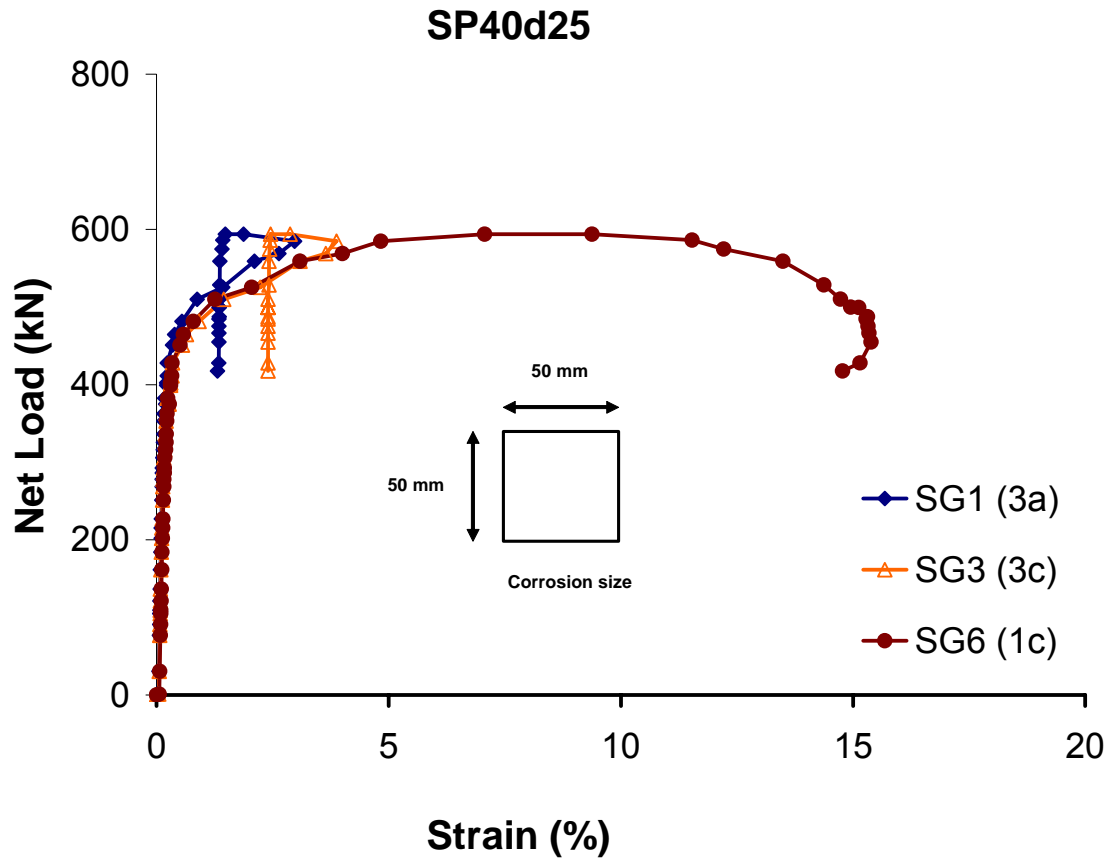
Figure 4.11 Net load vs. local strain value for specimen SP40d25

(The positive value indicates a compressive strain and number in the parenthesis in the legend indicates actual strain gauge position (as shown in Figure 3.14))
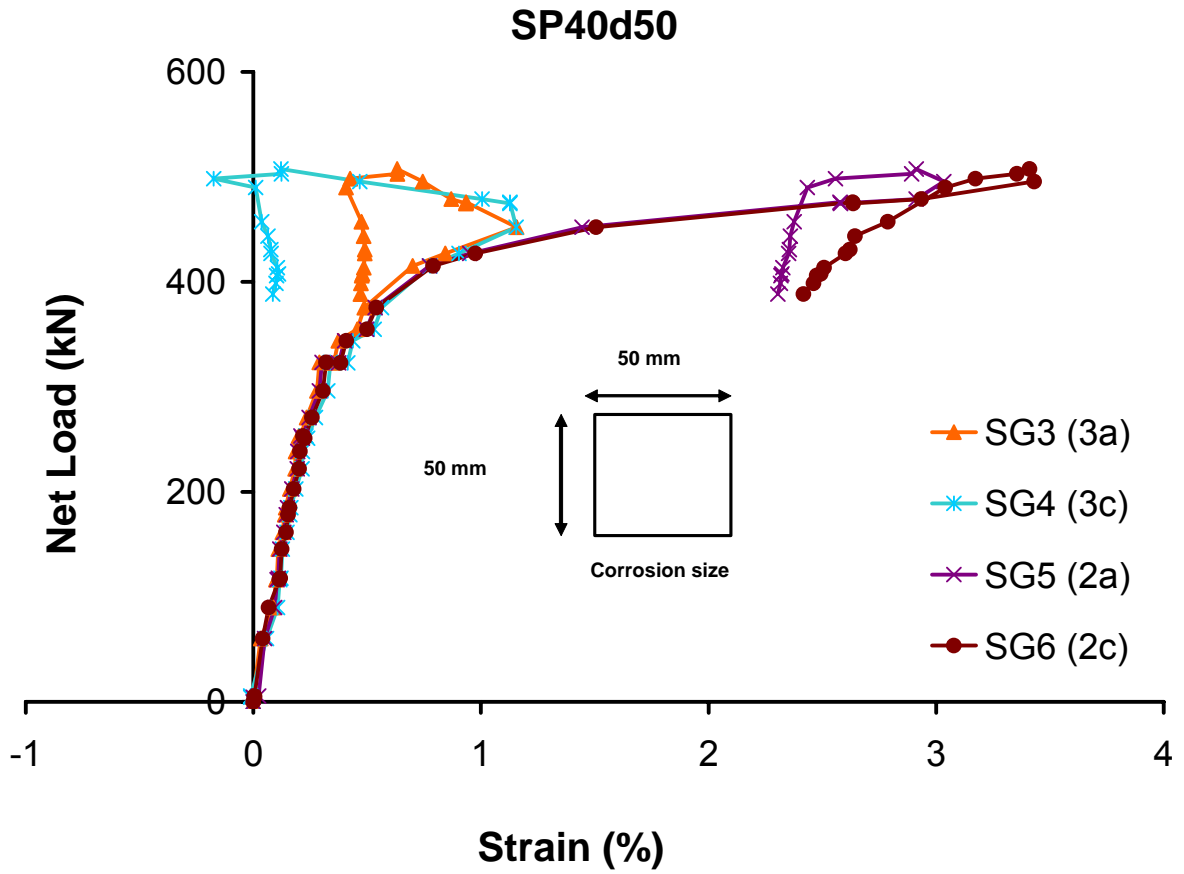
Figure 4.12 Net load vs. local strain value for specimen SP40d50 at the crest of the wrinkle

(The positive value indicates a compressive strain and the number in the parenthesis in the legend indicates actual strain gauge position (as shown in Figure 3.14))

Figure 4.13 Net load vs. local strain value for specimen SP40d50 at the foot of the wrinkle

(The positive value indicates compressive strain and number in the parenthesis in the legend indicates actual strain gauge position (as shown in Figure 3.14))

Figure 4.14 Net load vs. displacement for Group 2A specimen

Figure 4.15 Deformed shape of Group 2A specimen (Rectangular corrosion with $0.2 p_y$)

Figure 4.16 Net load vs. local strain value for specimen RP20d25 at the crest of the wrinkle

(The negative value of strain indicates a tensile strain and the number in the parenthesis in the legend indicates actual strain gauge position (as shown in Figure 3.15))

RP20d50

Net Load (kN)

Strain (%)

175 mm

50 mm

Corrosion Size

SG1 (3c)
SG3 (3d)
SG7 (3b)
SG10 (3a)

Figure 4.17 Net load vs. local strain value for specimen RP20d50 at the crest of the wrinkle

(The negative value of strain indicates a tensile strain and the number in the parenthesis in the legend indicates actual strain gauge position (as shown in Figure 3.15))

Figure 4.18 Net load vs. local strain value for specimen RP20d25 at the foot of the wrinkle

(The positive value of strain indicates a compressive strain and the number inside the parenthesis in the legend indicates actual strain gauge position (Figure 3.15) in the specimen)
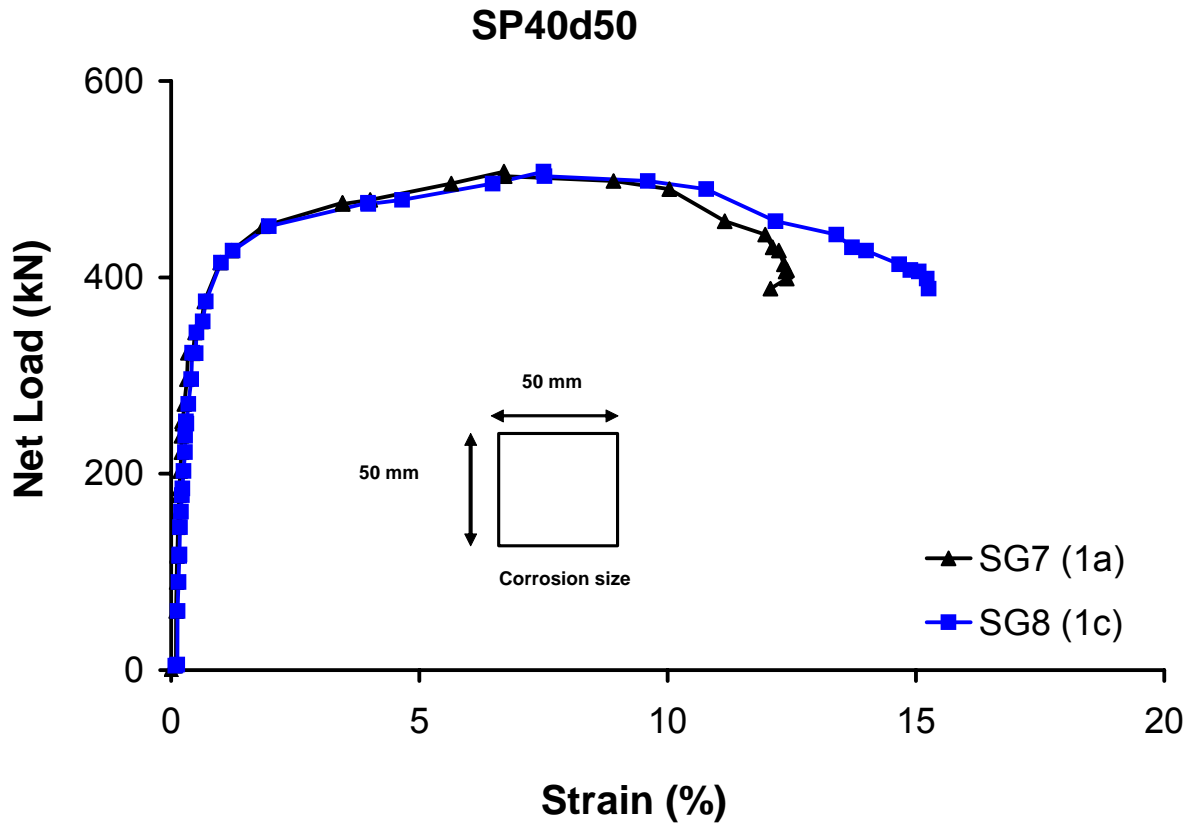
Figure 4.19 Net load vs. local strain value for specimen RP20d50 at the foot of the wrinkle

(The positive value of strain indicates a compressive strain and the number in the parenthesis in the legend indicates actual strain gauge position (as shown in Figure 3.15))
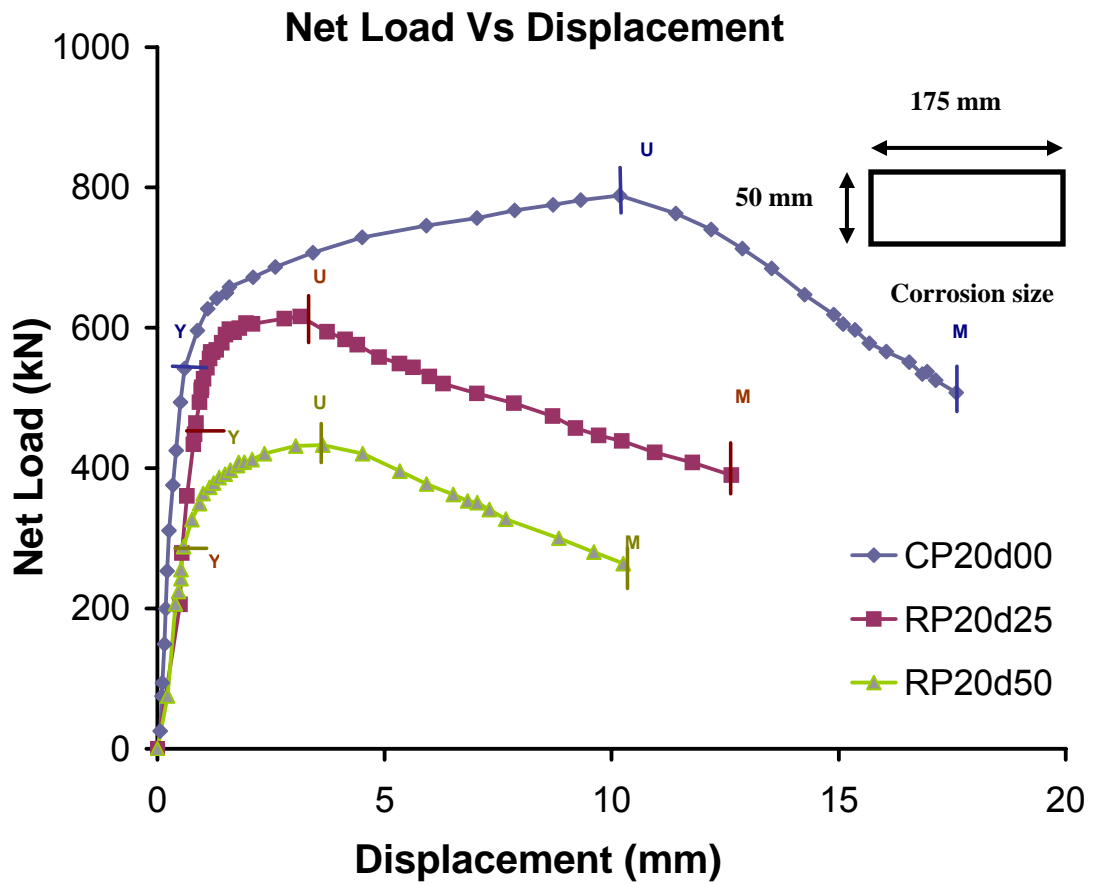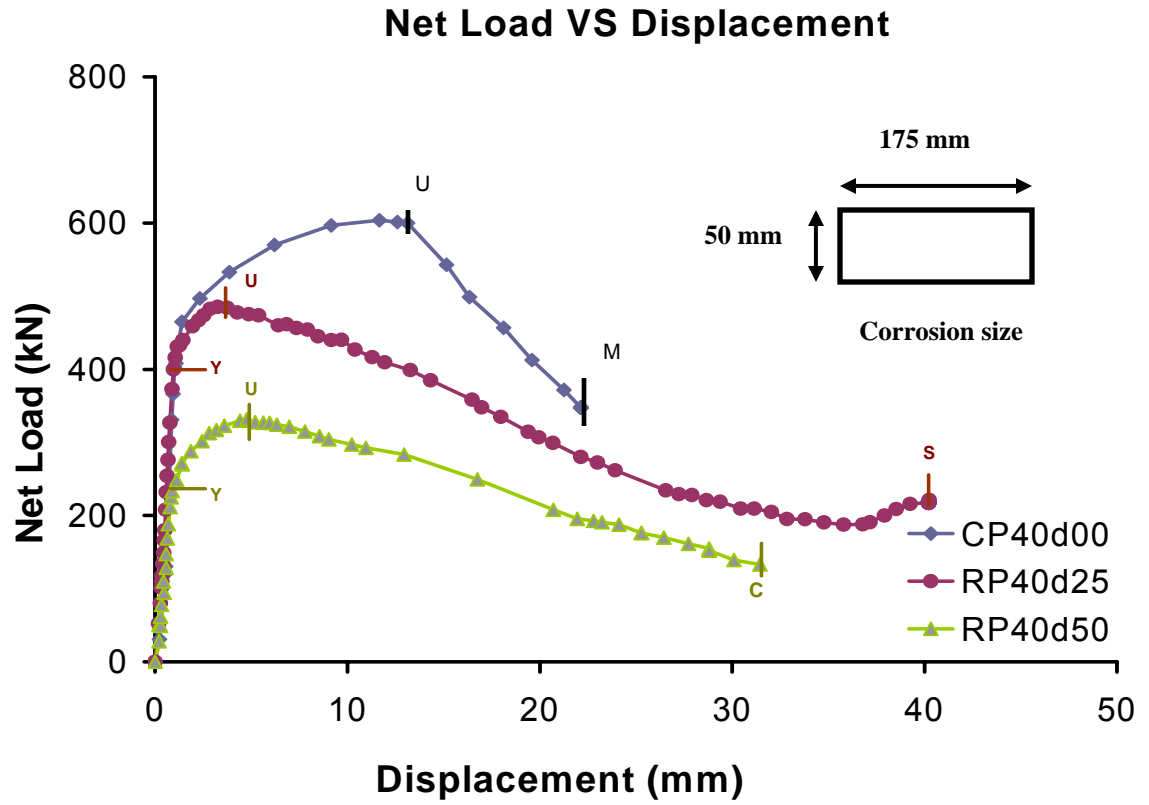
Figure 4.20 Net load vs. displacement for Group 2B specimen

| CP40d00 | RP40d25 | RP40d50 |

Figure 4.21 Deformed shape of Group 2B specimen　(Rectangular corrosion with $0.4p_y$)
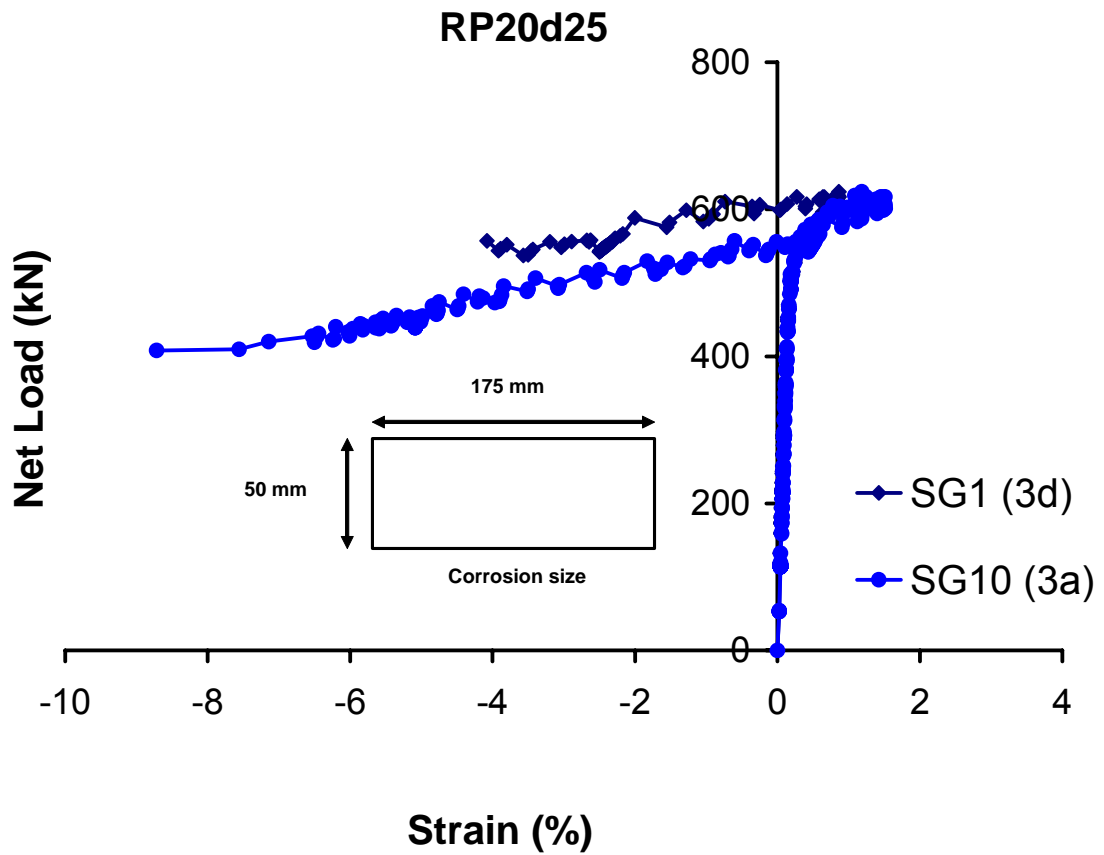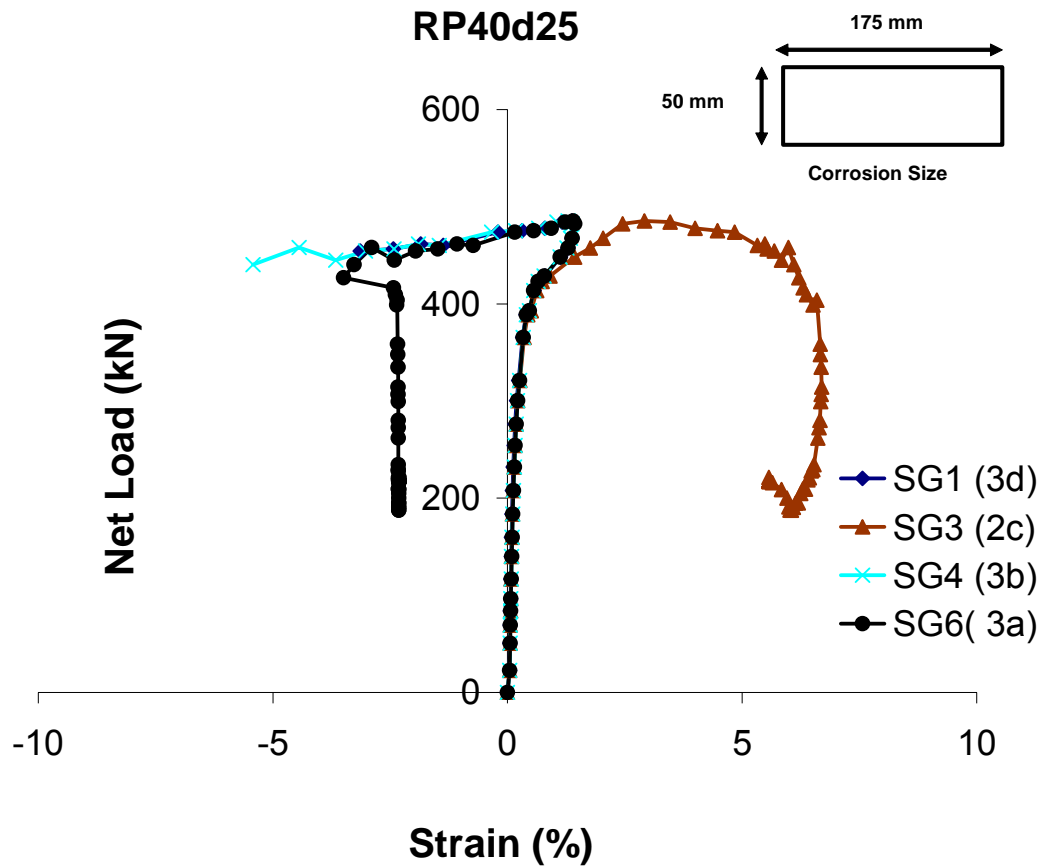
Figure 4.22 Net load vs. local strain value for specimen RP40d25 at the crest of the wrinkle

(The negative value of strain indicates a tensile strain and the number in the parenthesis in the legend indicates actual strain gauge position (as shown in Figure 3.15))
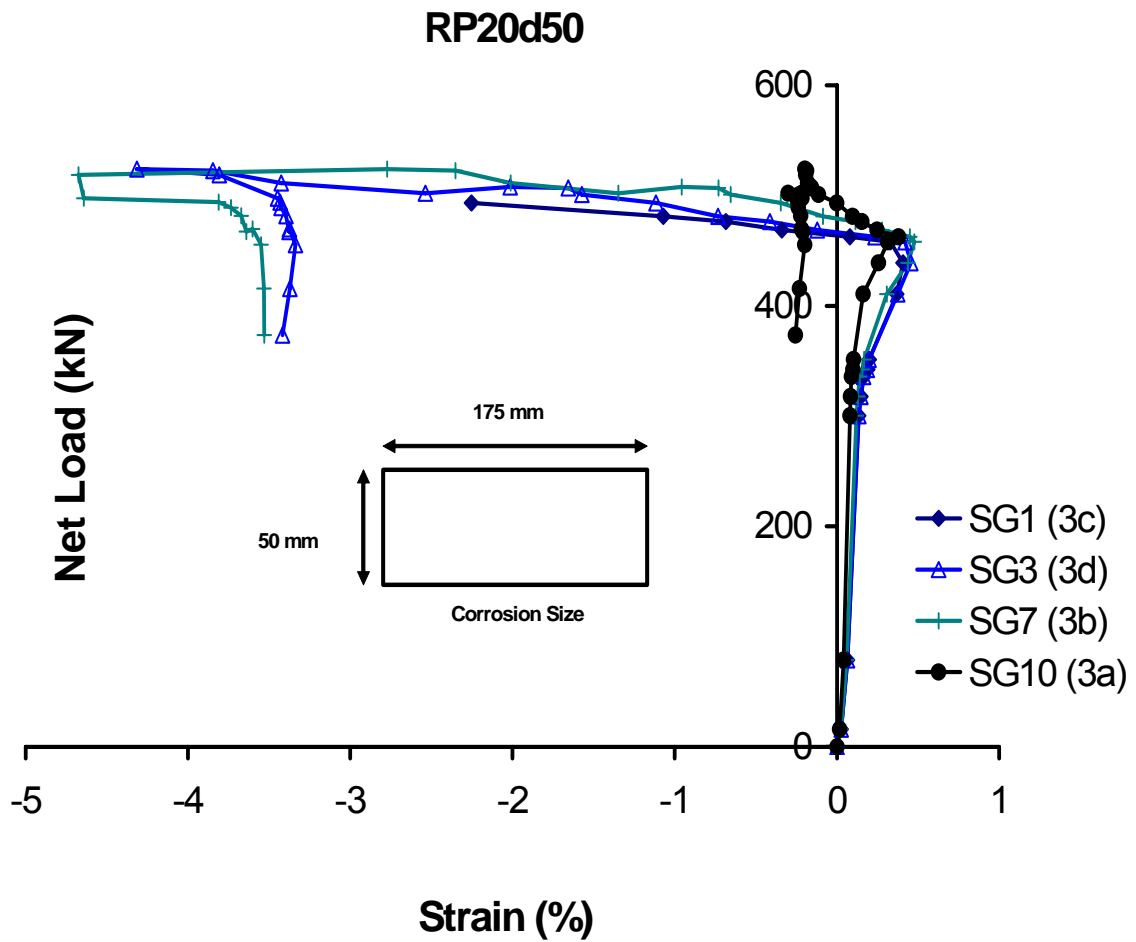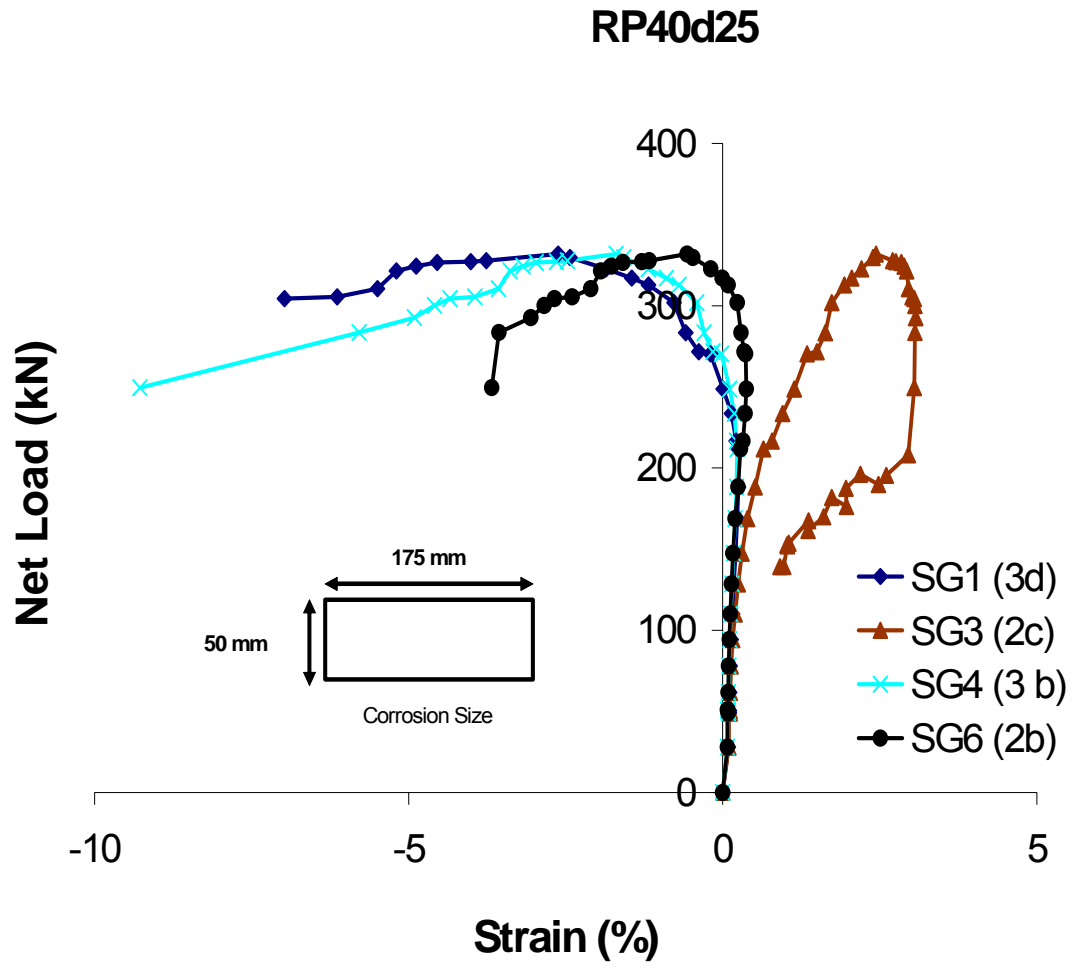
Figure 4.23 Net load vs. local strain value for specimen RP40d50 at the crest of the wrinkle

(The negative value of strain indicates a tensile strain and the number inside the parenthesis in the legend indicates actual strain gauge position (as shown in Figure 3.15))
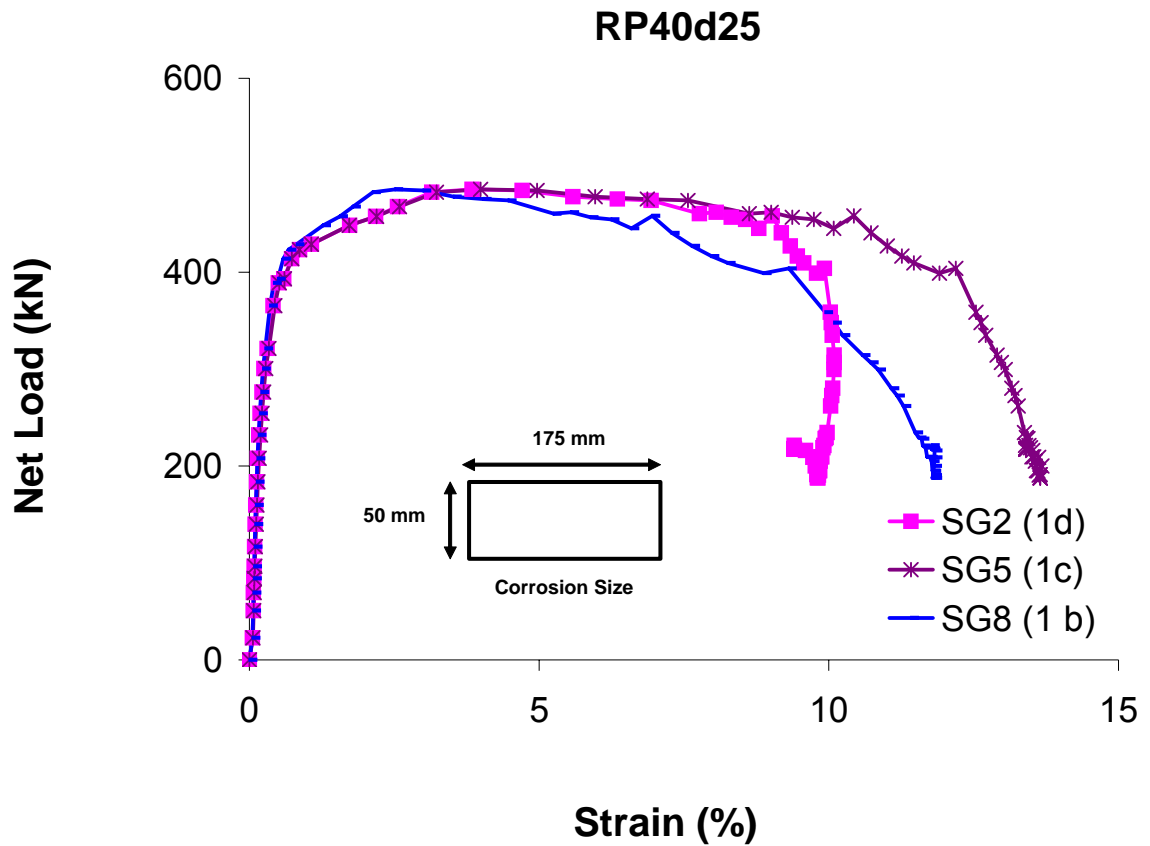
Figure 4.24 Net load vs. local strain value for specimen RP40d25 at the foot of the wrinkle

(The positive value of strain indicates a compressive strain and the number in the parenthesis in the legend indicates actual strain gauge position (as shown in Figure 3.15))
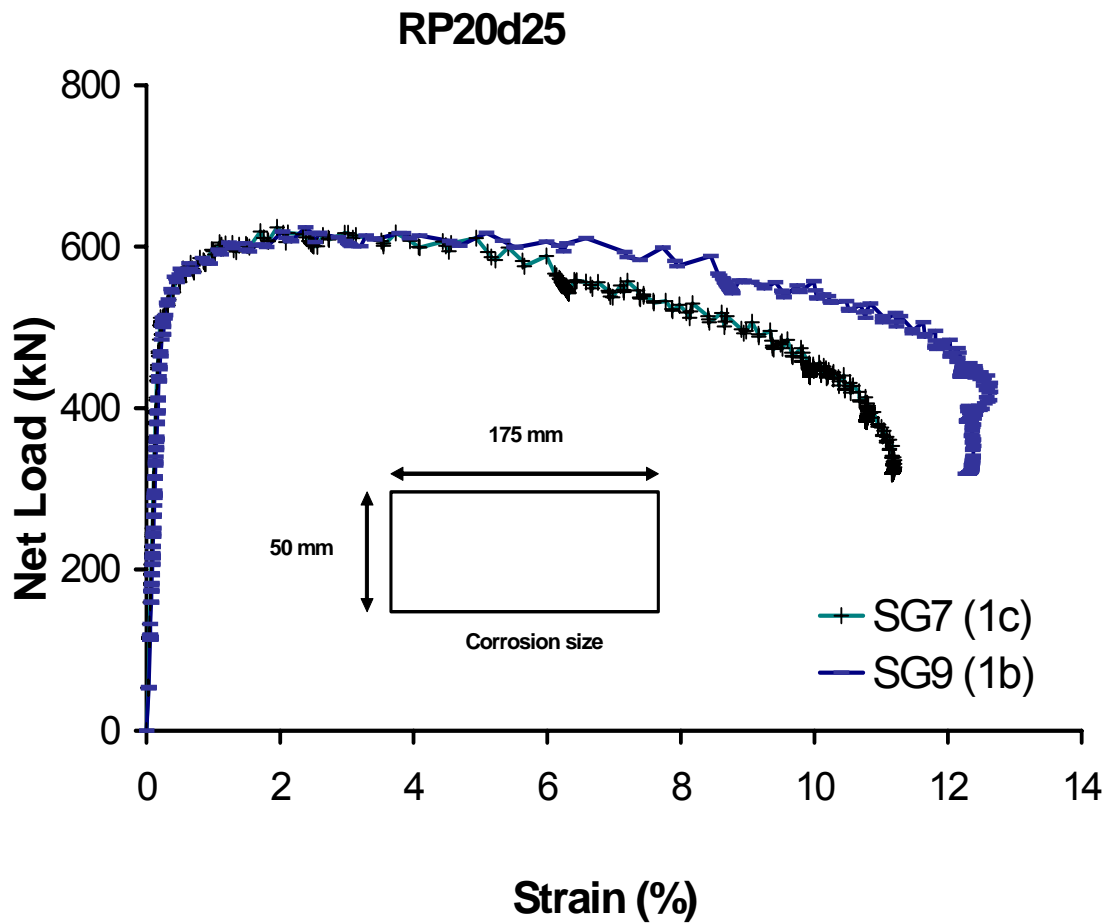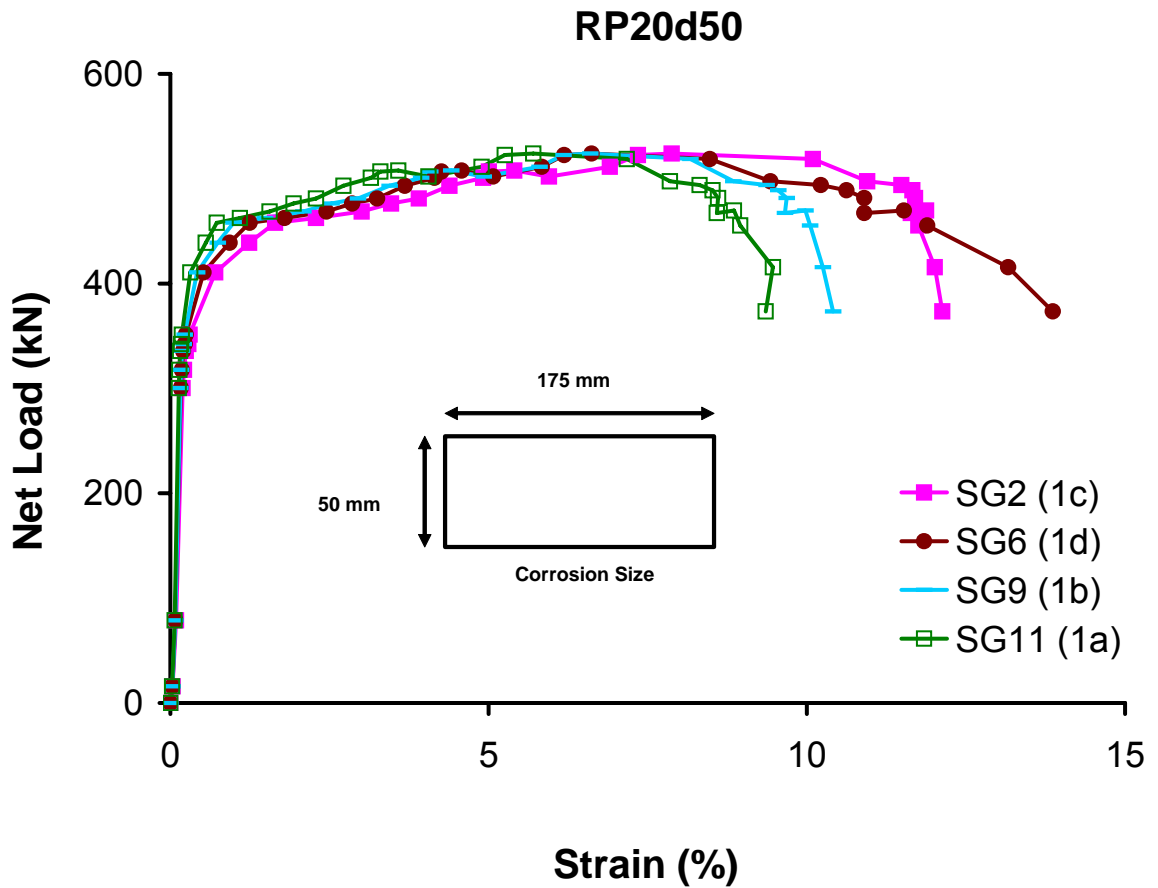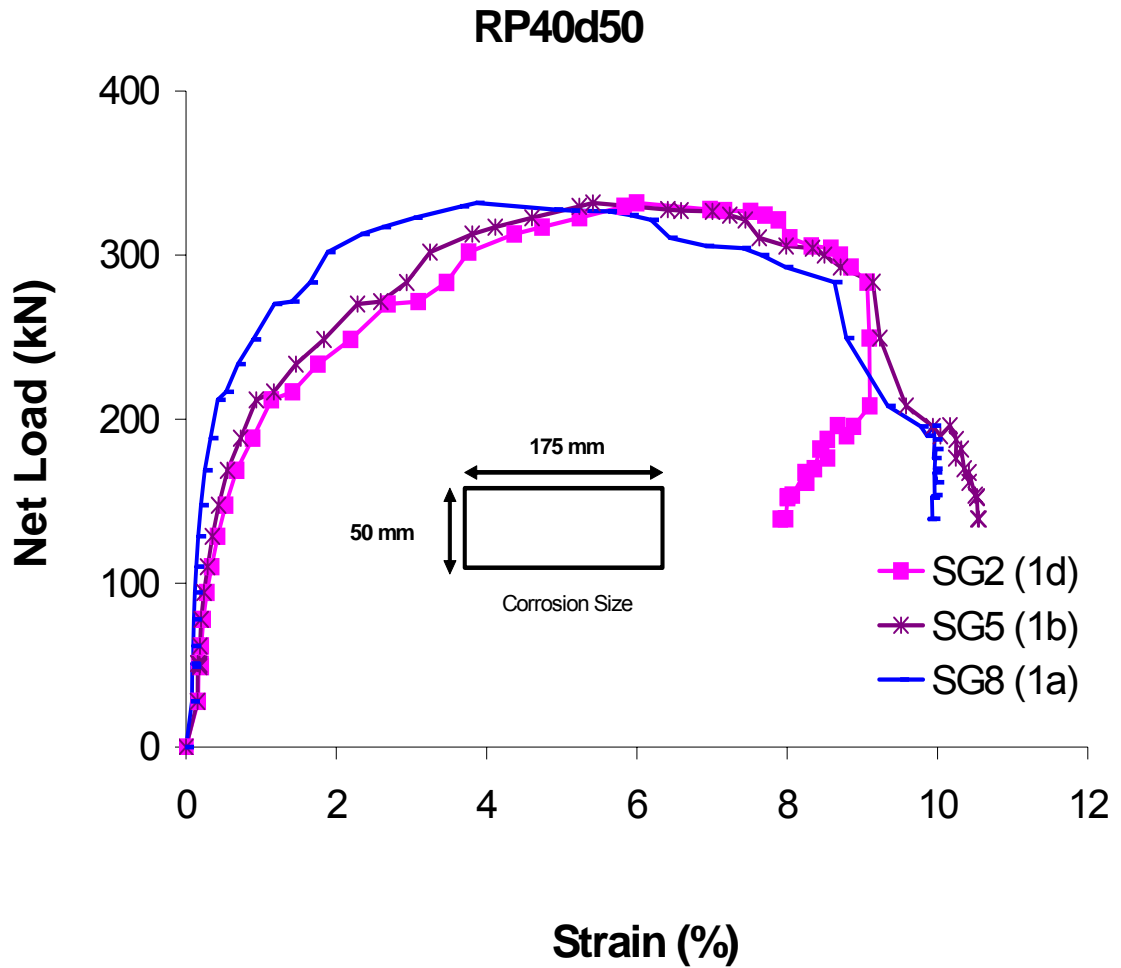
Figure 4.25 Net load vs. local strain value for specimen RP40d50 at the foot of the wrinkle

(The positive value of strain indicates a compressive strain and the number in the parenthesis in the legend indicates actual strain gauge position (as shown in Figure 3.15) in the specimen)
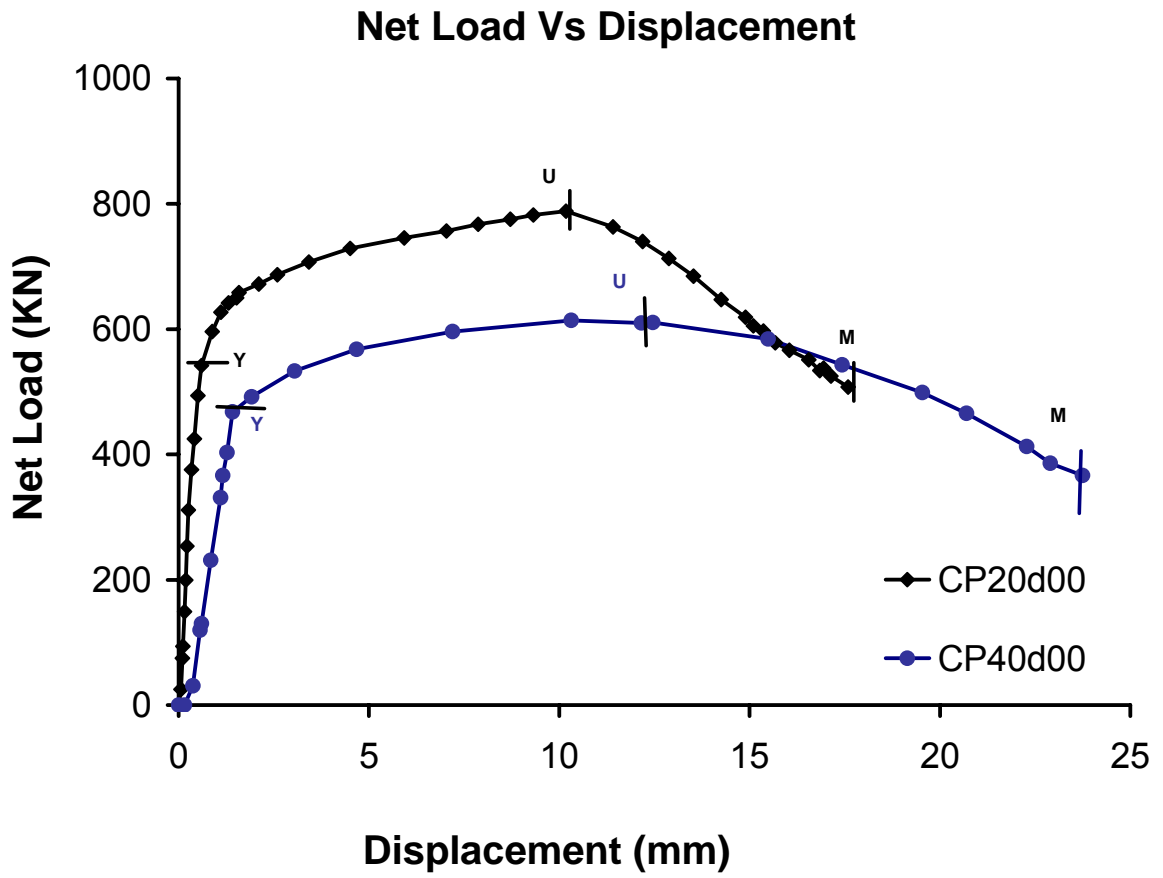
Figure 4.26 Effect of internal pressure on Control Specimens
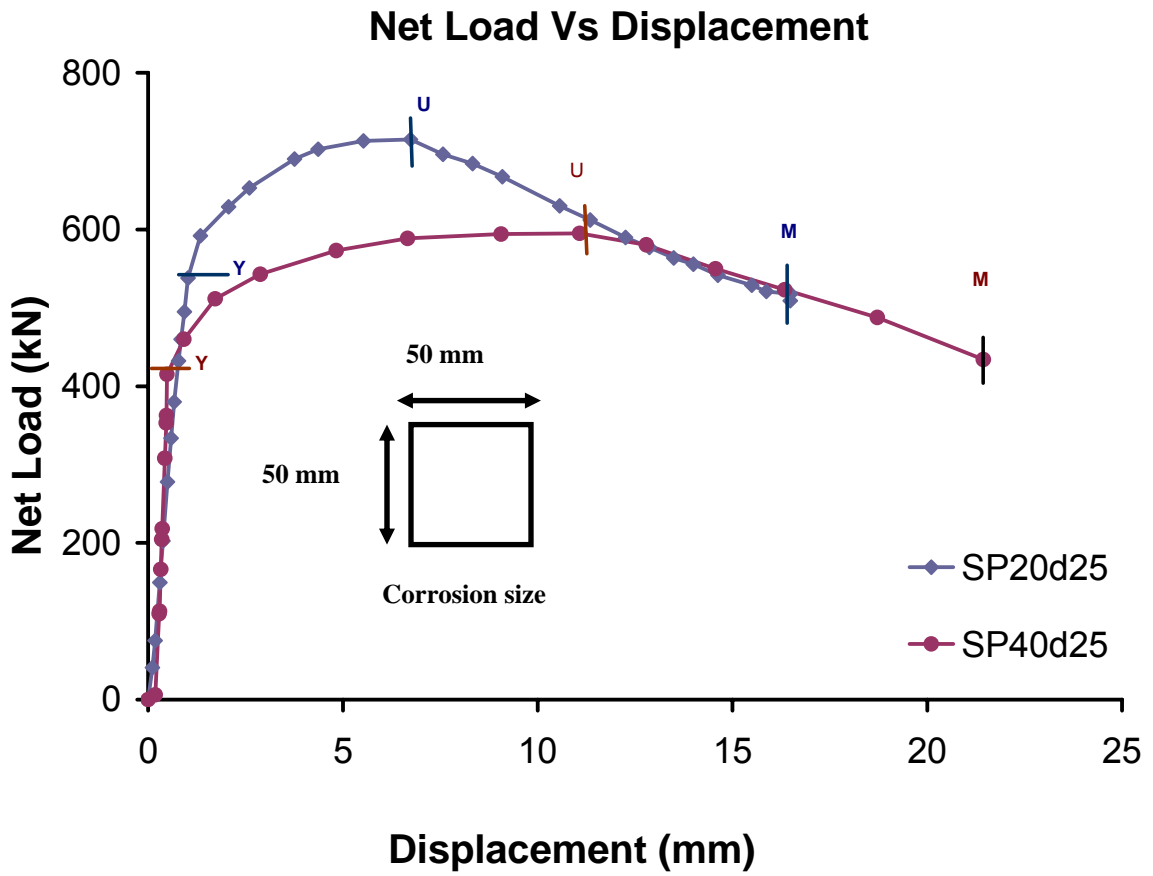
Figure 4.27 Effect of internal pressure on specimens SP20d25 and SP40d25
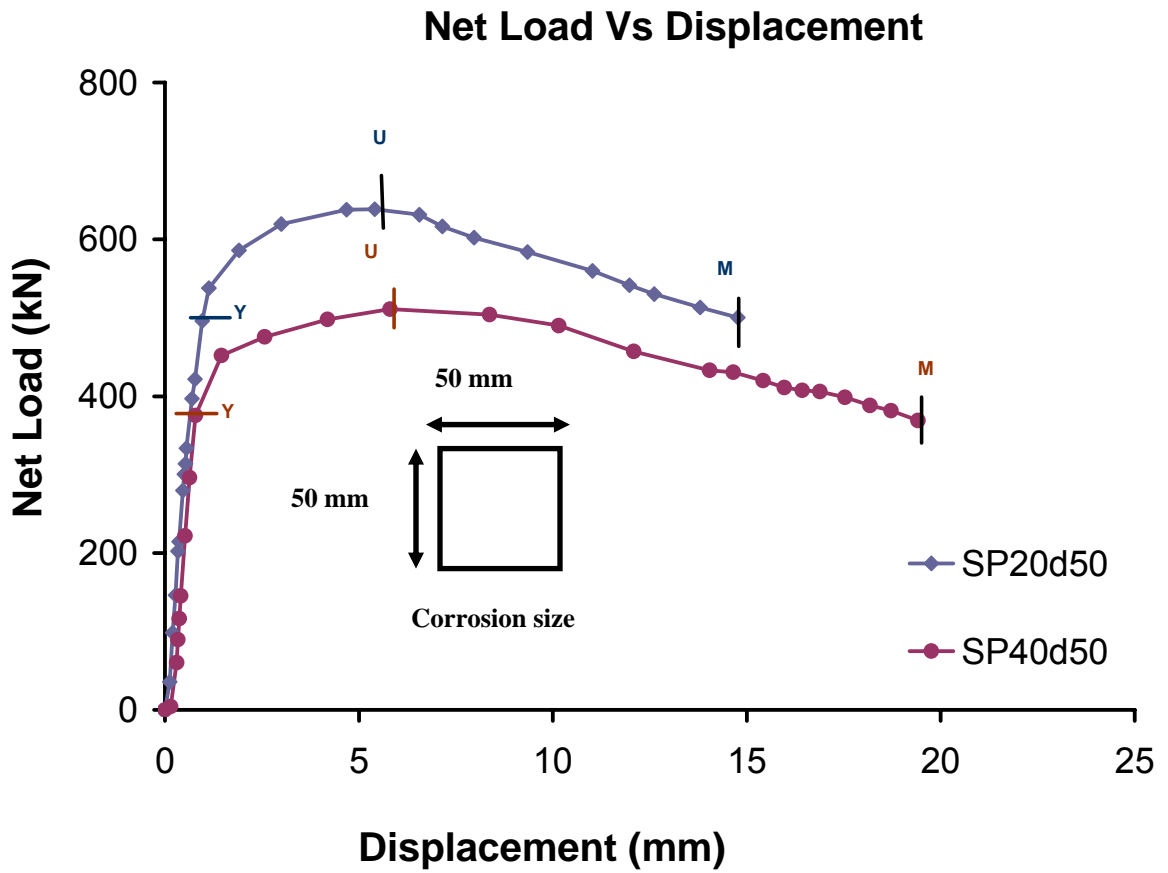
Figure 4.28 Effect of internal pressure on specimens SP20d50 and SP40d50
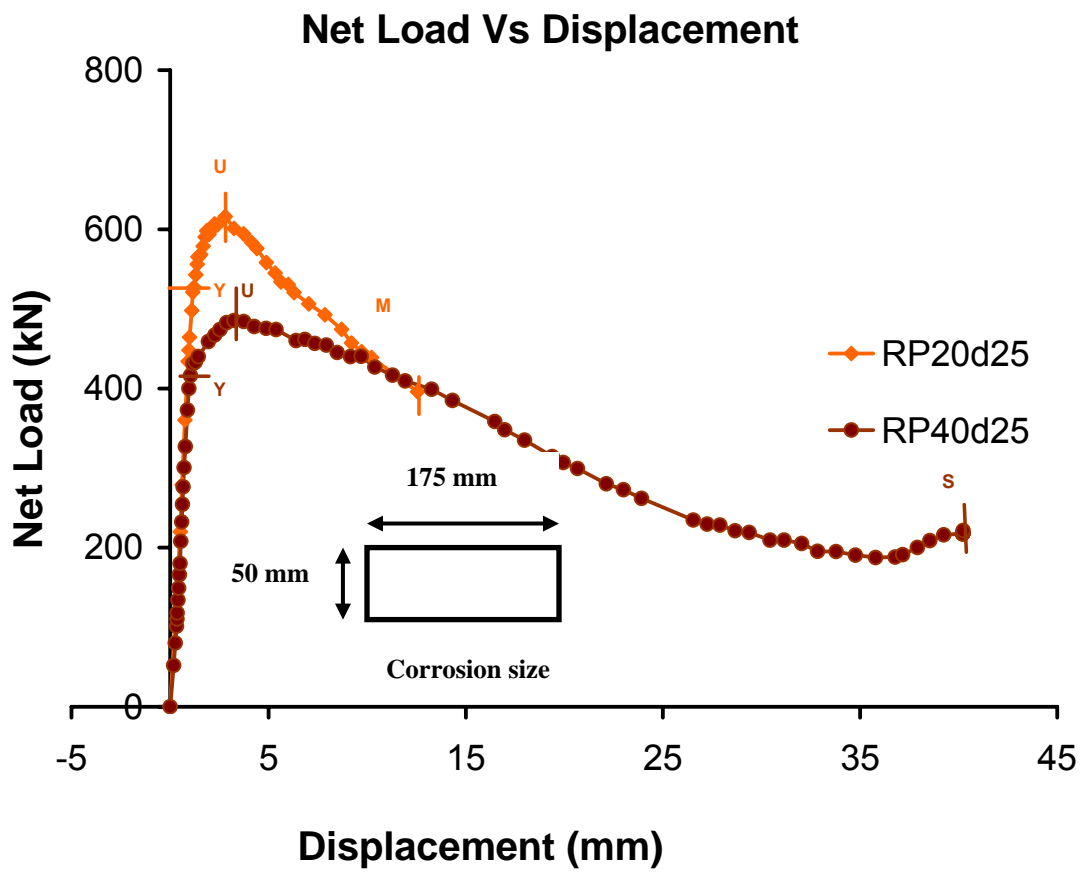
Figure 4.29 Effect of internal pressure on specimens RP20d25 and RP40d25

Net Load Vs Displacement
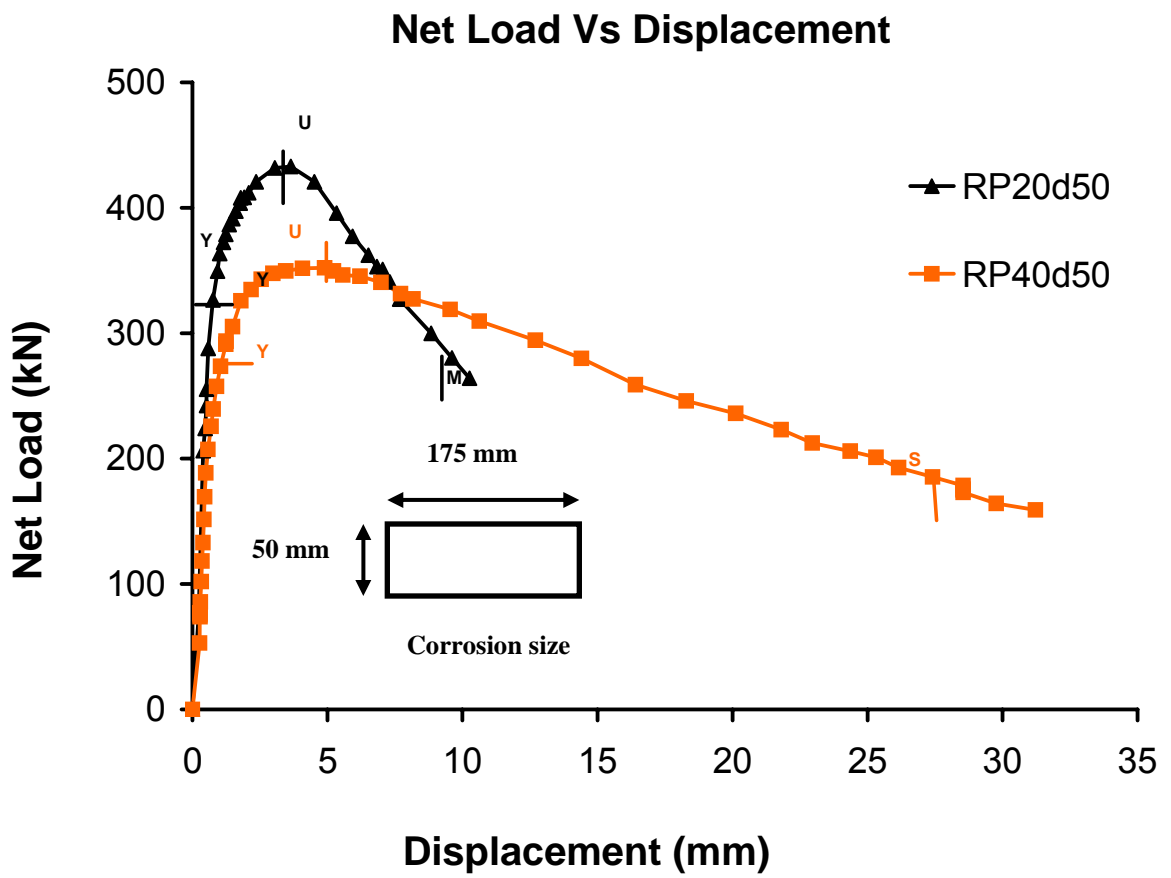
Figure 4.30 Effect of internal pressure on specimens RP20d50 and RP40d50
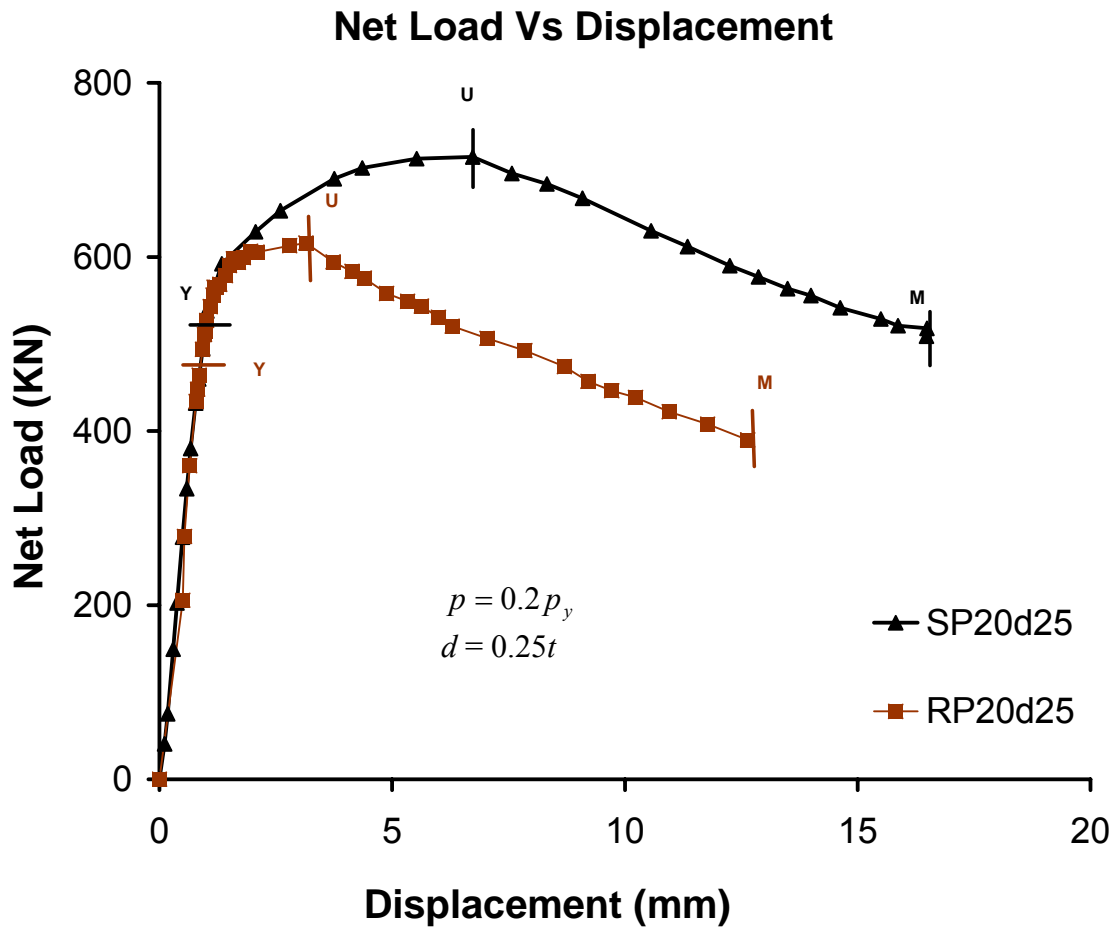
Figure 4.31 Effect of circumferential dimension of corrosion on specimens SP20d25 and RP20d25

Net Load Vs Displacement

Y-axis: **Net Load (KN)** (0, 200, 400, 600, 800)

X-axis: **Displacement (mm)** (0, 5, 10, 15, 20)

$$p = 0.2p_y$$
$$d = 0.5t$$

Legend:
- SP20d50
- RP20d50
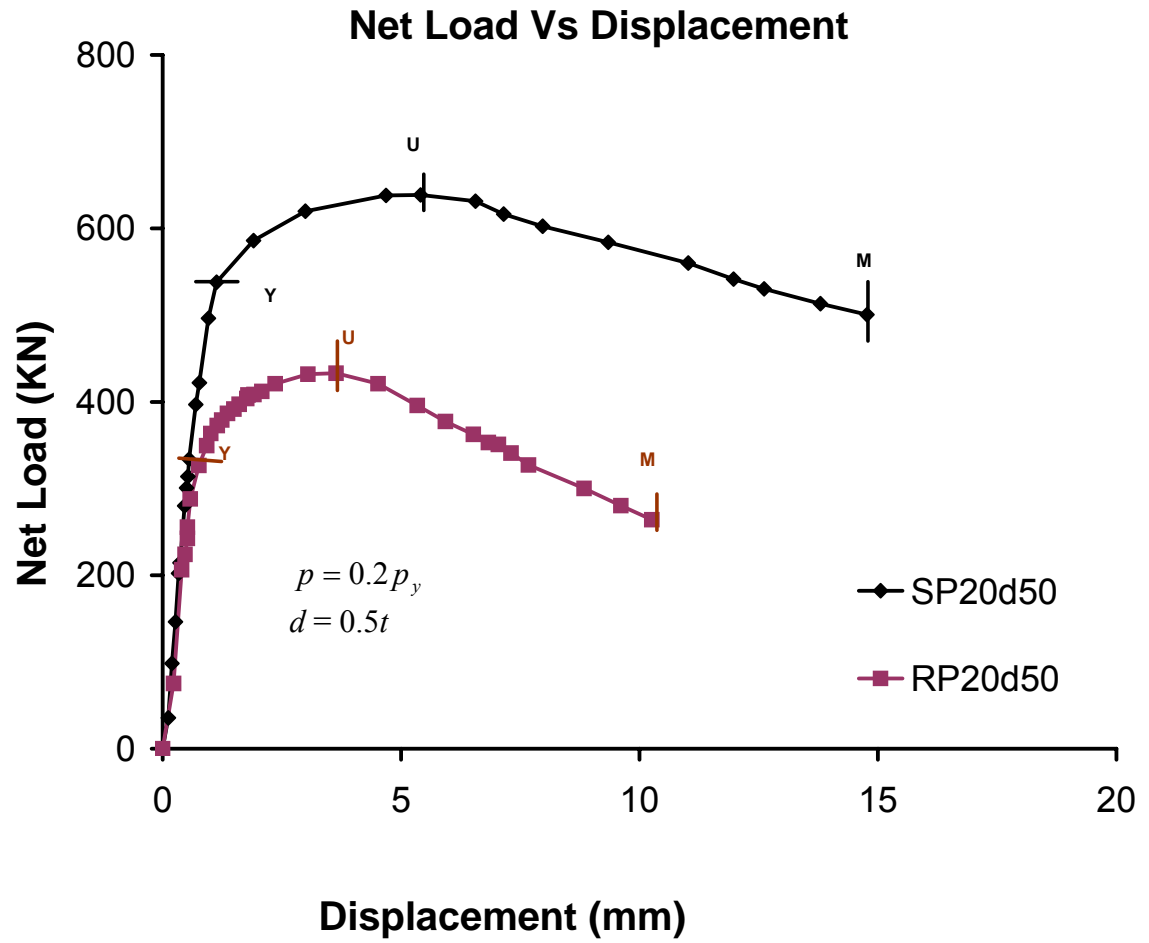
Figure 4.32 Effect of circumferential dimension of corrosion on specimens SP20d50 and RP20d50
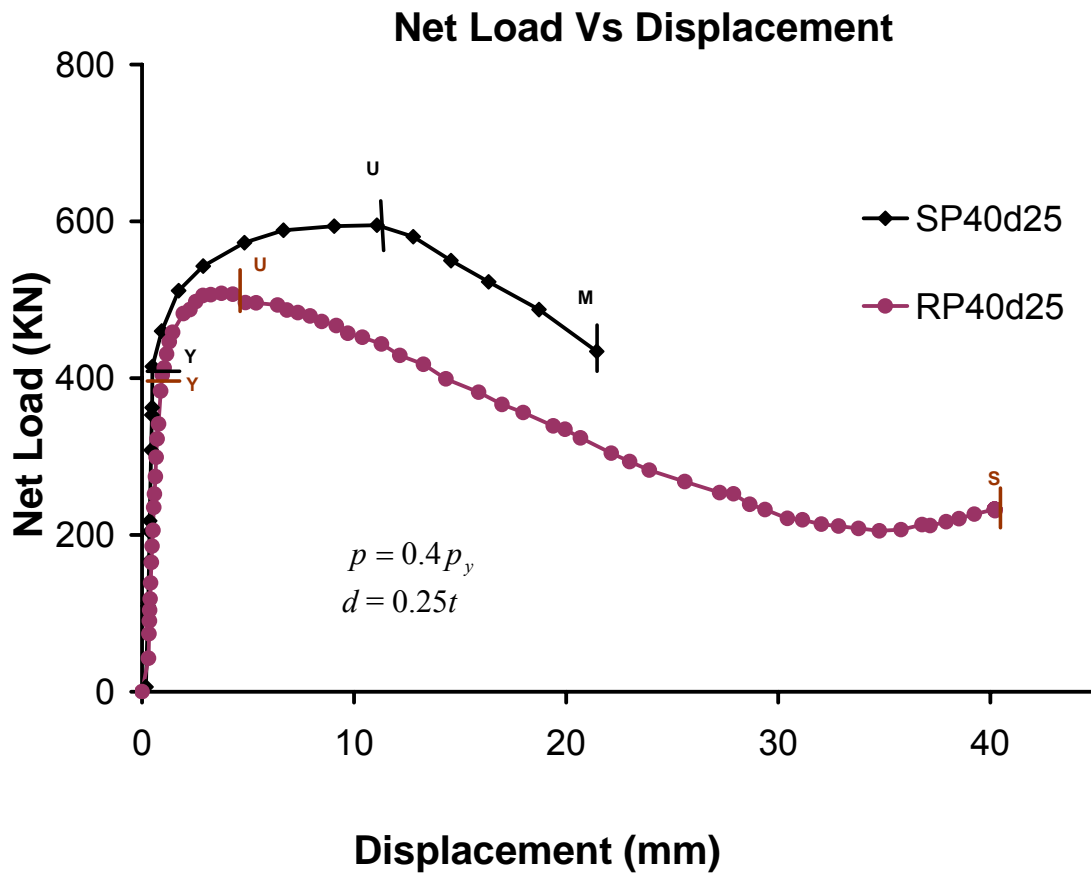
Figure 4.33 Effect of circumferential dimension of corrosion on specimens SP40d25 and RP40d25
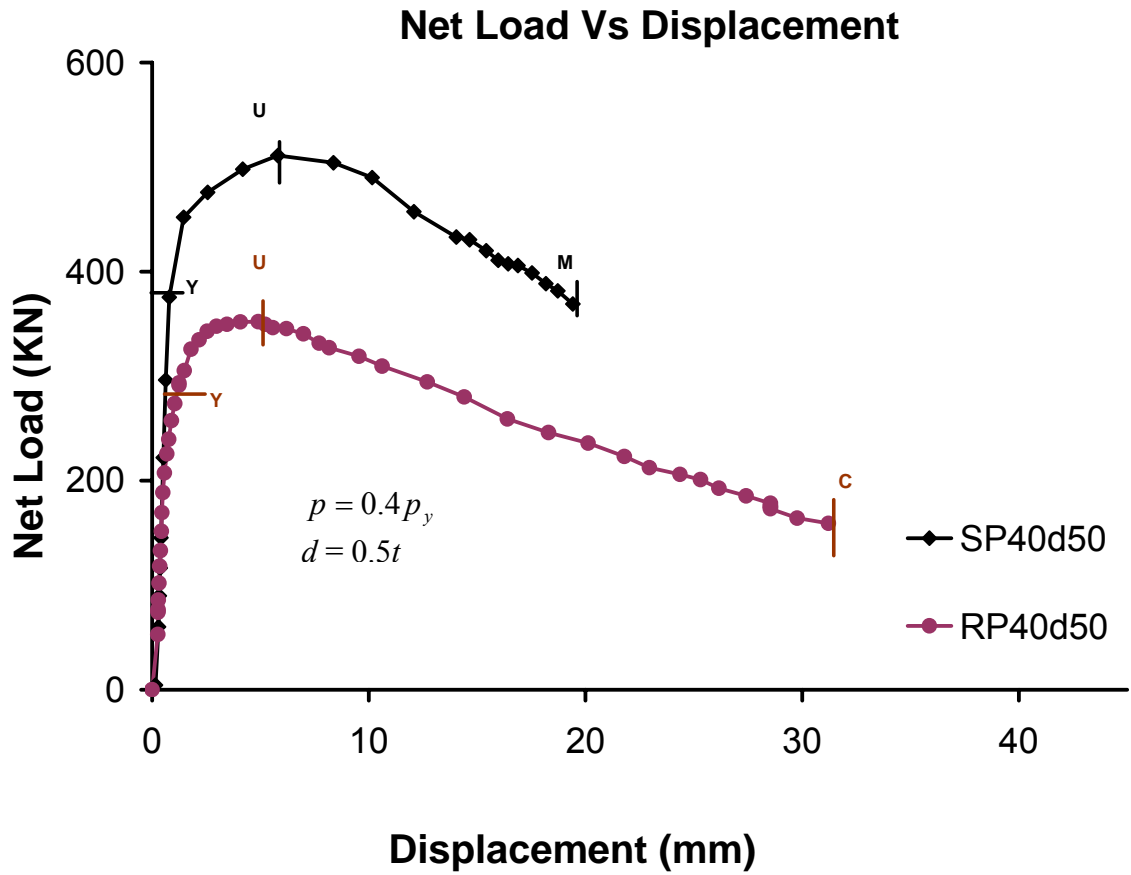
Figure 4.34 Effect of circumferential dimension of corrosion on specimens SP40d50 and RP40d50

5 Development of a Finite Element Model

5.1 General

Experimental testing is undoubtedly the most trusty and traditional way to study and understand the structural behaviour of corroded pipelines. However, experimental methods are expensive and time-consuming, and it is unrealistic to consider full scale tests for a wide range of test parameters. Nevertheless, tests cannot provide all the information that is required for a thorough study. For example, the information inside of the pipe could not be obtained using experimental methods. Following the development and easy availability of the computer and technology, an alternative method to study and predict the behaviour of pipeline structure is to use numerical tools such as Finite Element Analysis (FEA) method has become more popular. Therefore, the purpose of this chapter is to develop a numerical model and validate it with the results of the experimental program detailed in Chapter 3. The comparison between the FEA predictions and the experimental results focuses on both the strength and the deformation behaviour of the specimens. An accurate prediction of the load-deformation behaviour of corroded pipelines under the combined action of axial compressive load and internal pressure is difficult because it involves accurate modelling of various factors such as corrosion geometry, applied loading, large deformation, and nonlinear behaviour, contact simulation etc. However, with the increasing availability of high speed computer it is now possible to apply sophisticated numerical solution techniques to obtain satisfactory solutions to the integrity problem of the energy pipeline suffering corrosion problem.

In this study, a nonlinear (both material and geometry) FEA numerical modeling technique using FE method is employed to simulate the behavior of the test specimens using the commercially available finite element analysis software code ABAQUS/Standard 6.6-1 distributed by SIMULIA, Inc (which will be called as ABAQUS in the subsequent discussion). This software code was chosen to accomplish the simulation for several reasons. First of all, this has been used successfully in the past to model the pipe with corrosion defect since it supports nonlinear stress analysis which contained material nonlinearity, geometric nonlinearity, and boundary

nonlinearity. It allows pipe under large deformation using nonlinear geometry and finite strain formulation. It also offers models for a wide range of nonlinear material behaviors with various hardening rules. It offers finite sliding formation with strict slave and master algorithm for modeling pipe contact with various contact models, namely, constitutive model, damping model, and friction model.

Furthermore, ABAQUS offers both load controlled and displacement controlled solution strategies. The load controlled strategy could be used to only model the initial elastic loads applied to the pipes, and the displacement controlled strategy could be used to pass the ultimate load point and carry out to elastic-plastic analysis range. In addition, ABAQUS also allows to control on the solution process and convergence criteria.

The objectives of developing the numerical models are to conduct detailed parametric study for various corrosion geometries and internal pressures to (i) predict the corroded pipe deformation behavior under axial deformation and constant internal pressure, and, (ii) to develop a failure guideline of corroded X46 pipes for pipeline industry.

5.2 Concept of Finite Element Method

The powerful finite element method began in the 1950s, and with the widespread use of the digital computer it has since gained considerable favor relative to other numerical approaches. This method is applied in a wide scope of application from structural analysis, fluid problem, to electrical field and other engineering areas.

In structural engineering area, the finite element method may be viewed as an approximate Ritz method combined with variational principal applied to continuum mechanics. It permits the prediction of stress and strain in an engineering structure with unprecedented ease and precision. In the finite element method, the structure is discretized by a finite number of elements connected at their nodes. In addition to the nodal compatibility and equilibrium, the compatibility must also be satisfied along the boundaries between elements. Once the stiffness of each element is determined, all the elements are assembled through matrix algebra using force equilibrium and

displacement compatibility to obtain the global stiffness matrix of the structure. Then the necessary boundary conditions are applied. Finally, the loads and displacement are applied to the model and the global responses (reaction forces and displacements) and stresses/ strains are obtained by using global equilibrium equations for the structure. In nonlinear analysis, an incremental solution strategy is required to solve the equations of equilibrium. A more detailed description of FEA process can be reviewed in numerous references (for example, Cook, 1981).

5.3 Finite Element Modelling
5.3.1 Element Selection

Although the shell element is believed to be the most appropriate finite element for non linear collapse analysis of the pipeline (for example Dorey et al., 2006, Bruschi et al., 1995) solid FE models have been preferred by the majority of the researchers that use the finite element technique to perform failure analyses of corroded pipelines (for example Roy et al., 1997, Shim et al., 2002, and Noronha Jr.et al., 2002). In general solid finite elements are more accurate since they are capable of modeling the corrosion defect geometry precisely and can capture the stress concentration along the defect edge. Since, solid element needs more computation time many researchers used shell element for their analysis of the corroded pipeline as well (for example Nicolella and Smith, 1997, Smith et al., 1998)

In this study an attempt was made to model the corroded pipes with S4R element since this model is more cost effective as it requires less computer time to perform the analysis. However, due to the difficulties to model the corrosion defect accurately finally the second order reduced integration solid element C3D20R, which has twenty nodes, was used in this study. This element has three degrees of freedom at all nodes, which are displacement components u_1, u_2 and u_3. This element is a reduced-integration element with 8 integration points where its full integration version has 27 integration points (Figure 5.1). This reduced number of integration point increases computational efficiency and in ABAQUS/Standard these elements generally yield more accurate results than the corresponding fully integrated elements. The second order solid element with reduced

integration may suffer from hourglassing when only one layer of elements is used. But in ABAQUS/Standard the second-order reduced-integration elements, with the exception of the 27-node C3D27R and C3D27RH elements, do not have the same difficulty. This second order elements are also free from shear and volumetric locking problem.

5.3.2 Symmetry of the Model

Initially it was assumed that the test specimens had symmetry (about plane 1-3, Figure 5.2a) in geometry, boundary condition and loading. Therefore only one half of pipe as shown in Figure 5.2a and Figure 5.2b were considered to model for numerical analyses of pipe specimens and parametric study. Later on, it was found that the assumed symmetry was true for control (noncorroded) specimens. For corroded specimens with smaller corrosion dimensions (corrosion depth, d and circumferential length, L_C), the primary bending and rotation occurs about axis-2 (Figure 5.2b) and rotation about axix-1 is negligible. For this case (when corrosion dimension are small) the assumption of symmetry about plane 1-3 is reasonably valid. However, for larger corrosion dimensions, the rotation about axis 1 (Figure 5.2a) becomes quite significant and this rotation at the top end can reach up to 1.25 degree if the specimen is loaded to reach large plastic deformation. Therefore, later a full pipe as shown in Figure 5.3a and Figure 5.3b was modeled. Although this makes the model more expensive in terms of computational time, the full model of the pipe specimen was developed and used to obtain more accurate results.

5.3.3 Modelling of End Cap

In the full-scale tests, end caps (Figure 3.3) were used at both end of the pipe specimen to hold the internal water pressure. In the FEA model, these 50 mm thick caps as shown in Figure 5.3 are modeled as a perfectly-elastic part having Young's modulus (E) of 400 GPa. A higher value of E was used to small elastic deformation of the top end plate.

5.3.4 Modelling of Collar

In the full-scale tests, the two confining collars described in section 3.8 and shown in Figure 3.3 were successful in preventing the pipe from buckling locally at the ends of the

specimen. A perfect representation of these collars in the FEA model may possibly be done by collar-pipe interaction as a contact problem. However, in order to avoid the complication of such a model, the top and bottom 76 mm of the pipe specimen length with greater thickness (the region confined by the collars) was modeled as an elastic material with the same properties (Young's modulus and Poisson's ratio) as that of the pipe material. The top and the bottom parts of the specimens were, therefore, prevented from deforming plastically.

5.3.5 Modelling of Load Point

Two reference points as shown in Figure 5.3, *RP-1* and *RP-2* are created on longitudinal axis (axis-3) of the pipe 20 mm away (outward) from each end plate to apply the boundary conditions. Kinematic coupling constraint was applied between the top surface of top end plate and *RP-1* constraining all the degree-of-freedom. This was done to constraint the degree-of-freedoms of all the nodes of the top surface of the top end plate to the degree-of-freedoms assigned at reference node *RP-1*. In similar manner the degree-of-freedoms of the nodes of the top surface of the bottom end plate was restrained by the degree-of-freedoms assigned to the reference node *RP-2*.

5.3.6 Modelling of Corrosion Defect

In the test specimens the corrosion patches were located at the mid length of the pipe specimen (Figure 3.8). In the FEA model the corrosion patch of required dimension was also simulated at the mid length of the pipe. As shown in Figure 5.4 the transition between corroded and uncorroded area was modeled using 6 mm diameter filet on the four sides of the corrosion.

5.3.7 Boundary Conditions

The boundary conditions used in the numerical model followed the physical and kinematic boundary conditions used in the tests (Figure 5.3). All the boundary conditions were applied to two reference points *RP-1* and *RP-2*. These reference points act as master nodes and the slave nodes are the nodes on the outer surface of the two end plates of the pipe model. Due to the applied kinematic coupling constraint between the master node

and each slave node, the displacement and rotation at the slave nodes are constrained to the displacement and rotation assigned to the master node. Therefore the outer surface nodes of the end plates experienced same kinematic boundary conditions (deformations and rotations) as the master node. The displacement control axial load (u_1) and rotations (θ_1 and θ_2) were applied at top reference node *RP-1* to simulate the boundary conditions used in the top plate of the test specimens. The bottom end of the pipe in the test was fully constrained and hence, all the degrees of freedoms of the nodes at the bottom end of pipe model were constrained by restraining all the degree of freedoms of the bottom reference node *RP-2*. The fully constrained bottom master node was used to simulate the same physical boundary condition as that in the full scaled tests. It should be noted that for corroded test specimens, major rotation occurred about axis-2 and some rotation also occurred about axia-1 as well at the top end (*RP-1*).

5.4 Material Model

Five tension coupon specimens from the same pipe were tested to obtain the uniaxial stress-strain behavior of the pipe material. Test procedures and test results are discussed in Sections 3.11. All the five tension coupon tests indicated almost identical behaviors. Figure 5.5 shows the "average" behaviour for all five tension coupons. The curve exhibit an initial elastic behaviour followed by gradual softening characterized by plastic flow with hardening. The Point U is the ultimate or maximum stress point. The nominal values of fracture stress and fracture strain were determined after the completion of the material tests and the Point F corresponding to the fracture nominal stress and fracture nominal strain.

The tensile coupons were taken in the longitudinal direction of the pipe. Since no material tests were performed to measure the stress vs. strain relationship of the pipe material in compression, the compressive stress vs. strain behaviour is assumed to be identical to the tensile behaviour. No attempts were made to determine the pipe material properties in the circumferential direction. Therefore, for the scope of this work the material was assumed to be isotropic and to follow the observed longitudinal tensile stress vs. strain relationship as determined from coupon tests. The modulus of elasticity

(E) and Poisson's ratio (ν) used for the numerical analysis were 200 GPa and 0.26, respectively.

The material used in the tests experienced large plastic deformation. Therefore, an elastic-plastic material model using von Mises yield criterion and isotropic hardening with associated plastic flow rule was used for numerical analysis. The material property determined from the uniaxial coupon test is in terms of nominal stress and strain. However, in the ABAQUS material model, true stress (Cauchy stress) and logarithmic strain (true strain) are required. A simple conversion from nominal strain and stress to true stress and logarithmic strain for isotropic material that is adopted by ABAQUS is shown in Equation (5.1) and Equation (5.2).

$$\sigma_{true} = \sigma_{nom}\left(1 + \varepsilon_{nom}\right) \tag{5.1}$$

$$\varepsilon_{\ln}^{pl} = \ln(1 + \varepsilon_{nom}) - \frac{\sigma_{true}}{E} \tag{5.2}$$

Where σ_{true} is the true stress, $\varepsilon_{\ln}^{pl}$ is the logarithmic or true plastic strain, σ_{nom} is the nominal stress or engineering stress, ε_{nom} is the nominal strain or engineering strain and E is the Young's modulus. True total stress and true total strain behavior is shown in Figure 5.6. The point L on this plot was not obtained from the test, rather it is an extrapolated point based on point F and a point precedes point F. This was used to avoid numerical problem in FEA analysis. The collar of the pipe and end plates were modelled as elastic material, because they experienced elastic strain only.

A yield surface is the surface inside which the material is elastic, Figure 5.7 shows a typical two dimensional von Mises yield surface. The three dimensional von Mises yield surface has a cylindrical shape, centered on the hydrostatic stress line. As a result, yielding of the metal is independent of the equivalent pressure stress. This is reasonable assumption for initially isotropic metals like the one used in the pipe structure. Therefore, von Mises yield criterion was chosen in the numerical model.

The flow rule defines the inelastic deformation that occurs when the material is no longer responding purely elastically. ABAQUS uses associated plastic flow rule which means that, as the material yields, the inelastic deformation rate is in the direction of the normal to the yield surface (the plastic deformation is volume invariant). This assumption is generally acceptable for most calculations with metals including the pipe material in the current model.

Hardening is the way in which the yield and/or flow definitions change as inelastic deformation occurs. Perfect plasticity (no hardening) is available in ABAQUS, which means that the yield stress does not change with plastic strain. This is obviously not appropriate for the material (pipe steel) used in the tests. Another hardening available in ABAQUS is kinematic hardening, however, it is provided for material subjected to cyclic loading. Isotropic hardening was used in this model. In isotropic hardening, the yield surface increases its size uniformly in all directions such that the yield stress increases in all stress directions as plastic straining occurs as shown in Figure 5.7 Isotropic hardening is generally considered to be a suitable model for problems in which the plastic straining goes well beyond the incipient yield state where the Bauschinger effect is noticeable (Rice, 1975).

5.5 Loading Procedure

The loading scheme consisted of a series load steps in the ABAQUS model and same test loading procedure was followed. The load steps are discussed next.

The first step in the loading procedure was application of the internal pressure p. Two different internal pressures were applied: (i) 625 psi or 4.3 MPa for $0.2\,p_y$ and (ii) 1250 psi or 8.6 MPa for $0.2\,p_y$, where p_y is the internal pressure causing yielding in the circumferential direction of the pipe, calculated as follows.

$$p_y = \frac{\sigma_y t}{r} \qquad\qquad (5.3)$$

σ_y is the yield stress of the pipe material, t is the thickness of the pipe wall, and the r is the outer radius of the pipe.

In the second step, the displacement controlled axial compressive load, $C_{Applied}$ as described in section 3.15 was applied along with the rotations (θ_1 and θ_2), which were develop during the tests due to unsymmetrical geometry of the pipe specimen caused by the presence of the corrosion defect.

5.6 Mesh Study

Seeds are the markers that are placed along the edges of a region to specify the target mesh density in that region. The mesh of the pipe specimen was automatically generated by ABAQUS CAE Preprocessor using local seed by specifying the number of elements along the edge near the corrosion defect and using global seed (by specifying average element size) for rest of the pipe specimen. Different approximate global size of the element 17 mm x 17 mm, 15 mm x 15 mm, 12 mm x 12 mm, 10 mm x 10 mm, and 8 mm x 8 mm were used for mesh study. Relatively fine mesh was used at the corrosion defect. The ultimate load at point U (Figure 3.16) and displacement at point U were compared for the different mesh sizes for the control specimen CP20d25. It was found that the approximate global size 10 mm x 10 mm and 8 mm x 8 mm generate very close results as shown in Figure 5.8 and therefore, the mesh size 10 mm x 10 mm was taken as approximate global size of the element. A typical meshed pipe specimen is shown in Figure 5.9.

5.7 Contact Algorithm

In the experiential program, two of the pipe specimens from Group 2B (RP40d25 and RP40d50) were loaded until the axial displacement reached more than 30 mm. It was observed that despite of this large deformation the pipe specimen did not rupture, rather the inside wall of the pipe made self contact. Therefore a finite-sliding contact formulation was used to simulate this self-contact phenomenon.

The finite-sliding formulation allows for arbitrary separation, sliding, and rotation of the surfaces. Depending on the type of contact problem, two approaches are available to the user for specifying the finite-sliding capability: (i) defining possible contact conditions by identifying and pairing potential contact surfaces or (ii) using contact elements. With the first approach, ABAQUS automatically generates the appropriate contact elements. Contact element approach is usually used when contact between two bodies cannot be simulated with the first approach which is a surface-based contact approach. In this model, the first approach that is, surface based contact approach was used.

The strict "master-slave" algorithm was used to model this contact problem, as shown in Figure 5.10. In strict "master-slave" algorithm, each potential contact condition is defined in terms of a "slave" node and a "master" surface. The slave nodes are not able to penetrate into the master surface; however, the nodes of the master surface can, in principle, penetrate into the slave surface. The contact direction is always normal to the master surface.

The finite sliding contact formulation requires that master surfaces have unique surface normals at all nodes. Convergence problems can result if master surfaces that do not have smooth surface normals are used in finite-sliding contact analyses; slave nodes tend to get "stuck" at points where the master surface normals are discontinuous. ABAQUS/Standard automatically smoothes the surface normals of element-based master used in finite-sliding contact simulations.

The finite sliding contact formulation was used because this formulation can simulate two surfaces contacting with each arbitrarily without specifying the exact the contact areas which must be defined in other contact formulation.

Once the contact formulation is selected, the contact properties should be appropriately defined. Three contact properties were considered in the pipe contact problems: (i) a constitutive model for the contact pressure-overclosure relationship that governs the motion of the surfaces, (ii) a damping model that defines forces resisting the relative

motions of the contacting surfaces, and (iii) a friction model that defines the force resisting the relative tangential motion of the surfaces.

The "hard" contact pressure-overclosure relationship was used in the model, as shown in Figure 5.11. Contact pressure between two surfaces at a point, p_c, is a function of h, overclosure of the surfaces (the interpenetration of the surfaces). Two models for $p_c = p(h)$ are available as described below.

$$p_c = 0 \quad \text{for} \quad h < 0 \text{ (open)} \qquad (5.4)$$

$$p_c > 0 \quad \text{for} \quad h = 0 \text{ (closed)} \qquad (5.5)$$

When surfaces are in contact (closed condition), any contact pressure can be transmitted between them. The surfaces separate (open condition) if the contact pressure reduces to zero. Separated surfaces come into contact when the clearance C between them reduces to zero.

The contact constraint is enforced with a Lagrange multiplier method representing the contact pressure in a mixed formulation, which allows no penetration of the slave nodes into the master surface.

Damping is not considered important in this model, since the contact surfaces could not experience resistant before contact established because of damping. Comparing the results with damping in modeling and those without damping, no difference has been noticed.

When surfaces are in contact they usually transmit shear as well as normal forces across their interface. There is generally a relationship between these two force components. The relationship, known as the friction between the contacting bodies, is usually expressed in terms of the stresses at the interface of the bodies. The default interaction between two bodies is frictionless. The frictionless model could not be used because it is understood that metal (steel) is not smooth enough to be frictionless. The classical isotropic Coulomb friction model was adapted as the friction model. In its general form

it defines friction coefficient in terms of slip rate, contact pressure, average surface temperature at the contact point, and field variables.

The basic concept of the Coulomb friction model is to relate the maximum allowable frictional (shear) stress across an interface to the contact pressure between the contacting bodies as shown in the Figure 5.12. The isotropic friction model assumes that friction coefficient μ is the same in all directions. For a three-dimensional contact there are two orthogonal components of shear stress, τ_1 and τ_2, along the interface between the two bodies. These components act in the slip directions for the contact surfaces. These two shear stress components are combined into one equivalent frictional stress τ_{eq} as follow

$$\tau_{eq} = \sqrt{\tau_1^2 + \tau_2^2} \qquad (5.6)$$

The standard Coulomb friction model assumes that no relative motion of the contact surfaces (stick) occurs if the equivalent frictional stress τ_{eq} is less than the critical stress, τ_{crit}, which is proportional to the contact pressure, p_c, in the form

$$\tau_{crit} = \mu p_c \qquad (5.7)$$

where μ is the friction coefficient at the contact point and it was 0.01 for all the pipe models in this numerical study program. Beyond this point, the contact surfaces start to slide relative to each other. The stick/slip calculations determine a surface in the contact pressure- shear stress space when a point transitions from sticking to slipping or from slipping to sticking.

5.8 Solution Methods and Convergence

ABAQUS uses (by default) Newton's method to solve the nonlinear equilibrium equations. The motivation for this choice is primarily the convergence rate obtained by using Newton's method compared to the convergence rates exhibited by alternate

methods (usually modified Newton or quasi-Newton methods) for the types of nonlinear problems most often studied with ABAQUS is higher.

In ABAQUS, the total time history for a simulation consists of one or more steps, and each step is broken into a number of increments in nonlinear analyses that the nonlinear solution path can be followed, at the end of each increment the structure is in (approximate) equilibrium. The equilibrium solutions are attained by iteration using the Newton method to each time increment. The details of the Newton's method are described in ABAQUS manual (SIMULIA, 2008).

ABAQUS incorporates an empirical algorithm designed to provide an accurate, and at the same time economical solution of the equilibrium equations of nonlinear systems. In ABAQUS/Standard for structure stress analysis, four parameters checked for convergence are force, moment, displacement and rotation. For example, convergence is obtained when size of the residual (disequilibrium) force is less than a tolerance times a reference value and/or when the size of the increment in displacement is less than a tolerance times a reference value. In this model, only default tolerance values were used. For some difficult cases, it is often necessary to increase the number of increments and/or use some solution controls. Sometimes nonmonotonic convergence may occur because of various nonlinearities interaction, for example, the combination of friction, nonlinear material behavior, and geometric nonlinearity may lead to nonmonotonically decreasing residuals. In this case, some controls in the time increment such as increase the number of equilibrium iterations for residual check and the number of equilibrium for a logarithmic rate of convergence check may be used to get convergence.

Automatic incrementation scheme is selected because ABAQUS/Standard will automatically adjust the size of the time increments to solve nonlinear problems more efficiently based on the initial time step defined. It may increase the time increment when convergence is easily obtained. On the other hand, ABAQUS/Standard will abandon the increment and starts again with the increment size set to 25% of its previous value if the solution has not converged within certain numbers of iterations or if the solution appears to diverge.

5.9 Comparison FEA and Experimental Results

The result of the finite element analyses are presented in Table5.1 along with experimental results for the corresponding specimen. The primary focus of the validation was on applied load and the displacement value at ultimate load point U (Figure 3.16). It can be observed that the FEA model almost always predicts higher value than the experimental result. The *% Error* in prediction of the applied load at point Y and the applied load and displacement at point U is calculated using the Equation 5.8.

$$\%Error = \frac{FEA_{\mathrm{Pr}\,ediction} - Experimental_{\mathrm{Re}\,sult}}{Experimental_{\mathrm{Re}\,sult}} \times 100 \qquad (5.8)$$

Where $FEA_{\mathrm{Pr}\,ediction}$ is the applied load or displacement value at point Y or U predicted by the FEA model and $Experimental_{\mathrm{Re}\,sult}$ is the applied load or displacement value at point Y or U obtained from the experimental program.

Figure 5.13 through Figure 5.22 show a comparison between the applied load vs. displacement relationships for the FEA model and the ten specimens tested. Figure 5.23 through Figure 5.32 show the comparison between the deformed shape of the tested specimen and deformed shape of the FEA model for the corresponding specimen.

5.10 Summary

This chapter presented numerical modelling and solution techniques of the monotonic axially loaded test specimens. The model is able to simulate highly complicated plastic strain history of pipeline structure with wrinkling. This chapter also presented the results obtained from the FEA and compared those results with the test results. The comparisons show that a numerical tool like ABAQUS is able to simulate these test results successfully if might choices are made for various aspects of modelling and solution techniques. Comparisons between test results and FEA results are good for all the specimens. To the best knowledge of the author, no other work on this type of numerical

modelling has been done elsewhere. This model is the first of its kind but may not the best possible numerical model.

Table 5.1 Experimental and FEA Results For Ten Pipe Specimens

| Specimen | At First Yield (Point Y) | | | At Maximum Load (Point U) | | | | | |
| | Net Load (kN) | | | Net Load (kN) | | | Displacement (mm) | | |
	Experiment	FEA	% Error	Experiment	FEA	% Error	Experiment	FEA	% Error
CP20d00	542	560	3.32	788	836	6.09	10.2	10	-1.96
SP20d25	529	539	1.89	715	765	6.99	6.7	7.1	5.97
SP20d50	496	515	3.18	639	670	4.85	5.4	5.7	5.5
CP40d00	465	491	5.59	611	676	10.63	12.6	12.5	-0.79
SP40d25	410	429	4.63	595	656	10.25	11.1	11.5	3.6
SP40d50	376	391	3.98	511	539	5.47	5.8	6.18	6.55
RP20d25	443	456	2.93	616	656	6.49	3.2	3.5	9.37
RP20d50	288	299	3.81	433	463	6.92	3.6	3.8	5.55
RP40d25	403	415	2.97	509	546	7.26	3.7	4.1	10.81
RP40d50	273	290	6.2	352	381	8.23	4.8	4.9	2.08
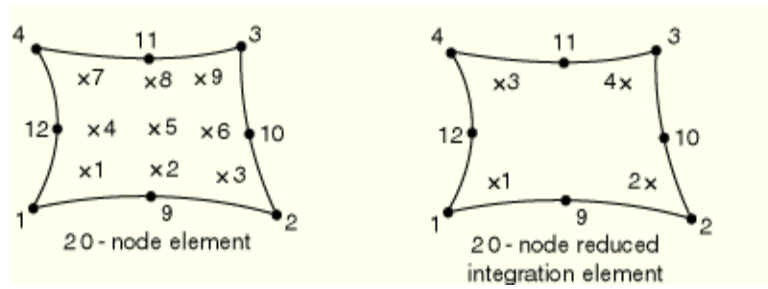
(a) Full Integration   (b) Reduced Integration

Figure 5.1 Integration points for C3D20 and C3D20R
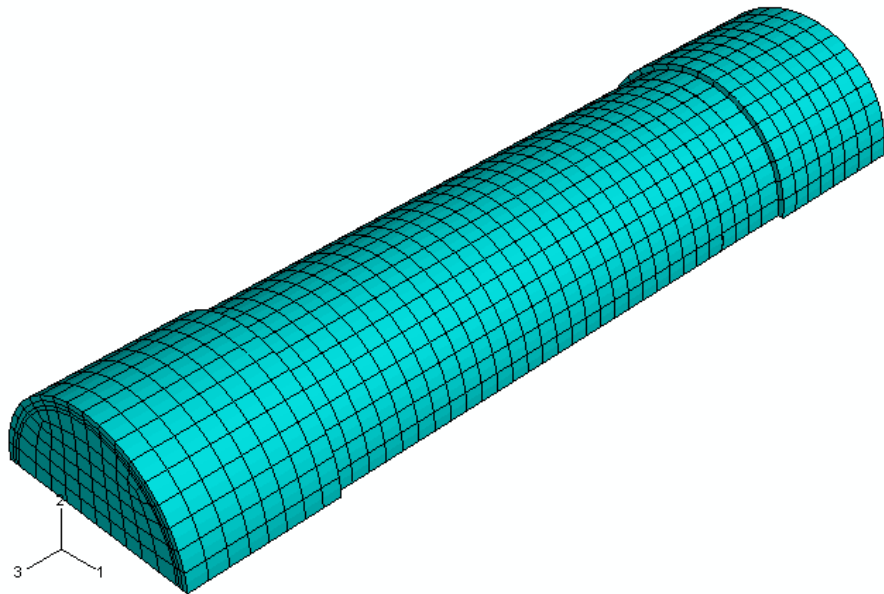
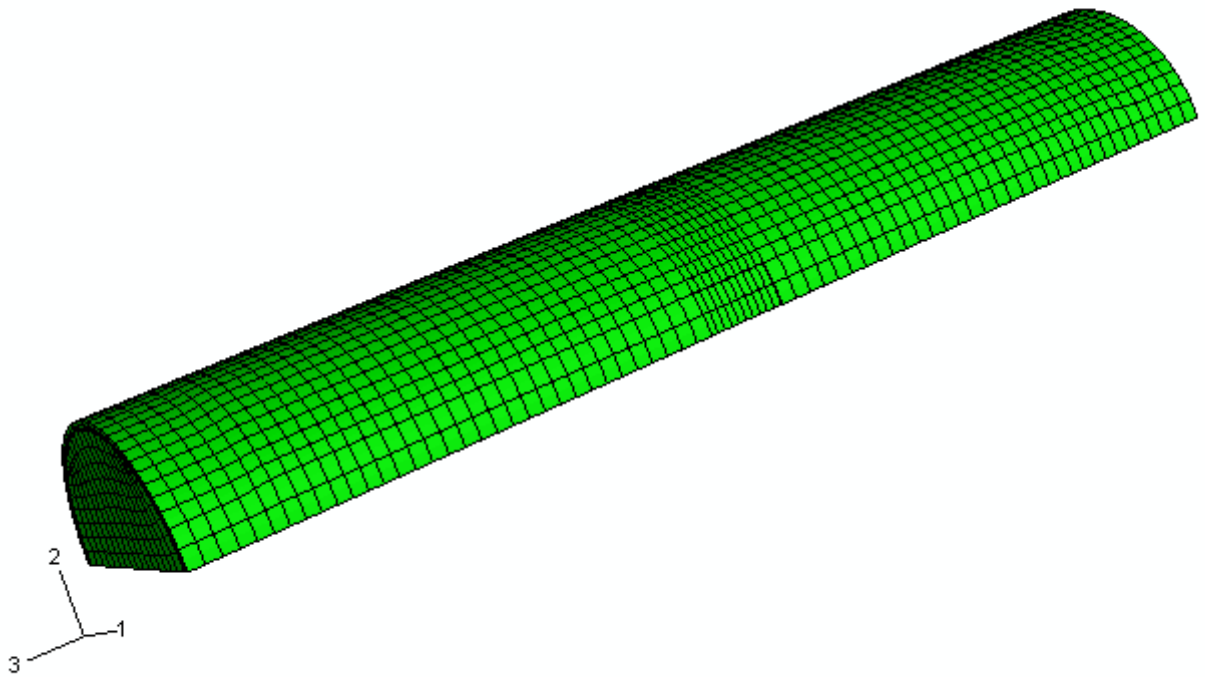Figure 5.2(a) Half pipe model – control specimen
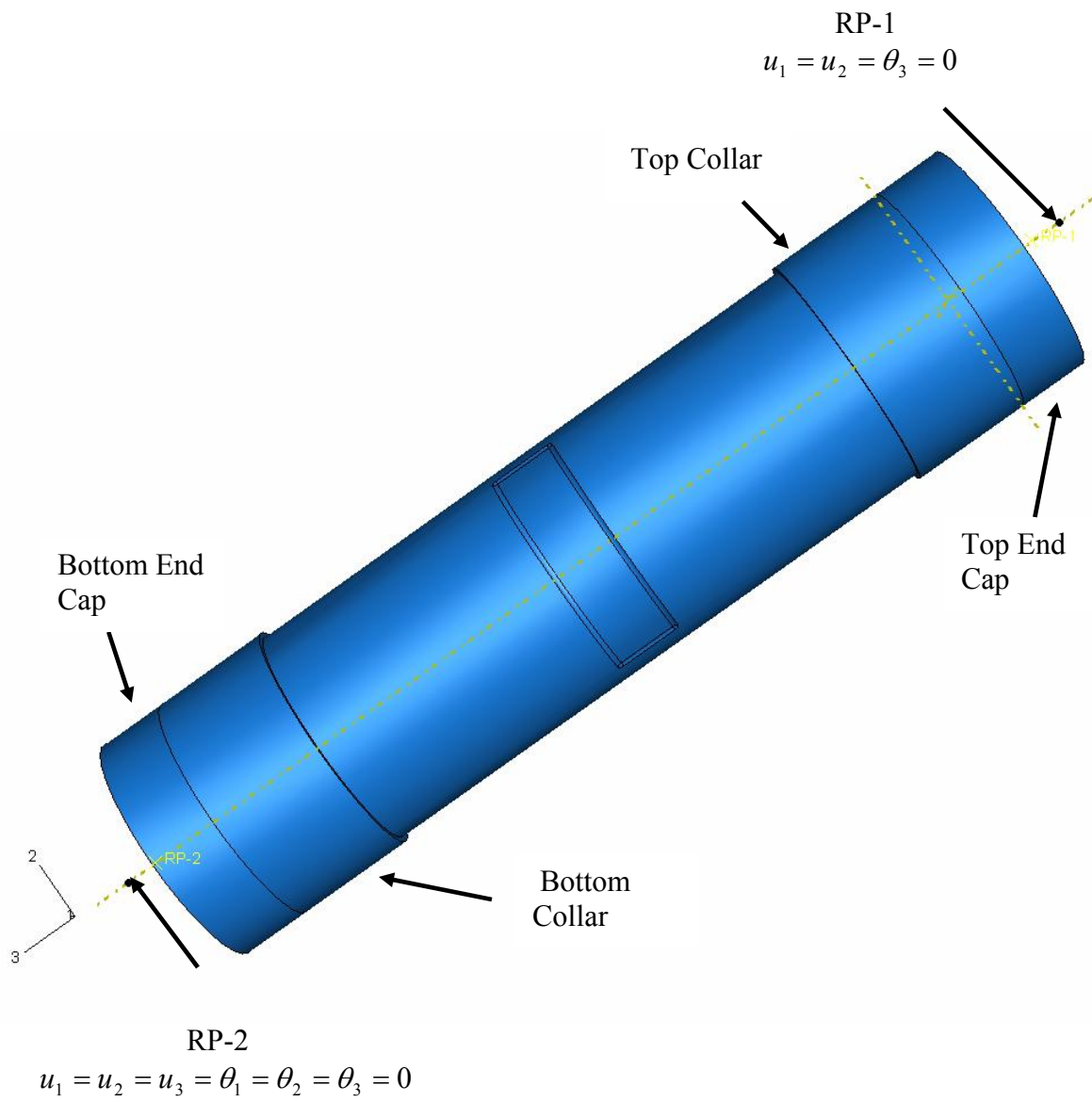
Figure 5.2(b) Half pipe model – corroded specimen

RP-1
$$u_1 = u_2 = \theta_3 = 0$$

Top Collar

Bottom End
Cap

Top End
Cap

Bottom
Collar

RP-2
$$u_1 = u_2 = u_3 = \theta_1 = \theta_2 = \theta_3 = 0$$

Figure 5.3(a) Full pipe model and boundary conditions

RP-1
$u_1 = u_2 = \theta_3 = 0$

Top Collar

Corrosion defect

3

2

Bottom Collar

RP-2
$u_1 = u_2 = u_3 = \theta_1 = \theta_2 = \theta_3 = 0$
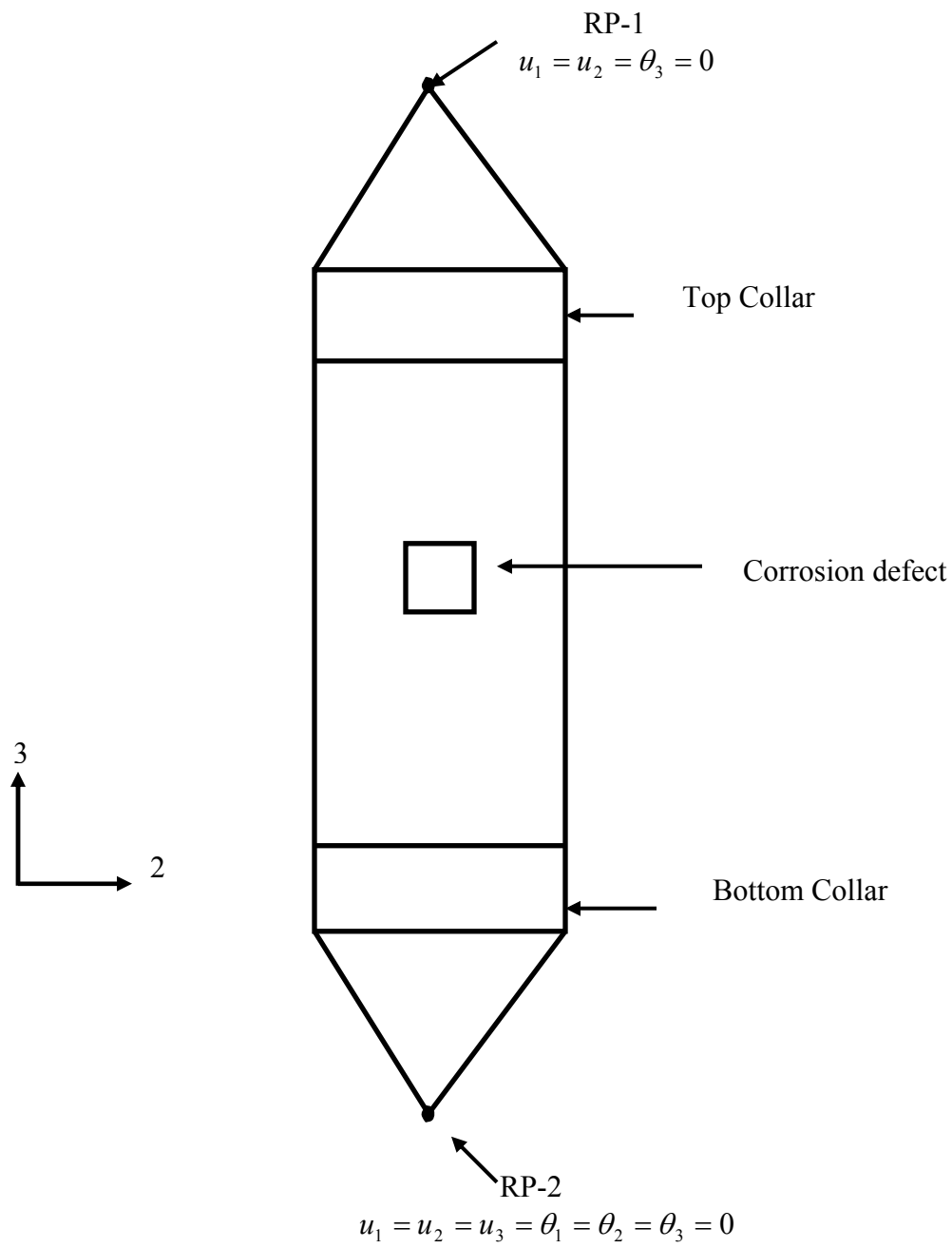
Figure 5.3(b) Schematic of full pipe model and boundary conditions

(a) Experiment

Fillet Radius = 3mm
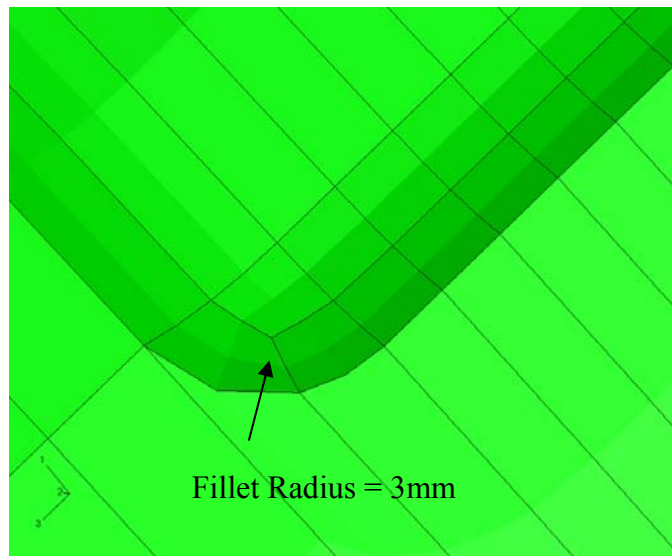
(b) FEA

Figure 5.4 Corrosion Defect

Stress Vs Strain
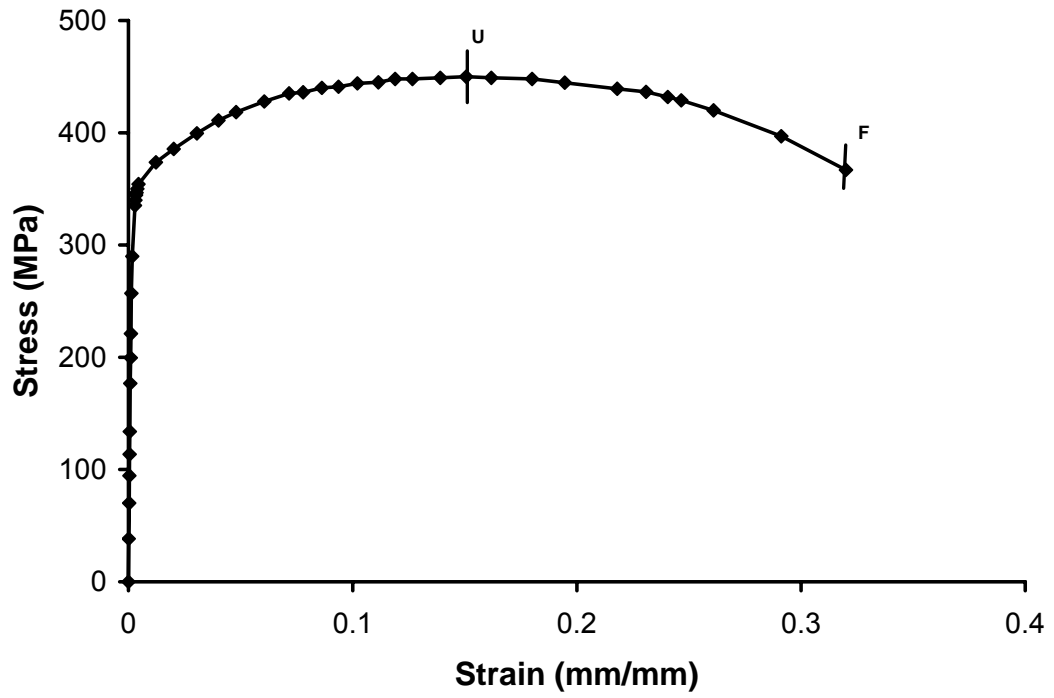
Figure 5.5 Stress strain behaviour of a typical coupon specimen
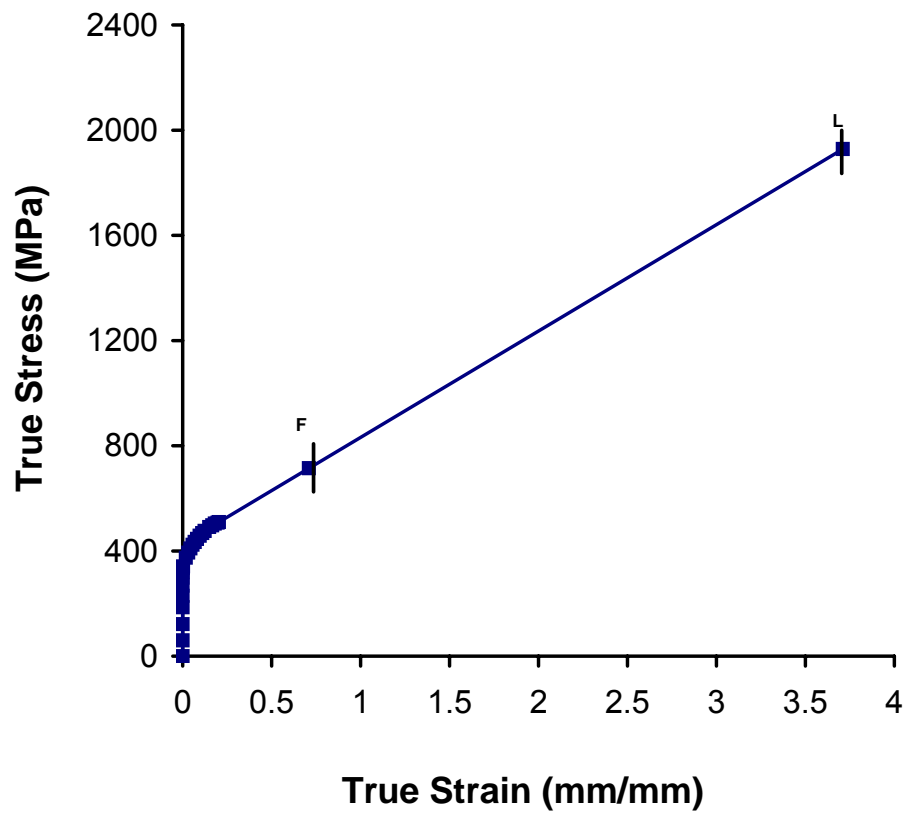
Figure 5.6 Typical true stress-strain behavior of pipe material
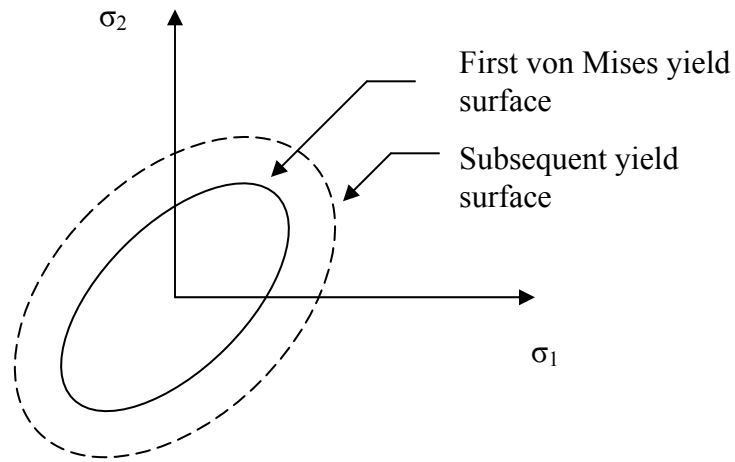
Figure 5.7 2-D von Mises' yield surface and isotropic work hardening
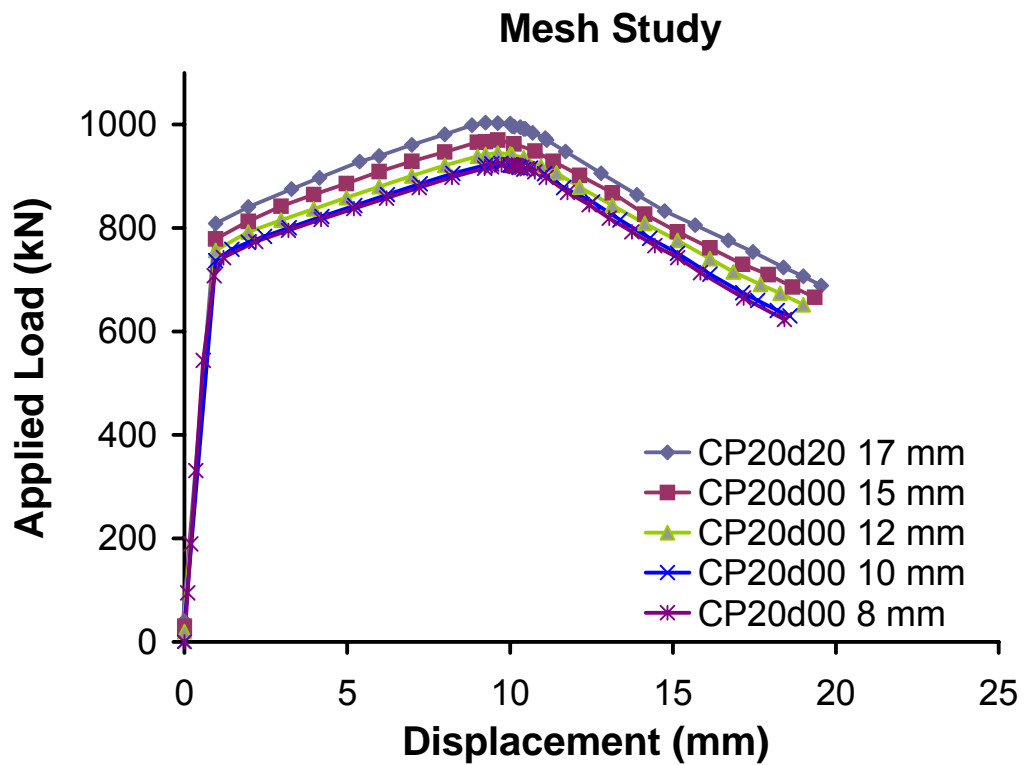
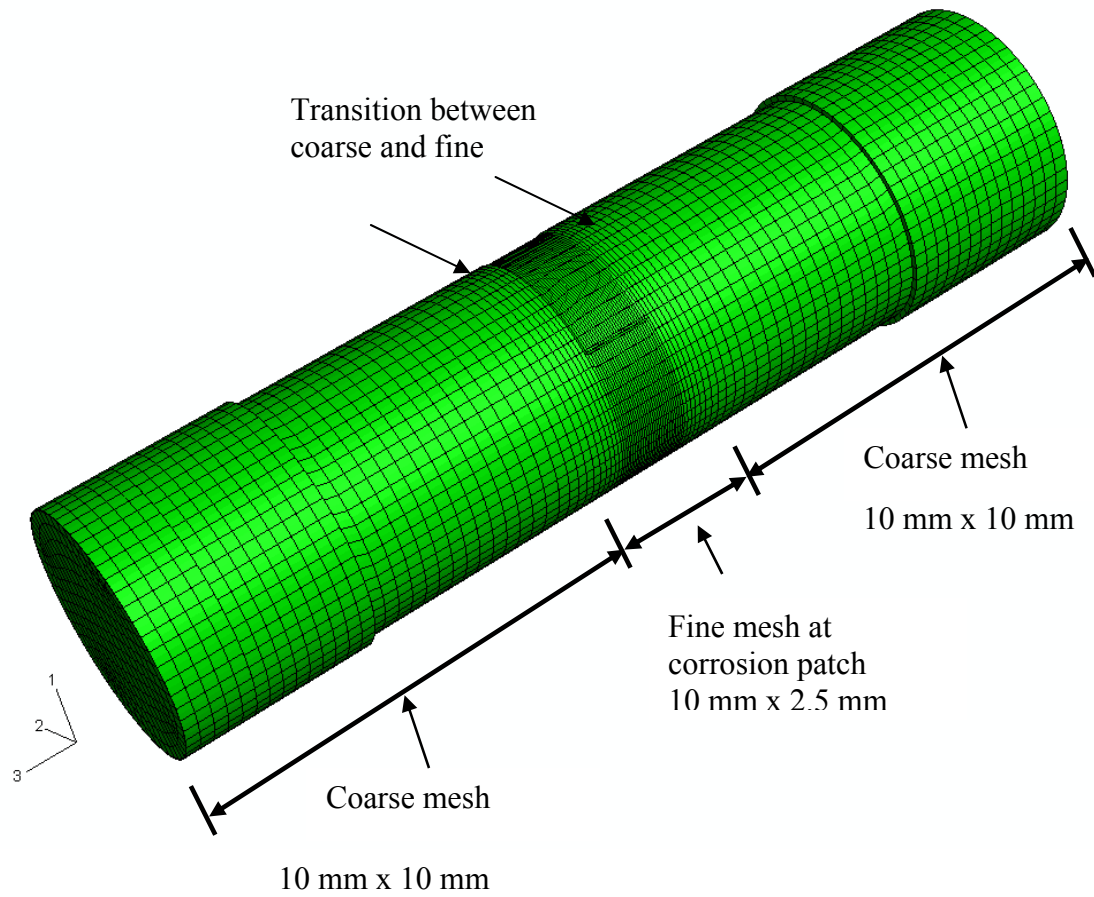Figure 5.8 Load-displacement plots for different densities

Transition between
coarse and fine

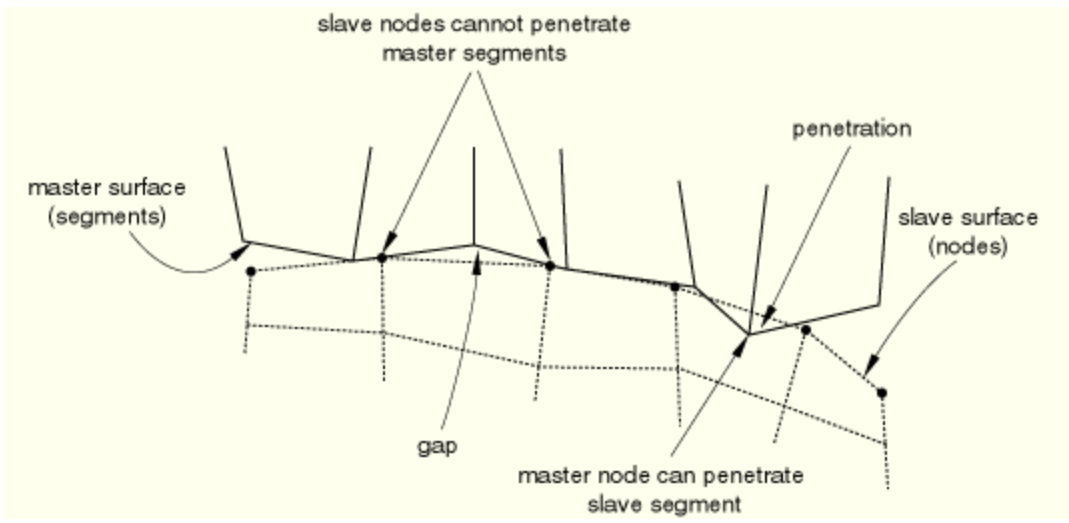Coarse mesh

10 mm x 10 mm

Fine mesh at
corrosion patch
10 mm x 2.5 mm

Coarse mesh

10 mm x 10 mm

Figure 5.9 A typical meshed pipe specimen

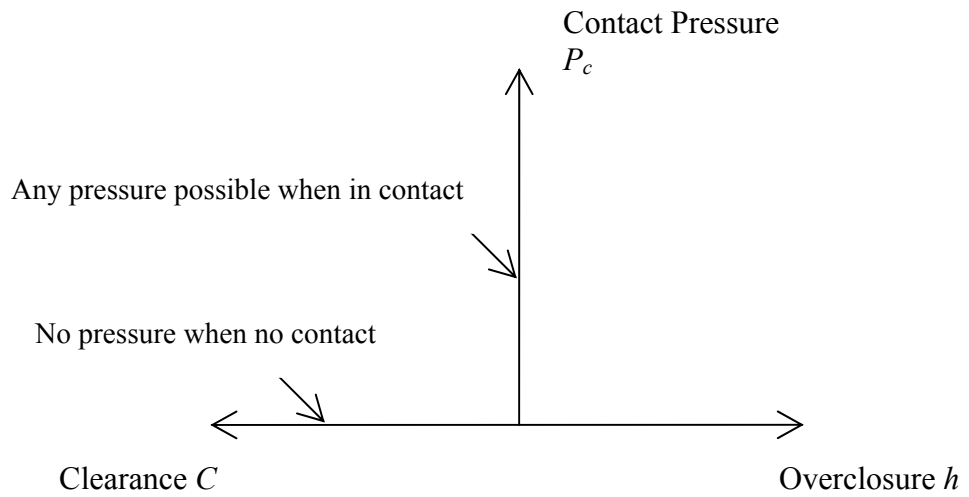Figure 5.10 Slave-master contact algorithm

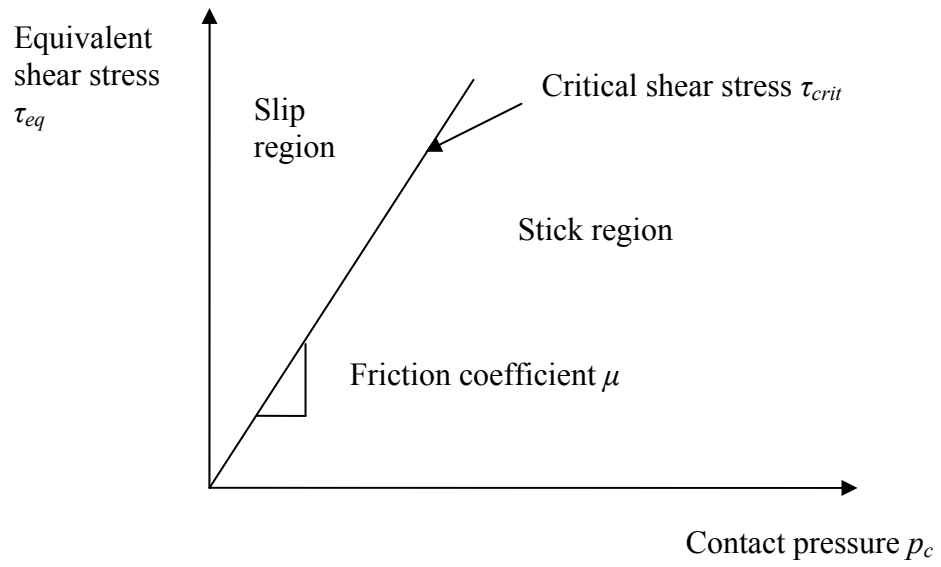Figure 5.11 Pressure-overclosure Relationship for "Hard" Contact

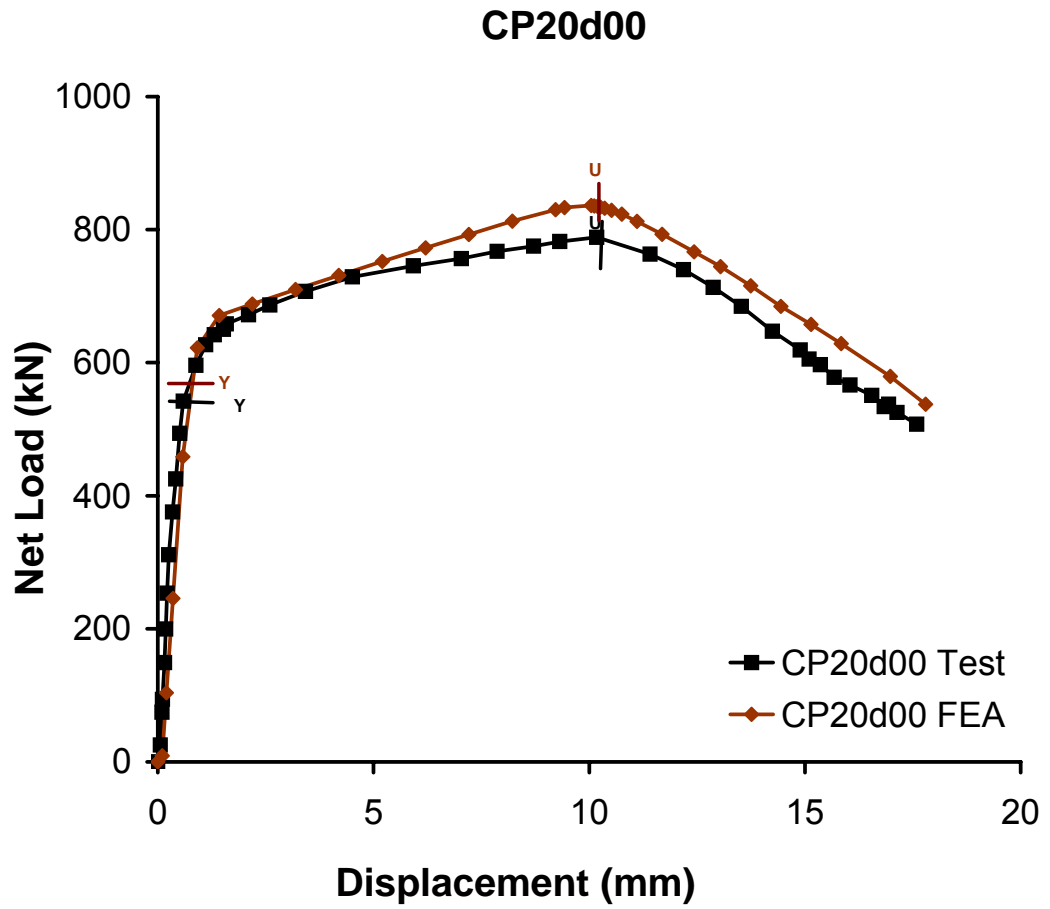Figure 5.12 The standard Coulomb friction model

CP20d00

Figure 5.13 Comparison between Load vs. Displacement plots for Experiment and FEA
for specimen CP20d00

Figure 5.14 Comparison between Load vs. Displacement plots for Experiment and FEA
for specimen SP20d25

Figure 5.15 Comparison between Load vs. Displacement plots for Experiment and FEA
for specimen SP20d50

Figure 5.16 Comparison between Load vs. Displacement plots for Experiment and FEA for specimen CP40d00
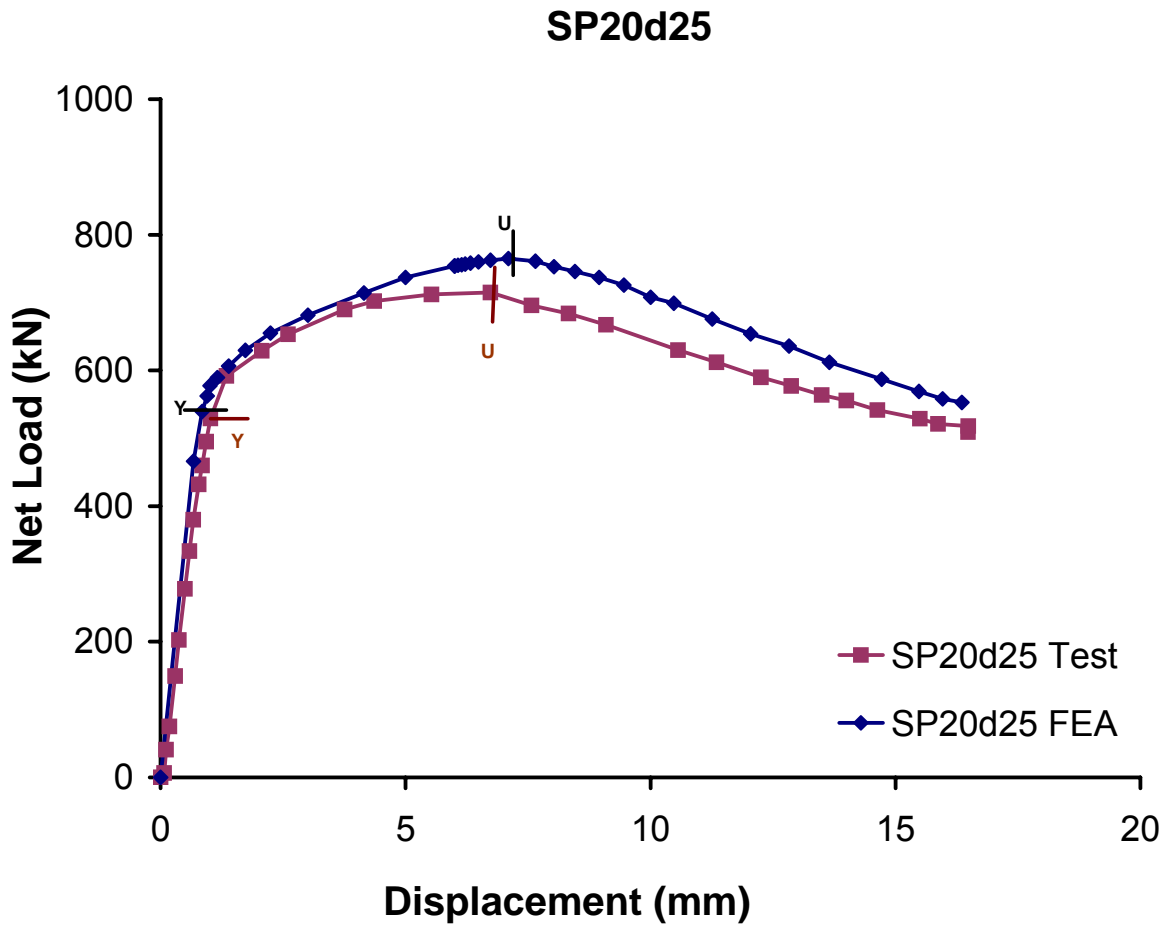
Figure 5.17 Comparison between Load vs. Displacement plots for Experiment and FEA
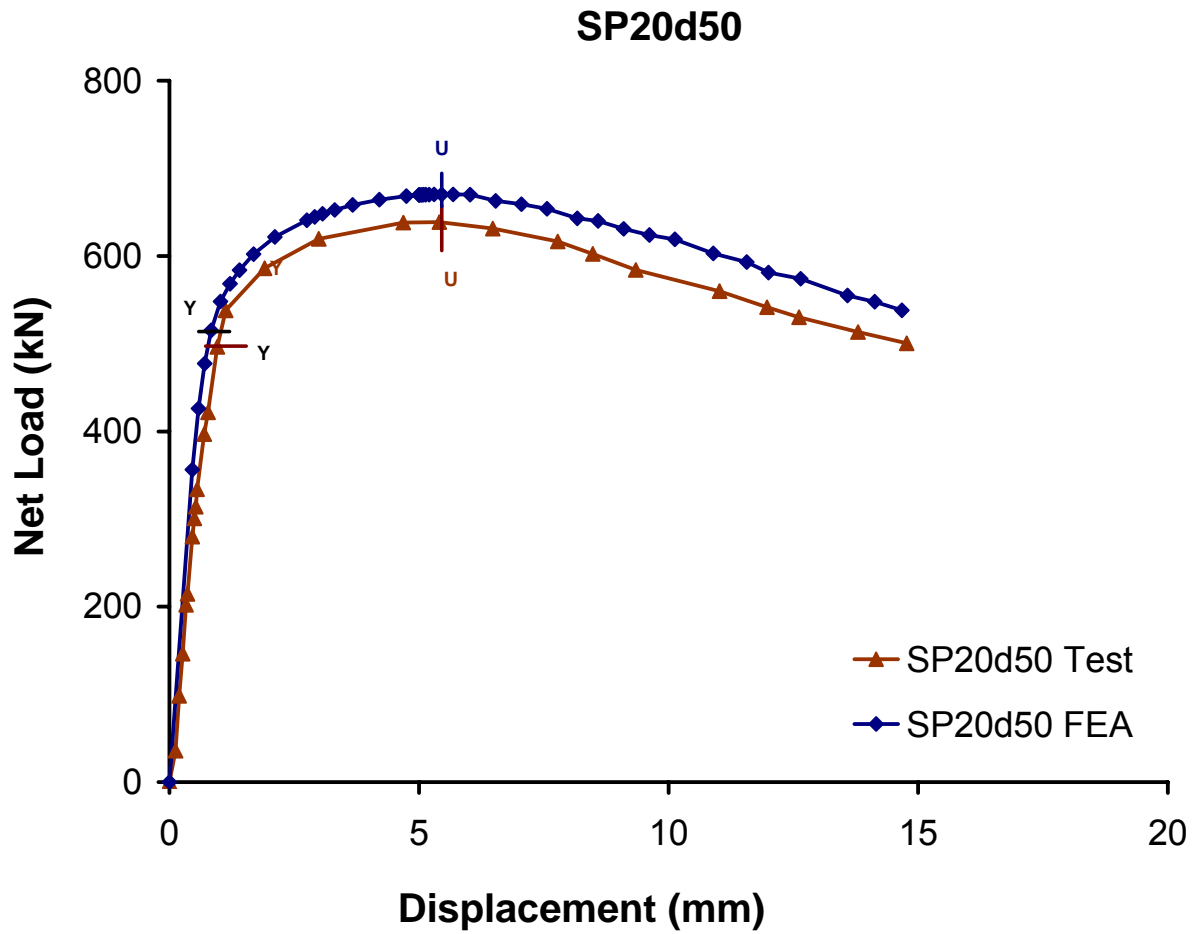for specimen SP40d25

Figure 5.18 Comparison between Load vs. Displacement plots for Experiment and FEA
for specimen SP40d50

Figure 5.19 Comparison between Load vs. Displacement plots for Experiment and FEA
for specimen RP20d25
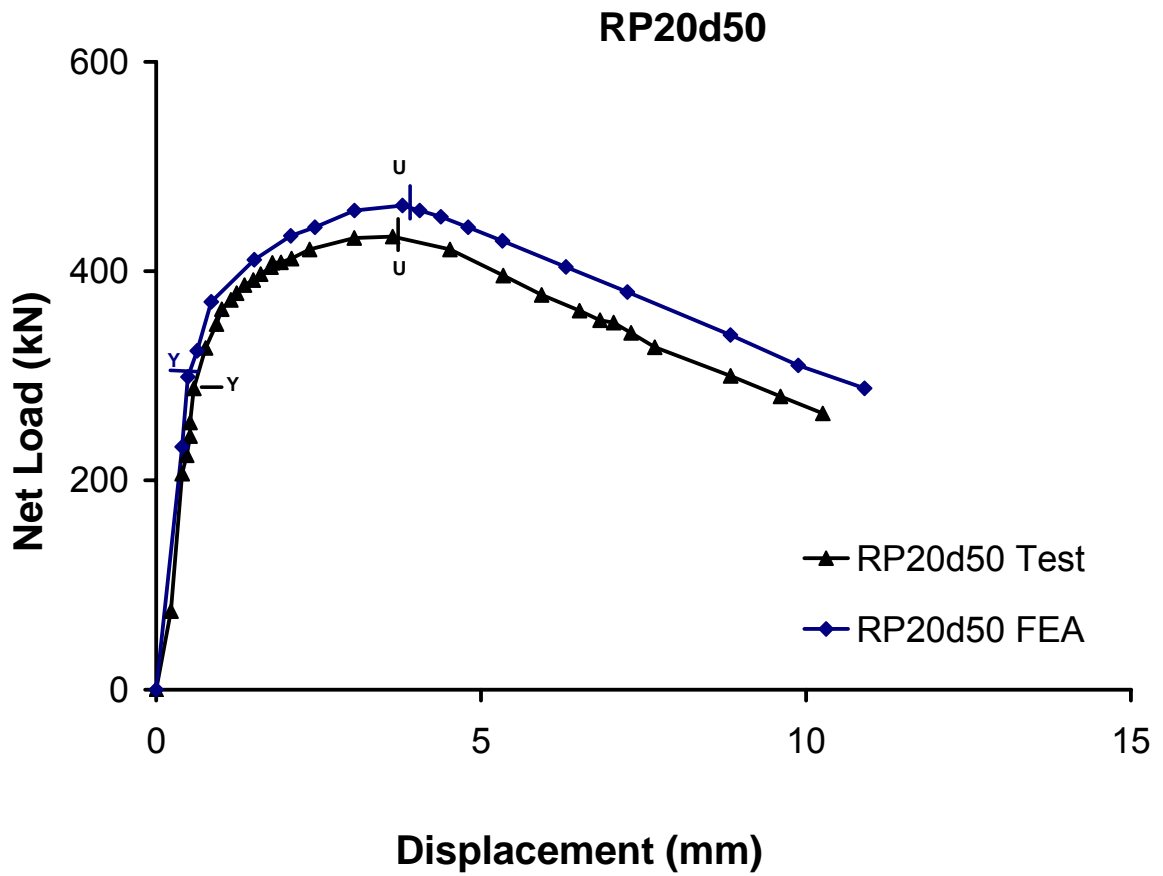
Figure 5.20 Comparison between Load vs. Displacement plots for Experiment and FEA
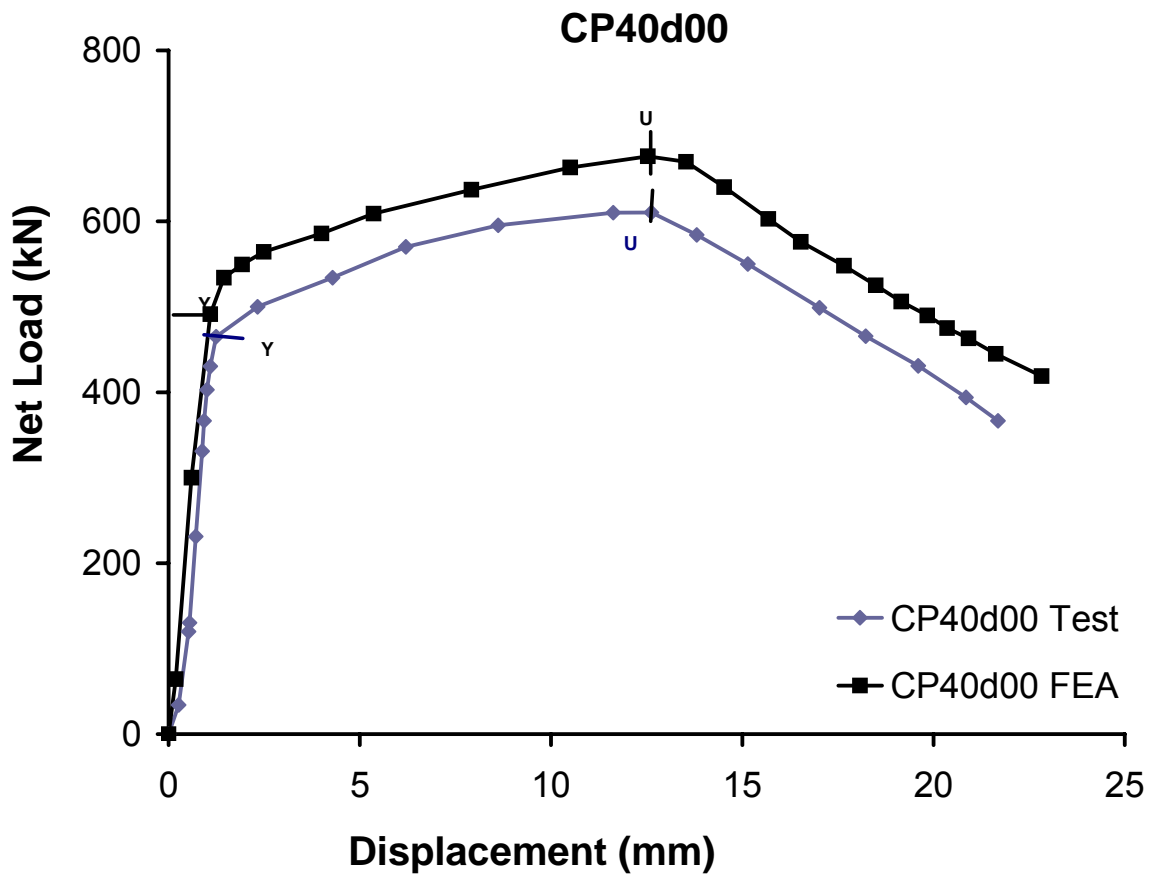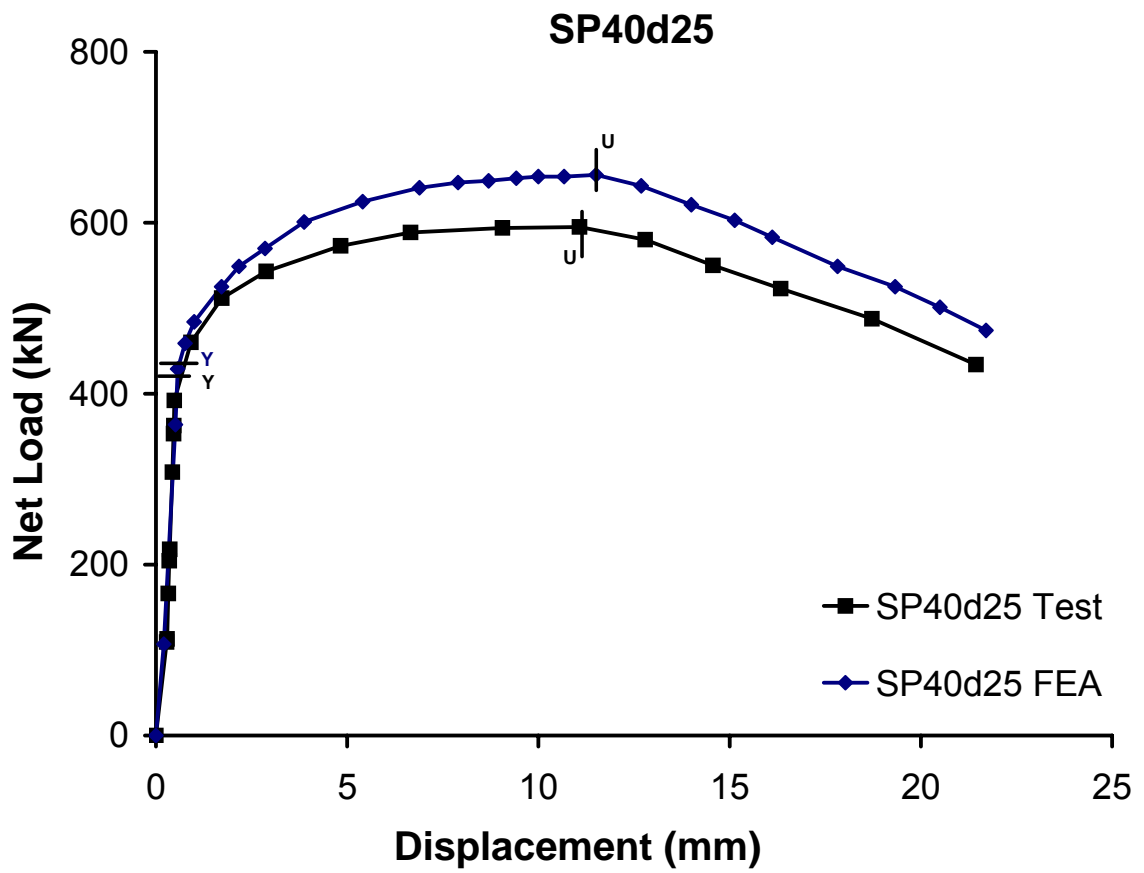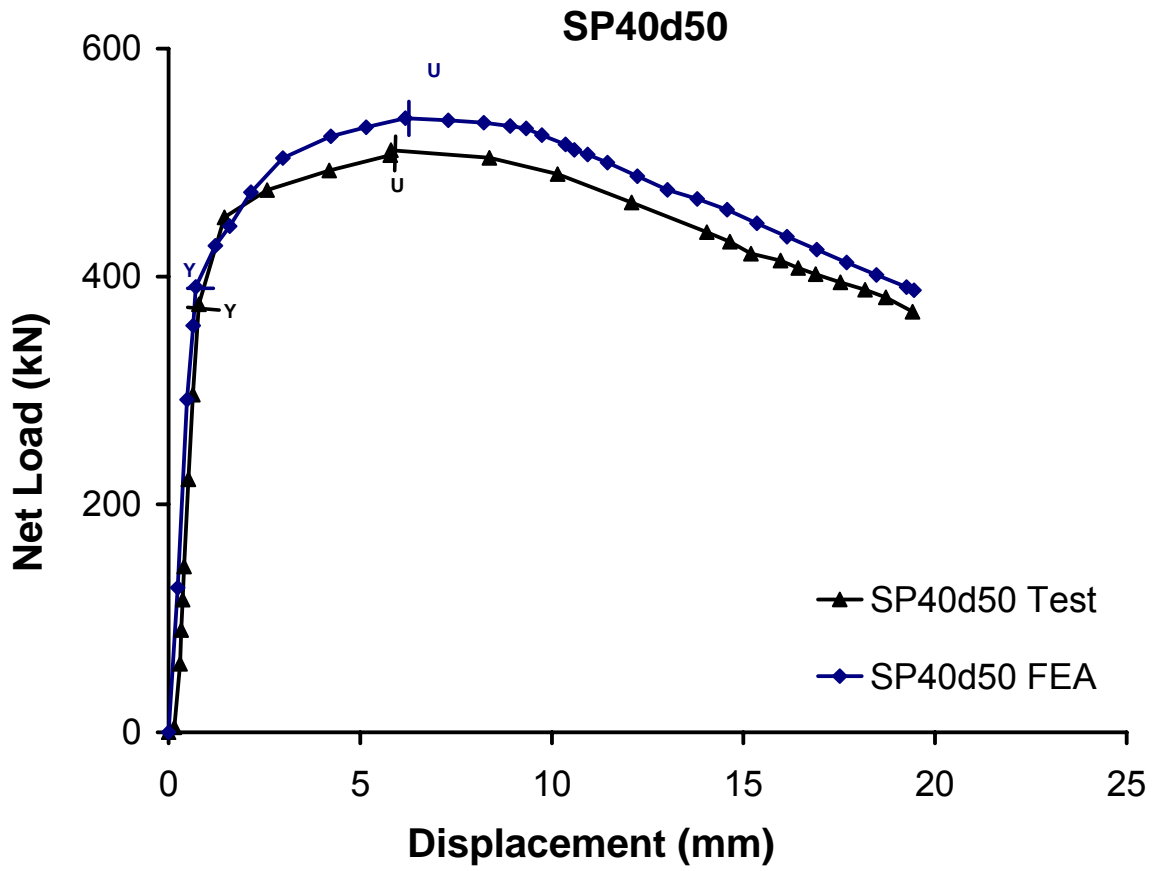for specimen RP20d50
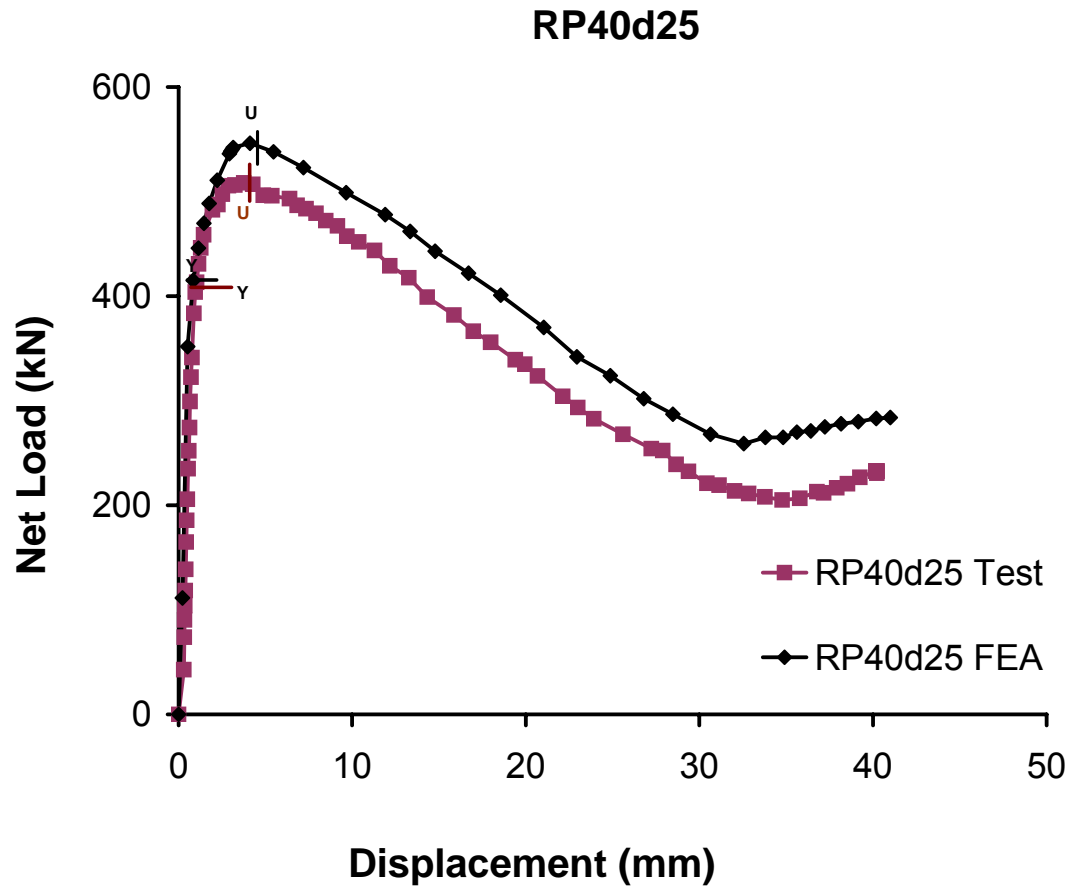
Figure 5.21 Comparison between Load vs. Displacement plots for Experiment and FEA
for specimen RP40d25
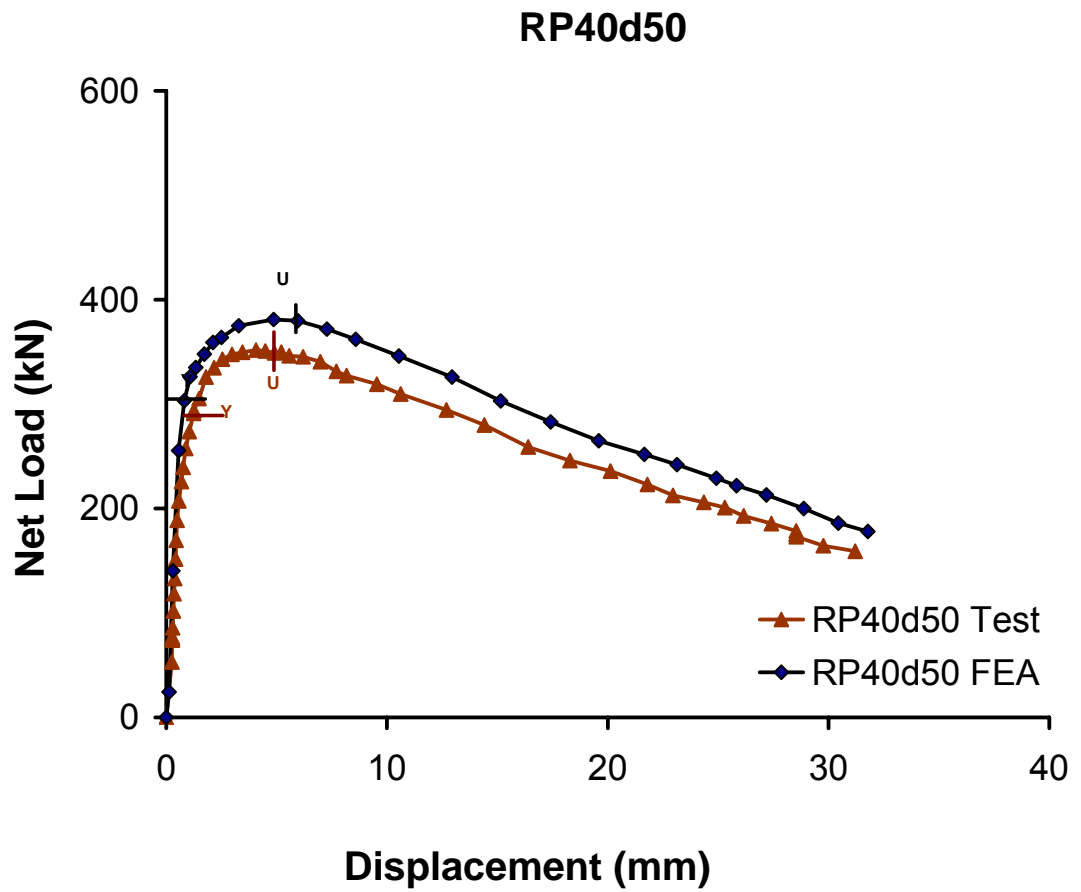
Figure 5.22 Comparison between Load vs. Displacement plots for Experiment and FEA
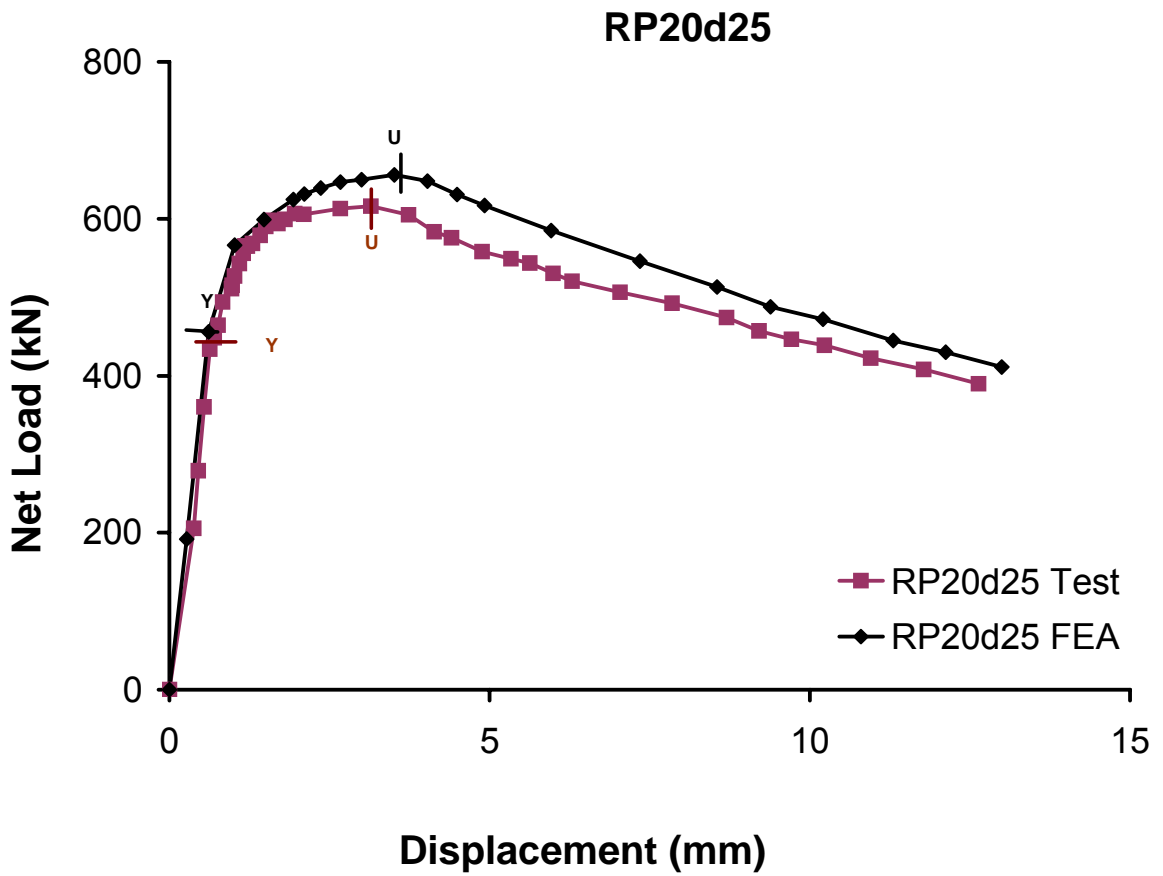for specimen RP40d50
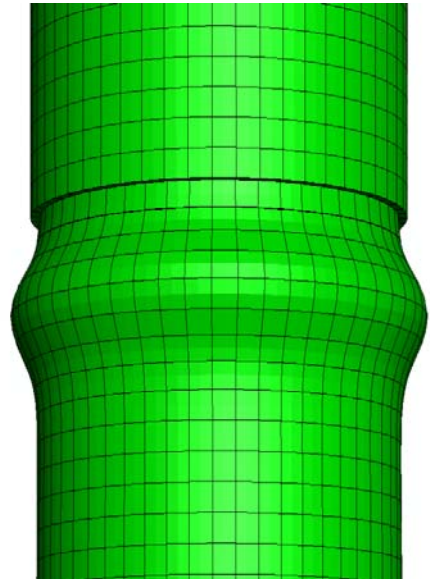
Test   FEA

Figure 5.23 Deformed Shape of Specimen CP20d00

Test   FEA

Figure 5.24 Deformed Shape of Specimen SP20d25

Test   FEA

Figure 5.25 Deformed Shape of Specimen SP20d50

Test   FEA

Figure 5.26 Deformed Shape of Specimen CP40d00

Test	FEA

Figure 5.27 Deformed Shape of Specimen SP40d25

Test	FEA

Figure 5.28 Deformed Shape of Specimen SP40d50

Test   FEA

Figure 5.29 Deformed Shape of Specimen RP20d25

Test   FEA

Figure 5.30 Deformed Shape of Specimen RP20d50

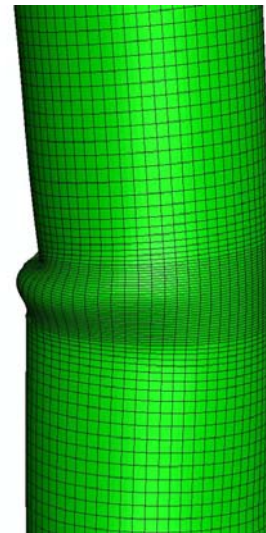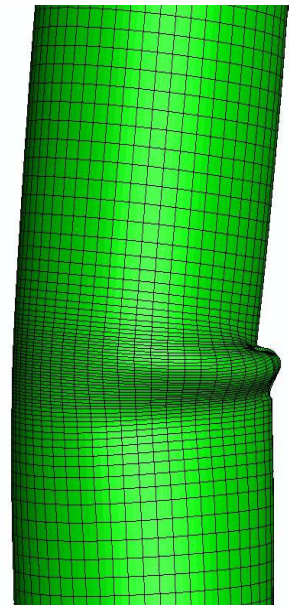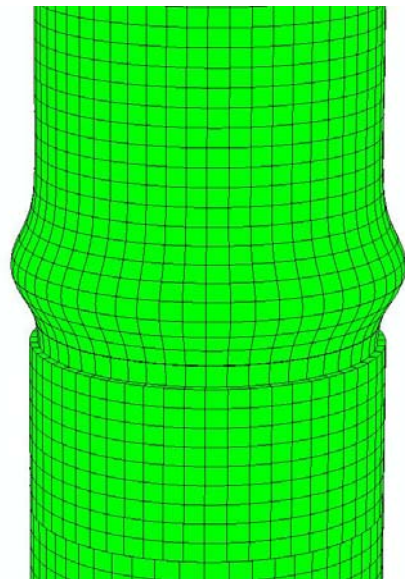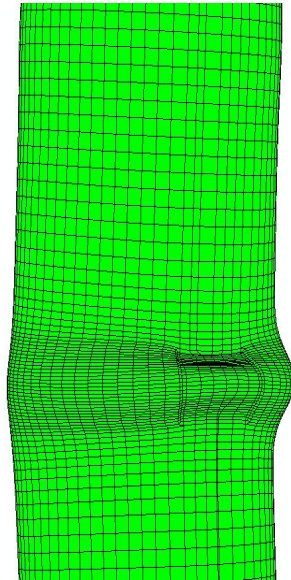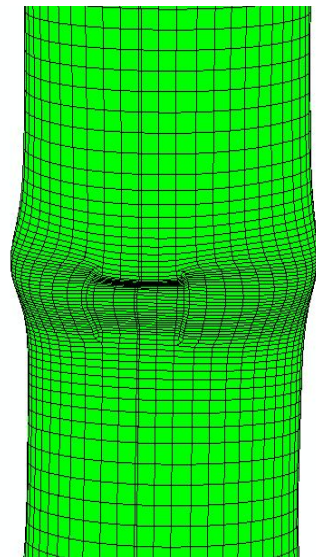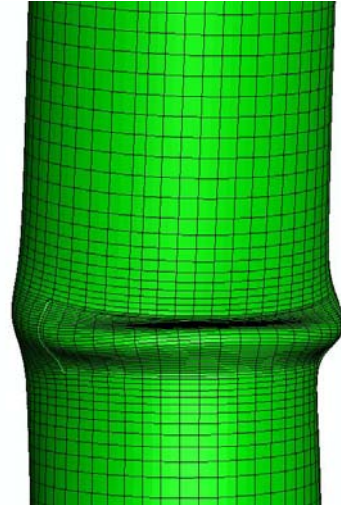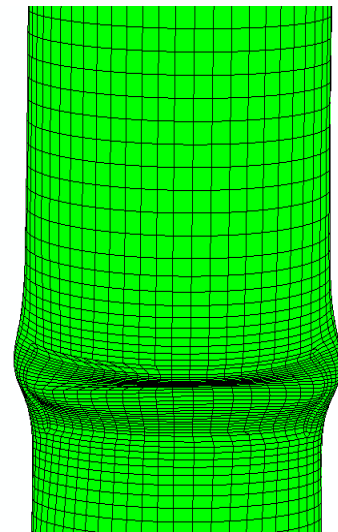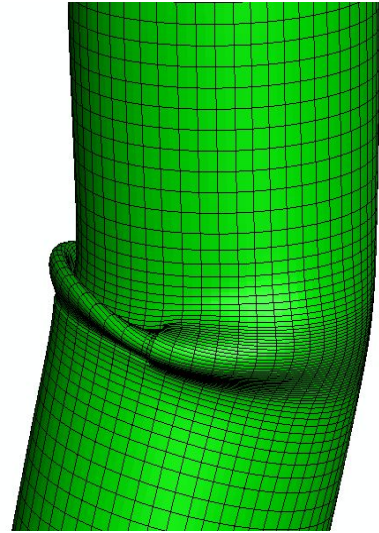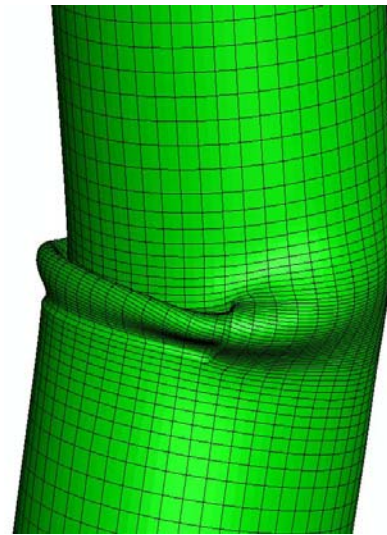Test   FEA

Figure 5.31 Deformed Shape of Specimen RP40d25

Test   FEA

Figure 5.32 Deformed Shape of Specimen RP40d50

6 Material Test Modelling
6.1 General

This chapter provides a brief description of the material coupon tests and numerical analyses to obtain material properties. Under the scope of this project, numerical simulation and analysis of these material tests were carried out using the same finite element code, ABAQUS. The purpose of these numerical analyses is to set up a fracture criterion for numerical models of pipe specimens.

6.2 Tests for Material Properties

The tensile coupons were cut in the longitudinal direction of the pipe. Since no material tests were performed to measure the stress vs. strain relationship of the pipe material in compression, the compressive stress vs. strain behaviour is assumed to be identical to the tensile behaviour. No attempts were made to determine the pipe material properties in the circumferential direction. Therefore for the scope of this work the material was assumed to be isotropic and to follow the observed longitudinal tensile stress vs. strain (Figure 3.6) relationship as determined from coupon tests.

The material properties of the test specimens discussed in Chapter 3 were obtained by tension coupon tests. The tension coupon specimens were cut from same pipe specimen of D/t ratio of 34 and X46 grade steel (SMYS = 340 MPa), prepared and tested according to ASTM E 8/E 8M-08 specifications (ASTM, 2008). Five tension coupon specimens with gauge length of 50.8 mm (2 in) and width of 12.5 mm (0.5 in) were made. All the specimens were cut from the longitudinal direction of the pipe and from a segment away from the seam weld to avoid any residual stress effect on the material behaviors. A clip-on extensometer of 50.8 mm (2 in) gauge length was mounted on one face of the specimen to obtain strains.

The load and overall deformation curve was recorded for each specimen throughout the range of deformation until rupture occurred. A typical load-deformation curve for a tension coupon specimen is shown in Figure 6.1. The extensometer was left on the

coupon specimen until rupture. The material properties obtained from these test are shown in Figure 3.6 and Table 3.3 in Chapter 3.

6.3 Numerical Model for Material Test

The numerical model (an ABAQUS/Standard model) for simulating material test was developed using the same commercially available finite element analysis code ABAQUS/Standard Version 6.6-1, details of these models are discussed in the following sections.

6.3.1 Material Model

The material used in the numerical modeling and analysis of the coupon specimen was modeled as elastic-plastic behaviour based on test data obtained from coupon tests.

6.3.2 Finite Element Mesh

The element used in this model was C3D20R, which was also used in pipe model. A uniform mesh using 2 mm global seed was used for this coupon model as shown in Figure 6. 2

6.3.3 Boundary and Loading Conditions

The nodes of one end of the coupon specimen were constrained from all rotational and translational degrees of freedom to simulate the real test condition. The nodes on other end (right end) of the coupon specimen had one translation degree of freedom in axis-1 ($u_1 \neq 0$) only (Figure 6.2).

The load was applied by displacing the right end nodes of the coupon specimen in the axis-1. A total 16.5 mm displacement was applied in one step, the way the test specimen was loaded. On average, this is the elongation when rupture occurred in the coupon specimen.

6.3.4 Failure Model

The shear failure model was used to identify fracture in the coupon finite element model. This shear failure model is based on the value of the equivalent plastic strain at element integration points. A failure in the pipe specimen is assume to occur when the damage parameter (ω) exceeds 1. The damage parameter (ω) is defined as

$$\omega = \frac{\bar{\varepsilon}_0^{pl} + \sum \Delta \bar{\varepsilon}^{pl}}{\bar{\varepsilon}_f^{pl}} \tag{6.1}$$

where, $\bar{\varepsilon}_0^{pl}$ is initial equivalent plastic strain, which is zero for both pipe and coupon specimens since, these specimens had no previous plastic strain, $\Delta \bar{\varepsilon}^{pl}$ is an increment of the equivalent plastic strain, and therefore, $\sum \Delta \bar{\varepsilon}^{pl}$ is equivalent plastic strains accumulated during whole loading path, and $\bar{\varepsilon}_f^{pl}$ is the equivalent plastic strain at failure that is determined from analysis of coupon model.

The failure model is available in ABAQUS/Explicit, and it is not available in ABAQUS/Standard. However, to use this model in ABAQUS/Standard the coupon test was modeled using ABAQUS/Standard. The equivalent plastic strain at failure ($\bar{\varepsilon}_f^{pl}$) of a coupon specimen was obtained by taking the value of equivalent plastic strain at 16.5 mm displacement in axis-1, which was found from the coupon specimens at its rupture. In the coupon test model, there is no initial plastic deformation, and thus the value of $\bar{\varepsilon}_0^{pl}$ in Equation (6.1) is zero. Because the increment of the equivalent plastic strain ($\Delta \bar{\varepsilon}^{pl}$) increased monotonically, the summation of increment of the equivalent plastic strain ($\sum \Delta \bar{\varepsilon}^{pl}$) is equal to equivalent plastic strain ($\bar{\varepsilon}^{pl}$). Therefore, failure occurs when the equivalent plastic strain ($\bar{\varepsilon}^{pl}$) equals the equivalent plastic strain at failure ($\bar{\varepsilon}_f^{pl}$).

The load-deformation plots from both the coupon test and the numerical model are shown in Figure 6.3 In these plots point F indicates the failure (rupture) point at 16.5 mm elongation. The main objective of modeling and analyses coupon test was to determine

the equivalent plastic strain at failure ($\bar{\varepsilon}_f^{pl}$) which could not be obtained from laboratory coupon tests. The equivalent plastic strain at point F (rupture point) was found 1.22 from the numerical model of the coupon test as shown in Figure 6.4. This value is considered as equivalent plastic strain at failure. Hence in the parametric study, which will be discussed in next chapter, the equivalent plastic strain 1.16 will be considered as equivalent plastic strain at failure.
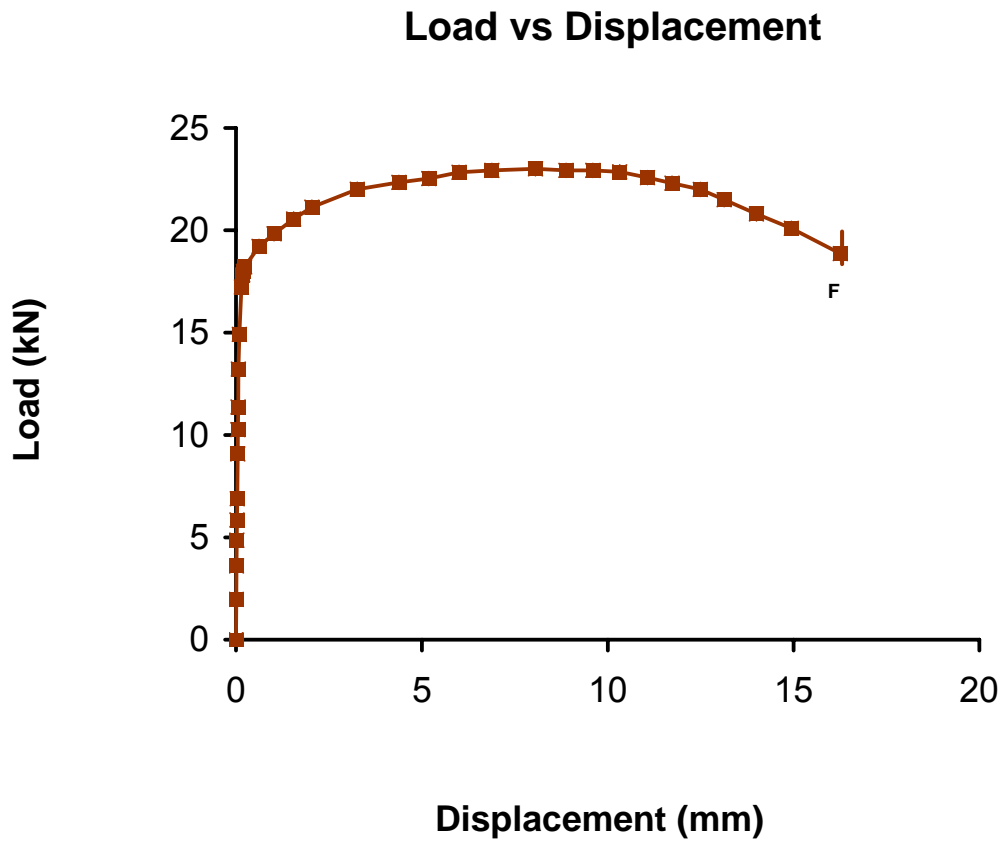
Load vs Displacement

Figure 6.1 Typical load vs. displacement plot for a tension coupon specimen
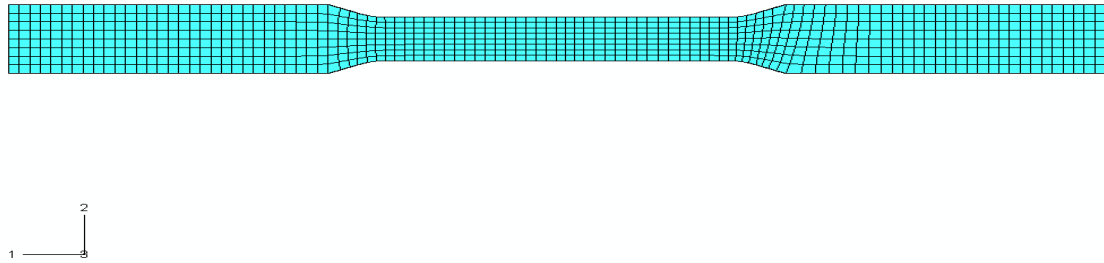
Figure 6.2 Finite element mesh of ABAQUS/Standard analysis model
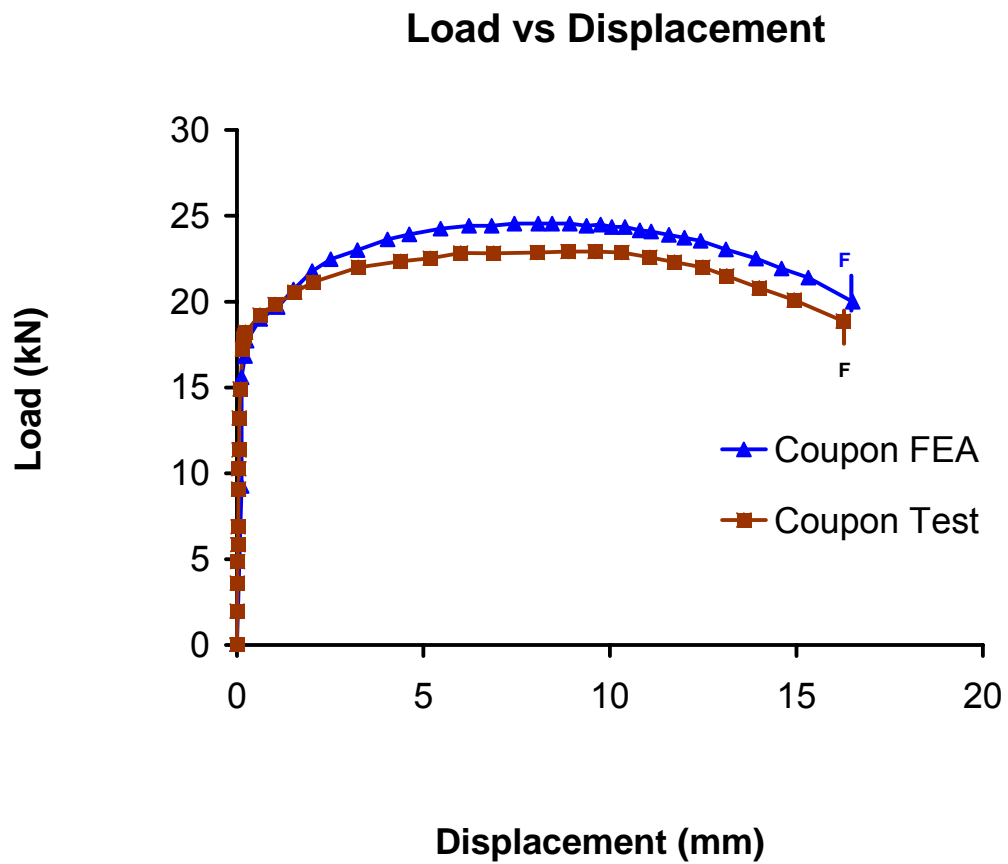
Load vs Displacement

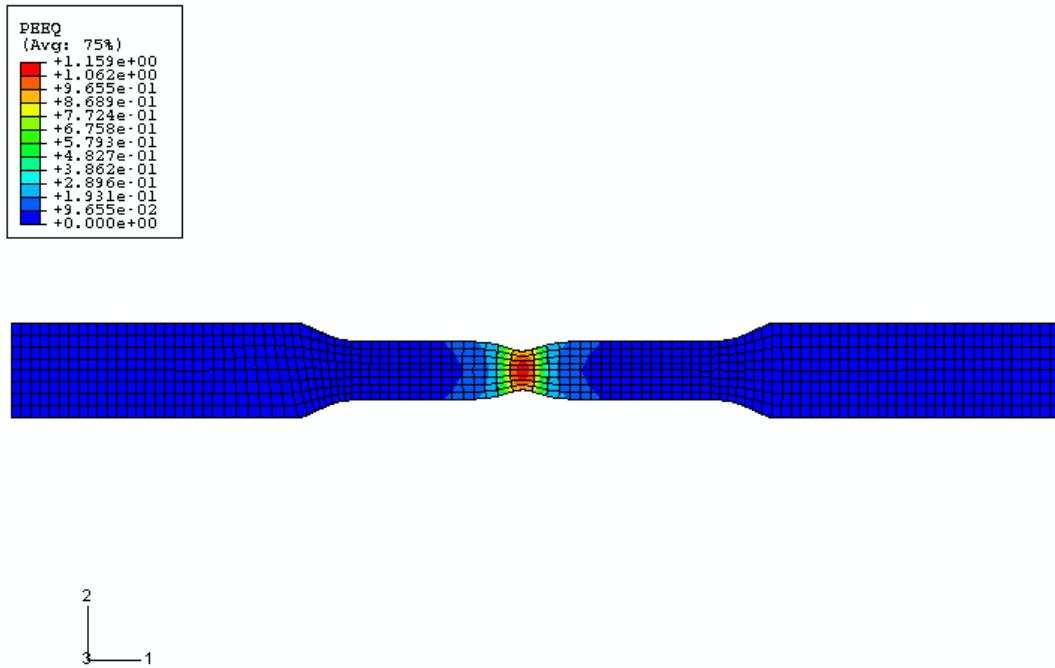Figure 6.3 Load vs. displacement plots (Test and FEA) for a tension coupon specimen

Figure 6.4 Deformed finite element analysis model and equivalent plastic strain at rupture

7 Parametric Study
7.1 General

As described in Chapter 5 and Chapter 6, a finite element (FE) model which is able to simulate and predict accurately the load-deformation behaviors of corroded energy pipe has been developed and validated. In the experimental program the first eight specimens were loaded until the load capacity of the specimens reached to ultimate load point U (Figure 3.16) and then dropped to 30% to 40% of ultimate load (upto 10 mm to 15 mm total deformation). The Last two specimens (RP40d25 and RP40d50) were loaded until the axial deformations reach to 30 mm to 45 mm in an attempt to investigate the failure mode (rupture or severe wrinkle deformation) the pipe specimens. It was observed that despite of this large deformation, these pipe specimens did not rupture, rather the inside walls of the pipe at the corrosion location came into contact. Although the pipe did not rupture, when the inside wall of the pipe at corrosion location comes into contact it may cause other problems, such as maintenance problem. Therefore this can be defined as a deformation failure. It is not realistic to expect that every pipeline segment will fail due to this kind of deformation and will not experience other failure mode such as rupture. However, an experimental study on every pipeline segment having different size of corrosion defect and level of internal pressure is expensive and time consuming. Therefore, a full spectrum parametric study was performed using the FE model to asses (i) the load-deformation behaviour and P_U under axial deformation and constant internal pressure, and, (ii) failure modes for pipelines having corrosion of various dimensions and subjected to axial monotonic deformation and various internal pressures. This chapter presents the parameters chosen and the results obtained from the parametric study.

7.2 Parameter
7.2.1 Parameter Selection

Including the control specimens (specimen that has no corrosion defect) a total of 65 parametric models were analyzed to investigate the effect of various key parameters on

the load deformation behaviour and the failure mode of the corroded X46 pipe under monotonic axial compressive load and constant internal pressure. The geometry and material properties for these specimens will be the same as the specimens used in the experimental program that is all the model will have the material property of the steel API 5L X46 grade and D/t ratio of 34. As discussed in section 3.4 of Chapter 3, it is considered that circumferential extent of the corrosion has greater effect on the strength of the corroded pipe subjected to axial compression and bending moment (Roy et al. 1997, Cosham and Hopkins, 2004). Therefore, circumferential dimension of the corrosion defect is one of the prime parameter that is chosen to be varied in this study. The depth of the corrosion (d) is another parameter that has significant effect on the load deformation behaviour of the corroded pipe under combined axial compressive load and internal pressure and therefore, it is chosen as another key parameter for this parametric study. It is also decided to investigate the effect of internal pressure on the load deformation behaviour and the failure mode of this particular kind of line pipe having varying shape and depth of corrosion.

7.2.2 Parameter Range Selection

Under the field operation condition, the level of the internal pressure in the oil and gas pipelines can range from zero to the maximum operation pressure which is usually $0.8p_y$ as indicated in the current design standards. Usually highest internal pressure occurs immediately downstream of the pump station while the lowest internal pressure which is nearly zero can be found immediately upstream of the pump station. The internal pressure is controlled by the maximum hoop stress allowed to develop in the pipeline. The hoop stress is limited to a portion design factor, F to the Specified Minimum Yield Stress (SMYS). According to current design standard, the maximum value of this design factor, F is 0.8. (CSA-Z662-07, 2007). The internal pressure can be calculated by the equation listed in Equation 3.4 Thus, for this study, the highest value of the internal pressure ratio is chosen as 0.8. The lowest internal pressure could be almost zero. Hence, the lowest limit of the internal pressure ratio was chosen as zero.

186

Three values of *d/t,* 0.25, 0.40, and 0.50 are chosen in this parametric study. In the experimental program it was found that the top end plate of the pipe specimen rotated about two major axes namely axis-1 and axis-2 due to unsymmetrical geometric condition caused by the corrosion defect (Figure 3.8 and Figure 5.3). During the test these rotation values were captured using two rotation meters and it was found the corrosion depth had the most significant effect on this top end plate rotation. Although the end rotation varied with the other two parameters, circumferential dimension of the corrosion (L_C) and internal pressure (p) but this variation was not very significant .Therefore, in this parametric study the rotation of the top end plate of the pipe specimen varies as a function of corrosion depth (*d*) and axial displacement of the top end plate. Since the experimental program was carried out with two different *d/t* values, 0.25 and 0.50, the amounts of the end plate rotation were available for these two values of *d/t*. These values are used in the parametric study for the specimens having d/t ratio 0.25 and 0.50 and varying internal pressure and circumferential dimension of the corrosion. Another value of d/t ratio 0.40 is chosen for the parametric study so that the corresponding top end plate rotation was interpolate from the other two values of *d/t*.

In the parametric study the circumferential dimension of the corrosion (L_C) is chosen such that the ratio, L_C / L_A has the values of 1, 1.75, 3.5 and 5.25. Here L_A is the axial dimension of the corrosion which remains to be constant as 50 mm. In the experimental program two L_C / L_A values, 1 and 3.5 were used. In the parametric study two additional L_C / L_A values, 1.75 and 5.25 are included so that each value differs by 1.75 from its previous value of L_C / L_A. The detail values of the key parameters used in this study is given in Table 7.1.

7.3 Designation of the Specimen in Parametric Study

Like the designation of the specimen in experimental program described in section 3.10, each of the specimens in the parametric study has also been given a designation as shown in Table 7.1. The first letter of the specimen name was given according to L_C / L_A ratio.

For L_C/L_A equal to 1, 1.75, 3.5 and 5.25 the first letter of the specimens are S, T, R and M, respectively. The next three characters indicate the level of internal pressure (% of p_y) and the last three characters indicate the dimension of corrosion depth (% of actual pipe thickness t) and these characters are interpreted exactly as the experimental program. For example, for specimen SP20d25, the first character (S) indicates that for this specimen L_C/L_A, ratio is 1; next three characters ($P20$) indicate that the internal pressure is 20% of p_y, and the last three characters ($d25$) indicate that the depth of corrosion d is 25% of actual pipe thickness t (5 mm).

7.4 Results of the Parametric study

Once all the analyses for the 65 pipe models were completed for the parametric study, the necessary data (information) was collected and summarized as shown in Tables 7.1 and 7.2 and the effects of the different p/p_y ratios, d/t ratio and L_c/L_A on ultimate net load and damage parameter were examined. The effects of the different p/p_y ratios, d/t ratio, and L_c/L_A on the Maximum Equivalent Plastic Strain (MEP) strains ($\bar{\varepsilon}_{max}^{pl}$) at contact were also determined. The influences of these parameters are presented in the graphic forms later in this chapter.

7.4.1 Variation in Maximum Net Load

In the parametric study the maximum (ultimate) net load variation was analyzed for (a) various internal pressures (p) such as $0\,p_y$, $0.20\,p_y$, $0.40\,p_y$, $0.60\,p_y$, and $0.80\,p_y$, and for (b) various $\dfrac{L_C}{L_A}$ ratios where the value of this ratio varied as 1, 1.75, 3.5, and 5.25. To investigate the effect of corrosion depth on the maximum net load the (c) depth of corrosion (d) was varied as $0.25t$, $0.40t$, and $0.50t$. The effect of these parameters (internal pressure, circumferential dimension of corrosion, and depth of corrosion) on the maximum net load (P_U) will be discussed in this section.

7.4.1.1 Effect of Pressure on Maximum Net Load

By examining Figures 7.1 to 7.3, it can be seen that for a particular *d/t* ratio, and for a specific $\frac{L_C}{L_A}$ the maximum net load (P_U) decreases with increasing internal pressure (*p*). This observation is similar to that observed from the experimental program where the maximum net load also decreased with increased internal pressure.

7.4.1.2 Effect of Circumferential Dimension of Corrosion (L_C) on Maximum Net Load

By examining Figures 7.4 to 7.8, it can be seen that for a particular *d/t* ratio, the maximum net load (P_U) decreases with increasing $\frac{L_C}{L_A}$ ratio. This observation is similar to that observed from the experimental program where the maximum net load also decreased with increased circumferential dimension of the corrosion. For a particular *d/t,* value rate of reduction in maximum net load with increasing $\frac{L_C}{L_A}$ ratio is more or less constant and when *d/t* is 0.50, the rate of reduction is sharper/ steeper than the other two values of d/t ratio. This observation is also confirmed from the plots shown in Figures 7.4 to 7.8 where each plot shows the variation in maximum net load (P_U) with $\frac{L_C}{L_A}$ for a specific *d/t* value and a constant internal pressure (*p*).

7.4.1.3 Effect of Corrosion Depth on Maximum Net Load

Like experimental program it can be observed from the parametric study that for a particular level of internal pressure the maximum net load capacity (P_U) decreases with increasing corrosion depth. The effects of corrosion depth on maximum net load for different levels of internal pressure are shown in Figures 7.9 to 7.13. From these figures, it can be observed that there is a sharper rate of reduction of maximum net load (P_U)

when the circumferential dimension ($\frac{L_C}{L_A}$) and depth of corrosion (d/t) has the highest

value i.e. when $\frac{L_C}{L_A}$ is 5.25 and d/t is 0.50.

7.4.2 Failure Mode

For all sixty models (excluding five control specimens), the deformations were applied in such a way that a failure criterion could be established. Two modes of failure were observed in this parametric study namely as i) rupture failure and ii) deformation failure. Rupture failure occurs when the maximum equivalent plastic (MEP) strain at any integration point of a finite element of pipe model reaches the maximum equivalent plastic strain at failure. This maximum equivalent plastic strain at failure was determined by the numerical simulation of coupon test using ABAQUS/Standard. As discussed in section 6.3.4 the maximum equivalent plastic strain at failure was determined 1.16. Hence, when the MEP strain ($\bar{\varepsilon}_{\max}^{pl}$) of an integration point of the pipe specimen reaches the value 1.16 the specimen is assumed to be failed in rupture. To be conservative the value of MEP strain ($\bar{\varepsilon}_{\max}^{pl}$) is taken as 1.10 for rupture failure. Another mode of failure observed during the parametric study was deformation failure. When the inside wall of the wrinkle comes into contact (before rupture) during the load-deformation path of the pipe specimen, it is assumed to be failed in contact and this type of failure is considered to be a deformation failure. Irrespective of failure mode (contact or rupture), all the FE models were run until contact in the inside wall occurred. To determine the effect of different test parameters on modes of failure the MEP strain ($\bar{\varepsilon}_{\max}^{pl}$) at contact for all 60 pipe specimens were recorded and shown in Table 7.2. If the value of MEP strain at contact is greater than the MEP strain ($\bar{\varepsilon}_{\max}^{pl}$) at failure (1.10), the pipe specimen is assumed to fail in rupture. If it is less than 1.10, the deformation failure is assumed to be occurred. In Table 7.2 the rupture failure is denoted by R and deformation failure is denoted by D. The broken horizontal lines in all the figures (Figure 7.14 to 7.24), is the limit between the two failure modes.

190

7.4.2.1 Effect of Pressure on Failure Mode

The sensitivity of models to the p/p_y ratio can be observed simply by plotting the MEP strain at contact ($\bar{\varepsilon}_{C\max}^{pl}$) as a function of the p (% of p_y) for a particular d/t ratio. Figure 7.14 to Figure 7.16 present effect of p/p_y ratio on MEP strain ($\bar{\varepsilon}_{\max}^{pl}$) at contact for different d/t ratios. From these plots, it can be seen that generally the MEP strain at contact decreased as with increasing internal pressure p (% of p_y) for a particular d/t ratio. This indicates that the increased internal pressure could prevent the rupture failure by increasing the chance of deformation failure due to contact of the inside wall of the wrinkle. The rate of reduction is almost constant for a particular $\dfrac{L_C}{L_A}$ ratio when d/t value is 0.25 (Figure 7.14). When d/t values are 0.4 and 0.5, for a particular $\dfrac{L_C}{L_A}$ ratio, the rate of reduction in MEP strain ($\bar{\varepsilon}_{\max}^{pl}$) at contact increases with increasing internal pressure.

7.4.2.2 Effect of Circumferential Dimension of Corrosion (L_C) on Failure Mode

From Figures 7.17, 7.18, and 7.19, it could be can observed that the MEP strain ($\bar{\varepsilon}_{\max}^{pl}$) at contact decreases with increasing $\dfrac{L_C}{L_A}$ ratio. This rate of reduction is higher at the transition of square shape corrosion ($\dfrac{L_C}{L_A} = 1$) to rectangular shape corrosion ($\dfrac{L_C}{L_A} = 1.75$) and for other rectangular shape corrosion ($\dfrac{L_C}{L_A} > 1.75$) this rate of reduction is almost same for different $\dfrac{L_C}{L_A}$ ratios provided that the level of internal pressure ratio (p/p_y) and d/t ratio are the same.

7.4.2.3 Effect of Corrosion Depth on Failure Mode

From Figures 7.20 to 7.24, it could be found that the MEP strain ($\bar{\varepsilon}^{pl}_{max}$) at contact decreases with increasing d/t ratio for all level of internal pressure and for all $\dfrac{L_C}{L_A}$ ratios.

This indicates that for greater corrosion depth (d) the susceptibility of deformation failure (due to contact of the inside wall of the wrinkle) is also great.

7.5 Summary

After analyzing 65 numerical model of the specimens with diameter to thickness (D/t) ratio 34 it is found that:

1) The ultimate net load (P_U) decreases with increasing internal pressure, increasing circumferential dimension of the corrosion (L_c), and with increasing corrosion depth (d).

2) The maximum equivalent plastic strain at contact decreases as internal pressure increases if d/t and $\dfrac{L_C}{L_A}$ ratios are kept unchanged.

3) The maximum equivalent plastic strain at contact decreases with increasing $\dfrac{L_C}{L_A}$ ratio if d/t ratio and level of internal pressure are kept unchanged.

4) The maximum equivalent plastic strain at contact also decreases as d/t ratio increases if the lever of internal pressure and $\dfrac{L_C}{L_A}$ ratio are not changed.

Table 7.1 Summary of the parameters and ultimate net load and displacement at point U
for the parametric study

Specimen Name	Pressure (% of p_y)	$\dfrac{L_C}{L_A}$	d (%of t)	Ultimate Net Load (kN)	Displacement at point U (mm)
CP00d00	0	0	0	925.02	9.25
SP00d25	0	1	25	813.3	6.97
SP00d40	0	1	40	764	6.30
SP00d50	0	1	50	710	6.00
TP00d25	0	1.75	25	784	5.38
TP00d40	0	1.75	40	725	4.75
TP00d50	0	1.75	50	669	4.49
RP00d25	0	3.5	25	721.11	3.00
RP00d40	0	3.5	40	632.88	3.55
RP00d50	0	3.5	50	543.33	3.68
MP00d25	0	5.25	25	699.07	2.46
MP00d40	0	5.25	40	609.61	2.90
MP00d50	0	5.25	50	435	3.05
CP20d00	20			836.38	10.04
SP20d25	20	1	25	765.11	7.10
SP20d40	20	1	40	710.97	6.35

Specimen Name	Pressure (% of p_y)	$\dfrac{L_C}{L_A}$	d (%of t)	Ultimate Net Load (kN)	Displacement at point U (mm)
SP20d50	20	1	50	670.32	5.68
TP20d25	20	1.75	25	727	6.86
TP20d40	20	1.75	40	676	6.10
TP20d50	20	1.75	50	630.76	5.51
RP20d25	20	3.5	25	656.5	3.51
RP20d40	20	3.5	40	572.70	3.65
RP20d50	20	3.5	50	462.67	3.79
MP20d25	20	5.25	25	614.92	3.05
MP20d40	20	5.25	40	534.39	3.15
MP20d50	20	5.25	50	356	3.38
CP40d00	40			676	12.53
SP40d25	40	1	25	656	11.51
SP40d40	40	1	40	600	7.91
SP40d50	40	1	50	539	6.18
TP40d25	40	1.75	25	637	10.32
TP40d40	40	1.75	40	570	7.56
TP40d50	40	1.75	50	514	5.86
RP40d25	40	3.5	25	560	4.11

Specimen Name	Pressure (% of p_y)	$\dfrac{L_C}{L_A}$	d (%of t)	Ultimate Net Load (kN)	Displacement at point U (mm)
RP40d40	40	3.5	40	484	4.61
RP40d50	40	3.5	50	381	4.87
MP40d25	40	5.25	25	534.79	3.76
MP40d40	40	5.25	40	447.59	4.36
MP40d50	40	5.25	50	302	4.56
CP60d00	60			625	13.29
SP60d25	60	1	25	584.06	12.65
SP60d40	60	1	40	543.34	10.43
SP60d50	60	1	50	502	8.89
TP60d25	60	1.75	25	549.29	12.00
TP60d40	60	1.75	40	499.84	9.82
TP60d50	60	1.75	50	470	8.34
RP60d25	60	3.5	25	465.94	6.96
RP60d40	60	3.5	40	423.08	7.44
RP60d50	60	3.5	50	349	7.64
MP60d25	60	5.25	25	434.30	6.23
MP60d40	60	5.25	40	366.12	6.56
MP60d50	60	5.25	50	269	6.81

Specimen Name	Pressure (% of p_y)	$\dfrac{L_C}{L_A}$	d (%of t)	Ultimate Net Load (kN)	Displacement at point U (mm)
CP80d00	80			473	16.80
SP80d25	80	1	25	446.09	16.57
SP80d40	80	1	40	418.96	15.81
SP80d50	80	1	50	378.4	15.30
TP80d25	80	1.75	25	415.03	15
TP80d40	80	1.75	40	383	14.52
TP80d50	80	1.75	50	351.85	14.36
RP80d25	80	3.5	25	349.79	12.04
RP80d40	80	3.5	40	324	12.53
RP80d50	80	3.5	50	281.8	12.65
MP80d25	80	5.25	25	322.16	10.67
MP80d40	80	5.25	40	282.35	10.69
MP80d50	80	5.25	50	210	10.82

Table 7.2 Maximum equivalent plastic strain at contact for the parametric study

Specimen Name	Pressure (% of p_y)	$\dfrac{L_C}{L_A}$	d (%of t)	Maximum equivalent plastic strain at contact ($\bar{\varepsilon}_{max}^{pl}$)	Failure Mode
SP00d25	0	1	25	2.10	R
SP00d40	0	1	40	1.78	R
SP00d50	0	1	50	1.46	R
TP00d25	0	1.75	25	1.88	R
TP00d40	0	1.75	40	1.56	R
TP00d50	0	1.75	50	1.32	R
RP00d25	0	3.5	25	1.54	R
RP00d40	0	3.5	40	1.31	R
RP00d50	0	3.5	50	1.11	R
MP00d25	0	5.25	25	0.97	D
MP00d40	0	5.25	40	0.94	D
MP00d50	0	5.25	50	0.85	D
SP20d25	20	1	25	1.95	R
SP20d40	20	1	40	1.68	R
SP20d50	20	1	50	1.38	R
TP20d25	20	1.75	25	1.71	R
TP20d40	20	1.75	40	1.45	R

Specimen Name	Pressure (% of p_y)	$\dfrac{L_C}{L_A}$	d (%of t)	Maximum equivalent plastic strain at contact ($\bar{\varepsilon}_{max}^{pl}$)	Failure Mode
TP20d50	20	1.75	50	1.27	R
RP20d25	20	3.5	25	1.41	R
RP20d40	20	3.5	40	1.20	R
RP20d50	20	3.5	50	1.08	D
MP20d25	20	5.25	25	0.95	D
MP20d40	20	5.25	40	0.89	D
MP20d50	20	5.25	50	0.83	D
SP40d25	40	1	25	1.82	R
SP40d40	40	1	40	1.55	R
SP40d50	40	1	50	1.27	R
TP40d25	40	1.75	25	1.59	R
TP40d40	40	1.75	40	1.38	R
TP40d50	40	1.75	50	1.17	R
RP40d25	40	3.5	25	1.25	R
RP40d40	40	3.5	40	1.14	R
RP40d50	40	3.5	50	1.02	D
MP40d25	40	5.25	25	0.90	D
MP40d40	40	5.25	40	0.85	D

Specimen Name	Pressure (% of p_y)	$\dfrac{L_C}{L_A}$	d (%of t)	Maximum equivalent plastic strain at contact ($\bar{\varepsilon}_{max}^{pl}$)	Failure Mode
MP40d50	40	5.25	50	0.82	D
SP60d25	60	1	25	1.66	R
SP60d40	60	1	40	1.37	R
SP60d50	60	1	50	1.12	R
TP60d25	60	1.75	25	1.41	R
TP60d40	60	1.75	40	1.18	R
TP60d50	60	1.75	50	0.98	D
RP60d25	60	3.5	25	1.15	R
RP60d40	60	3.5	40	0.99	D
RP60d50	60	3.5	50	0.89	D
MP60d25	60	5.25	25	0.88	D
MP60d40	60	5.25	40	0.82	D
MP60d50	60	5.25	50	0.79	D
SP80d25	80	1	25	1.46	R
SP80d40	80	1	40	1.16	R
SP80d50	80	1	50	0.98	D
TP80d25	80	1.75	25	1.27	R

Specimen Name	Pressure (% of p_y)	$\dfrac{L_C}{L_A}$	d (%of t)	Maximum equivalent plastic strain at contact ($\bar{\varepsilon}_{max}^{pl}$)	Failure Mode
TP80d40	80	1.75	40	0.97	D
TP80d50	80	1.75	50	0.8	D
RP80d25	80	3.5	25	1.06	D
RP80d40	80	3.5	40	0.86	D
RP80d50	80	3.5	50	0.74	D
MP80d25	80	5.25	25	0.82	D
MP80d40	80	5.25	40	0.69	D
MP80d50	80	5.25	50	0.62	D
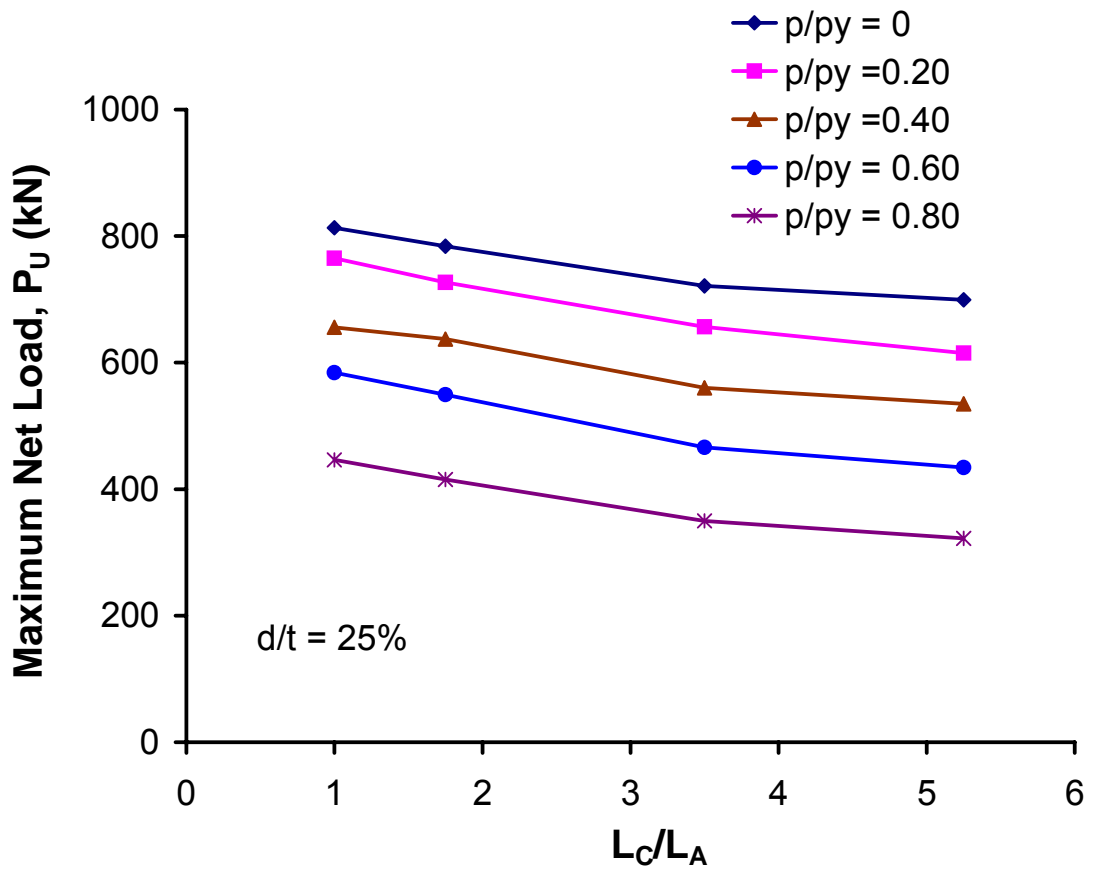
Figure 7.1 Effect of internal pressure on ultimate net load when d/t is 0.25
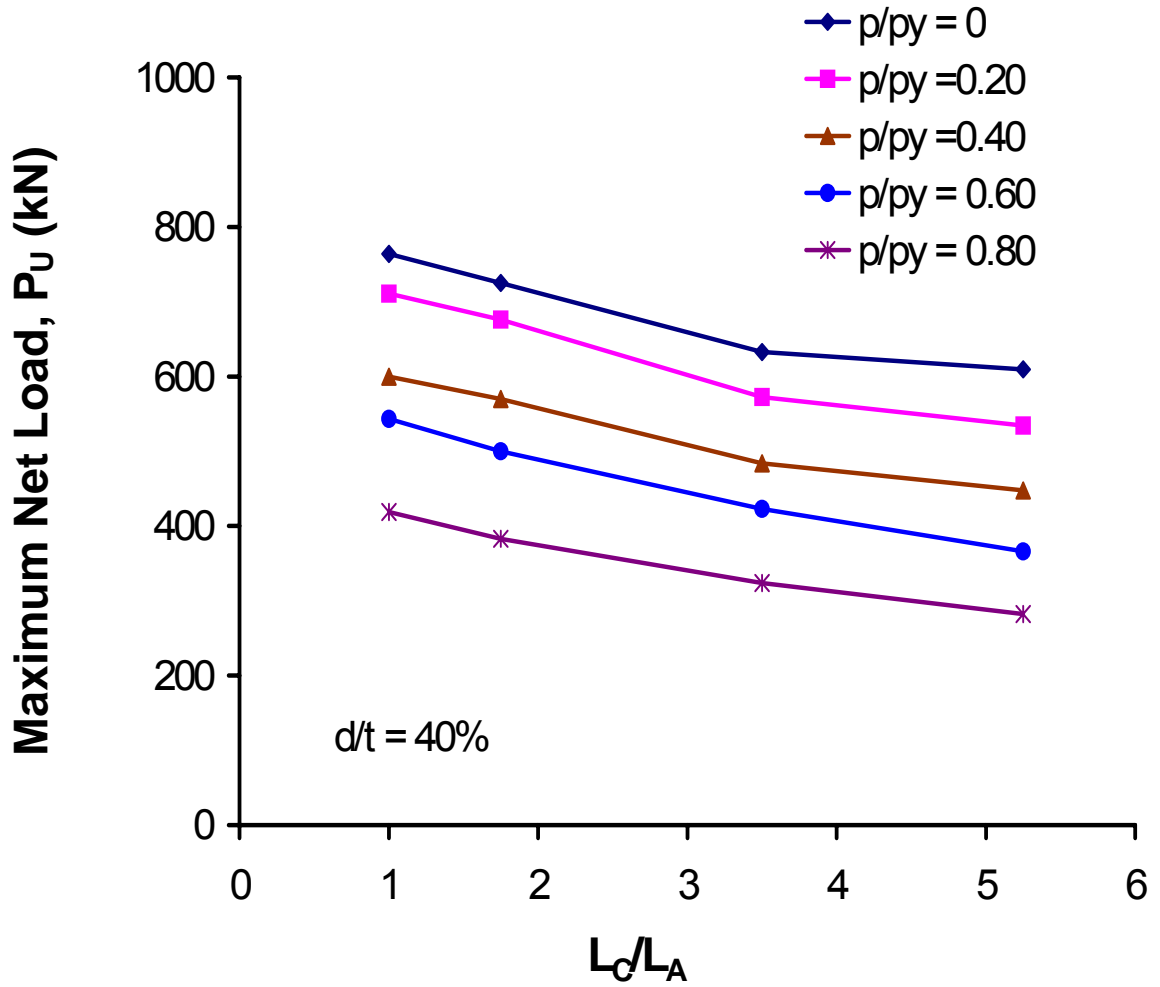
Figure 7.2 Effect of internal pressure on ultimate net load when d/t is 0.40
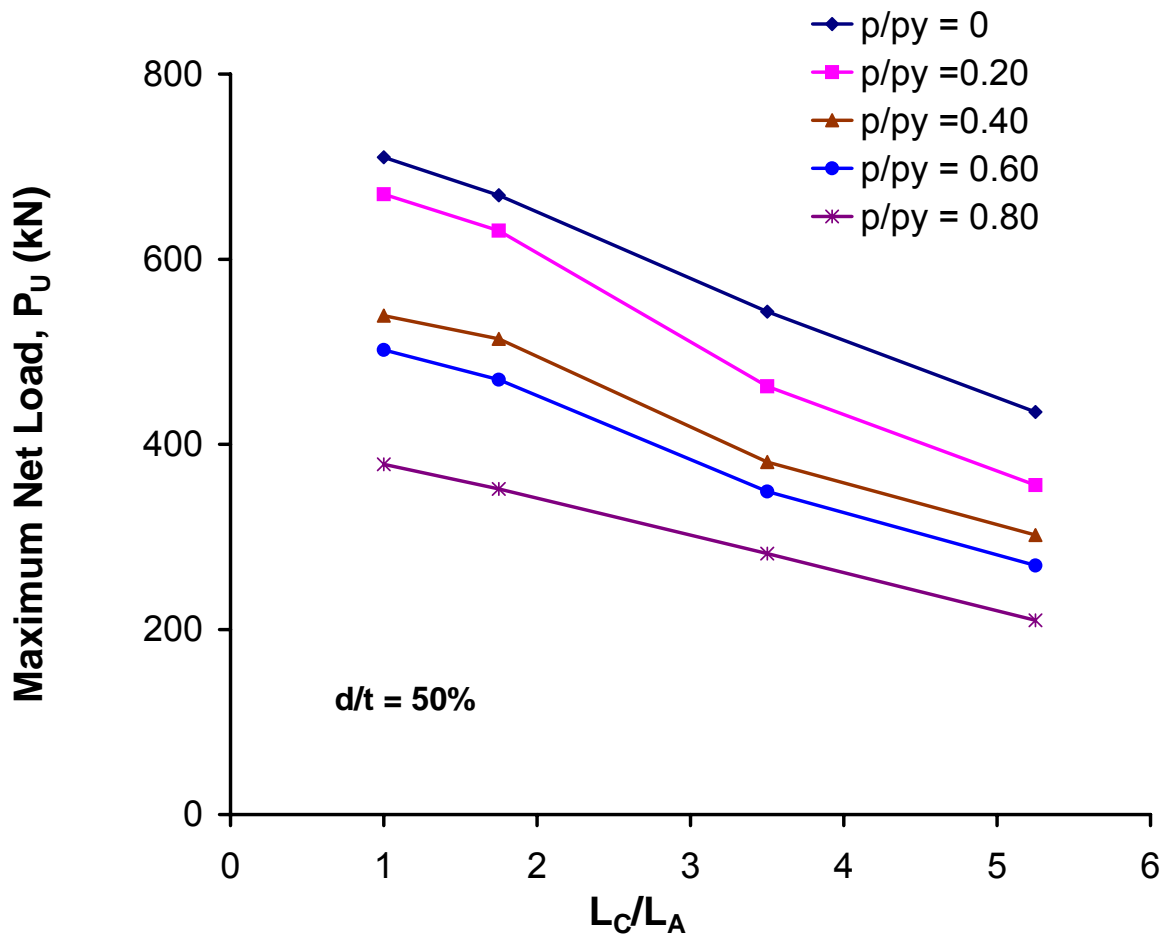
Figure 7.3 Effect of internal pressure on ultimate net load when d/t is 0.50
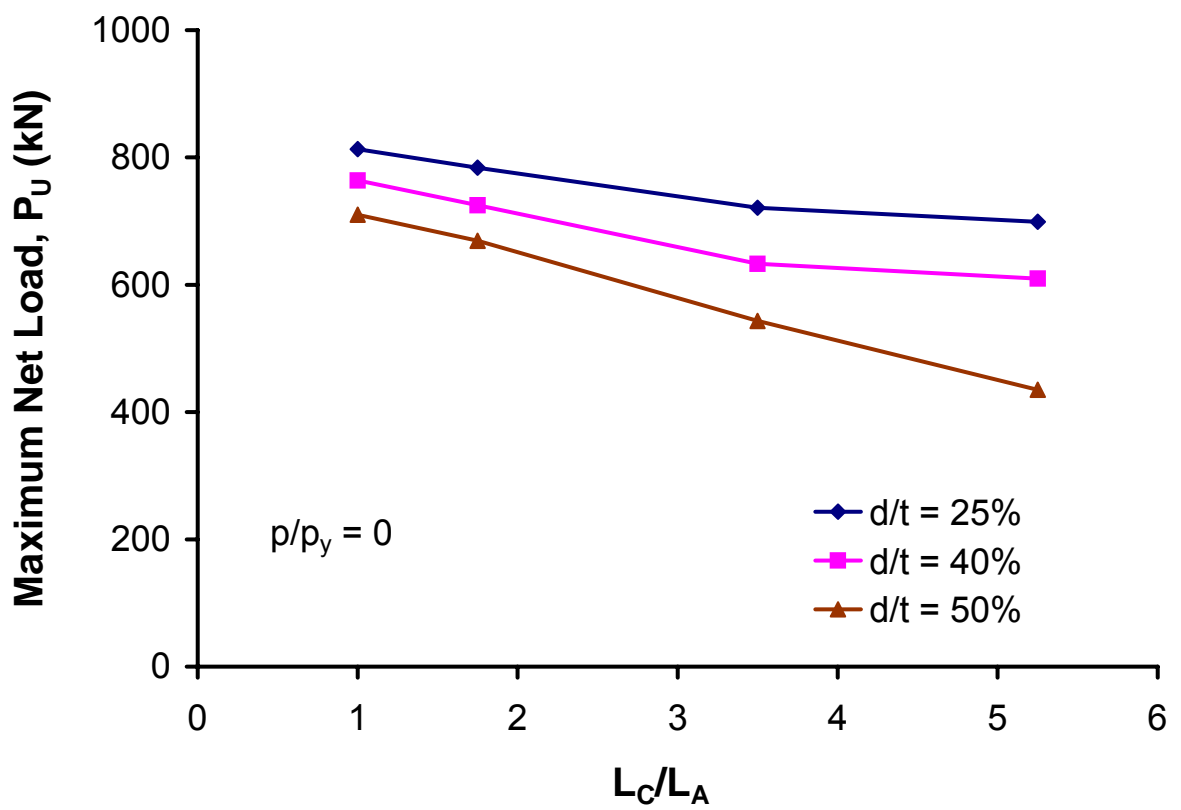
Figure 7. 4 Effect of $\dfrac{L_C}{L_A}$ on ultimate net load when p/p_y is 0
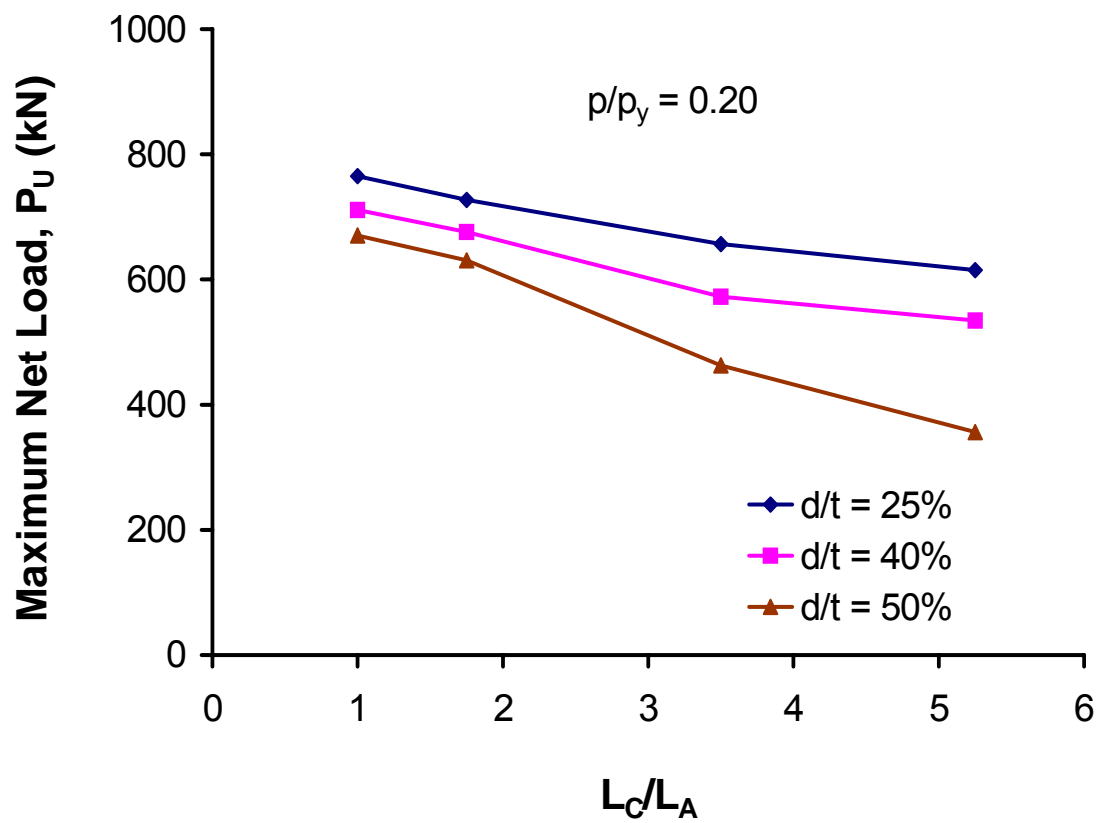
Figure 7.5 Effect of $\dfrac{L_C}{L_A}$ on ultimate net load when p/p_y is 0.20
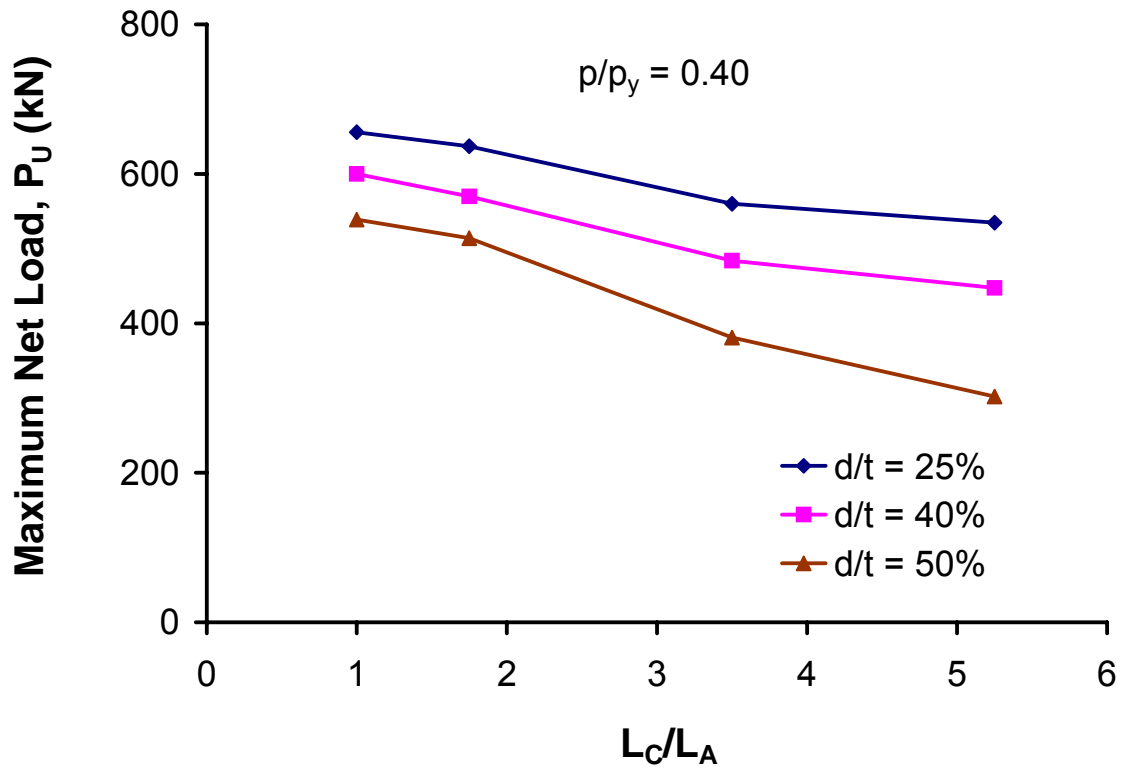
Figure 7.6 Effect of $\dfrac{L_C}{L_A}$ on ultimate net load when p/p_y is 0.40
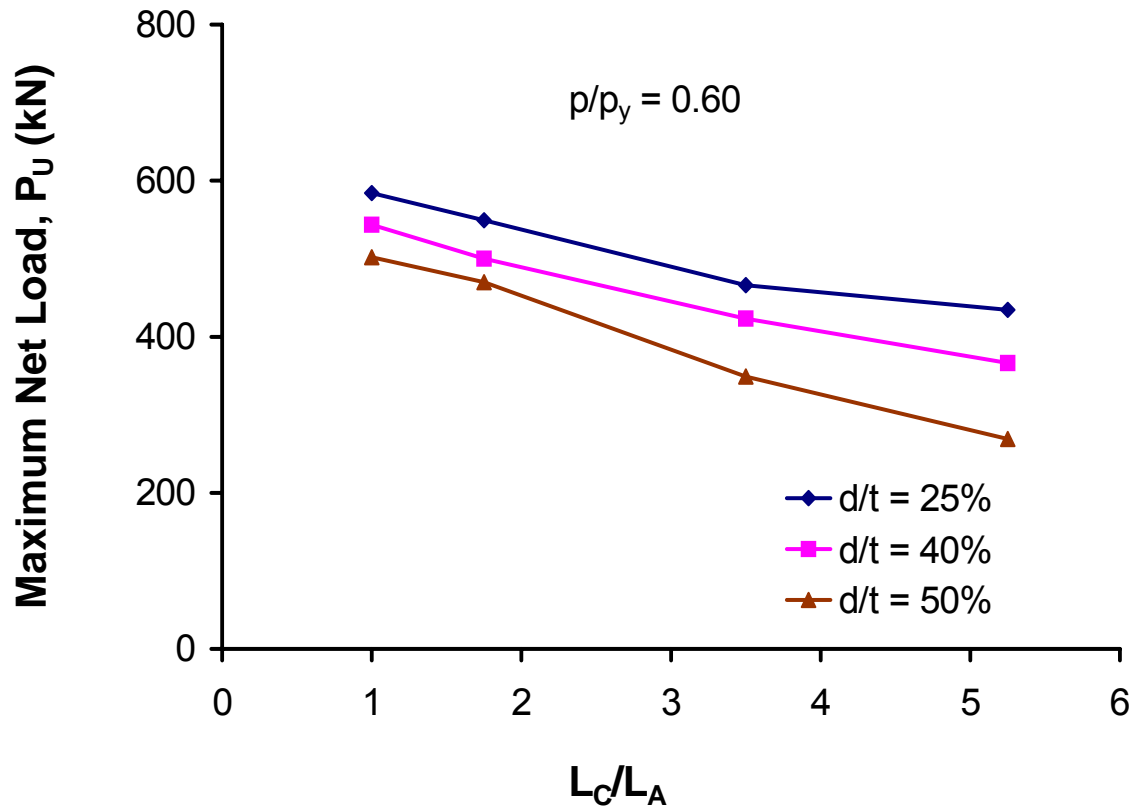
Figure 7.7 Effect of $\dfrac{L_C}{L_A}$ on ultimate net load when p/p_y is 0.60
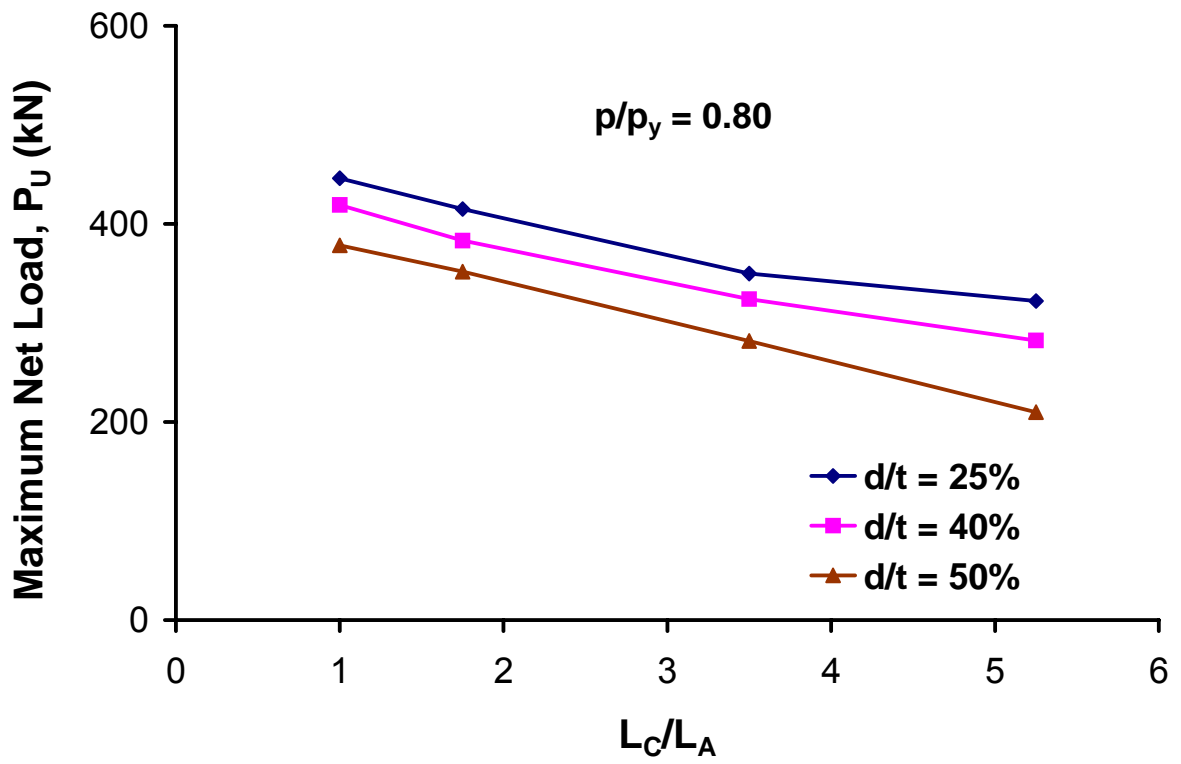
Figure 7.8 Effect of $\dfrac{L_C}{L_A}$ on ultimate net load when p/p_y is 0.80
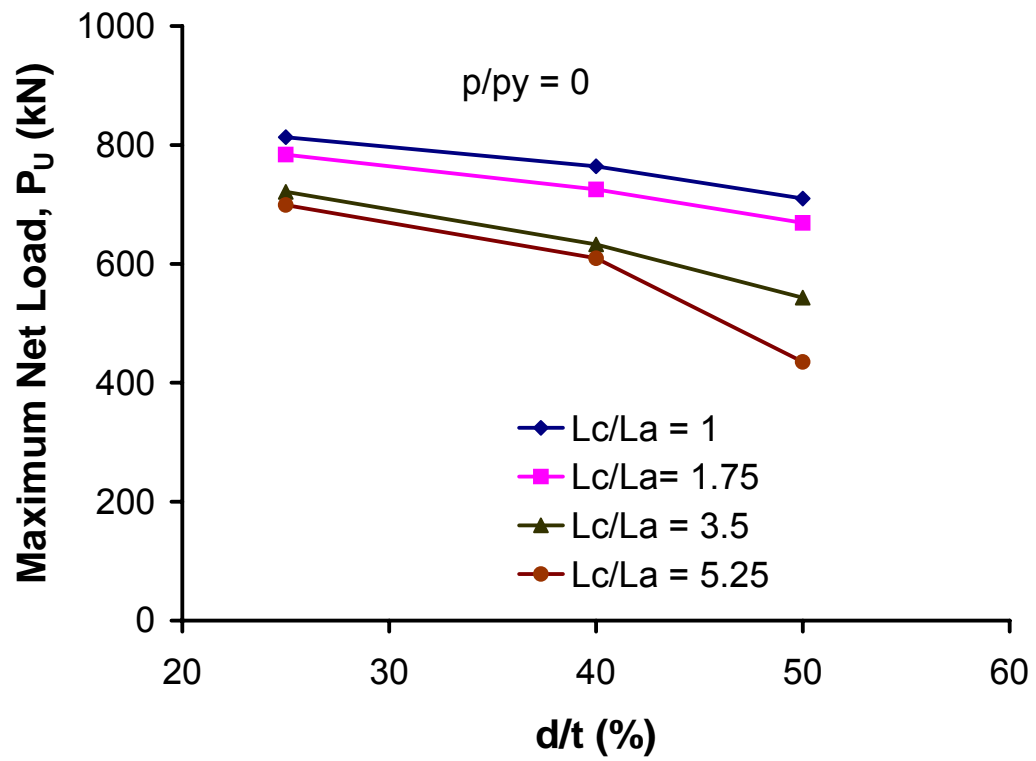
Figure 7.9 Effect of *d/t* on ultimate net load when p/p_y is 0.0
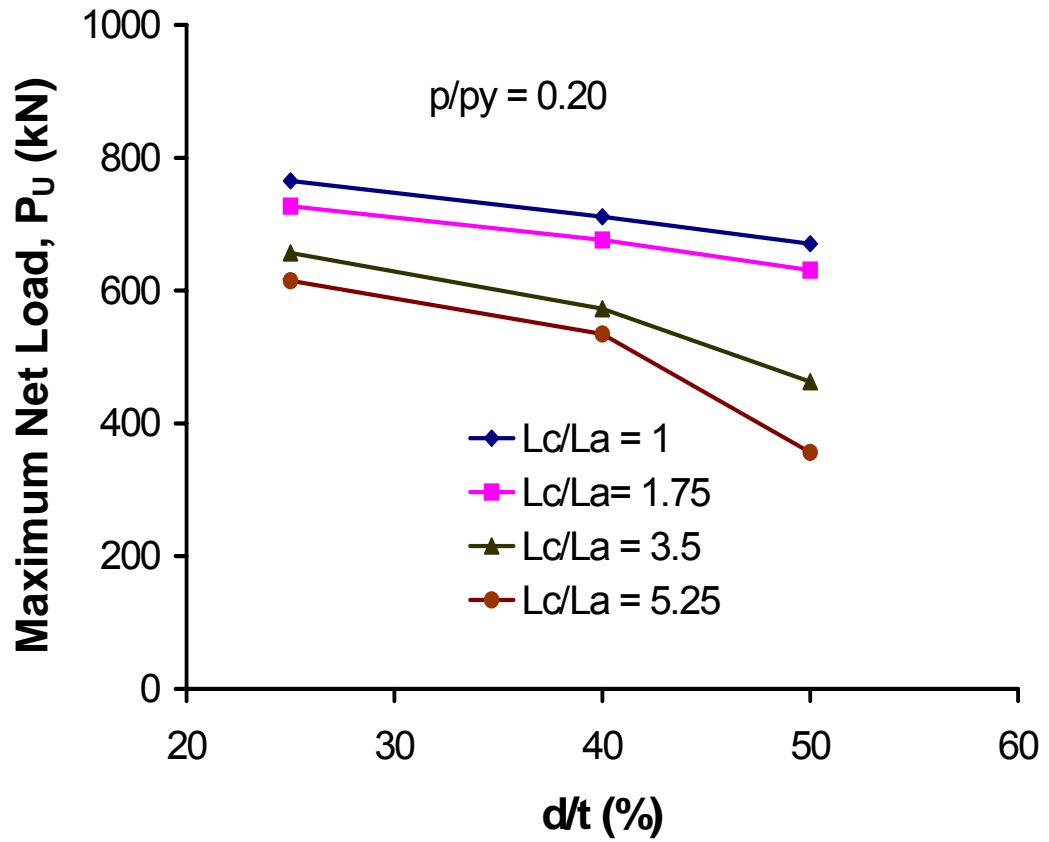
Figure 7.10 Effect of *d/t* on ultimate net load when p/p_y is 0.20
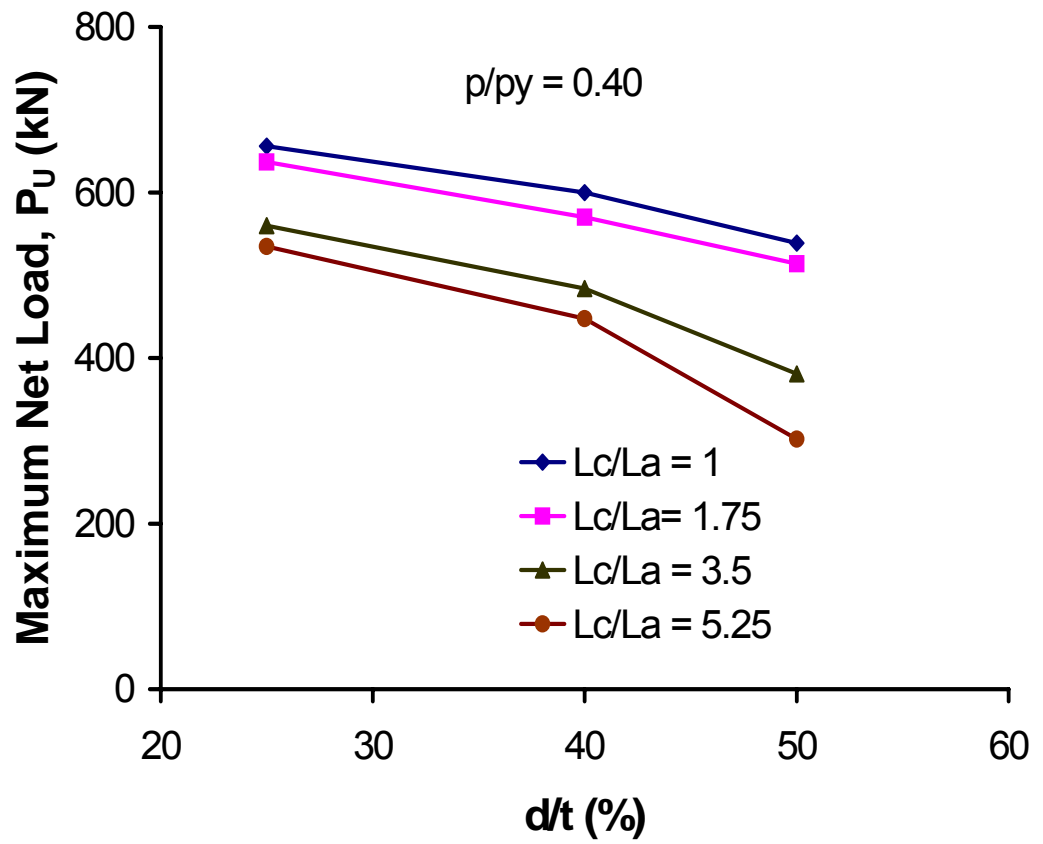
Figure 7.11 Effect of *d/t* on ultimate net load when p/p_y is 0.40
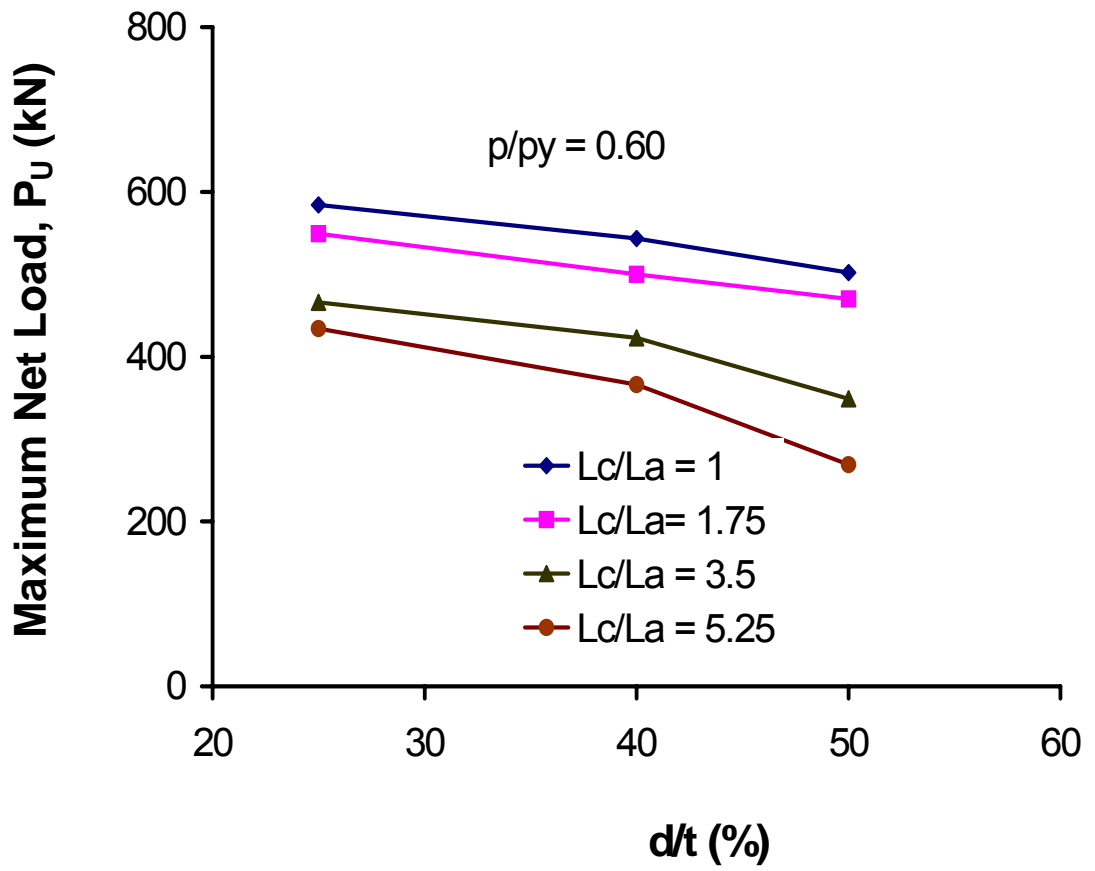
Figure 7.12 Effect of *d/t* on ultimate net load when p/p_y is 0.60
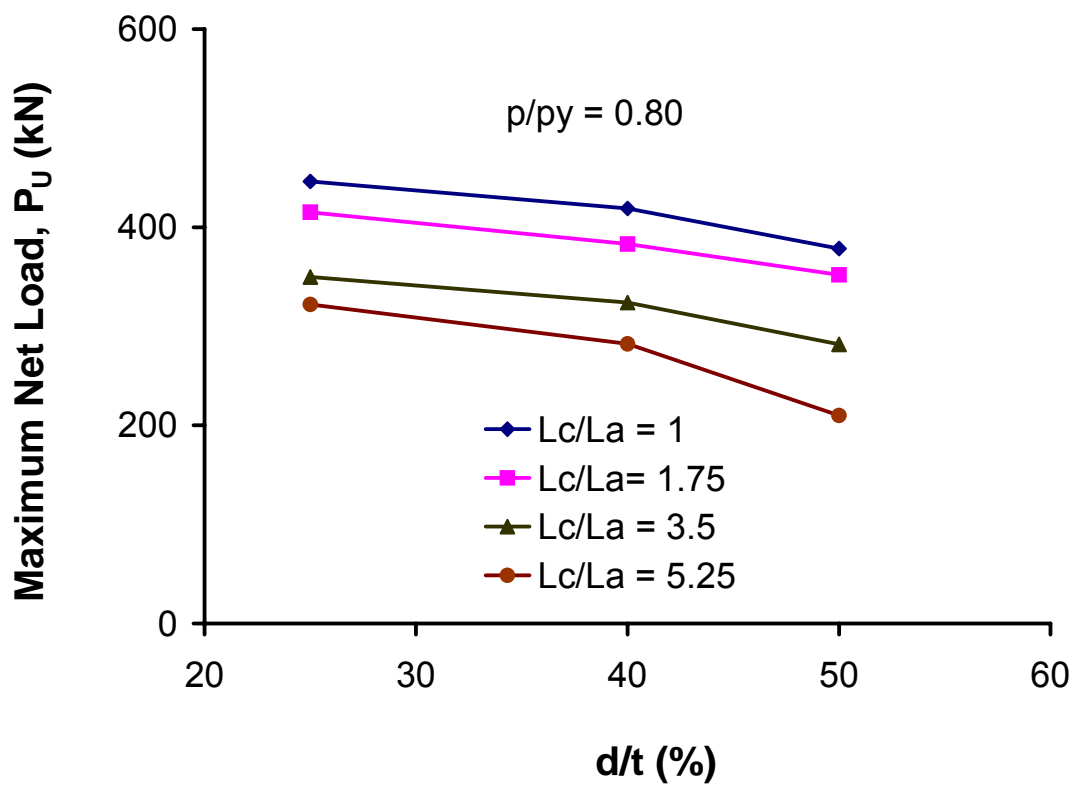
Figure 7.13 Effect of *d/t* on ultimate net load when p/p_y is 0.80
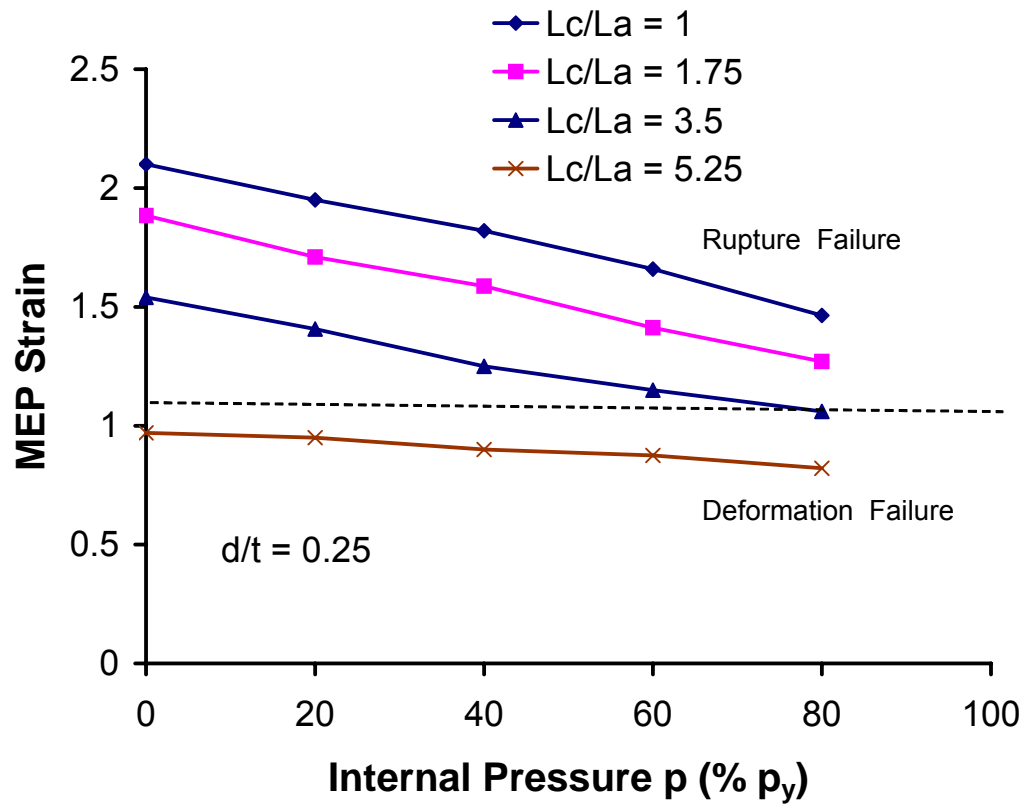
Figure 7.14 Effect of internal pressure on MEP strain when d/t is 0.25
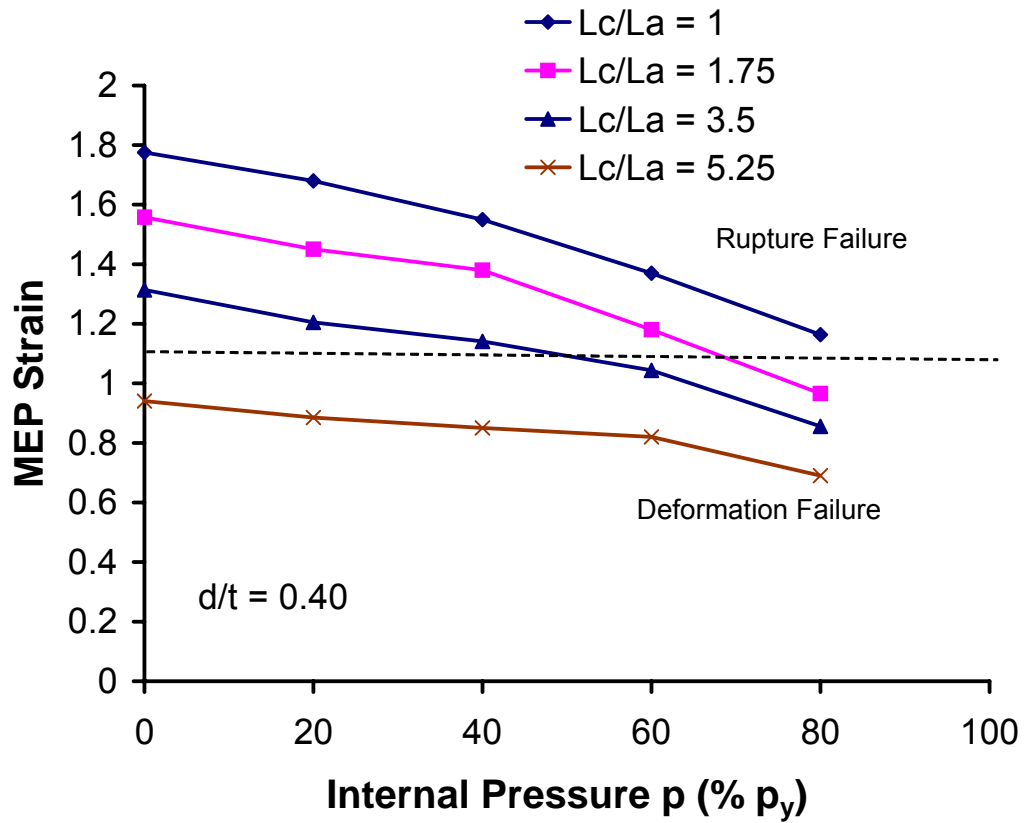
Figure 7.15 Effect of internal pressure on MEP strain when d/t is 0.40
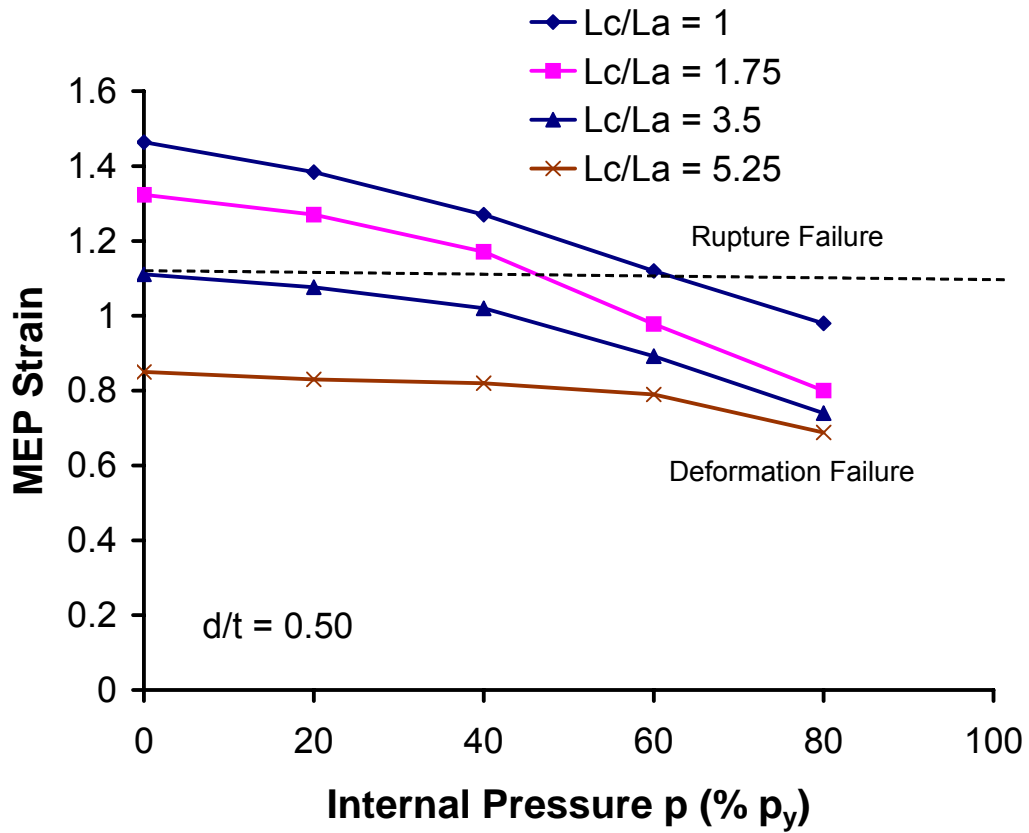
Figure 7.16 Effect of internal pressure on MEP strain when d/t is 0.50
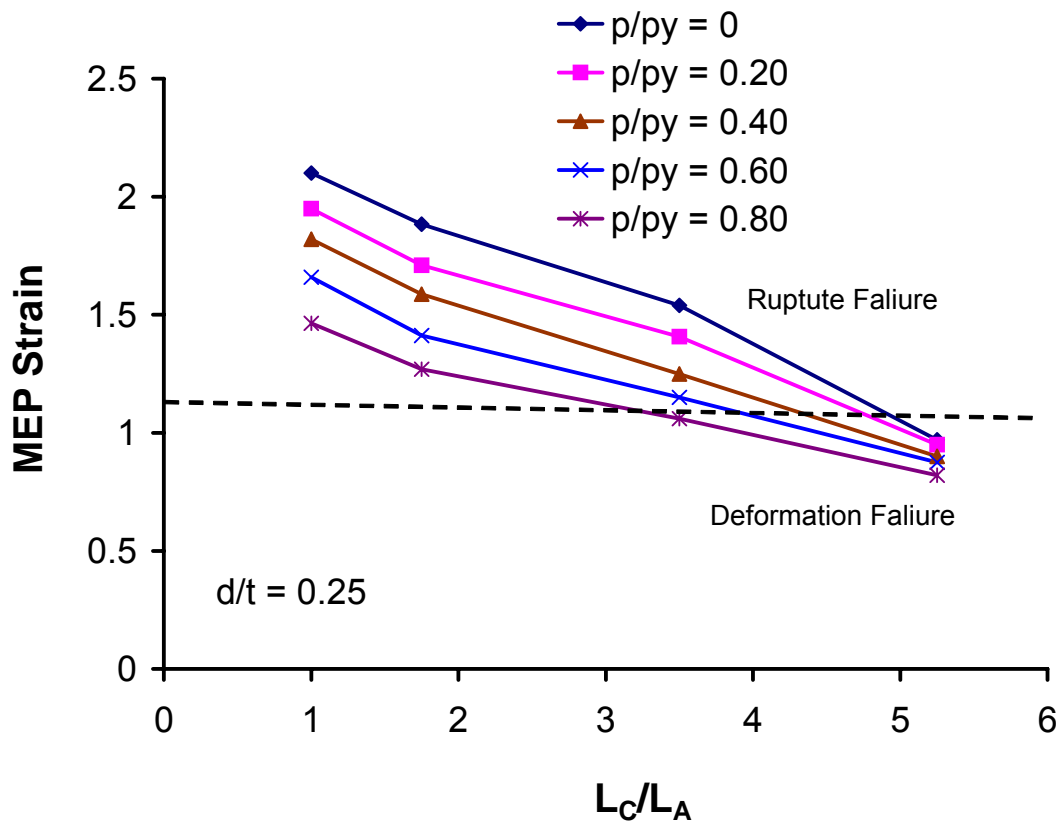
Figure 7.17 Effect of $\dfrac{L_C}{L_A}$ on MEP strain when *d/t* is 0.25
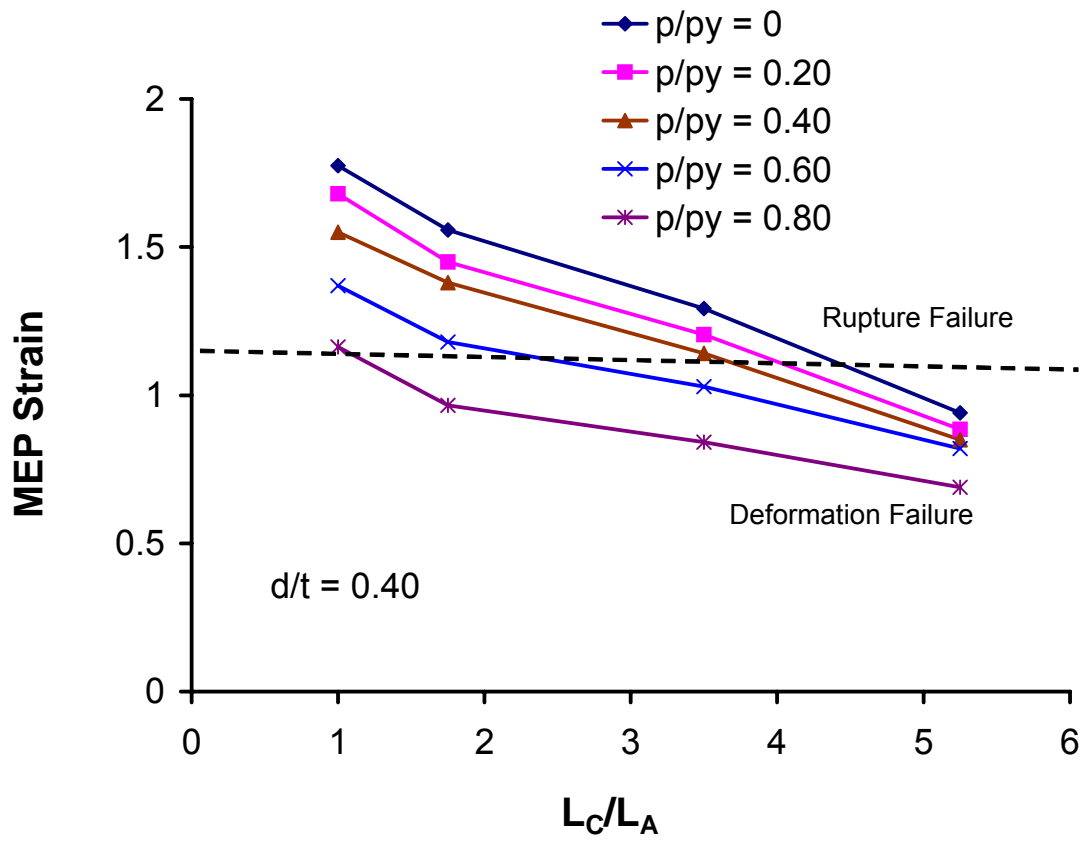
Figure 7.18 Effect of $\dfrac{L_C}{L_A}$ on MEP strain when *d/t* is 0.40
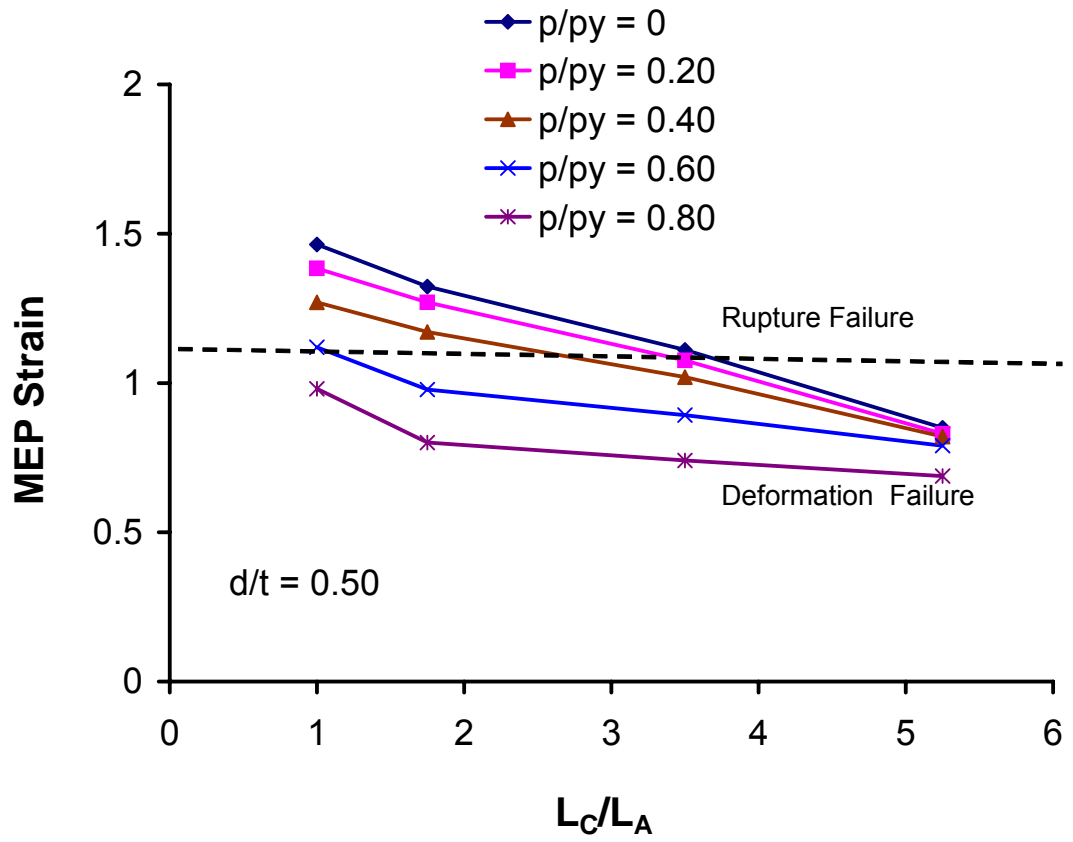
Figure 7.19 Effect of $\dfrac{L_C}{L_A}$ on MEP strain when d/t is 0.50
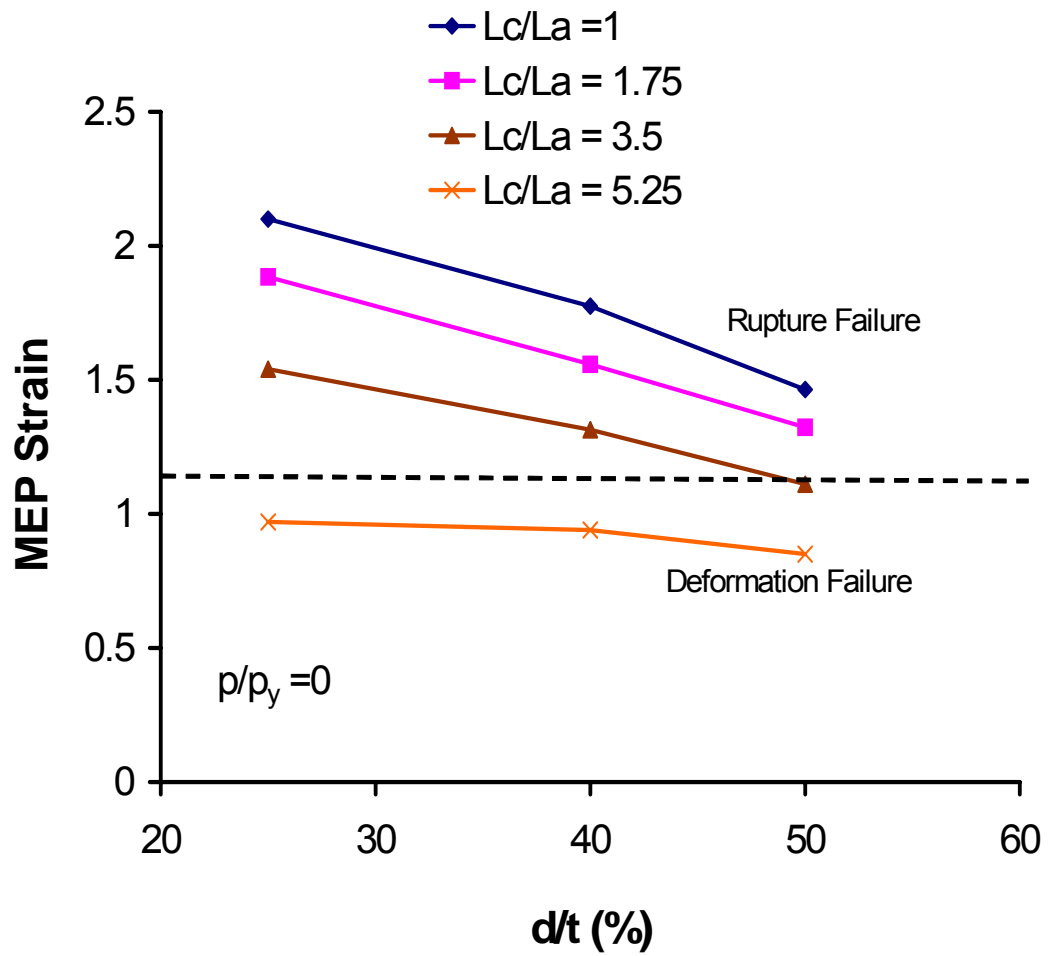
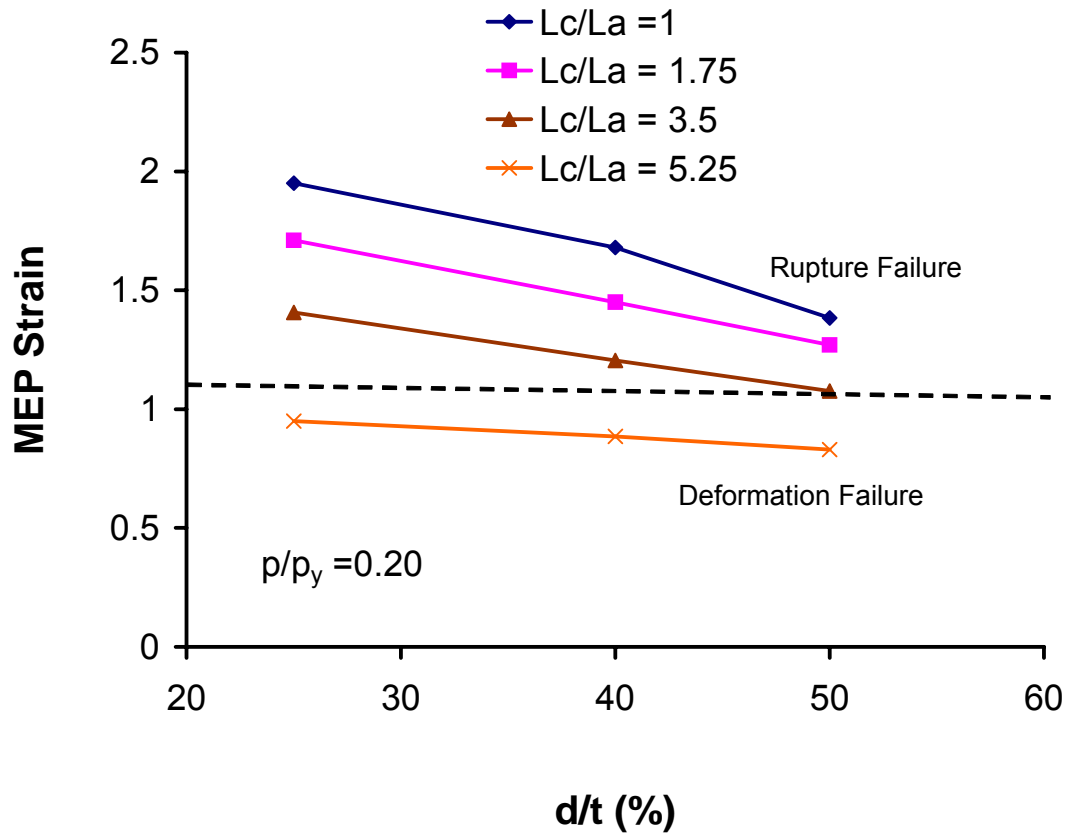Figure 7.20 Effect of *d/t* on MEP strain when p/p_y is 0.0

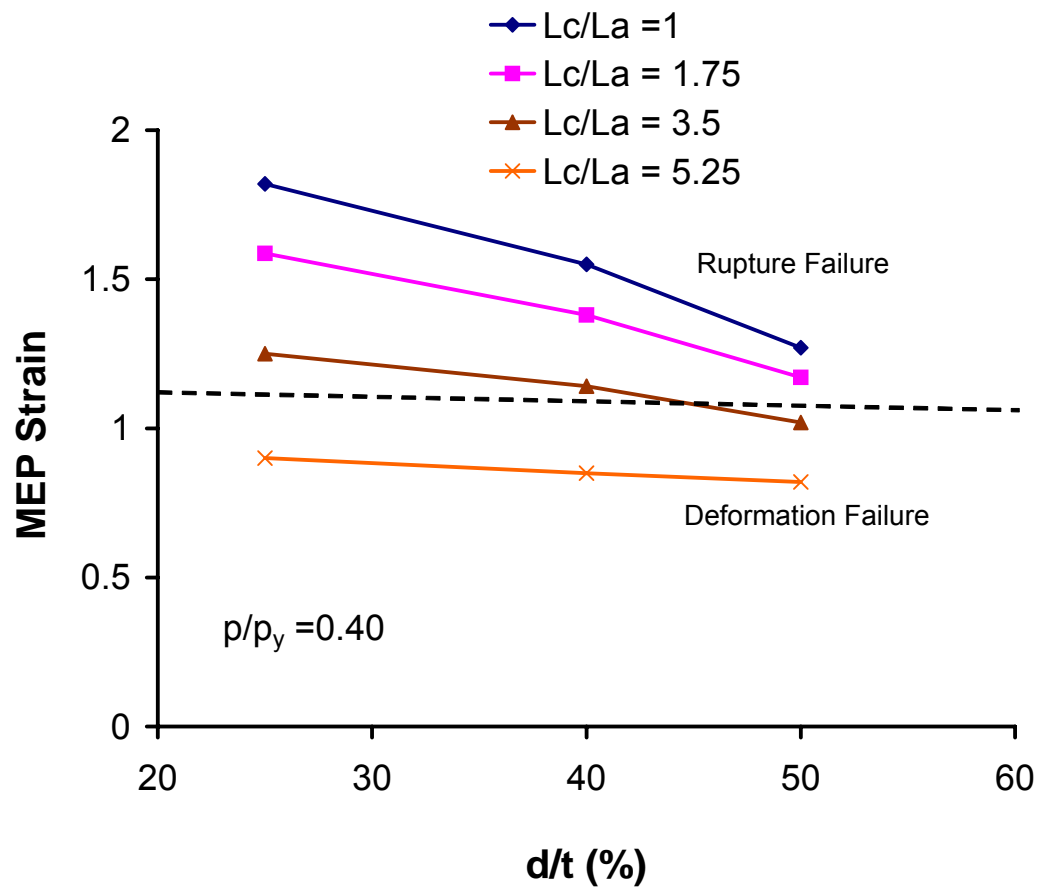Figure 7.21 Effect of *d/t* on MEP strain when p/p_y is 0.20

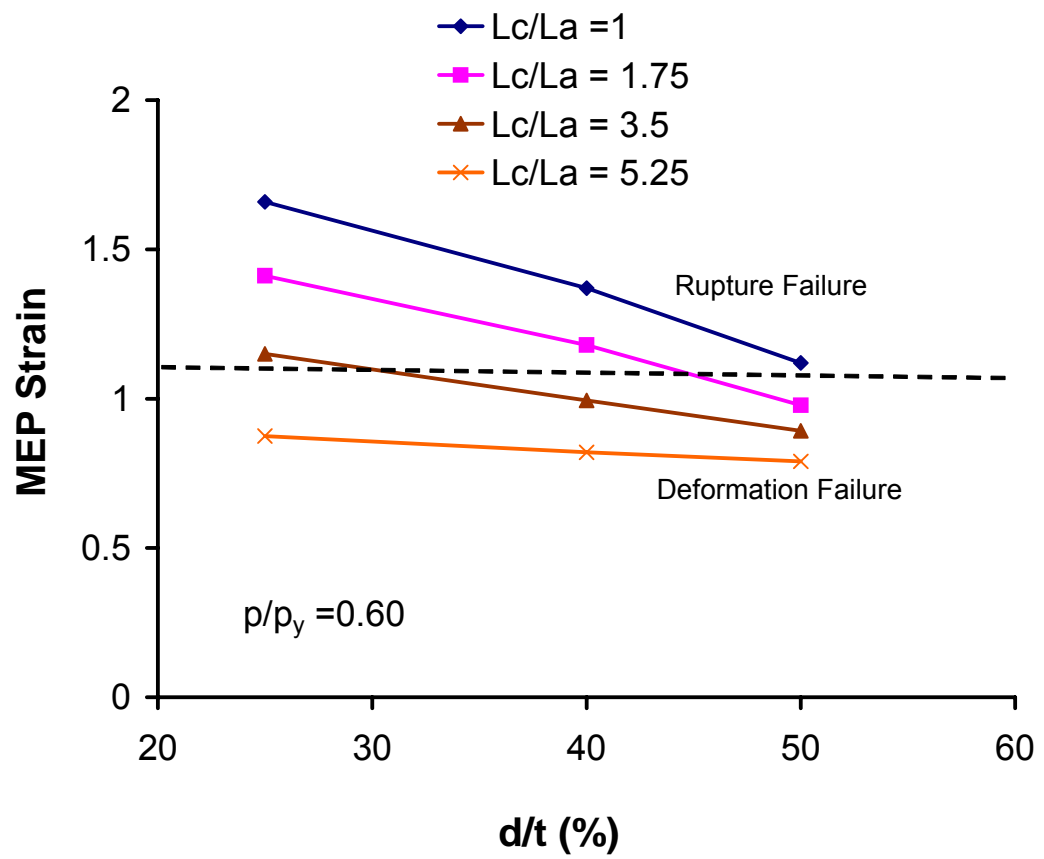Figure 7.22 Effect of *d/t* on MEP strain when p/p_y is 0.40

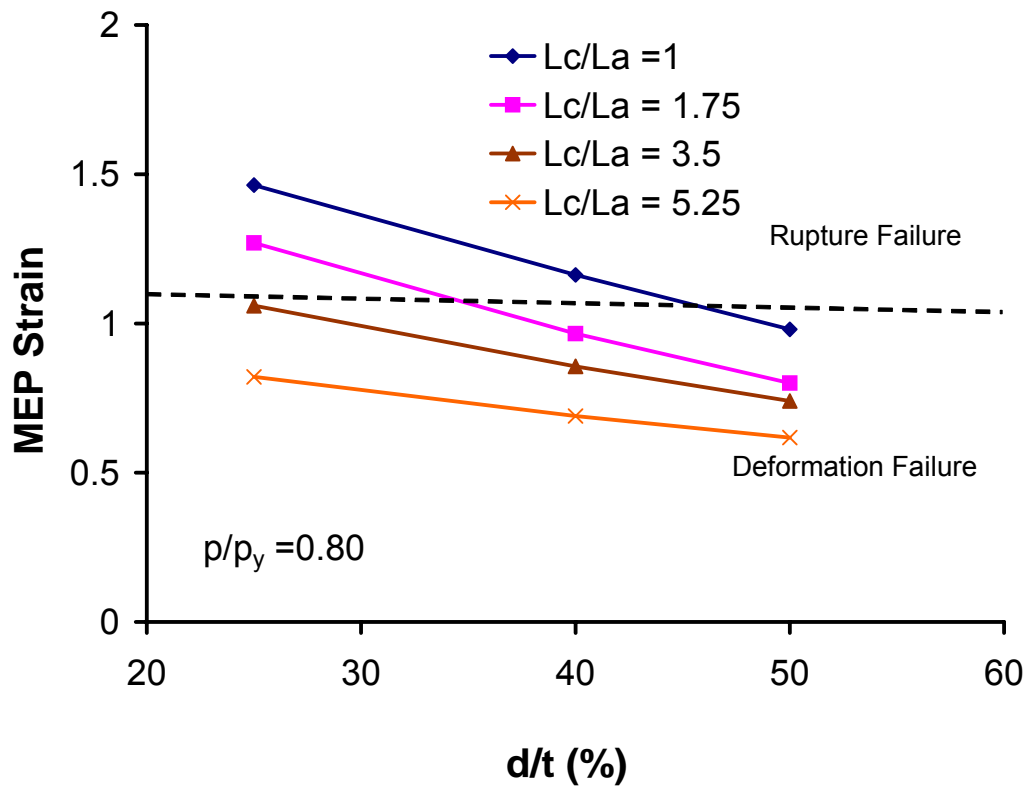Figure 7.23 Effect of *d/t* on MEP strain when p/p_y is 0.60

Figure 7.24 Effect of *d/t* on MEP strain when p/p_y is 0.80

8 Summary, Conclusions, and Recommendations
8.1 General

This chapter summarizes the research and findings, and provides conclusions on the work that has been done under the scope of this thesis, and recommends further work that is necessary and can be undertaken in future research.

8.2 Summary

The main objective of this project was to investigate the load-deformation behaviour and the effect of different parameters such as level of internal pressure, corrosion depth, and circumferential dimension of the corrosion on load-deformation behaviour of the externally corroded pipe subjected to combined monotonically increasing axial load and constant internal pressure. Furthermore, the modes of failure and effect of the above mentioned parameters on the mode of failure were also investigated.

A detailed parametric study using finite element (FE) method was conducted to accomplish the objectives of this research project. A general purpose FE code, ABAQUS/Standard version 6.6-1 (SIMULIA (2008)) was used for numerical modeling, analyses, and parametric study. The FE models for pipe specimens and coupon (material) specimen were validated using the laboratory test data.

8.3 Conclusions

Based on this study, a number of conclusions are drawn:

1) Increased internal pressure reduces the net load capacity (P_U) of the corroded steel pipe but increases the deformation ability (Δ_U) for the specimens having same corrosion geometry and the depth.

2) Increased corrosion depth reduces the net load capacity (P_U) for all the specimens having square and rectangular shape (L_C is 3.5 times of L_A) corrosion defect. It is observed from the experimental program that increased corrosion depth reduces

225

the deformation ability (Δ_U) for the specimen having square shape corrosion but increases the deformation ability (Δ_U) for the specimen having rectangular shape (L_C is 3.5 times of L_A) corrosion.

3) Increased circumferential dimension of corrosion reduces both the net load capacity (P_U) and the deformation ability (Δ_U) of the corroded steel pipe.

4) The ultimate net load decreases with increasing internal pressure, increasing circumferential dimension of the corrosion (L_c), and with increasing corrosion depth (d).

5) Two modes of failure: rupture failure and deformation failure were observed within the scope of the current research project.

6) The maximum equivalent plastic strain at contact decreases as internal pressure of the corroded steel pipe increases if d/t and $\dfrac{L_C}{L_A}$ ratios are kept unchanged. This implies that the increased level of internal pressure reduces the chance of rupture failure.

7) The maximum equivalent plastic strain at contact decreases with increasing $\dfrac{L_C}{L_A}$ ratio if d/t ratio and level of internal pressure are kept unchanged. This means that increased circumferential dimension of corrosion increases the chance of deformation failure and subsequently reduces the chance of rupture failure.

8) The maximum equivalent plastic strain at contact also decreases as d/t ratio increases if the level of internal pressure and $\dfrac{L_C}{L_A}$ ratio are not changed, that is, the chance of deformation failure increases with increasing depth of corrosion.

9) Both failure modes (deformation or rupture) should be avoided. The deformation type failure poses maintenance problems for the operating pipeline since the cleaning and inspecting instrument may not be able to pass through. The rupture failure is even more serious problem since a rupture in the field line pipe wall causes integrity and safety problem of pipe line structure and also creates environmental disaster. The parametric study completed in this work provided

226

guidelines on when these two failures are expected for API X46 grade pipe with D/t of 34.

8.4 Recommendations

This study provided a number of significant enhancements toward the objectives of the project. To the best of the author's knowledge, this study is the first of its kind and no other similar work has been carried out. In order to achieve more confidence in the understanding the behaviour and risk assessment of corroded pipes, more researches are recommended:

1) According to major codes and standards, when the depth of corrosion is more than 80% of the pipe wall thickness, that section of pipe cannot be assessed for remaining pressure strength and has to be repaired. In future studies the depth of corrosion can be extended up to 80% of pipe thickness for the investigation of the axial load-deformation behavoiur and modes of failure.

2) The circumferential dimension of the corrosion can be increased to such an extent that it covers the entire periphery of the pipe.

3) For completeness, a similar study can be done with the steel pipe having different material and geometric properties.

4) In the finite element model collars need to be modelled separately from the actual pipe wall, and hence proper interaction between collar and pipe wall can be taken into account.

5) A similar study to determine the influence of material behaviour in circumferential and longitudinal directions is necessary.

References

1) ASME B31G (1991). "Manual for Determining the Remaining Strength of Corroded pipelines, A Supplement to ASME B31 Code for Pressure Piping".

2) ASTM (2008). "ASTM Specification A 370-94: Standard Test Methods for Tension Testing of Metallic Materials."

3) Bai , Yong and Hauch, Soren (2001). "Collapse Capacity of Corroded Pipes under Combined Pressure, Longitudinal Force and Bending". International Journal of Offshore and Polar Engineering Vol. 11, No. 1, pp. 55-63.

4) Bjørnøy, O.H. and Sigurdsson, G. (2000). "Residual Strength of Corroded Pipelines, DNV Test Results". International Offshore and Polar Engineering Conference, Seattle, USA.

5) Bruschi, Roberto; Monti, Paolo; Bolzoni, Gainluca and Tagliaferri, Roberto (1995). "Finite Element Method as Numerical Laboratory for Analysis Pipeline Response under Internal Pressure, Axial Load, Bending Moment". ASME, OMAE – Vol. V, Pipeline technology, pp. 389-401.

6) Cook, R. D. (1981). "Concepts and Applications of Finite Element Analysis". Second Edition, John Wiley and Sons, New York.

7) Cosham, Andrew and Hopkins, Phil (2004). "The Assessment of Corrosion in Pipeline- Guidance in the Pipeline Defect Assessment Manual (PDAM)". Pipeline Pigging and Integrity Management Conference, Amsterdam, The Netherlands.

8) CSA Z662-07 (2007). "Oil and Gas Pipeline Systems". Canadian Standards Association.

9) DNV Recommended Practice (2004). "DNV-RP-F101, Corroded Pipelines". Det Norske Veritas.

10) Dorey, A.B; Murry, D.W and Cheng, J.J.R. (2006). "Critical Buckling Strain Equations for Energy Pipelines-a Parametric Study". Journal of Offshore Mechanics and Artic Engineering, Vol. 128, pp. 248-255.

11) Grigory, Stephen C. and Smith, Marina Q. (1996). "Residual Strength of 48-inch Diameter Corroded Pipe Determined by Full Scale Combined Loading Experiments". International Pipeline Conference – Vol 1, pp. 377 – 386, ASME.

12) Jeglic, Dr. Franci (2004). "Analysis of Ruptures and Trends on Major Canadian Pipeline Systems". National Energy Board, Calgary, Canada, http://www.neb.gc.ca/clf-nsi/rsftyndthnvrnmnt/sfty/pplnrptrs/nlyssrptrstrnds-eng.pdf, viewed on 15 May 2009.

13) Kiefner, J.F. and Vieth, P.H. (1990). "Evaluating Pipe: New Method Corrects Criterion for Evaluating Corroded Pipe". Oil and Gas Journal.

14) Kim, Jin Weon and Park, Chi Yong (2002). "An Experimental Study on the Evaluation of Failure Behaviour of Pipe with Local Wall Thinning". PVP-Vol. 440, Design and Analysis of Piping, Vessels and Components, pp. 9 -15.

15) Kolovich, Carolyn E. And Haines, Harvey (2004). "Analysis of US Liquid and Gas Incident Data". International Pipeline Conference, Calgary, Alberta, Canada.

16) Mohareb, ME; Elwi, AE; Kulak, GL; and Murry, DW. (1994)." Deformation Behaviour of Line Pipe". Structural Eng Rept No 22, Univ. of Alberta.

17) Mroz, Z. (1967). "On the Description of Anisotropic Work-Hardening". J. of Mech. Physics and Solics, Vol. 15, pp. 163 – 175.

18) National Energy Board (NEB) of Canada (2008). "Focus on Safety and Environment A Comparative Analysis of Pipeline Performance 2000-2006". http://www.neb.gc.ca/clf-nsi/rsftyndthnvrnmnt/sfty/sftyprfrmncndctr/fcsnsfty/ 2008/ fcsnsfty2008-eng.pdf, viewed on June 9, 2009.

19) Nicolella, Daniel P. and Smith, Marina Q. (1997). "Non-Linear Finite Element Prediction of Wrinkling in Corroded Pipe". Proceedings of the Seventh International Offshore and Polar Engineering Conference , Honolulu , USA, Vol. 11, pp. 343 – 348.

20) Noronha Jr., Dauro Braga; Benjamin, Adilson Carvalho and Andrade, Edmundo Queiroz de (2002). "Finite Element Models for the Prediction of the Failure Pressure of Pipelines with Long Corrosion Defects". Proceedings of IPC'02 4th International Pipeline Conference, Calgary, Alberta, Canada, pp.1751-1758.

21) Papavinasam, Sankara; Doiron, Alex; Revie, and R. Winston (2006). "Integrity Management of New Pipelines: Internal Corrosion Control". Corrosion NACExpo 2006, 61st Annual Conference and Exposition.

22) Rice, J. R.(1975). "Continuum Mechanics and Thermodynamics of Plasticity in Relation to Microscale Deformation Mechanisms". Constitutive Equations in Plasticity, Argon, A. S., Editor, MIT Press, Cambridge, Massachusetts.

23) Roy,S.; Grigory, S.; Smith, M.; Kanninen, MF.; Anderson, M. (1997). "Numerical Simulations of Full-Scale Corroded Pipe Tests with Combined Loading". Journal of Pressure Vessel Technology, Vol. 119, pp. 457 – 466.

24) Shim, D.J.; Choi, J.B.; Kim, Y.J.; Kim, J.W. and Park, C.Y. (2002). "Assessment of Local Wall Thinned Pipeline under Combined Bending and Pressure". ASME Pressure Vessels and Piping Conference, Vancouver, B.C, Canada.

25) SIMULIA (2008). "ABAQUS user's manuals". SIMULIA, Rising Sun Mills, Providence, RI, USA.

26) Smith, Marina Q. and Grigory, Stephen C. (1996). "New Procedure for the Residual Strength Assessment of Corroded Pipe Subjected to Combined Loads". International Pipeline Conference – Vol 1, pp. 387 – 400, ASME.

27) Smith, Marina Q.; Nicolella, Daniel P.; Waldhart, Christopher J. (1998). "Full-Scale Wrinkling Tests and Analyses of Large Diameter Corroded Pipes". International Pipeline Conference, ASME, Vol. 1, pp. 543 – 551.

28) The Pipeline Operators Forum (POF) (2005). "Specifications and requirements for intelligent pig inspection of pipelines". Version 3.2.

29) Transportation Safety Board (TSB) of Canada (1997). "TSB Reports- Pipeline 1997-P97H0024".http://www.tsb.gc.ca/eng/rapports-reports/pipeline/1997/ p97h0024/ p97h0024.asp, viewed on June 9, 2009.

Appendix A: Load-Deformation Behaviour of X46 Corroded Steel under Cyclic Loading

SP40d25-C
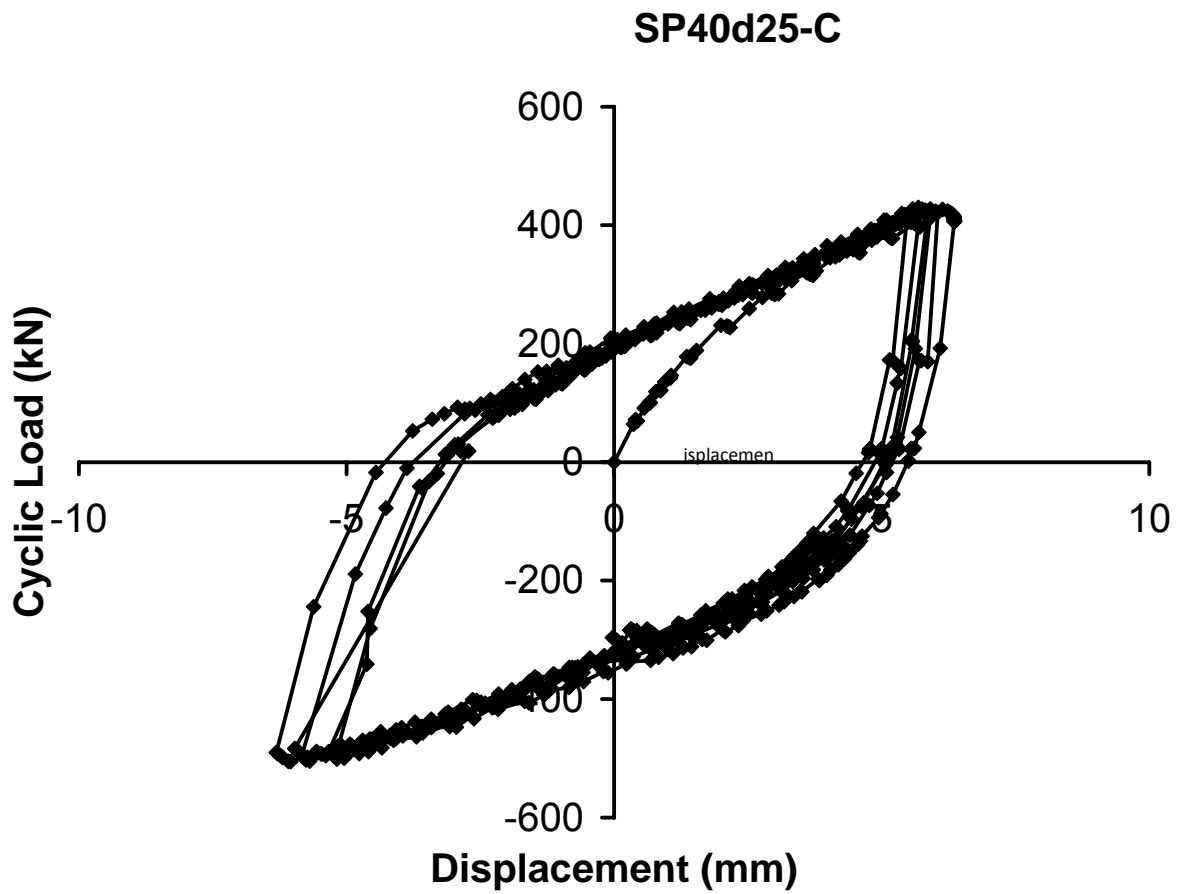
Figure A.1 Load vs. displacement for SP40d25 under cyclic load
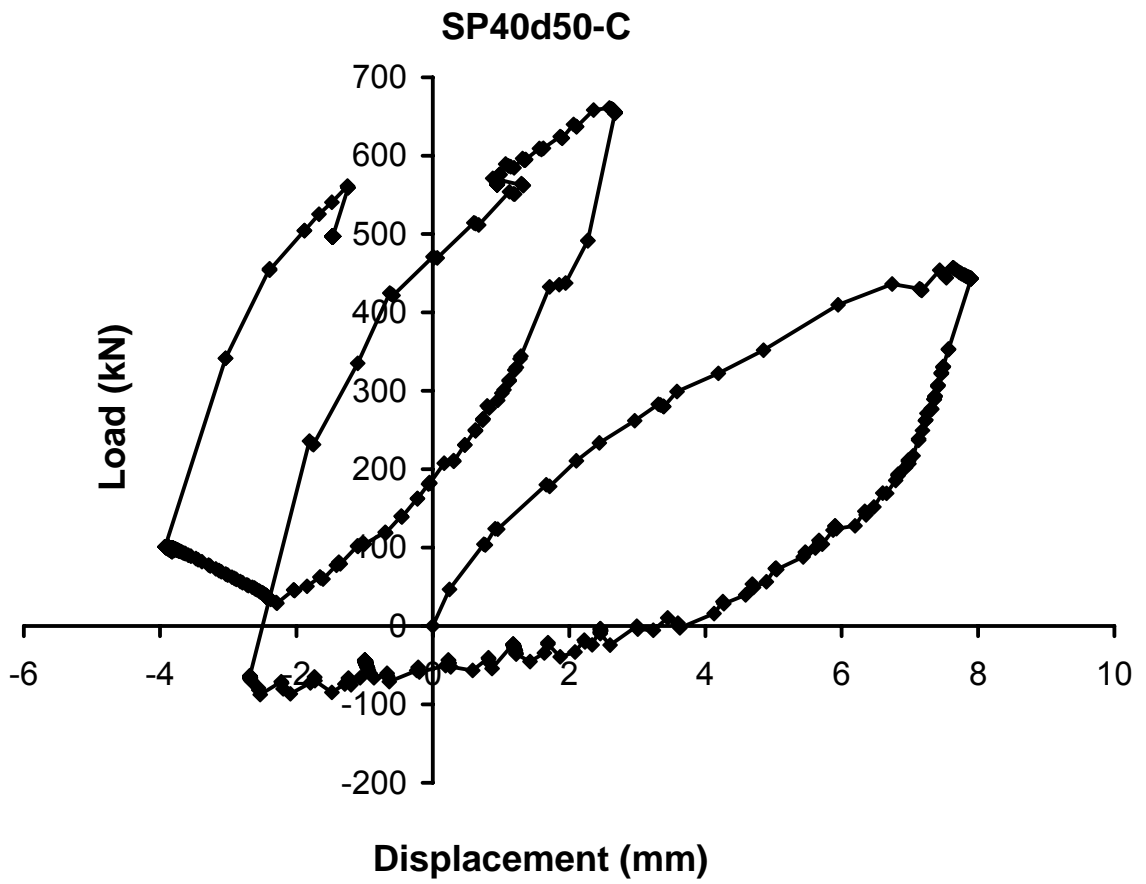
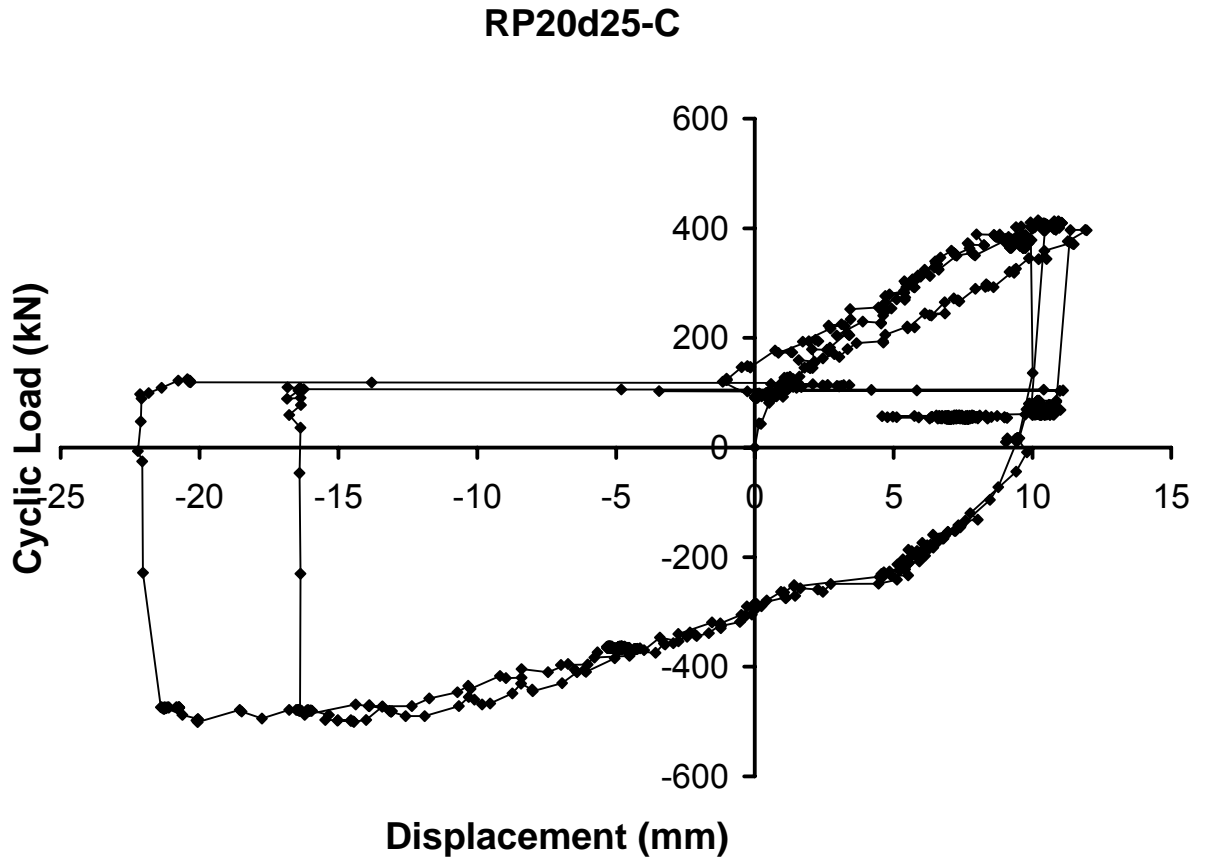Figure A.2 Load vs. displacement for SP40d50 under cyclic load

RP20d25-C

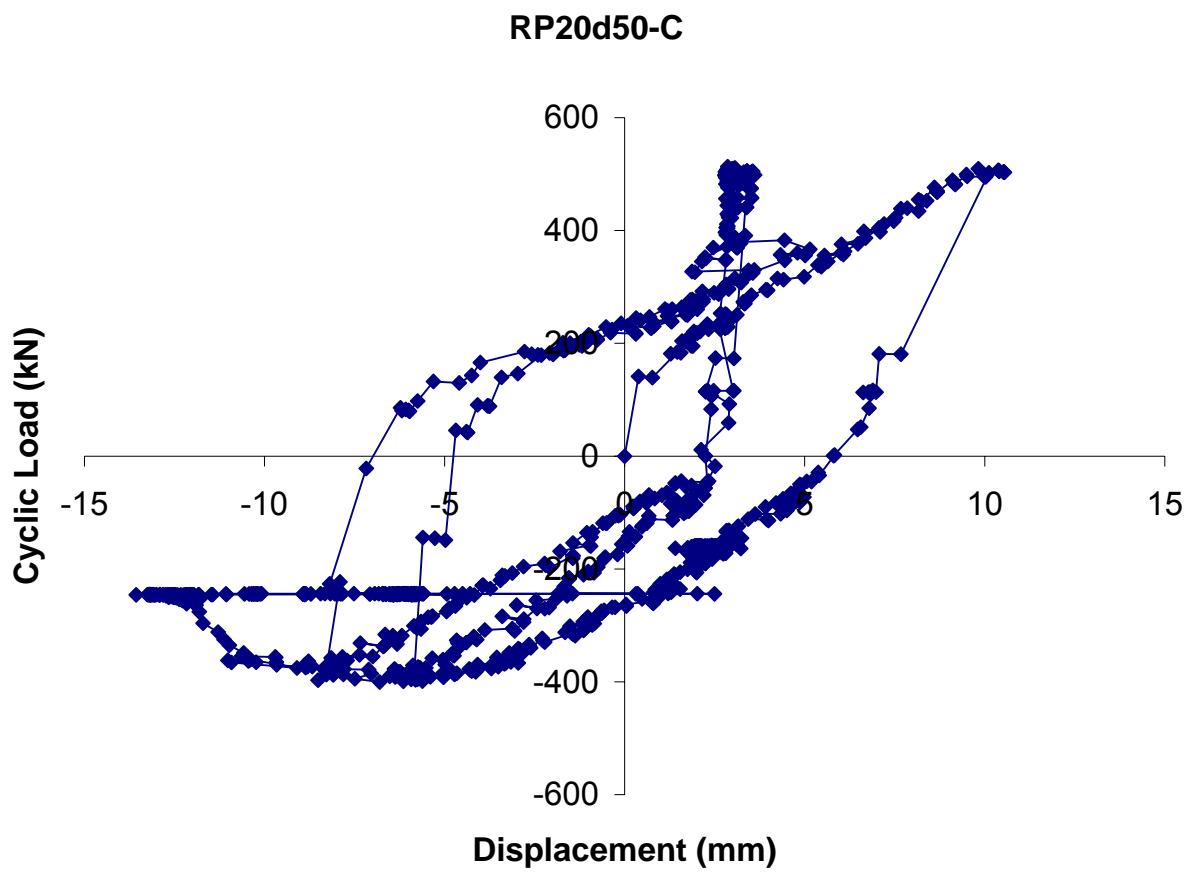Figure A.3 Load vs. displacement for RP20d25 under cyclic load

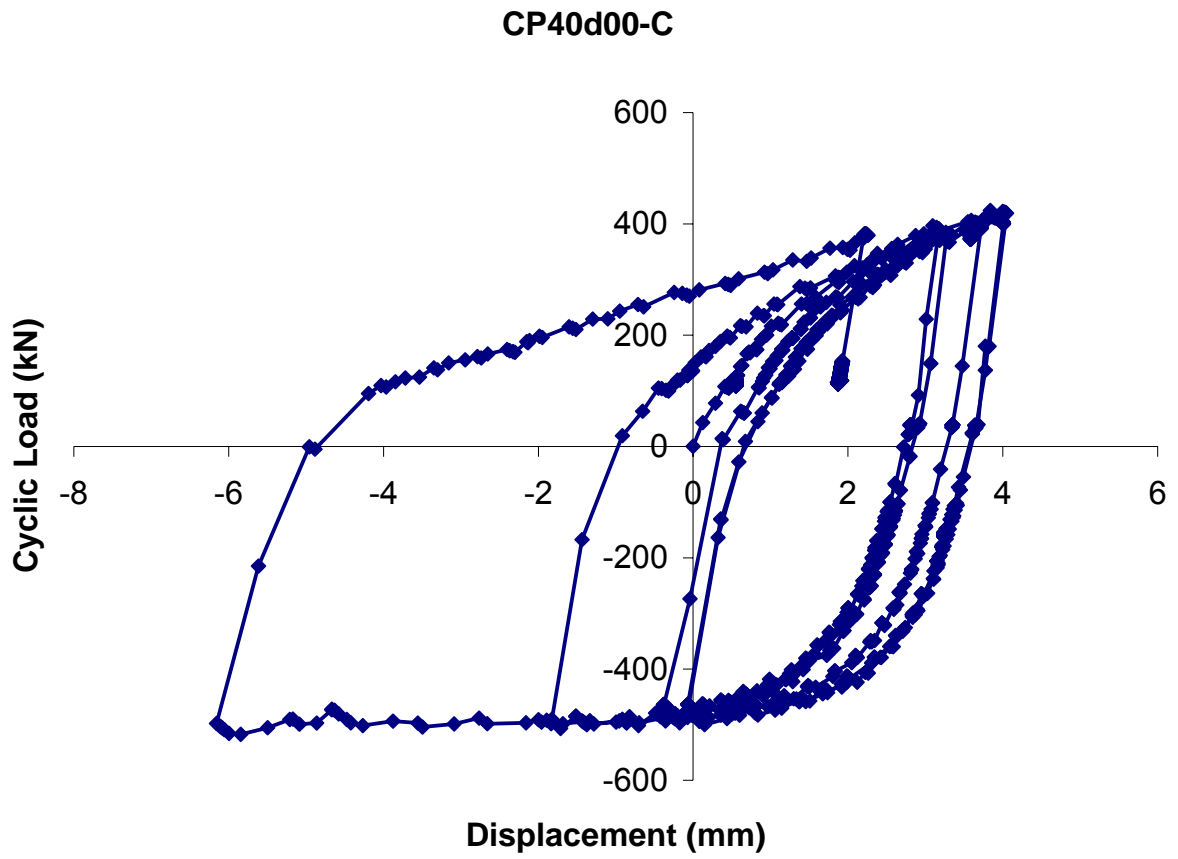Figure A.4 Load vs. displacement for RP20d50 under cyclic load

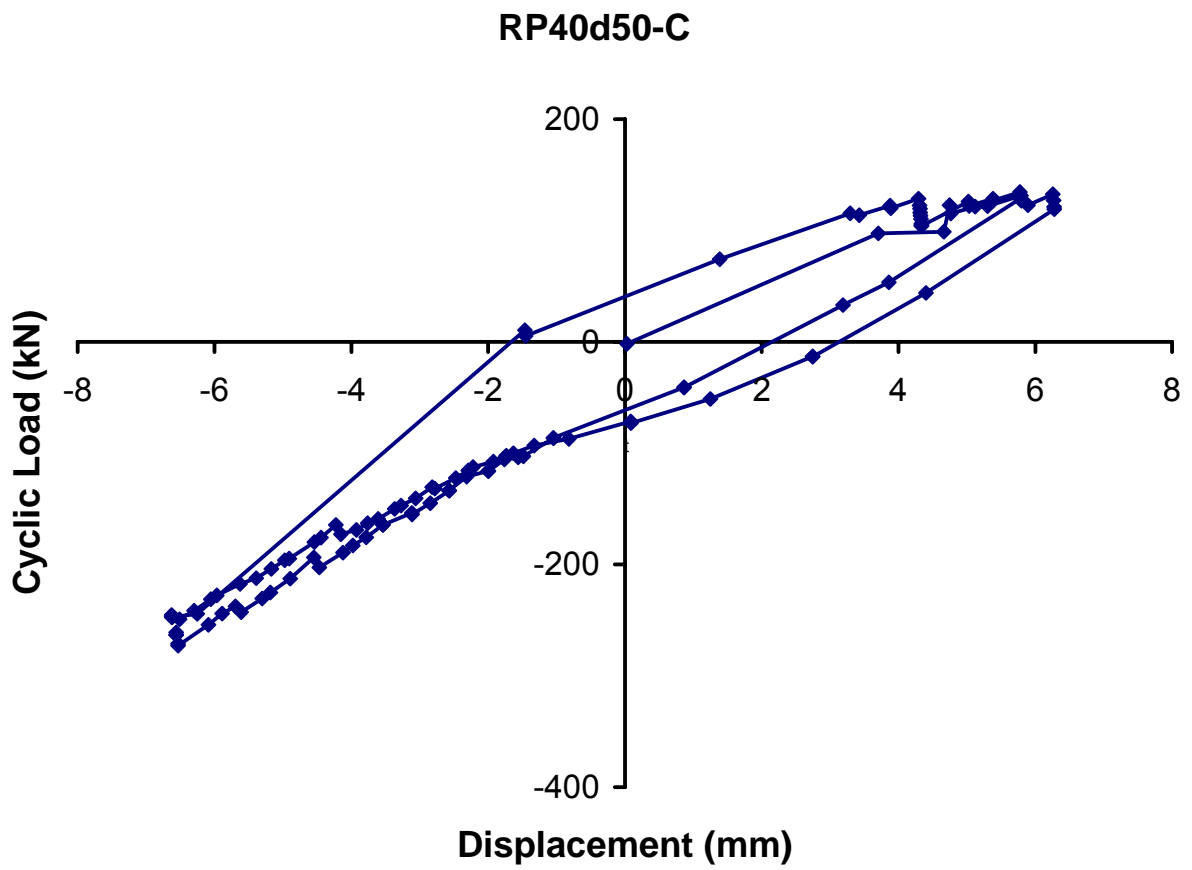**CP40d00-C**

Figure A.5 Load vs. displacement for CP40d00 under cyclic load

Figure A.6 Load vs. displacement for RP40d50 under cyclic load
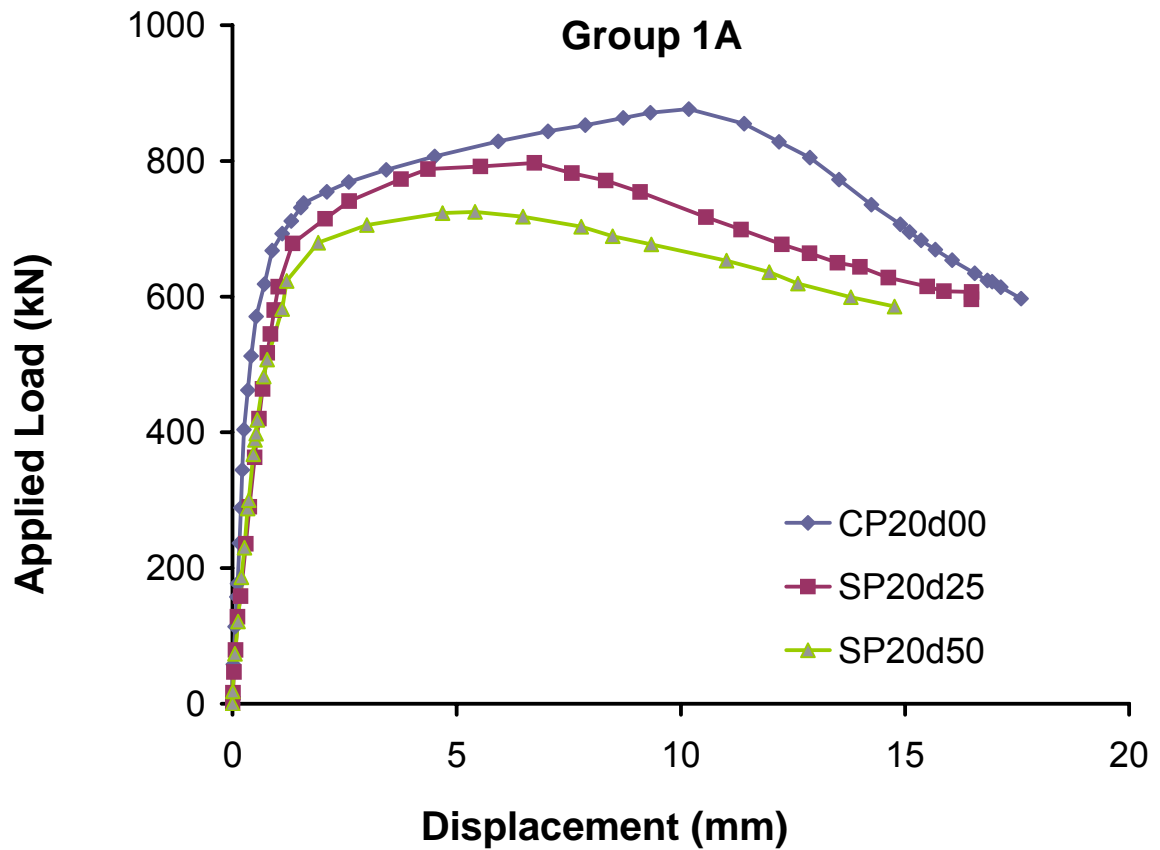
Appendix B: Applied Load-Deformation Behaviour

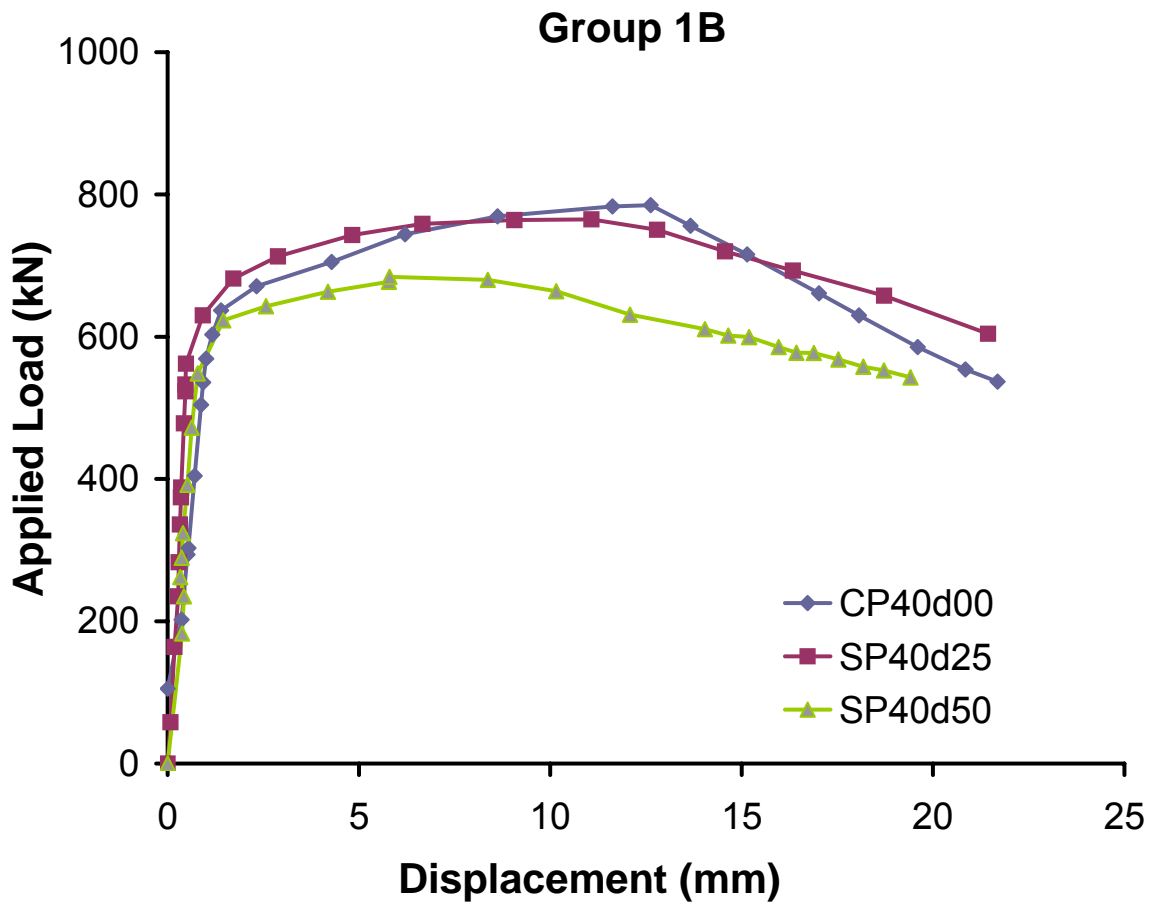Figure B.1 Applied load vs. displacement for Group 1A specimens

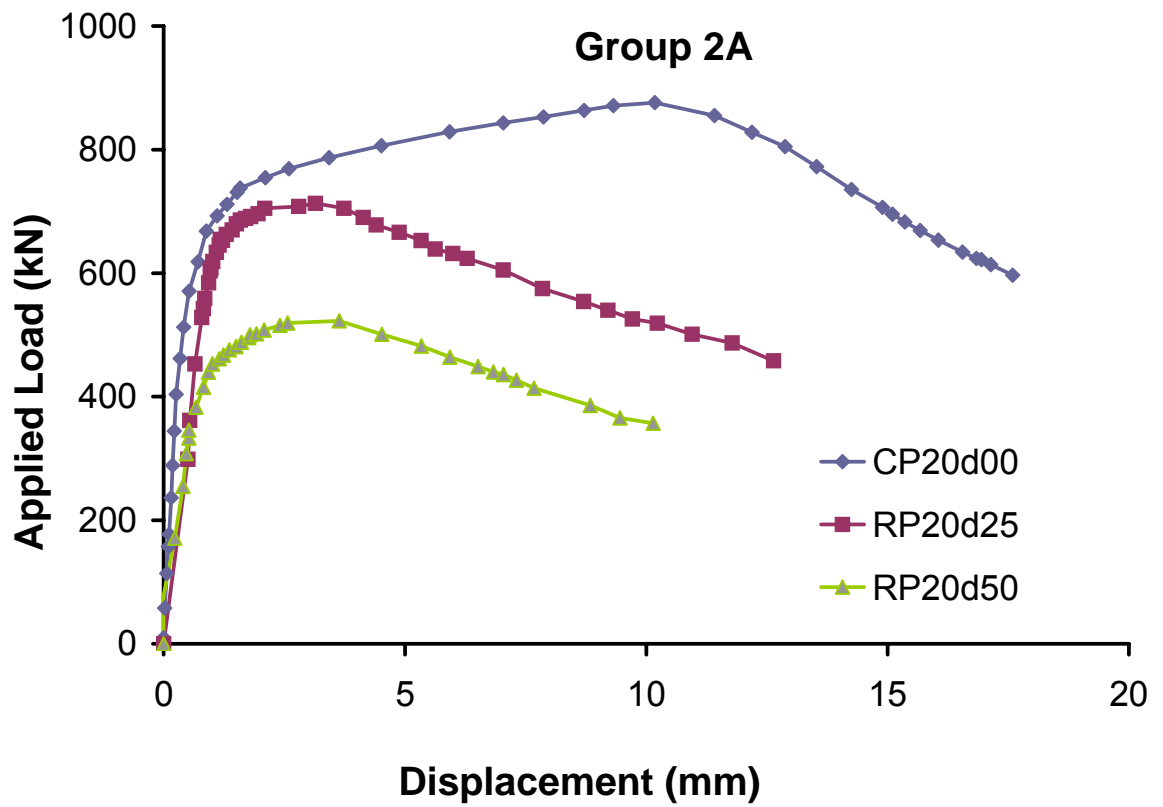Figure B.2 Applied load vs. displacement for Group 1B specimens

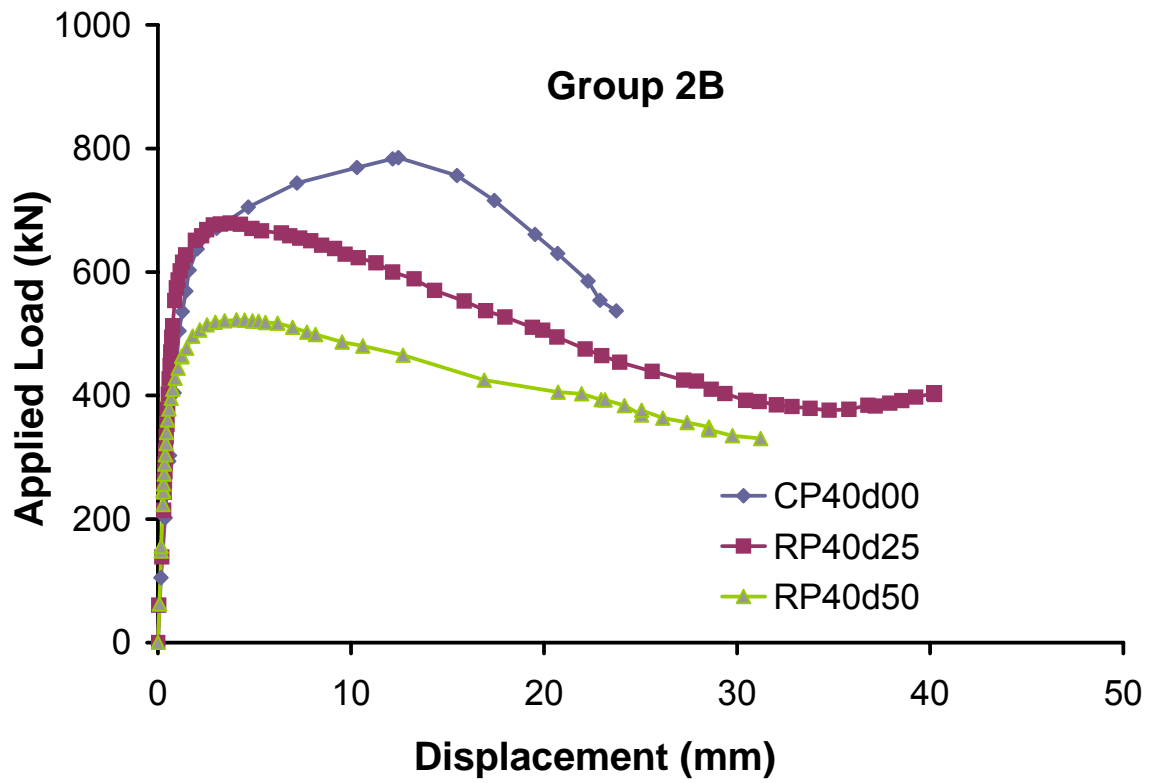Figure B.3 Applied load vs. displacement for Group 2A specimen

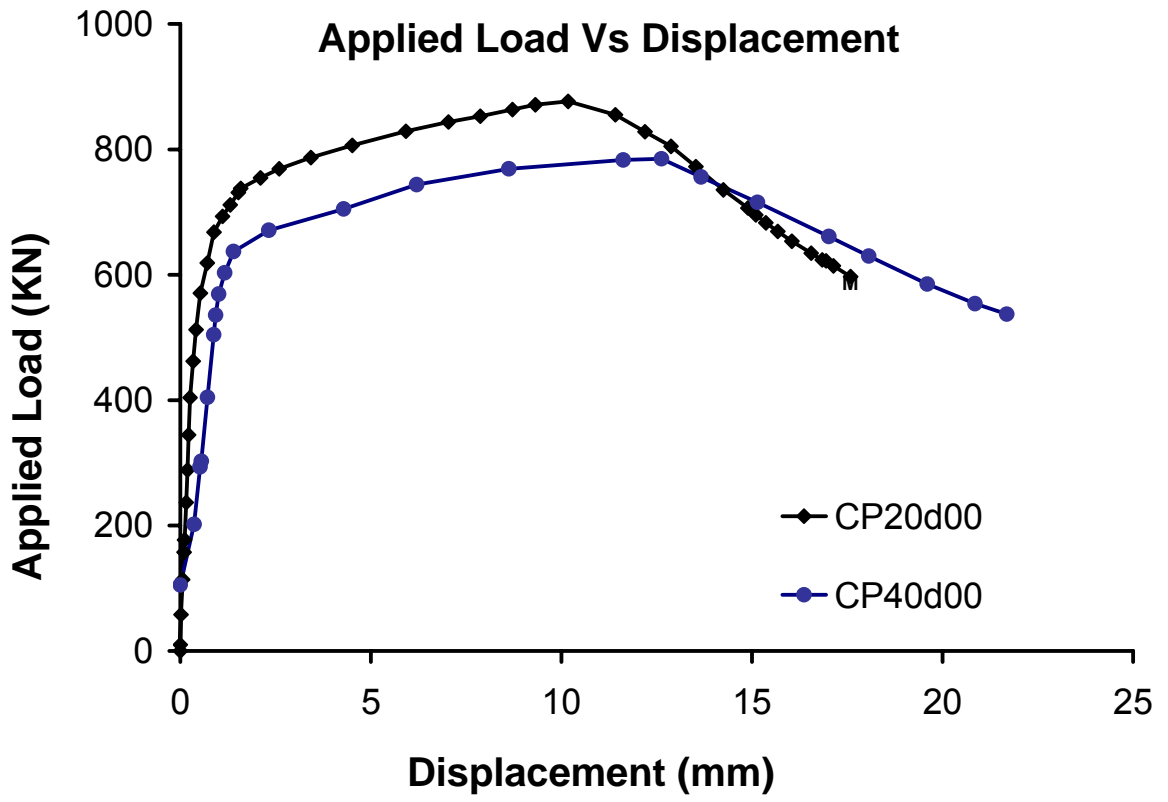Figure B.4 Applied load vs. displacement for Group 2B specimen

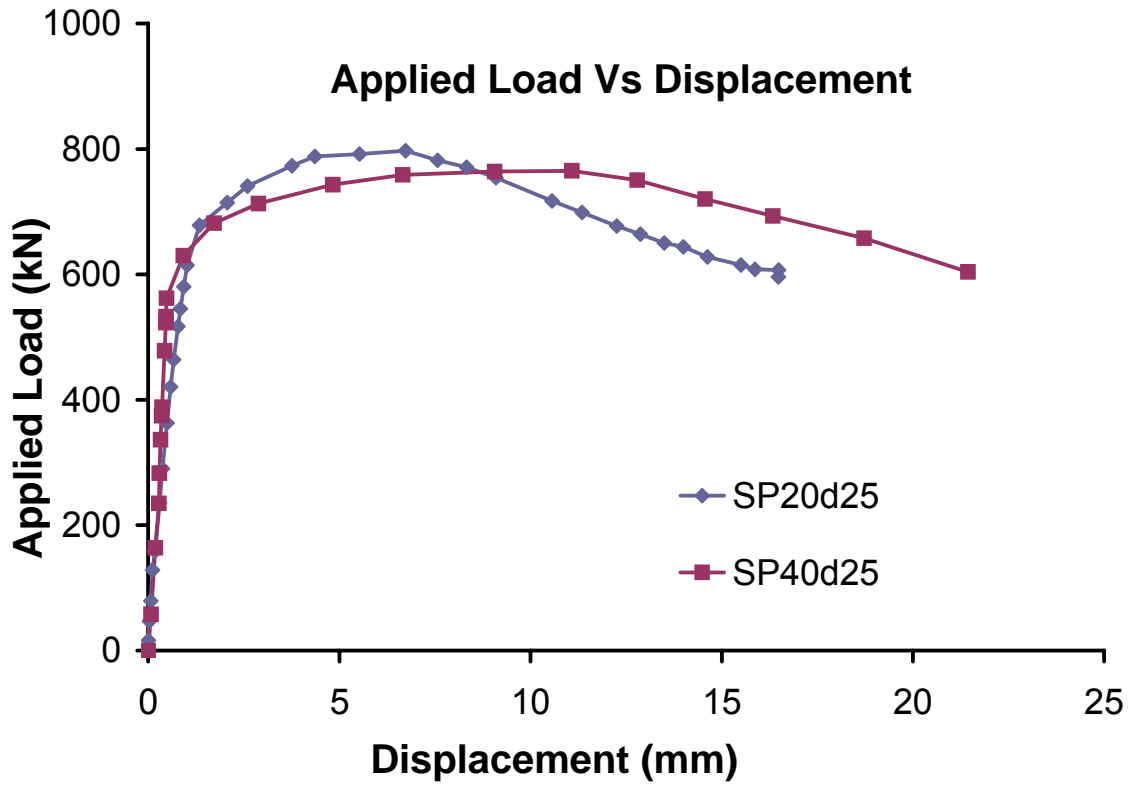Figure B.5 Effect of internal pressure on specimen CP20d00 and CP40d00

Figure B.6 Effect of internal pressure on specimen SP20d25 and SP40d25
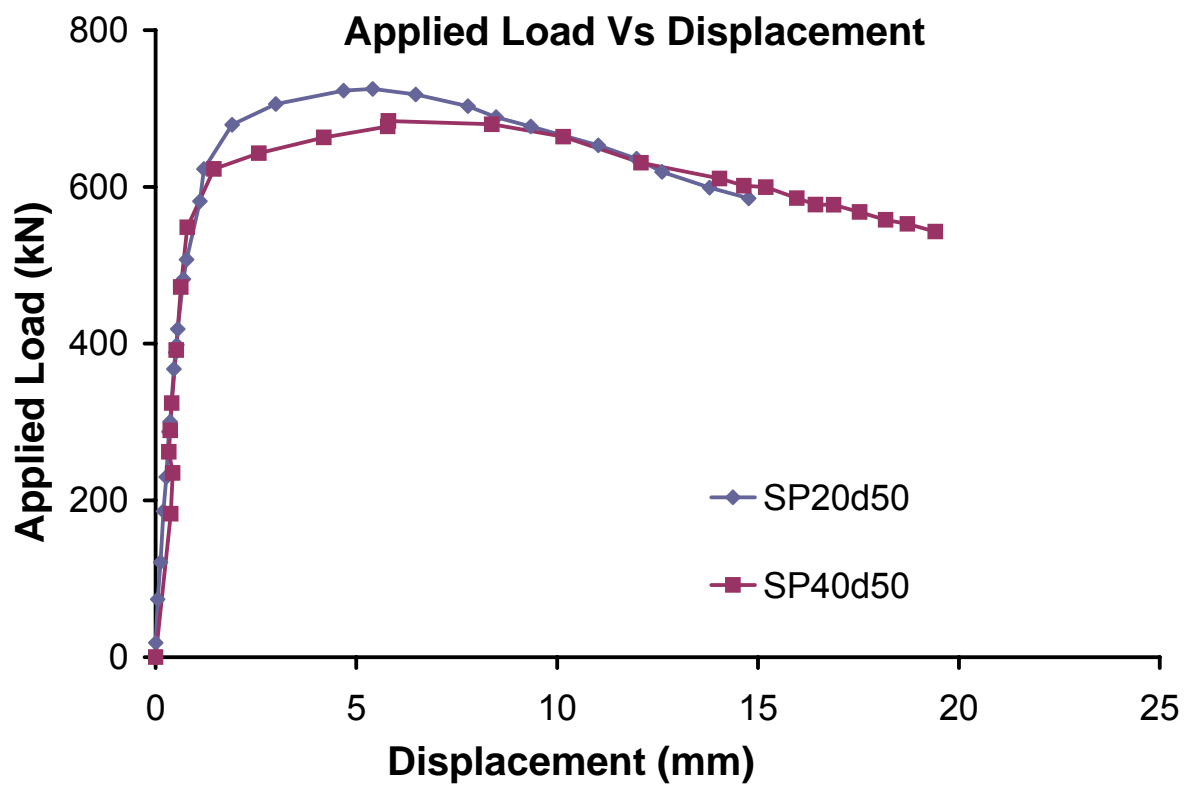
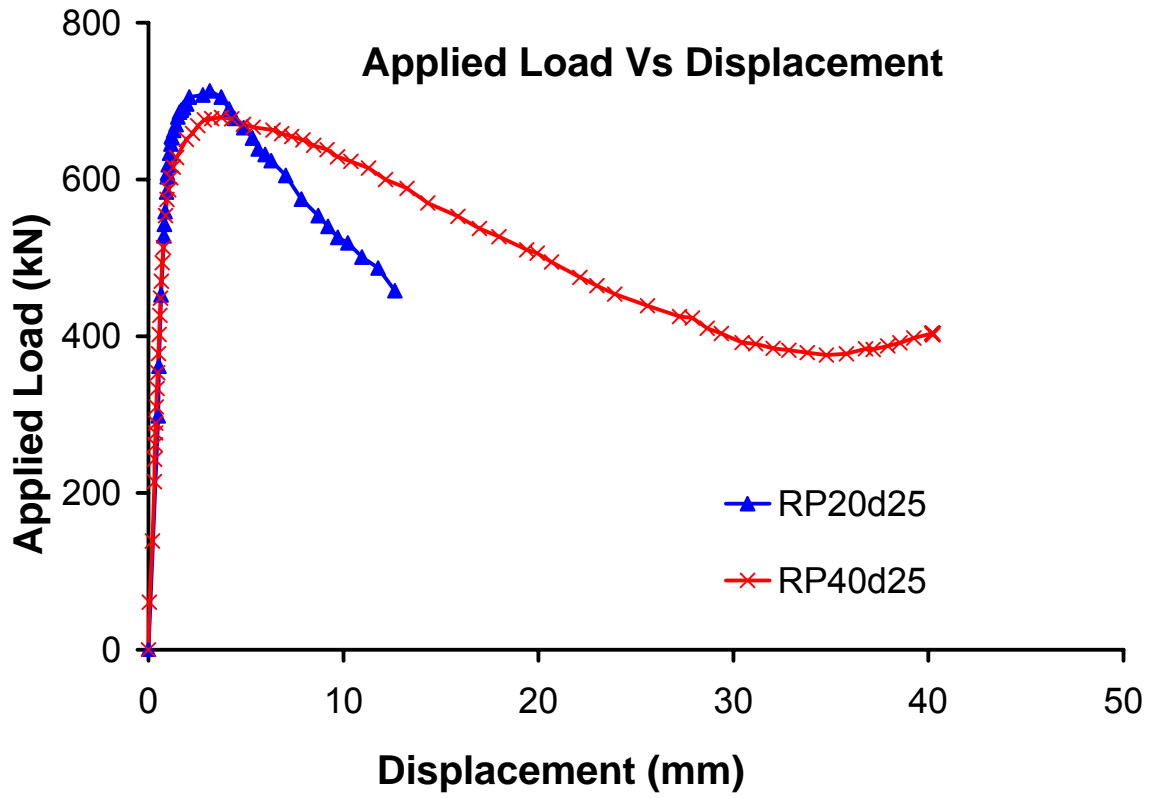Figure B.7 Effect of internal pressure on specimen SP20d50 and SP40d50

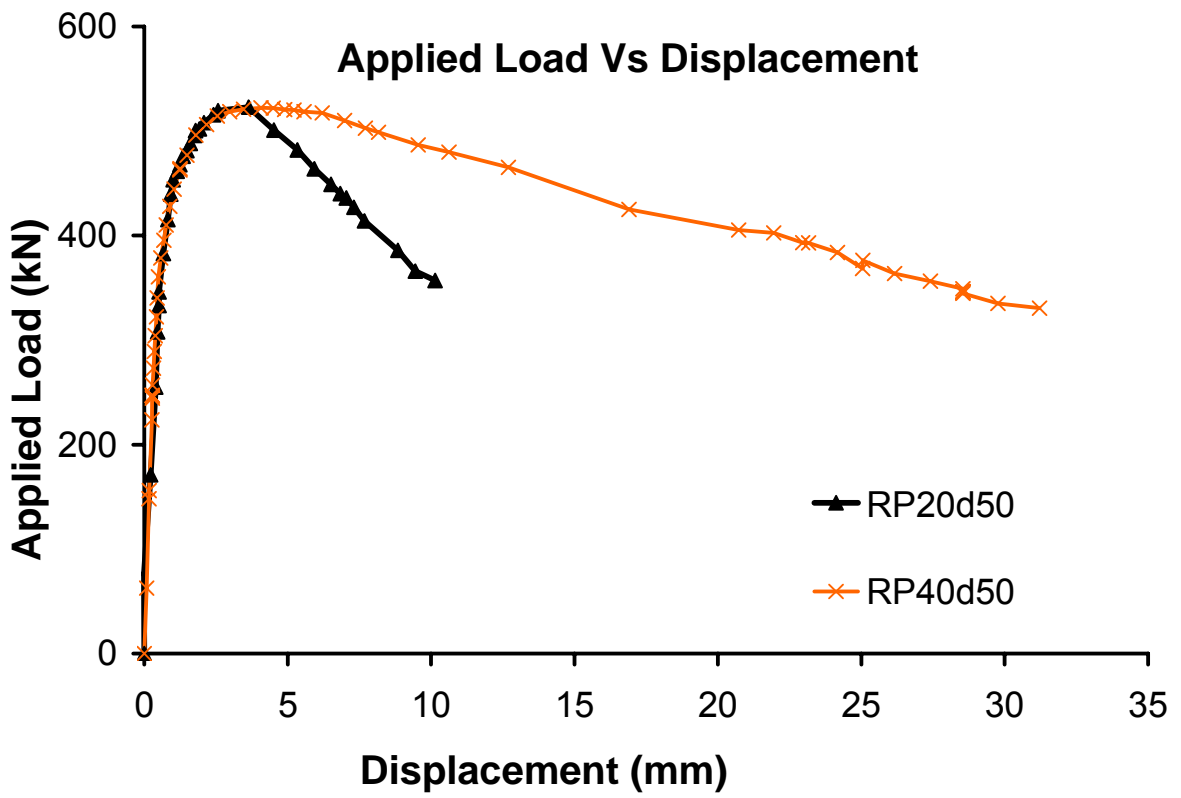Figure B.8 Effect of internal pressure on specimen RP20d25 and RP40d25

Figure B.9 Effect of internal pressure on specimen RP20d50 and RP40d50

Appendix C: Letters of Permission
C.1 Permission from The Pipeline Operators Forum

Hello Halima,

Sorry for the late reply, but I am travelling and had no access to the mail for some days. On your request; feel free to use some of the documentation, but if you modify figures or other items, also please indicate this. If you thesis is available for us, I would appreciate a copy.

Kind Regards,
POF-admin (Peter van der Veer)

On 14/05/2009, **Dewanbabee H** <dewanba@uwindsor.ca> wrote:

Dear Sir:

I would like to use Figure 1: Location and dimensions of metal loss anomaly and Figure 2: Graphical presentation of metal loss anomalies per dimension class from your paper "Specifications and requirements for intelligent pig inspection of pipelines" Version 3.2, January 2005 in the Literature Review Chapter of my master's thesis paper. I will be submitting my thesis in 3 weeks time. I will be grateful to you if you allow me to use those figures in my thesis paper.

Regards,

Halima Dewanbabee

M.A.Sc Candidate

Department of Civil and Environmental Engineering

University of Windsor

Windsor, ON

Canada

C.2 Permission from ASME

Dear Mr. Dewanbabee,
It is our pleasure to grant you permission to publish the following ASME Figure 5 from "New Procedure for the Residual Strength Assessment of Corroded Pipe Subjected to Combined Loads," by Smith, Marina Q. and Grigory, Stephen C, International Pipeline Conference, Vol 1, pp. 387-400, cited in your letter for inclusion in a publication entitled Behaviour of Corroded X46 Steel Pipe under Internal Pressure and Axial Load to be published by University of Windsor. As is customary, we request that you ensure proper acknowledgment of the exact sources of this material, the authors, and ASME as original publisher.

In accordance with ASME policy, this permission is contingent upon payment of a royalty fee of US$30 for 2 figures ($20.00 for the first figure/table, $10 thereafter). This is solely charged to non-authors of the requested ASME papers. We accept payments on all major credit cards such as: Visa, MasterCard, American Express, Discover, and Diners Club, or by check payable to ASME. Please send payment to the attention Michelle DeBlasi, ASME Accounting, 22 Law Drive, Fairfield, NJ 07007, and indicate A/C# 1-1150-0000-4303. Should you have any questions regarding payment form or transfer, please contact Ms. DeBlasi; P: 973-244-2268, F: 973-882-4924; E:deblasim@asme.org.

Many thanks for your interest in ASME publications.

Sincerely,
Beth Darchi
Copyrights & Permissions
ASME International
Three Park Avenue
New York, NY 10016
P: 212-591-7700
F: 212-591-7292
E: darchib@asme.org

>>> <webmaster@asme.org> 6/17/2009 5:13 AM >>>

ASME PUBLICATIONS PERMISSION REQUEST FORM HAS BEEN SUBMITTED:

ASME Publication Title: New Procedure for the Residual Strength Assessment of Corroded Pipe Subjected to Combined Loads
Complete List of Authors: 26)Smith, Marina Q. and Grigory, Stephen C
Paper Title (Conference/Journal): International Pipeline Conference
Paper Number (Conference):   International Pipeline Conference Vol 1, pp. 387 - 400
Volume Number (Journal):   0
Page(s) in the publication of

the permission request: 387
Year of Publication: 1996
I would like to...   Republish in a Doctoral Thesis
Portion to be used: Figure/Table
List Figure Numbers: 5
List Table Numbers: 0
Number of Copies:
Usage: Print
Title of outside publication: Behaviour of Corroded X46 Steel Pipe under Internal Pressure and Axial Load
Publisher: University of Windsor
Comments: I want to use these figures in the literature review part of my master's thesis paper
First Name: Halima
Last Name: Dewanbabee
Address Line 1:   University of Windsor
Address Line 2:   401 Sunset Ave.
City: Windsor
State: Ontario
Zip: N9B 3P4
Phone: 519 253 3000 - 2549
Email: dewanba@uwindsor.ca

Vita Auctoris

Name:	Halima Dewanbabee
Place of Birth:	Dhaka, Bangladesh
Year of birth:	1975
Education	Bangladesh University of Engineering & Technology (BUET), Dhaka, Bangladesh. 1995-2000, B.A.Sc., Civil Engineering